PROGRAMME AND ABSTRACTS

Intermetallics 2017

International Conference

02–06 October 2017

Educational Center Kloster Banz • Germany

www.intermetallics-conference.de

Dear Colleagues and Friends,

Following the first two successful conferences in this series, it is again our pleasure to welcome you to the Intermetallics 2017 Conference at the Educational Center Kloster Banz, Germany.

Materials based on intermetallic phases – Intermetallics for short – constitute a new class of materials, which encompasses alloys for structural as well as for functional applications. With a beneficial combination of high strength, low density and excellent corrosion resistance, they are specifically suited for applications at high temperatures and in severe environments. As some intermetallic phases show unique physical properties, they are also of interest for various functional applications. In addition, their possible appearance and thermodynamic stability in High Entropy Alloys (HEAs) and their potential use as strengthening second phases in Compositionally Complex Alloys (CCAs) are recent scientific issues which are addressed at Intermetallics 2017 as well.

The choice of local organisers and members of the international advisory board has brought together a total number of 110 presentations spanning from fundamental research towards application-oriented subjects. Following the feedback of the participants of the previous conferences, the number of parallel sessions has been substantially reduced. Also the number of sessions devoted to specific classes of intermetallic materials has been reduced, thus, giving more room for sessions of more general scope such as processing, corrosion, modelling and phase stability. A high-profile poster session rounds off the conference.

Following the last successful educational seminar, a "School on mechanical behavior of intermetallic phases" specifically devoted to young researchers precedes the conference.

The conference again takes place at Kloster Banz in the northern part of Bavaria near Bamberg. As the cloister is situated in a remote place above the valley of the river Main, we believe this to be the ideal place for conferences with its good infrastructure and relaxing atmosphere.

We are delighted to welcome you again in Kloster Banz,

Your Intermetallics 2017 Organising Team

Registration fees

University/institute	600 EUR
Industry	750 EUR
Student	300 EUR
Accompanying person*	150 EUR
Workshop: School on mechanical behaviour of intermetallic phases **	included

Social programme***

Get together, 02 October	included
Bus tour to Bayreuth with conference dinner, 05 October	included

*   Get together and conference dinner is included.
**   Number of participants limited and only for students.
***   Registration for the social programme is required.

General terms and conditions
Please find our General Terms and Conditions at **www.intermetallics-conference.de**.

Opening hours

Check-In	Monday	08:00 a.m.–20:00 p.m.
	Tuesday	08:30 a.m.–17:00 p.m.
	Wednesday	08:30 a.m.–18:00 p.m.
	Thursday	08:30 a.m.–14:00 p.m.
	Friday	08:30 a.m.–12:00 p.m.

Internet
Voucher for Wireless-Lan are available at the registration desk of Kloster Banz.

Certificate of attendance
Certificates of attendance will first be made available on the last day of the conference at the check-in desk.

Poster prizes
The three best posters will be awarded with 300 EUR each.

Poster Session
Posters will be rated on Tuesday, 03 October, 19:00 p.m. Authors are requested to be present at their posters during the poster session. Drinks and finger food will be served during the poster session.

Pinboards will be numbered. The pinboards are only to be used with the designated pins. You will find your poster number in the programme book on page 17–18.
Please note that all posters should be hanging on Tuesday, 03 October, by 16:00 p.m. and be removed at the latest by Friday, 06 October, 11:00 a.m. Posters that have not been removed by that time will be considered as waste.

Catering
Foods and drinks during the breaks will be provided.
The restaurant "Klosterschänke" is directly located on the premises of Kloster Banz and is open daily from 10:00 a.m.–22:00 p.m..
For your information: the closest city with alternative restaurants is Bad Staffelstein, which is 5.5 km away (approximately 1 hour by foot, 7 minutes by car).

Smoking
Smoking is prohibited inside the entire conference centre.

Taxi
Taxi Dütsch • Phone +49 9573 52 06/+49 9571 52 06

Price from Bad Staffelstein to Kloster Banz	about 10 EUR*
Price from Lichtenfels to Kloster Banz	about 13 EUR*

* Prices are subject to change.

Submitting your presentation/technical information
Please prepare your presentation as PDF, MS Office Power-Point2007, 2010 for Windows or key for Macintosh DVD in 4:3 aspect ratio.

A presentation notebook with a PDF reader and MS Office Power-Point 2010/2007 will be provided. Notebook, presenter and laser pointer will be available at the speaker's podium in the lecture hall. The use of personal notebooks is possible upon agreement. However, it may interrupt the flow of the programme in the lecture hall. You will be assisted by a technical supervisor.

To guarantee a smooth running programme please upload your presentation on time – at least 2 hours before your presentation starts.

For submission, please use a USB flash drive, CD or DVD disc that is not protected by any software. Professional staff and equipment will be available for you to arrange and preview your presentation.
Please note: certain encodings for video and audio files could lead to technical problems.
....

Time Allotment
Please prepare your presentation for the allotted amount of time. Chairs and moderators may interrupt should you overrun your time limit.

Allotted time is assigned as follows (speaking + discussion time):
1. Invited talk   20 + 5 minutes discussion
2. All other single-session and parallel session talks   15 + 5 minutes discussion

Get together* • Monday, 02 October
Come together for drinks and snacks. Enjoy the evening and allow yourself interesting conversations with colleagues, old friends and new acquaintances.

18:30 p.m.	Welcome
20:00 p.m.	Opening
20:30 p.m.	TiAl Alloy Technology Trends and Future Opportunities in Aircraft Engines Bernard P. Bewlay (Niskayuna, NY/US)

Bus tour to Bayreuth and conference dinner* • Thursday, 05 October
Enjoy the trip to Bayreuth with a guided tour through the "Festspielhaus" as well as the brewery "Brauerei Maisel". Afterwards take the chance to get in touch with colleagues and friends and have an enjoyable evening at the restaurant "Liebesbier". The conference dinner includes the awarding of the poster prizes aswell as the "Intermetallics Award". At around 21:15 p.m. the bus returns from Bayreuth to Kloster Banz.

Start	14:00 p.m. at Kloster Banz (car park)
Activities	15:15 p.m.–18:15 p.m. guided tours "Festspielhaus" and "Brauerei Maisel"
	18:15 p.m.–21:15 p.m. dinner and award ceremony
	21:15 p.m. departure to Kloster Banz
End	aprox. 22:30 p.m.
Fee	included in the conference fee (dinner & 3 drinks at the restaurant "Liebesbier")

* A registration is necessary.

Monday, 02 October School on mechanical behaviour of intermetallic phases*	Tuesday, 03 October	Wednesday, 04 October		Thursday, 05 October	Friday, 06 October
Seminar room 6	Seminar room 1	Seminar room 1	Seminar room 6	Seminar room 1	Seminar room 1
09:00–10:30	09:00–10:25	09:00–10:30		09:00–10:50	08:30–10:30
Session 1 Ductility and fracture of intermetallics p. 9	Mechanical behaviour of intermetallic phases I p. 10	Functional intermetallics/HEAs I p. 12		Titanium aluminides III p. 15	Corrosion I p. 16
Coffee break	Coffee break	Coffee break		Coffee break	Coffee break
11:00–12:30	10:55–12:40	11:00–12:30		11:20–12:40	10:45–11:55
Session 2 Experimental methods (with emphasis on high T) p. 9	Mechanical behaviour of intermetallic phases II p. 10	Functional intermetallics/HEAs II p. 12		Modelling/Laves phases p. 15	Corrosion II p. 16
Lunch	Lunch	Lunch		Lunch	Lunch
14:00–15:30	14:00–15:50	14:00–16:00	14:00–16:00	14:00–22:30	
Session 3 Dislocations and plastic deformation in intermetallics p. 9	Titanium aluminides I p. 10	Processing p. 13	High temperature intermetallics p. 13		
	Coffee break	Coffee break			
	16:20–18:20	16:30–18:30	16:30–18:30	Bus tour Bayreuth with guided tours and conference dinner p. 7	
	Phase stability p. 11	Titanium aluminides II p. 14	Iron aluminides p. 14		
	19:00–21:00				
	Poster session p. 17				

Foyer
18:30–20:00
Get together   p. 7
Seminar room 1
20:00–21:00
Opening talk   p. 9

* The school is especially intended for students and young scientists, the possible number of participants is limited. A registration is necessary.

09:00 a.m.–15:30 a.m. Seminar room 6	**School on mechanical behaviour of intermetallic phases**

09:00 a.m.–10:30 a.m.	Ductility and fracture of intermetallics Easo George (Oak-Ridge, TN/US)

The application of ordered intermetallic compounds for structural parts requires from a mechanical point of view a judicious balance of strength, deformability or ductility, as well as sufficient toughness. While strength at various temperatures and loading conditions may not be an issue (at least in close-packed structures), ductility is often a limiting factor. Therefore, in the present contribution origins of ductility and fracture in iron and nickel aluminides will be discussed. In particular, the impact of lattice imperfections such as (i) vacancies, (ii) antisite defects stemming from alloy stoichiometry and (iii) grain boundaries and their chemistry will be presented. Finally, environmental effects such as hydrogen embrittlement will be discussed.

....

10:30 a.m.–11:00 a.m.	*Coffee break*

....

11:00 a.m.–12:30 p.m.	Experimental methods (with emphasis on high T) Martin Heilmaier (Karlsruhe/DE)

Intermetallic compounds for usually exhibit a beneficial combination of rather low density, high strength and creep resistance and outstanding oxidation resistance making them attractive candidates for high temperature structural applications. However, they often lack of sufficient ductility or toughness at ambient temperatures. Quite a number of experimental techniques exist for characterizing their mechanical properties over a broad temperature range, such as testing of compressive and tensile creep, 3 and 4 point bending, fracture toughness, to mention the most important one. The capabilities of these techniques will be briefly introduced. Discussion will focus on practical aspects, e.g. how to carry out a high quality test to obtain sound data, limitations and possibilities. A few experimental examples round up the presentation.

....

12:30 p.m.–14:00 p.m.	*Lunch*

....

14:00 p.m.–15:30 p.m.	Dislocations and plastic deformation in intermetallics Alain Couret (Toulouse/FR)

Dislocations are the main carriers of plasticity in intermetallic compounds. This presentation, thus, focuses in the first part on the crystallographic nature of dislocation slip in the most common aluminides based on Ti, Ni and Fe. This includes the introduction of ordinary, superlattice and partial dislocations, including the relevant dissociation reactions. Next, transmission electron microscopy is introduced as the most commonly accepted method to analyse dislocations in crystalline materials. Subjects like (i) the origin of contrast, (ii) Burgers vector and (iii) dislocation characteristics determination will be explained. In the 3rd part deformation mechanisms as a function of temperature will be discussed, starting from dislocation glide at low temperature over cross-slip and dynamic strain aging to climb controlled creep at high temperatures. The role of twinning on deformation of intermetallics is also included. In the final part, alloy strengthening will be tackled, discussing the interaction between dislocations and other microstructural defects such as solute atoms, precipitates and interfaces.

....

18:30 p.m.–21:00 p.m. Foyer	**Get together**

....

20:00 p.m.–20:15 p.m. Seminar room 1	Conference opening Martin Heilmaier (Karlsruhe/DE)

....

20:15 p.m.–21:00 p.m. O–IT 01	Opening talk TiAl alloy technology trends and future opportunities in aircraft engines Bernard P. Bewlay (Niskayuna, NY/US)

09:00 a.m.–10:25 a.m. Seminar room 1 Chair	**Mechanical behaviour of intermetallic phases I** Easo George (Oak-Ridge, TN/US)
09:00 a.m. O–IT 13	Oxidation and creep behaviour of novel intermetallic Mo-Si-Ti alloys Martin Heilmaier (Karlsruhe/DE)
09:25 a.m. O–MB 01	Low temperature ductility of B2 structured transition metal intermetallic compounds YCu and YAg Werner Skrotzki (Dresden/DE)
09:45 a.m. O–MB 02	In-situ micro-cantilever tests to study the fracture properties of phases in a NiAl-Cr eutectic system Stefan Gabel (Erlangen/DE)
10:05 a.m. O–MB 03	Microstructure control and plastic deformability of two- phase heat resistant alloys based on $E2_1$-type Co_3AlC_{1-x} Yoshisato Kimura (Yokohama/JP)

....

10:25 a.m.–10:55 a.m.	*Coffee break*

....

10:55 a.m.–12:40 a.m. Seminar room 1 Chair	**Mechanical behaviour of intermetallic phases II** Sharvan Kumar (Providence, RI/US)
10:55 a.m. O–IT 03	**Invited talk:** Mechanical properties and high-temperature applications of MoSiBTiC alloy Kyosuke Yoshimi (Sendai/JP)
10:20 a.m. O–MB 04	Deformation behavior of Fe-Al single crystals containing $Ni_2Al(Ti,V)$ precipitates Hiroyuki Yasuda (Osaka/JP)
11:40 a.m. O–MB 05	Stacking faults in C14 Fe_2Nb Laves phase Christian Liebscher (Düsseldorf/DE)
12:00 a.m. O–MB 06	Chemical order in plastically deformed 18-carat red gold alloy Marina Garcia Gonzalez (Villigen/CH)
12:20 p.m. O–MB 07	Diffraction based determination of single crystalline elastic constants on polycrystalline alloys Alexander E. Heldmann (Garching/DE)

....

12:40 p.m.–14:00 p.m.	*Lunch*

....

14:00 p.m.–15:50 p.m. Seminar room 1 Chair	**Titanium aluminides I** Svea Mayer (Loeben/AT)
14:00 p.m. O–IT 04	**Invited talk:** Status of titanium aluminides for aero engine applications Wilfried Smarsly (Munich/DE)
14:25 p.m. O–IT 05	**Invited talk:** Behavior of the IRIS alloy at service temperature of aircraft engines Alain Couret (Toulouse/FR)
14:50 p.m. O–TA 01	Application of a forged γ-TiAl alloy as low pressure turbine blade in an aircaft engine Ulrike Habel (Munich/DE)
15:10 p.m. O–TA 02	In situ synchrotron X-ray diffraction study on the room temperature tensile behaviour of γ-TiAl based sheets Petra Erdely (Leoben/AT)
15:30 p.m. O–TA 03	Thermodynamic database for multicomponent Ti- and TiAl-based alloys Andreas Markström (Solna/SE)

....

15:50 p.m.–16:20 p.m.	*Coffee break*

16:20 p.m.–18:20 p.m. Seminar room 1 Chair	**Phase stability** Martin Friák (Brno/CZ)
16:20 p.m. O–PS 01	Ab initio thermodynamics and kinetics of precipitate formation in Al-Sc alloys Tilmann Hickel (Düsseldorf/DE)
16:40 p.m. O–PS 02	Structural units in intermetallics: a topological study Tatiana Akhmetshina (Samara/RU)
17:00 p.m. O–PS 03	Relative stability of intermetallic compounds in the AMn_2Al_{20} alloys (where A=lanthanide/actinide/rare earth) Gili Yaniv (Beer Sheva/IL)
17:20 p.m. O–PS 04	Bi-Rh and Bi-Mn-Rh – phase equilibria Herbert Ipser (Wien/AT)
17:40 p.m. O–PS 05	Effect on Al and Cr substitution on TCP structure of Fe_2Nb Laves phase Ryosuke Yamagata (Tokyo/JP)
18:00 p.m. O–PS 06	Impact of magnetism on the stability of topologically close-packed (TCP) phases in Fe-Nb alloys Ali Zendegani (Düsseldorf/DE)

....

19:00 p.m. Foyer	*Poster session with snacks and drinks*

09:00 a.m.–10:30 a.m. Seminar room 1 Chair	**Functional intermetallics/HEAs I** Yoshisato Kimura (Yokohama/JP)
09:00 a.m. O–IT 06	**Invited talk:** Analysis of chemical bonding and prediction of new intermetallic compounds Yuri Grin (Dresden/DE)
09:25 a.m. O–IT 07	**Invited talk:** Unravelling material requirements for the steam reforming of methanol applying intermetallic compounds Marc Armbrüster (Chemnitz/DE)
09:50 a.m. O–FI 01	Intermetallic compound $Al_{13}Fe_4$ as a platform or precursor for catalysis materials Satoshi Kameoka (Sendai/JP)
10:10 a.m. O–FI 02	Microstructures and crystal structures of Ni-Sn and Cu-Sn intermetallics grown by solid-state diffusion Andreas Leineweber (Freiberg/DE)

....

10:30 a.m.–11:00 a.m.	*Coffee break*

....

11:00 a.m.–12:30 p.m. Seminar room 1 Chair	**Functional intermetallics/HEAs II** Haruyuki Inui (Kyoto/JP)
11:00 a.m. O–IT 08	**Invited talk:** Cyclic deformation response of NiTi for medical devices Sharvan Kumar (Providence, RI/US)
11:25 a.m. O–FI 03	Size effect on superelasticity in Cu-Al-Ni shape memory intermetallics Jose San Juan (Bilbao/ES)
11:45 a.m. O–IT 09	**Invited talk:** Massive calphad calculations of high entropy alloys and comparison with experiments Jean-Marc Joubert (Paris/FR)
12:10 p.m. O–FI 04	Alloy design and microstructure of refractory Mo-V-Nb-W-Ti$_x$ HEAs Georg Hasemann (Jülich/DE)

....

12:30 p.m.–14:00 p.m.	*Lunch*

14:00 p.m.–16:00 p.m. Seminar room 1 Chair	**Parallel sessions** **Processing** Wilfried Smarsly (Munich/DE)
14:00 p.m. O–PR 01	Microstructural shaping and viscoplastic behavior of a TiAl alloy obtained by powder metallurgy Pierre Serrano (Châtillon/FR)
14:20 p.m. O–PR 02	Structural and phase transformations occurring during fabrication of TiAl-based composite reinforced by TiB_2 particles Daria Lazurenko (Novosibirsk/RU)
14:40 p.m. O–PR 03	Features of complex technology (PREP + HIP) for obtaining intermetallic alloys Alla I. Logacheva (Korolev/RU)
15:00 p.m. O–PR 04	Development of a reliable hybrid joining between steel and aluminum Xiangfan Fang (Siegen/DE)
15:20 p.m. O–PR 05	Additive manufacturing of iron aluminide alloys Martin Palm (Düsseldorf/DE)
15:40 p.m. O–PR 06	Processing of iron aluminides using selective electron beam melting Lucas Adler (Fürth/DE)

....

14:00 p.m.–16:00 p.m. Seminar room 6 Chair	**High temperature intermetallics** Kyosuke Yoshimi (Sendai/JP)
14:00 p.m. O–HT 01	Alloy design concept for bcc-T2 silicide-B2 aluminide multi-component alloys in conjunction with Laves phase Seiji Miura (Sapporo/JP)
14:20 p.m. O–HT 02	Effect of microstructure on room-temperature fracture toughness of ZrC-added Mo-Si-B alloys Shunichi Nakayama (Sendai/JP)
14:40 p.m. O–HT 03	Creep properties of the Mo_3Si and Mo_5SiB_2 phases in the Mo-Si-B alloy system Olha Popovych (Magdeburg/DE)
15:00 p.m. O–HT 04	Formation of silicides in mechanically alloyed V-Si solid solution powders Janett Schmelzer (Magdeburg/DE)
15:20 p.m. O–HT 05	Microstructure and creep properties of near-eutectic Mo-Zr-B and Mo-Hf-B alloys Volodymyr Bolbut (Magdeburg/DE)
15:40 p.m. O–HT 06	High-entropy alloys under high-pressure high-temperature Kirill V. Yusenko (Swansea/UK)

....

16:00 p.m.–16:30 p.m.   *Coffee break*

16:30 p.m.–18:30 p.m. Seminar room 1 Chair	**Parallel sessions** **Titanium aluminides II** Alain Couret (Toulouse/FR)
16:30 p.m. O–TA 04	Effect of oxygen on phase equilibria among $\beta/\alpha/\gamma$ phases in TiAl alloys using soft X-ray spectroscopy Arata Kinouchi (Tokyo/JP)
16:50 p.m. O–TA 05	The order/disorder transformation of β/β_o phase in binary and ternary γ-TiAl based alloys studied by synchrotron and neutron diffraction Victoria Kononikhina (Geesthacht/DE)
17:10 p.m. O–TA 06	Elemental redistribution during formation and growth of the ω_o phase in β_o phase containing TiAl alloys Thomas Klein (Leoben/AT)
17:30 p.m. O–TA 07	Influence of W on the high temperature properties of the TNM® alloy Melissa Allen (Nuremberg/DE)
17:50 p.m. O–TA 08	Near surface residual stress in TiAl before and after elevated temperature exposure Jonathan D. H. Paul (Geesthacht/DE)
18:10 p.m. O–TA 09	Time and space resolved HEXRD study during transient liquid phase bonding of a γ-TiAl alloy with a Ti-29Fe solder Katja Hauschildt (Geesthacht/DE)

....

16:30 p.m.–18:30 p.m. Seminar room 6 Chair	**Iron aluminides** Martin Palm (Düsseldorf/DE)
16:30 p.m. O–IA 01	Theory-guided design of novel Fe-Al-based superalloys Martin Friák (Brno/CZ)
16:50 p.m. O–IA 02	Fe-Al-Ni-Ti strengthened by $L2_1$-$(Fe,Ni)_2TiAl$ precipitates Flora Godor (Leoben/AT)
17:10 p.m. O–IA 03	Structural properties and room temperature mechanical properties of ultrafine eutectic $Fe_{50}Al_{50-n}Nb_n$ alloys Mehmet Yildirim (Selcuklu-Konya/TR)
17:30 p.m. O–IA 04	Low-temperature phase of η-Fe_2Al_5 with an ordered arrangement of aluminium atoms in the C-Axis chain sites Norihiko L. Okamoto (Kyoto/JP)
17:50 p.m. O–IA 05	Microstructure formation due to phase transformation between η-Al_5Fe_2 and η'-Al_8Fe_3 Hanka Becker (Freiberg/DE)
18:10 p.m. O–IA 06	Thermodynamic modeling and heat capacity measurements in the binary Al-Fe system Maximilian Rank (Eggenstein-Leopoldshafen/DE)

09:00 a.m.–10:50 a.m. Seminar room 1 Chair	**Titanium aluminides III** Masao Takeyama (Tokyo/JP)
09:00 a.m. O–IT 10	**Invited talk:** Qualification of additively manufactured titanium aluminide blades Silvia Sabbadini (Turin/IT)
09:25 a.m. O–TA 10	Laser additive manufacturing of titanium aluminides Andreas Vogelpoth (Aachen/DE)
09:45 a.m. O–IT 11	**Invited talk:** The evolution of the orthorhombic titanium aluminides Dipankar Banerjee (Bangalore/IN)
10:10 a.m. O–TA 11	α_2/O-phase domains in Nb containing lamellar gamma-TiAl Heike Gabrisch (Geesthacht/DE)
10:30 a.m. O–TA 12	Study of the NbTiAl system – influence of the Al-content and Si-doping Laurence Sikorav (Châtillon/FR)

....

10:50 a.m.–11:20 a.m.	*Coffee break*

....

11:20 a.m.–12:40 p.m. Seminar room 1 Chair	**Modelling/Laves phases** Frank Stein (Düsseldorf/DE)
11:00 a.m. O–ML 01	Partitioning of elements in multi-phase alloys – modeling vs experiment David Holec (Leoben/AT)
11:25 a.m. O–ML 02	Ab-initio study of C and N point defects in Fe_2Nb C14-Laves phase Alvin Noe Ladines (Bochum/DE)
11:50 a.m. O–ML 03	Prediction of formation enthalpies using machine learning techniques for C14-Laves phase Satoshi Minamoto (Tsukuba/JP)
12:10 p.m. O–ML 04	Investigation of precipitation and stability of complex intermetallic phases in a Co-3.9Nb alloy Toshiaki Horiuchi (Sapporo/JP)

....

12:40 p.m.–14:00 p.m.	*Lunch*

....

14:00 p.m.–22:30 p.m.	*Bus tour to Bayreuth and conference dinner*

08:30 a.m.–10:30 a.m. Seminar room 1 Chair	**Corrosion I** Manja Krüger (Magdeburg/DE)
08:30 a.m. O–IT 02	**Invited talk:** Ambient-temperature plasticity of brittle intermetallics at micron-meter size scales Haruyuki Inui (Kyoto/JP)
09:00 a.m. O–IT 12	**Invited talk:** Oxidation behavior of TiAl alloy in the atmospheres containing water vapor at 650°C Shigenari Hayashi (Hokkaido/JP)
09:25 a.m. O–CO 01	MoSi2 – a candidate material for biomass gasification atmospheres Uwe Gaitzsch (Dresden/DE)
09:45 a.m. O–CO 02	Oxidation protection of gamma-TiAl by the F-effect – towards an industrial application Hans-Eberhard Zschau (Wurzen/DE)
10:05 a.m. O–CO 03	High temperature oxidation behavior of TiAl based alloys Alexander Donchev (Frankfurt a. M./DE)

....

10:30 a.m.–10:45 a.m.   *Coffee break*

....

10:45 a.m.–11:55 a.m. Seminar room 1 Chair	**Corrosion II** Martin Heilmaier (Karlsruhe/DE)
10:45 a.m. O–CO 04	Investigation of the damage behaviour of a β-stabilised TNM TiAl alloy by low cycle fatigue tests and hot corrosion experimentse Christian Löffl (Landshut/DE)
11:05 a.m. O–CO 05	Influence of the Al content on the aqueous corrosion resistance of binary Fe-Al alloys in H_2SO_4 Jian Peng (Düsseldorf/DE)
11:25 a.m. O–CO 06	The effect of alloying elements on the corrosion properties of DO3-FeAl intermetallics in naturally aerated acidic environments Tatiana Nicole Kutz (Aachen/DE)
11:45 a.m.	Closing remarks Martin Heilmaier (Karlsruhe/DE)

Titanium aluminides

P–01   Hot deformation of dual phase titanium aluminide
        Nitish Bibhanshu (Bangalore/IN)

P–02   Crystal viscoplasticity modeling of Al-rich Ti-61.8at.%Al at 1050°C
        Helal Chowdhury (Magdeburg/DE)

P–03   High temperature deformation behavior of B2-type Ti-Mo-Al alloys
        Yuanyuan Lu (Sendai/JP)

P–04   Carbide growth in TiAl alloys studied by SAS
        Sören Gayer (Geesthacht/DE)

P–05   Precipitation in Ti-Al-Nb alloys with Si and C additions
        Maria Victoria Castro Riglos (Geesthacht/DE)

P–06   P-type carbides in TiAl alloys – a study on stability and morphology development
        Li Wang (Geesthacht/DE)

P–07   Oxidation behavior of two different titanium aluminides and its impact on mechanical properties
        Lukas Mengis (Frankfurt a. M./DE)

P–08   High temperature oxidation of γ-TiAl with Si modified aluminide coatings
        Radoslaw Swadzba (Gliwice/PL)

P-09   Effect of microstructure containing β-Ti phase on crack propagation behavior of wrought γ-TiAl based alloys
        Loris Signori (Tokio/JP)

Nickel aluminides

P–10   Powder metallurgy of intermetallic alloys – peculiarities of technology
        Igor M. Razumovskiy (Korolev/RU)

P–11   Tensile creep of directionally solidified eutectic NiAl-(Cr/Mo) micro-specimens
        LiKang Luan (Eggenstein-Leopoldshafen/DE)

P–12   Characterising the interaction of a NiAl-based anchor phase with CMSX-4
        Megan R. McGregor (Cambridge/UK)

P–13   Phase-field simulation of the microstructure evolution during directional solidification in the eutectic NiAl-9Mo system
        Kaveh Dargahi Noubary (Karlsruhe/DE)

P–14   Characterisation of Al/Ni intermetallic formed by High Energy Ball Millng (HEBM) at low temperature
        Mingu Han (Daejeon/KR)

P–15   As-cast and directionally solidified microstructures along the eutectic trough of the NiAl-Cr-Mo system
        Camelia Gombola (Karlsruhe/DE)

Silicides

P–16   Microstructure and oxidation behavior of Si- and Ti-enriched MoSiBTiC alloys
        Tomotaka Hatakeyama (Sendai/JP)

P–17   Tensile creep resistance of 65Mo-5Si-10B-10TiC (at. %) alloy in the range of 1400-1700 °C
        Shiho Kamata (Sendai/JP)

P–18   Development of high temperature Mo-Si-B based alloy through laser additive manufacturing
        Surendra Kumar Makineni (Düsseldorf/DE)

P–19   Effects of Hf and Zr additions on the microstructure and properties of Nb-Si based ultrahigh temperature alloys
        Xiping Guo (Xi'an/CN)

Miscellaneous

P–20   Formation, structures and electronic bandstructure of Ga-rich (Mo/Ga/In, Mo/Ga/Sn and Mo/Ga/In/Sn) and Zn-rich alloys (Mo/Zn/Ga)
Jan Platzek (Freiburg/DE)

P–21   Concentration dependences of structural characteristics, magnetic and superconducting properties in V-Ta-Zr, V-Zr-Hf and V-Zr-Fe systems
Boris N. Kodess (Moscow/RU)

P–22   Casting of Cr,Ti-containing iron aluminides
Bruna N. Ramirez (São Paulo/BR)

P–23   Hydrogen embrittlement in FeAl revealed via in-situ microcantilever tests
Yun Deng (Trondheim/NO)

P–24   Creep properties of co-based superalloys with improved oxidation resistance
Zhenghao M. T. Chen (Kyoto/JP)

P–25   Plastic deformation in the equiatomic CrMnFeCoNi high entropy alloy with the FCC structure
Makoto Asakura (Kyoto/JP)

P–26   Deformation of micropillars of cubic and hexagonal $NbCo_2$ Laves phases under uniaxial compression at room temperature
Wei Luo (Düsseldorf/DE)

P–27   In-situ observation of phase and microstructure evolution during directional solidification of novel intermetallic structural materials
Manja Krüger (Magdeburg/DE)

P–28   Microstructure evolution and mechanical properties of a multi-phase alloy in the Cr-Mo-Nb system
Li Peng (Sapporo/JP)

P–29   Novel rotatable load frames for neutron diffraction studies on stress/strain, texture, phase transformations or elastic constants
Markus Hoelzel (Garching/DE)

P–30   Effect of Pd-site substitutional elements on phase stability and mechanical property of B2 compound PdAl
Tomonori Soma (Sapporo/JP)

P–31   Grain boundary precipitation behavior of Fe_2Ti-Laves phase in Fe-Cr-Ti ternary ferritic alloy
Yutaro Oki (Meguro-ku/JP)

P–32   Ab initio full-potential study of structural properties and magnetic phase stability of SmX_2 (X = Co and Fe) intermetallic compounds
Ali Bentouaf (Saida/DZ)

P–33   Thermodynamic assessment of Co-Cr-Mn system for improved calphad prediction of σ-phase in high entropy alloys
K. Guruvidyathri (Chennai/IN)

P–34   Microstructure evolution of diffusion welded SS-304L/Zircaloy4 with copper interlayer/influence of the holding temperature
Djaafar Aboudi (Algers/DZ)

![KIT – Karlsruher Institut für Technologie]

EXTENDED ABSTRACTS

Intermetallics 2017

02–06 October 2017

Oral abstracts

Poster abstracts

O–IT 01

TiAl alloy technology trends and future opportunities in aircraft engines

Bernard P. Bewlay[1], Michael Weimer[2]

[1]General Electric Global Research, Niskayuna, NY, United States.

[2]GE Aviation, Cincinnati, OH, United States.

This presentation will describe the development of TiAl alloys for commercial aircraft engine applications. The GENX™ engine is the first commercial aircraft engine that is using titanium aluminide (alloy 4822) in the Boeing 787 and 747-8. More recently, the use of TiAl in engines for the Airbus 320 and the Boeing 737 has occurred. The GENX™ engine provides a major advance in propulsion efficiency, a reduction in fuel consumption, and a reduction in noise and NOx compared to prior engines, such as the General Electric CF6.

This presentation will describe the history of implementation of TiAl in low pressure turbine blades. GE has developed a range of manufacturing approaches for TiAl blades, including conventional gravity casting, near net shape casting approaches, and additive manufacturing methods. To date more than 100,000 TiAl low pressure turbine blades have been manufactured for the GENX™. Production has also started on smaller thrust engines, such as the Pratt and Whitney PurePower™ 1000G engine, and the CFM LeapX™ engine. These use of second and third generation TiAl alloys will be discussed.

O–IT 02

Ambient-temperature plasticity of brittle intermetallics at micron-meter size scales

Haruyuki Inui[1], Norihiko L. Okamoto[2] and Kyosuke Kishida[3]

[1]Department of materials Science and Engineering, Kyoto University, Sakyo-ku, Kyoto 606-8501, Japan <inui.haruyuki.3z@kyoto-u.ac.jp>

[2]Department of materials Science and Engineering, Kyoto University, Sakyo-ku, Kyoto 606-8501, Japan <okamoto.norihiko.7z@kyoto-u.ac.jp>

[3]Department of materials Science and Engineering, Kyoto University, Sakyo-ku, Kyoto 606-8501, Japan <kishida.kyosuke.6w@kyoto-u.ac.jp>

There are many hard materials that are considered to be candidates for structural applications under extreme conditions such as very high temperatures. This stems from the fact that many of them possess peculiar properties such as high hardness, high melting temperature, and so on. But, one of the common characteristics for these hard materials is their brittleness. They usually fail in cleavage without showing any plastic deformation at ambient temperature. So, even, fundamentals for plasticity such as operating slip systems and their CRSS values have yet to be known for many of them. However, there is a chance for these hard materials to plastically deform in the form of micropillars of the micron-meter size even at ambient temperature, from which we can obtain the information of operating slip systems and their CRSS values. We have investigated the compression deformation behavior of brittle transition-metal silicides of the M_5Si_3-type such as Mo_5Si_3, Nb_5Si_3 and Mo_5SiB_2 and those of the MSi_2-type such as $MoSi_2$, VSi_2, $CrSi_2$, $NbSi_2$ and $TaSi_2$. Although none of them listed above deform plastically at room temperature in the bulk form, plasticity is clearly observed at room temperature for all of them in the micropillar forms. Plasticity observed in the micropillar form at room temperature has made us to clearly identify their operative slip systems with their CRSS (critical resolved shear stress) values. For transition-metal silicides of the MSi_2-type, slip systems operative at high temperatures in the bulk form are observed also to operate in the micropillar form at room temperature. The room-temperature bulk CRSS values for these slip systems can be obtained by extrapolating the power-law of the CRSS-specimen size dependence to the bulk size, which can be estimated to be 30-50 μm.

O–IT 03

Mechanical properties and high-temperature applications of MoSiBTiC alloy

Kyosuke Yoshimi[1], Sadahiro Tsurekawa[2], Hiroyuki Fukuyama[3] and Yutaka S. Sato[4]

[1]Department of Materials Science, Tohoku University, 6-6-02, Aramaki Aza Aoba, Aoba-ku, Sendai, 980-8579, Japan, yoshimi@material.tohoku.ac.jp

[2]Division of Materials Science, Faculty of Advanced Science and Technology, Kumamoto University, 2-39-1 Kurokami, Chuo-ku, Kumamoto, 860-8555, Japan, turekawa@kumamoto-u.ac.jp

[3]Institute of Multidisciplinary Research for Advanced Materials, Tohoku University, 2-1-1 Katahira, Aoba-ku, Sendai, 980-8577, Japan, fukuyama@tagen.tohoku.ac.jp

[4]Department of Materials Processing, Tohoku University, 6-6-02, Aramaki Aza Aoba, Aoba-ku, Sendai, 980-8579, Japan, ytksato@material.tohoku.ac.jp

Introduction

Recently, TiC-added Mo-Si-B alloys, so-called MoSiBTiC alloy, have been developed as ultrahigh-temperature materials (UHTMs) beyond Ni-based superalloys [1,2]. The alloy has a density reduced to ~ 8.8 g/cm^3 [1] comparable to that of Ni-based superalloys and show excellent high-temperature creep strength [3]. Of particular importance is finding that the room-temperature fracture toughness of the MoSiBTiC alloy has been improved to be over 15 $MPa(m)^{1/2}$ [4]. The melting temperature of MoSiBTiC alloy lies around 1920°C, and thus ingot metallurgy is applicable to produce large bulks of the alloy. The large-size ingots of the alloy make it possible to provide specimens able to use for conventional engineering tests such as bending and tensile (creep) tests and for high-temperature applications such as mold and working tools. On the other hand, casting technology becomes more serious to achieve microstructural homogeneity and suppress cast defects. In this paper, our recent advances on the material properties of the MoSiBTiC alloy produced using a conventional arc melting technique are reviewed with a special attention to mechanical properties. Furthermore, our recent challenges on large-size ingot production by drop casting, plasma melting and induction melting and on high-temperature applications for the MoSiBTiC alloy will be shown briefly.

Materials and Methods

Button ingots of a 65Mo-5Si-10B-10Ti-10C (at.%) alloy were produced by a conventional arc-melting technique using pure Mo, Si, B and TiC. The size of the ingots was about 45 mm in diameter, 10 mm in height and 100 g in weight. Heat treatment was carried out at 1800°C for 24 h. Cylinder-shape ingots of 300 g in weight were produced by drop casting into a water-cooled Cu mold under arc melting, those of about 1 kg in weight by plasma melting with a water-cooled pulling-down Cu mold and about 3.5 kg in weight by induction melting with an oxide casting mold. Their cast defects were examined by radiographic nondestructive testing (RT). Working tools for friction stir welding (FSW) were made by machining from the drop-cast ingots of the alloy and were applied to the joining of SUS304 stainless steel.

Results and Discussion

Constituent phases of the as-cast MoSiBTiC alloy produced by a conventional arc melting were Mo solid solution (Mo_{ss}), Mo_5SiB_2, (Ti,Mo)C and Mo_2C [1,2]. Mo_2C decomposed into Mo_{ss} and (Ti,Mo)C during heat treatment [5], and thus it is considered to be a metastable phase at a higher temperature. Thermal expansion coefficient of the MoSiBTiC alloy was approximately 7.2×10^{-6} K^{-1} in the range of 900 – 1500°C, which is relatively close to that of Mo_5SiB_2 though the volume fraction of Mo_5SiB_2 in the alloy was less than 35 % [4]. Young's and shear moduli and Poisson's ratio of the alloy at room temperature were approximately 360 GPa, 140 GPa and 0.26, respectively [4]. The Larson-Miller plots and the Monkman–Grant relationship of the creep data obtained by tensile creep tests

suggested that the creep rupture time of 1000 h under 137 MPa is attainable at 1350 – 1400°C [6], which appears to be better than that of SiC/SiC composites. The stress exponent, *n*, was about 3 in the temperature range of 1400 – 1700°C and the stress range of 100 – 300 MPa [6], suggesting that creep deformation in the conditions is controlled by an identical mechanism. The average room-temperature fracture toughness value evaluated by three different bending tests using Chevron-notched specimens was approximately 15.2 MPa(m)$^{1/2}$ [4]. The fracture toughness values showed a good linear relationship with the volume fraction of Mo_{ss} + (Ti,Mo)C, suggesting that not only the ductile-phase toughening by Mo_{ss} but also an extra-toughening mechanism by (Ti,Mo)C are responsible for the goodness of the room-temperature fracture toughness of the MoSiBTiC alloy.

Cylinder-shape ingots of about 300 g in weight were successfully made by drop casting without notable cast defects as shown in Fig. 1. The deadhead was important to suppress cast defects. The plasma melting (Fig. 2 left) and induction melting were also successful. However, it was detected by RT that some notable voids remained inside the ingots. Casting conditions such as liquid temperature, mold material and temperature needed to be controlled more carefully. Working tools for FSW were made from the drop-cast ingots (Fig. 2 right). SUS 304 sheets of 4 mm in thickness were well joined by the process. The MoSiBTiC alloy would have good abrasion resistance.

Fig. 1: Appearance and polished cross section of a cylinder-shape (d ≥ 20 mm) MoSiBTiC ingot produced by drop casting under arc melting.	Fig. 2: Appearance of (left) a cylinder-shape (*d* ≈ 40 mm) MoSiBTiC ingot produced by plasma-melting with a water-cooled pulling-down Cu mold and (right) a work tool of the MoSiBTiC alloy for FSW.

References

[1]   S. Miyamoto, K. Yoshimi, S.H. Ha, T. Kaneko, J. Nakamura, T. Sato, K. Maruyama, R. Tu, T. Goto, Metallugical and Materials Transactions A. **2014,** *45*, 1112–1123.

[2]   K. Yoshimi, J. Nakamura, D. Kanekon, S. Yamamoto, K. Maruyama, H. Katsui, T. Goto, JOM. **2014**, *66*, 1930–1938.

[3]   K. Yoshimi, D. Kanekon, S. Yamamoto, J.W. Kim, J. Nakamura, K. Maruyama, Proc. Advanced High-Temperature Materials Technology for Sustainable and Reliable Power Engineering (123HiMAT-2015). JSPS Report of the 123rd Committee on Heat Resisting Materials and Alloys, **2015**, 350–353.

[4]   T. Moriyama, K. Yoshimi, M. Zhao, T. Masnou, T. Yokoyama, J. Nakamura, H. Katsui, T. Goto, Intermetallics. **2017**, *84*, 92–102.

[5]   J. Nakamura, D. Kanekon, K. Yoshimi, Materials Letters. **2016**, *180*, 340 – 343.

[6]   S. Yamamoto Kamata, D. Kanekon, T. Saito, Y. Lu, K. Maruyama, K. Yoshimi, to be submitted.

O–IT 04

Status of titanium aluminides for aero engine applications

Wilfried Smarsly[1], Jörg Esslinger[1], Helmut Clemens[2]

[1]MTU Aero Engines AG, Dachauer Str. 665, 80995 Munich, Germany,

wilfried.smarsly@mtu.de, jörgesslinger@mtu.de

[2]Motanuniversität Leoben, Rosseggerstr. 12 ,8700 Leoben, Austria,
helmut.clemens@unileoben.ac.at

Introduction

Due to their attractive properties, γ-TiAl-based alloys are considered for high-temperature applications in aerospace and automotive industries. Their advantage is mainly seen in low density (3.9 - 4.2 g/cm3, depending on composition and constitution), high specific yield strength, high specific stiffness, good oxidation resistance, resistance against "titanium fire", and good creep properties up to high temperatures. Particularly at temperatures between 600°C and 800°C γ-TiAl-based alloys are superior to titanium alloys in terms of their specific strength. Compared to the heavier Ni base alloys, their specific strength is at least similar.

Materials and Methods

In the last years, high-strength γ-TiAl-based alloys have been developed. These alloys are characterized by a high content of β-stabilizing alloying elements, such as Nb and Mo [5-6]. At room temperature strength levels like for nickel superalloys can be achieved by appropriate thermo-mechanical processing. It is also important to note that the high temperature properties, such as creep resistance, were considerably improved, thus extending the application range of γ-TiAl-based alloys. For engineering γ-TiAl-based alloys , the optimum balance between fracture toughness and creep resistance on one side and room temperature tensile ductility/strength on the other side is expected for microstructures composed of relatively small lamellar colonies exhibiting narrow lamellar spacing and a small volume fraction of globular γ and β grains [8].

Hot-working of γ -TiAl-based alloys is conducted exclusively above their brittle-to-ductile transition temperature, i.e. at temperatures considerably higher than 700°C and can be divided in primary and secondary hot-working steps. The aim of primary hot-working of cast ingots is to convert (or breakdown) the coarse-grained microstructure into a fine-grained and uniform microstructure suitable for subsequent wrought processing or heat treatments. This is usually accomplished by employing hot-working parameters at which dynamic recrystallization is prevalent and macroscopic as well as microscopic damage can be neglected, i.e. at temperatures between the eutectoid temperature and the γ - transus temperature and at relatively low de γ - formation rates. During the last decade several wrought γ -TiAl alloys with complex alloy compositions have been developed [1-3,10]. These alloys exhibit excellent mechanical properties, but show narrow processing windows. Therefore, these alloys can be forged only under isothermal conditions. However, isothermal forging of γ -TiAl based alloys must be performed at high temperatures, requiring special dies and environmental conditions which increase manufacturing costs. Therefore, Nb and Mo containing TNM™ alloys have been developed which are equally suited. Recently, the technical feasibility of manufacturing a turbine blade by means of a near conventional hot-die process has been demonstrated [8,11]. Subsequent, two-step heat treatments were conducted to adjust balanced mechanical properties, i.e. a sufficiently high plastic fracture strain at room temperature and good creep properties at elevated temperatures [8].

Results and Discussion

There are at least three major payoff areas for γ-TiAl-based alloys in advanced aero engines and gas turbines [1,2,9,12]: (a) γ-TiAl has a specific elastic stiffness 50% greater than structural materials commonly used in aircraft engines. The higher specific stiffness (E/ρ) also shifts acoustically excited vibrations towards higher frequencies, which is usually beneficial for structural components, e.g.,

compressor and turbine blades and parts within the exhaust nozzle area. (b) The good creep resistance of advanced γ-TiAl-based alloys in the temperature regime of 600 to 800°C, enables the substitution of Ni-based alloys (twice the density as γ-TiAl alloys) for certain applications. (c) The high fire resistance of γ-TiAl-based alloys (nearly as resistant as Ni-based alloys) can enable the substitution of heavy and expensive fire resistant designed Ti-based alloys in some components. Aero engine manufacturer announced the application of investment cast and forged γ-TiAl blades for future engines [7].

Intermetallic γ -TiAl-based alloys are considered as a very important candidate material for advanced applications in aerospace, automotive and related industries. World-wide research and development on γ -TiAl alloys have led to a better understanding of the fundamental influence of alloy composition and microstructure on mechanical properties and processing behavior. In the last years industry has started to make use of this new class of light-weight high-temperature materials. In particular, all major aircraft and automotive engine manufacturers are advancing the qualification and introduction of - γ TiAl components. γ -TiAl-based alloys can be processed using advanced metallurgical methods - a factor, which is decisive for these specific materials to be economically competitive with other state-of-the-art materials. In current γ -TiAl-based alloys balanced properties like room temperature ductility, fracture toughness, high-temperature strength, creep and oxidation resistance can be achieved.

References

[1] Y-W. Kim, H. Clemens, A. Rosenberger (EDs.), Gamma Titanium Aluminides, TMS, Warrendale, PA, USA **2003**.

[2] Y-W. Kim, D.Morris, R. Yang, C. Leyens (Eds.), Structural Aluminides for Elevated Temperature Applications, TMS, Warrendale, PA, USA **2008**.

[3] M. Peters, C. Leyens (Eds.), Titanium and Titanium Alloys, Wiley-VCH, Weinheim, Germany **2003**.

[4] F. Appel, M. Oehring, in [3], 89.

[5] F. Appel, M. Oehring, R. Wagner: Intermetallics 8, **2000**,1283.

[6] H. Clemens, W. Wallgram, S. Kremmer, V. Guther, A. Otto, and A. Bartels: Adv. Eng. Mater. 10, **2008**,707.

[7] T. Kelly: Presentation at the Symposium on "Structural Aluminides for Elevated Temperature Applications", TMS 2008 Annual Meeting, New Orleans, LA, USA **2008**.

[8] W. Wallgram, T. Schmoelzer, G. Das, V. Guther, and H. Clemens: Int. J. Mat. Res. 100 **2009**,1021.

[9] H. Clemens, H. Kestler: Adv. Eng. Mater. 2, **2000**, 551.

[10] F. Appel, J. D. H. Paul, M. Oehring, H. Clemens, F.D. Fischer: Z. Metallkd. 95, **2004,** 585.

[11] S. Kremmer, H.F Chladil, H. Clemens, A. Otto, V. Guther: Ti-Science and Technology, M. Niinomi, S. Akiyama, M. Hagiwari, M. Ikeda, K. Maruyama (Eds.), **2007**.

[12] W. Smarsly, H. Baur, G. Glitz, H. Clemens, T. Khan, M. Thomas: Structural Intermetallics 2001,K. Hemker, D. Dimiduk, H. Clemens, R. Darolia, J. Larsen, V. Sikka, M. Thomas, D. Wittenberger (Eds.), TMS, Warrendale, PA, USA **2001**, 25.

O–IT 05

Behavior of the IRIS alloy at service temperature of aircraft engines

Soumaya Naanani[1], Catherine Mabru[2], Anis Hor[3],
Jean-Philippe Monchoux[4] and Alain Couret[5]

[1]*ICA, ISAE-SUPAERO, Département Mécanique des Structures et Matériaux (DMSM), 10 avenue Edouard Belin - BP 54032 - 31055 Toulouse, France*, and *CEMES-CNRS, BP 94347, 29 rue Jeanne Marvig, 31055 Toulouse cedex 4, France,* Soumaya.naanani@cemes.fr

[2]*ICA, ISAE-SUPAERO, Département Mécanique des Structures et Matériaux (DMSM), 10 avenue Edouard Belin - BP 54032 - 31055 Toulouse, France*, catherine.mabru@isae.fr

[3]*ICA, ISAE-SUPAERO, Département Mécanique des Structures et Matériaux (DMSM), 10 avenue Edouard Belin - BP 54032 - 31055 Toulouse, France*, Anis.Hor@isae.fr

[4]*CEMES-CNRS, BP 94347, 29 rue Jeanne Marvig, 31055 Toulouse cedex 4, France*, monchoux@cemes.fr

[5]*CEMES-CNRS, BP 94347, 29 rue Jeanne Marvig, 31055 Toulouse cedex 4, France*, alain.couret@cemes.fr

Introduction

During the last decade, extensive works have been performed by the Toulouse's group to develop TiAl alloys produced by Spark Plasma Sintering (SPS). SPS is a technique of powder metallurgy for which the densification is due to the simultaneous application of a direct pulsed electric current of high intensity and of a uniaxial pressure on a graphite assembly containing the powder [1].
A TiAl based alloy (Ti-48Al-2W-0.08B) densified by SPS, called IRIS, has been found to possess a high strength at high temperature associated with an interesting ductility at room temperature. For instance it exhibits a creep life of 4071h at 700°C/300MPa for a minimum creep rate of $3.1 \ 10^{-9} \ s^{-1}$ and a plastic elongation of 1.6% at room temperature [2]. Its microstructure is formed by small lamellar colonies (~ 35 µm) surrounded by single phased γ borders containing β_0 precipitates [3].
The aim of the present work is to study the behavior of the IRIS alloy under thermomechanical strengths reproducing the solicitation supported by the alloy in service in aero and automotive engines at temperatures ranging between 800°C and 900°C. Ageing cycles as well as creep and Low-Cycle Fatigue (LCF) experiments are performed. Post-mortem analyses by Scanning and Transmission Electron Microscopies (SEM and TEM) are developed to investigate the deformation mechanisms and to determine the microstructural characteristics controlling the alloy strength.

Materials and Methods

A new batch of powder with the IRIS chemical composition was gas atomized by the ATI Powders Metal Company (Pittsburgh, USA). Using the same SPS conditions as with the former powder, a similar fine microstructure was obtained (Fig. 1), which demonstrates a high reproducibility of the process.
The procedure of Low-Cycle Fatigue experiments was established during this work. They were conducted in air in a Servohydraulic MTS machine (809 Axial/Torsional Test System), with a furnace allowing to reach a temperature of 1200°C. The extensometers were directly attached to the gauge of the specimens. Tensile creep tests were performed under constant stress following the procedure described in Ref. [4].
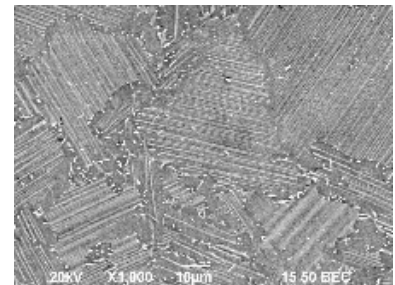
Fig. 1 : Microstructure of the IRIS/SPS alloy.

Results

Fig. 2 displays results of LCF and creep tests at 800°C. The LCF experiment (Fig. 2,a) was performed with the following conditions : Strain ratio $R_\varepsilon = \varepsilon_{min}/\varepsilon_{max} = -1$, Strain amplitude $\Delta\varepsilon = \pm 0.3\%$ and Strain rate $\dot{\varepsilon} = 10^{-3} \ s^{-1}$. The sample was broken after 5276 cycles. The stress amplitude of 304

MPa appears to be nearly constant all along the 5276 cycles. The creep experiment at 800°C-200MPa (Fig. 2,b) demonstrates a creep life of 817h, for a minimum creep rate of $1.6 \cdot 10^{-8}$ s^{-1}, with times to reach 0.5 and 1% of plastic elongation of 31h and 118h, respectively.
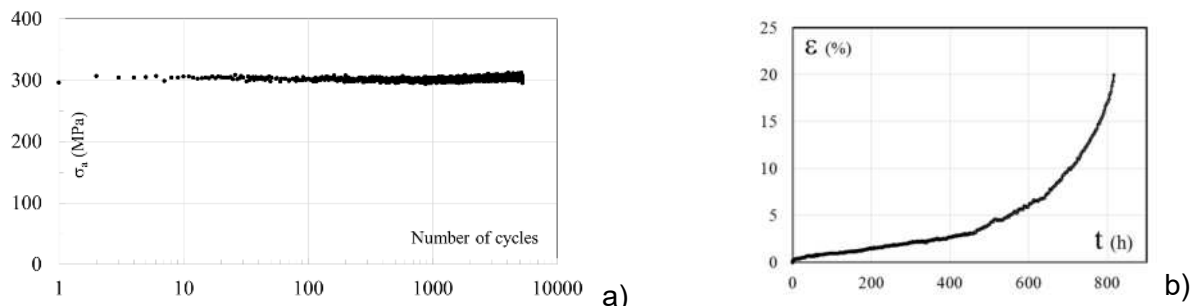
Fig. 2: Mechanical tests at 800°C. a) Low-cycle fatigue. b) Creep.

The deformation microstructures in fatigued and crept samples have been analyzed by TEM. Fig. 3 displays some structures of dislocations in a sample crept at 850°C-150 MPa up to 1.6% of plastic strain. All these dislocations were moving by climb. Whether Fig. 3,a shows classical ordinary dislocations, Fig. 3,b exhibits unusual [001] dislocations which are probably activated due to a particular orientation of the γ grains of the borders with respect to the loading axis. In Fig. 3,c, it can be seen that lamellar zones can deform by the same climbing ordinary dislocations. It is worth to be noted that twinning is scarcely activated
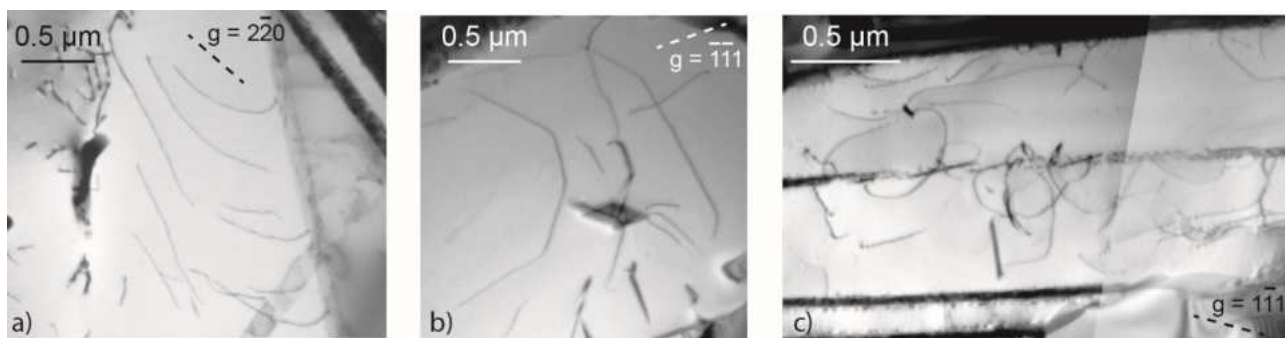
Fig. 3: Climbing dislocations in a sample crept at 850°C/150 MPa. a) Ordinary dislocations. b) [001] dislocations. c) Lamellar zone.

Concluding remarks

In this talk, fatigue and creep properties of the as-SPSed IRIS alloy in a temperature range of 800°C-900°C will be extensively presented and compared to the current literature. The properties of the alloy after ageing at 800°C will be also described. From the SEM and TEM post-mortem investigations, for fatigue and creep, attempts to answer the following questions will be made: in which part of the microstructure does the deformation spread? What are the activated modes? What are the corresponding mechanisms? Is twinning activated? What are the controlling microstructural features (grain size, lamellae width, precipitates, local chemical composition …)?

References
[1] R. Orru, R. Licheri, A. Mario Locci, A. Cincotti, G. Cao, Materials Science and Engineering. **2009**, *R63*, 127-287.
[2] T. Voisin, J.P. Monchoux, M. Thomas, C. Deshayes, A. Couret, Metallurgical and Materials Transaction. **2016**, *47*, 6097-6108.
[3] T. Voisin, P. Monchoux, M. Perrut, A. Couret, Intermetallics. **2016**, *71*, 88-97.
[4] J. Malaplate, A. Couret, Matériaux et Techniques. **2004**, *1-2*, 51-57.

O–IT 06

Chemical bonding and prediction of intermetallic compounds

Yuri Grin[1]

[1]Max-Planck-Institut für Chemische Physik fester Stoffe,

Nöthnitzer Str. 40, 01187 Dresden, Germany,

e-mail: grin@cpfs.mpg.de

Introduction

Intermetallic compounds are formed by elements located left from the Zintl line in the Periodic Table. For interpretation of their chemical and physical properties a better understanding of the chemical composition and bonding in crystal structures of these substances is necessary. Especially the chemical bonding in intermetallic compounds is a rather open question [1].

Materials and Methods

An application of new quantum-chemical tools in real space like electron localizability approach [2-5] opens the way to real-space definition of the basic categories for chemical bonding description like covalence or ionicity [6] or polarity [7].

Results and Discussion

The Pauling's 8–N rule is re-defined for the real space and used for a consistent and quantitative treatment of heteropolar bonding situations exemplarily for compounds of the MgAgAs-type crystal structure and their relatives [8]. The QTAIM Madelung energy calculated using effective charges and the exchange energy obtained by point-charge approximation from the delocalization indexes were used to identify favorable element combinations for new MgAgAs-type compounds. The observed trends in QTAIM Madelung energy and nearest-neighbor electron sharing explain the occurrence of recently reported in the literature substances TiPtGe [9] and TaIrGe [10], equiatomic MgAgAs-type compounds at the boundary to the TiNiSi-type crystal structure. The new phases - the high-temperature VIrGe and the low-temperature modification of HfPtGe are prepared and characterized by powder X-ray diffraction and differential thermal analysis show this type of crystal structure [11].

References

[1] Yu. Grin. In: Comprehensive Inorganic Chemistry II, Vol 2. Oxford Elsevier, **2013**, 359-373.

[2] M. Kohout, Int. J. Quantum Chem. **2004**, *97*, 651-658.

[3] M. Kohout, Faraday Discuss. **2007**, *135*, 43-54.

[4] F. R. Wagner, V. Bezugly, M. Kohout, Yu. Grin. Chem. Eur. J. **2007**, *13*, 5724-5741;

[5] A. Martin-Pendas, M. Kohout, M. A. Blanco and E. Francisco. In: Modern Charge Density Analysis, Springer Heidelberg, **2012**, 303-358.

[6] D. Bende, Yu. Grin, F. R. Wagner. Chem. Eur. J. **2014**, *20*, 9702-9708.

[7] D. Bende, F. R. Wagner, Yu. Grin Inorg. Chem. **2015**, *54*, 3970-3978.

[8] F. R. Wagner, D. Bende, Yu. Grin. Dalton Trans. **2016**, *45*, 3236-3243.

[9] S.-V. Ackerbauer, A. Senyshyn, H. Borrmann, U. Burkhardt, A. Ormeci, H. Rosner, W. Schnelle, M. Gamza, R. Gumeniuk, R. Ramlau, E. Bischoff, J. C. Schuster, F. Weitzer, A. Leithe-Jasper, L. H. Tjeng, Yu. Grin, Chem. Eur. J. **2012**, *18*, 6272-6283.

[10] R. Gautier, X. Zhang, L. Hu, L. Yu, Y. Lin, T. O. L. Sunde, D. Chon, K. R. Poeppelmeier, A. Zunger, Nat. Chem. **2015**, *7*, 308-316.

[11] D. Bende, F. R. Wagner, O. Sichevych, Yu. Grin. Angew. Chem. **2016**, *128*, 1313-1318.

O–IT 07

Unravelling material requirements for the steam reforming of methanol applying intermetallic compounds

Marc Armbrüster[1], Axel Knop-Gericke[2], Marc Heggen[3]

[1]Faculty of Natural Sciences, Institute of Chemistry, Materials for Innovative Energy Concepts, Chemnitz University of Technology, 09107 Chemnitz, Germany
marc.armbruester@chemie.tu-chemnitz.de

[2]Fritz Haber Institute of the Max Planck Society, 14195 Berlin, Germany, knop@fhi-berlin.mpg.de

[3]Ernst Ruska-Centrum and Peter Grünberg Institute, Forschungszentrum Jülich, 52425 Jülich, Germany, m.heggen@fz-juelich.de

Introduction

With the use of fossil fuels, severe environmental drawbacks are coming along. This comprises but is not limited to pollution during extraction of coal, crude oil and natural gas as well as the release of fast amounts of carbon dioxide during combustion to use the stored energy. The latter is influencing our climate and it is very hard to predict the consequences on humankind – but they might not only be beneficial.

Two energy-harvesting paths are available besides fossil fuels. One is nuclear power; the second one is the more or less direct use of the sun´s energy. The first has been explored and used for decades with at least two big accidents (Chernobyl 1986 and Fukushima 2011) – resulting in the decision to shut down all German nuclear power stations until 2022.

On the long run, i.e. within the next seven years, we are facing three possibilities: i) cut back our living standard, ii) replacing the nuclear power by fossil fuels, thus increasing the drawbacks coming along with it or iii) replacing our energy infrastructure by sun´s energy. The latter can be sustainable and is summarised as "Energiewende".[1]

Many different methods are available to convert the sun´s energy into electricity. In Germany photovoltaic cells and wind power plants are mostly used and contribute 25-30% of the electric power.[2] Unfortunately, neither wind, nor sunshine are available 24/7. This results in a strong fluctuation of available electric power over time, which leads to unusable peaks and deep valleys in the power supply. This is a challenge for the stability of the electric grid and as a result, it is desirable to store the energy during peak times and release it during valleys.[3]

Electric energy can be directly stored by various methods (batteries, capacitors, in the form of kinetic energy) but these methods are either expensive and/or come along with severe energy losses in form of heat. Using the electric energy to convert water into hydrogen and storing the hydrogen in form of small molecules is a promising way to overcome many of the Energiewende challenges. In this context methanol (CH_3OH) is a good storage candidate. Methanol is produced on a 100 t/a scale, can be stored easily and has a high volumetric energy density. These advantages lead to Olah´s "Methanol Economy" which is based upon methanol as energy storage and platform chemical.[4]

While the synthesis of methanol is well established, the release of hydrogen from methanol is still under investigation. Converting a 1:1 mixture of water and methanol into hydrogen and CO_2 – the so-called methanol steam reforming (Eq. 1) – is an attractive process.

$$H_2O + CH_3OH \rightarrow 3\,H_2 + CO_2 \qquad\qquad (1)$$

The challenge is to avoid formation of carbon monoxide by methanol decomposition (Eq. 2) to the low ppm range to allow the direct feed of the product gases to hydrogen fuel cells.

$$CH_3OH \rightarrow 2\,H_2 + CO \qquad\qquad (2)$$

Materials and Methods

To allow for a detailed understanding, the unsupported intermetallic compound ZnPd was used as single-phase material with different compositions lying within the homogeneity range. Samples were synthesised by powder metallurgical methods, i.e. mixing of the elements and sealing them in evacuated quartz glass ampoules which were subsequently heated to 900 °C for two weeks. After the synthesis, the ampoules were quenched in water, opened and the obtained samples were subjected to powder X-ray diffraction, metallography and elemental analysis for characterisation. Prior to catalytic tests, the materials were crushed and sieved (20-32 microns). Catalytic tests were carried out in a Microactivity Reactor (PID Eng&Tech) up to 400 °C and the product mixture was analysed by means of a MicroGC (Varian). [5]

In addition, the samples were investigated by *operando* near-ambient pressure X-ray photoelectron spectroscopy (NAP-XPS) at BESSY[5], Berlin and by HR-TEM at the Forschungszentrum Jülich.[6]

Results and Discussion

Combining the catalytic properties of ZnPd with different composition and the presence of different compounds identified during the in-depth *operando* study as well as the TEM investigations revealed a synergistic effect between ZnPd and ZnO. Depending upon the Pd-content in the samples, the oxidisability of ZnPd changes. Samples lean in palladium are partially oxidised under reaction conditions, leading to the formation of very small ZnO islands. On the other hand, samples rich in palladium are not oxidised. Only palladium-lean samples show high selectivity to carbon dioxide, revealing a synergistic interplay between ZnPd and ZnO (Fig. 1).[5,6]

Fig. 1: Catalytic properties of ZnPd with different elemental composition in the steam reforming of methanol

Based on the results, noble-metal free materials are under development.[7]

References

[1]   D.J.C. MacKay, *Sustainable Energy – without the hot air*, UIT Cambridge, **2009**.

[2]   http://www.ag-energiebilanzen.de/index.php?article_id=29&fileName=20160128_brd_stromerzeugung1990-2015.xlsx

[3]   P. Gruss, F. Schüth, *Die Zukunft der Energie: Die Antwort der Wissenschaft*, C.H. Beck, **2008**.

[4]   G.A. Olah, et al., *J. Am. Chem. Soc.* 133, **2011**, 12881.

[5]   M. Friedrich, S. Penner, M. Heggen, M. Armbrüster, *Angew. Chem. Int. Ed.* 52, **2013**, 4389.

[6]   M. Friedrich, D. Teschner, A. Knop-Gericke, M. Armbrüster, *J. Catal.* 285, **2012**, 41.

O–IT 08

Cyclic deformation response of NiTi for medical devices

S. Kumar[1] and H. Kim[1], D. Janda[1,2] and D. Catoor[3]

[1]School of Engineering, Brown University, Providence, RI, USA
Sharvan_Kumar@brown.edu; Hyunmin_Kim@brown.edu

[2]Current Address: W.L. Gore and Associates, Inc, Metals Technology, Flagstaff, AZ, USA
janda.d@icloud.com

[3]Medtronic, Minneapolis, MN 55432
dhiraj.catoor@medtronic.com

Introduction

NiTi shape memory alloys (SMA) are used in the medical devices sector in tube and wire form for fabricating stents, stent grafts and heart valve frames. The material is capable of experiencing a stress-induced reversible martensite phase transformation from its parent austenite (B2) form. A full loading and unloading cycle includes a complete transformation of the austenite phase to martensite (the forward transformation) and martensite back to austenite (the reverse transformation) that results in a hysteresis loop as the stress plateau for the reverse transformation is lower than that for the forward transformation. In service, the material experiences cyclic loading but determining fatigue life in such stents is non-trivial due to the small dimensions coupled with the complex geometry [1]. The problem is exacerbated by the fact the tube or wire is usually composed of a fine-scale microstructure, is textured from the prior processing steps [2] and therefore is anisotropic, the texture can further evolve during cycling, and tensile and compression responses are different [3]. The herring bone/diamond pattern in the final stent (by laser cutting the tube or forming the wire) leads to a complex bending state of stress in the individual ligaments during cycling. Lastly, the austenite-to-martensite transformation progresses heterogeneously in tension but is not the case in compression and therefore the correlation between the measured global strain and the existing local transformation strain is tenuous [4]; mechanistically, interpreting the cyclic response of ultrafine ligaments in bending thus poses a challenge. In this study, we use both, i) a dog-bone specimen geometry obtained from strip specimens coupled with digital image correlation to examine cyclic tensile deformation, and ii) micropillar specimen geometry milled from textured tubes to understand cyclic compression response in the r, θ and z orientations to characterize cyclic anisotropy. We compare the results obtained on the textured tube with single-crystal micropillar response in different crystallographic orientations to understand the effect of texture on cyclic response.

Materials and Methods

Both, the NiTi strip and the tube, were provided to us by Medtronic in Minneapolis, MN. Dog-bone specimens were machined from the strip material for conducting displacement-controlled cyclic tensile tests. These specimens were laser-cut and electropolished. To restrict the nucleation of the austenite-to-martensite transformation to a single event, the dog-bone specimen was marginally tapered (2°) in the center of the gage section and digital image correlation (DIC) was used to obtain the strain distribution in the gage section during a full transformation cycle of loading and unloading in tension, and this was used to determine suitable displacement amplitudes for the cyclic tensile tests. For the tube material (5.5 mm outer diameter and a wall thickness of 0.15 mm), micropillars were FIB milled in the r, θ and z orientations and cycled in compression in a displacement controlled mode using a flat-punch mounted in the nanoindenter. TEM Specimens were excised from the tube and sheet for microstructural analysis. Texture was measured using X-ray diffraction in the as-received tube and strip, and after cyclic testing of the strip. A 1.5 mm thick sheet of NiTi was also obtained, annealed at 650°C for 1h to grow the grains, mounted polished and characterized using EBSD. Single crystal micropillars were then milled from selected orientations and similarly evaluated in compression and these results were compared to the response of the textured micropillars obtained from the different orientations in the tube.

Results and Discussion

Micropillar Cyclic Compression Response:
The microstructure of the tube was characterized using TEM in the bright field and diffraction mode and it was confirmed that the B2 microstructure was composed of elongated grains with a high dislocation density and subgrains within these grains. There was no evidence for the presence of B19' martensite in the initial structure. The tube was textured with a strong {112}-{111} duplex structure along the drawing direction, a strong {111}-{123} along the R-direction and a near {011} - {012} texture in the θ-direction. Micropillars were cycled to 100 cycles to a strain of 6% with the loading axis in the **r**, θ and **z** orientations. In each instance, the transformation onset stress decreases while the maximum stress attained at 6% strain increases with increasing cycles (i.e. the hysteresis loop rotates counter clockwise with increasing cycles). These changes are most vivid in the first 20-30 cycles after which the response stabilizes. Furthermore, a strong anisotropy as a function of orientation is recognized (Figure 1). Single crystal micropillars milled from the annealed sheet with specific loading orientations and similarly cycled demonstrated good correlation with the texture tube results (Figure 1).

Macroscopic Cyclic Tensile Response:
The tensile response for a single cycle was first obtained as a function of displacement rate, both in air and in water, to determine consequences of adiabatic heating on the response. Tensile specimens with a single transformation band along with strain distribution along the gage section obtained from DIC were used to cycle the specimen from the lower plateau and the consequences are illustrated in Figure 2. An upward shift in the upper plateau and a step in the lower plateau are noted after 10^7 cycles. Texture measurement confirms [110] texture evolution during cycling in austenite and this shift is associated with this texture. These and other results will be discussed.
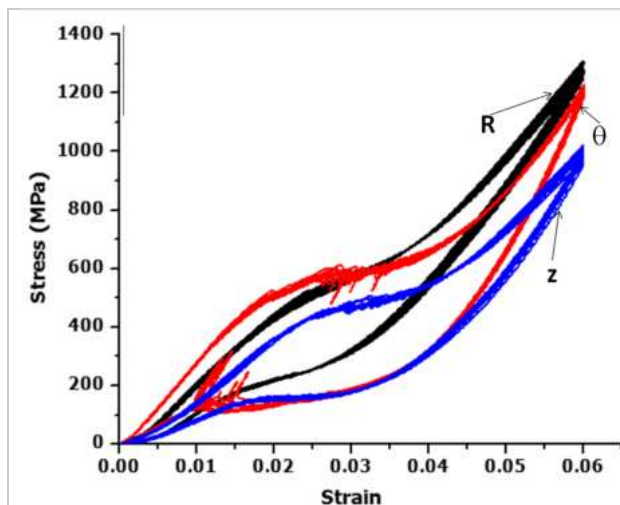
Fig. 1: NiTi Micropillars anisotropic *compression* response in the **r**, θ and **z** orientations after 10 cycles.
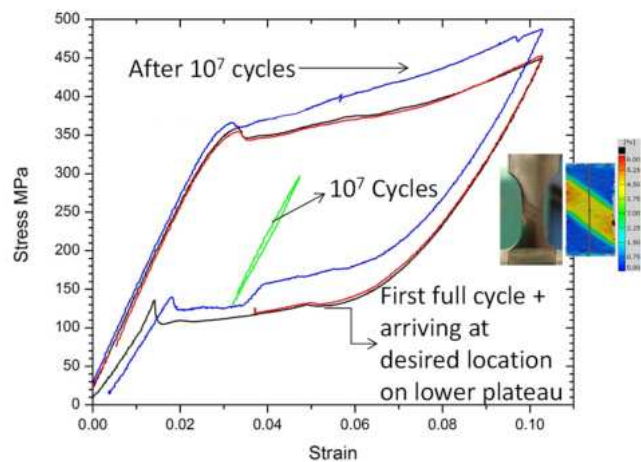
Fig. 2: Tensile cycling (10^7 cycles) of NiTi from the lower plateau and a comparison of transformation loops before and after cycling.

References

[1] A.R. Pelton, V. Schroeder, M.R. Mitchell, Xiao-Yan Gong, M. Barney and S.W. Robertson, J. Mech. Behav. Biomed. Mater., **2008**, 1, 153-164.

[2] S.W. Robertson, A.R. Pelton andR.O. Ritchie, Inter. Materials Reviews, **2012,** 57, 1-36.

[3] K. Gall, H. Sehitoglu, Int. J. Plasticity, **1999,** 15, 69–92.

[4] B. Reedlunn, C.B. Churchill, E.E. Nelson, J.A. Shaw and S.H. Daly, J. Mech. Phys. Solids, **2014,** 63, 506-537.

O–IT 09

Massive calphad calculations of high entropy alloys and comparison with experiments

Jean-Marc Joubert, Guillaume Bracq, Mathilde Laurent-Brocq, Jean-Philippe Couzinié and Ivan Guillot

Université Paris Est, ICMPE (UMR 7182), CNRS, UPEC, F-94320, Thiais, France, joubert@icmpe.cnrs.fr and bracq@icmpe.cnrs.fr

Introduction

High Entropy Alloys (HEA) have emerged as a promising class of materials derived from new metallurgical concepts. They were initially obtained by mixing equal amounts of five or more elements in order to obtain single phase solid solutions [1, 2]. A new trend is to make these already complex alloys even more complex considering that:

 – there is no reason to limit to equiatomic compositions [3]
 – not only single phase but also two phase alloys may be required in order to improve the structural properties [4, 5]

For these two reasons, the field of compositions to be investigated has been tremendously expended making really impossible complete experimental investigations and necessary the use of modeling tools in order to be able to predict the microstructure. Among the existing tools, the Calphad method has already proven to be the most efficient for complex multi-component systems.

Materials and Methods

Massive calculations were carried out using the Calphad method and the recently developed TCHEA1 database. The two systems Co–Cr–Fe–Mn–Ni and Al–Co–Cr–Fe–Ni–Ti were studied. In addition to the calculation of selected isopleths, systematic composition scans were programmed allowing to calculate the phase equilibrium in 10626 compositions for the first system and 44275 compositions for the second system, this at two different temperatures. Confirmation experiments were also conducted after synthesis by induction melting using scanning electron microscopy (EDS and EBSD) and X-ray diffraction.

Results and Discussion

For the system Co–Cr–Fe–Mn–Ni, our goal was to define the extent of the single phase *fcc* solid solution in this prototype system [6]. This was done following selected isopleths (see Fig. 1) in the quinary system and after a systematic calculation of the complete composition space.

Experiments (see Fig. 2) are found to be in agreement with the calculations in most case. Our main conclusions are that:

- the homogeneity domain of the *fcc* phase is fairly well described by the TCHEA1 database
- the description of the stability of the σ phase could however be improved
- we identified the elements and the combination of elements stabilizing or destabilizing the solid solution
- the solid solution domain was accurately defined and allows now the synthesis of new compositions far away from the equiatomic composition, the measurement of their properties and in a final step optimization of the properties.

In the system Al–Co–Cr–Fe–Ni–Ti, our goal was to obtain a two-phase microstructure combining *fcc* solid solution and $L1_2$ structure. Among the 44275 compositions investigated in the senary system maintaining Al and Ti composition below 10 at.%, 1954 present this two-phase equilibrium at 1273 K. In most case, these compositions are purely *fcc* at higher temperature allowing a solution treatment and a possible coherent precipitation of $L1_2$ phase in the microstructure. This is similar to what is done for Ni-based superalloys but at rather different compositions. Again, for this system, confirmation experiments were conducted and the results have been compared to the calculations.
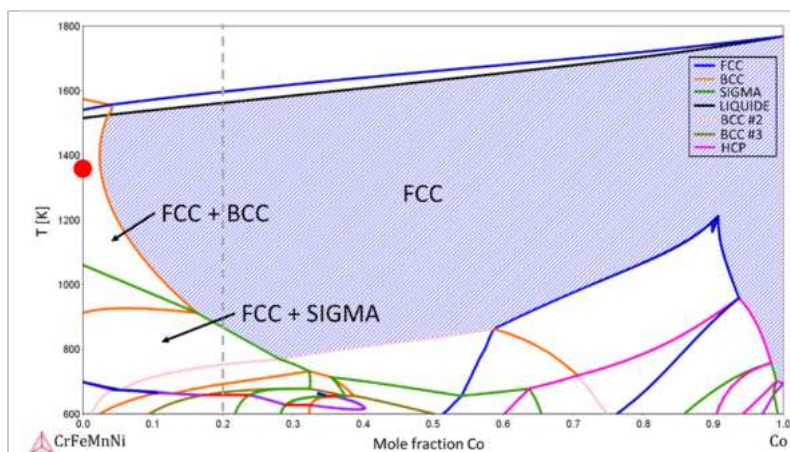
Fig. 1: Isopleth section calculated with the Calphad method and the TCHEA1 database for Co-CrFeMnNi and showing the extent of the *fcc* phase.	Fig. 2: EBSD mapping of CrFeMnNi alloy shown as a dot in Fig.1 (red : fcc, green : bcc)
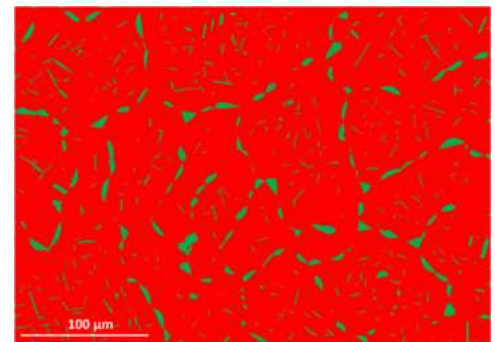
References

[1] B. Cantor, I. T. H. Chang, P. Knight, A. J. B. Vincent, Materials Science and Engineering A. **2004**, *375-377*, 213-18.

[2] J.-W. Yeh, S.-K. Chen, S.-J. Lin, J.-Y. Gan, T.-S. Chin, T.-T. Shun, C.-H. Tsau, S.-Y. Chang, Advanced Engineering Materials. **2004**, *6* (5), 299–303.

[3] M. Laurent-Brocq, L. Perrière, R. Pirès, Y. Champion, Materials & Design. **2016**, *103*, 84-89.

[4] Z. Li, K. Gokuldoss Pradeep, Y. Deng, D. Raabe, C. Cem Tasan, Nature. **2016**, *534* (9 June), 227-231.

[5] T.-K. Tsao, A.-C. Yeh, H. Murakali, Metallurgical and Materials Transactions A. **2017**, in press.

[6] G. Bracq, M. Laurent-Brocq, L. Perrière, R. Pirès, J.-M. Joubert, I. Guillot. Acta Materialia, **2017**, *128*, 327-336.

O–IT 10

Qualification of additively manufactured titanium aluminide blades

Silvia Sabbadini

Additive manufacturing applications are rapidly growing in aviation industry, providing several technical benefits such as the possibility of new design features and a high flexibility, particularly important in new products development phase.

The challenges related to the industrial implementation have been identified and include, among others, the complexity of manufacturing process controls, the very limited field experience, the lack of design allowances and industry standards, etc.

Particularly important is to gain a good understanding of the defects that are generated by additive processes that are substantially different from the defects that are typical for conventional manufacturing routes such as forging and casting. The anomalies that can be found in a component are pores, lack of fusion due to an incomplete melting of two adjacent layers, microstructural inhomogeneity, etc. The nature, size and geometrical distribution of these defects in the component are the key for designing the part, as well as the knowledge on how these defects affect the fatigue resistance of the part.

In this scenario, the applicability of conventional nondestructive inspection (NDI) methods plays a critical role: the new nature of the flaws might require a new NDI technique or a new combination of existing ones to ensure the soundness of the parts.

All these challenges were faced while developing the Electron Beam Melting (EBM) process for manufacturing Titanium Aluminide blades for a new wide-body commercial engine, which has recently started the certification phase. An overview of the development path, from the first feasibility trials launched in 2007, through demo engine tests until the certification hardware production will be presented along with the approach to process qualification and part validation. Special attention will be paid to the analysis of defects generated by EBM and to the impact of those defects, peculiar to EBM, on component performances and quality controls.

O–IT 11

The evolution of the orthorhombic titanium aluminides

Dipankar Banerjee[1], Ashok Gogia[2], Tapash Nandy[2], K. Muraleedharan[3], Jean Loup Strudel[4]

[1]Indian Institute of Science, Bangalore India

[2]Defence Metallurgical Research Laboratory, Hyderabad, India

[3]Central Glass and Ceramics Research Institute, Kolkata, India

[4]Mines ParisTech, 91003-Évry Cedex, France

The development of titanium aluminides based on the intermetallic phases in the Ti-Al system consumed almost three decades of intensive research through the seventies and eighties, and into this century. In the late eighties, we discovered that alloys with Nb contents greater than about 15at% Nb were based on a ternary intermetallic, Ti_2AlNb that we christened the O phase [1]. In the following years we defined the physical metallurgy of the higher Nb alloys covering phase equilibria and transformations, mechanical behaviour and processing [2], and in the mid-nineties, we significantly improved the properties of this class of alloys through extensive studies on compositional effects on processing, structure and properties [3]. There appears to be a recent resurgence of interest in the O phase related transformations and mechanical behaviour based upon its identification in recently developed alloys based on TiAl with high Nb contents, as well as in O phase based alloy systems themselves. We therefore feel it is an opportune time to review the totality of this effort in this presentation.

Alloys used in these studies covered a wide range of scales ranging from small non consumable arc melts in preliminary studies to consumable arc melts ranging from 25kg to 250kg. Processing usually involved primary forging in the β phase field following by hot rolling to rod in the α2+O+β or O+β phase field, and was optimised to induce recrystallisation in the multiphase structures. For large ingots the ingot forging was followed by upset forging at lower temperatures. A wide range of heat treatments involving different thermal processing paths finishing in the O+β phase were carried out. Composition was varied over a range of Al, Nb, Mo, Zr and Si content.

Phase equilibrium in the ternary Ti-Al-Nb system was established. A good understanding on microstructural effects including the role of $α_2$ and O phase morphology and volume fraction on tensile, creep, and fatigue properties was achieved. Superplastic properties were demonstrated and oxidation behaviour examined. Composition, processing and microstructural optimization carried out over a decade led significant improvements in these properties.
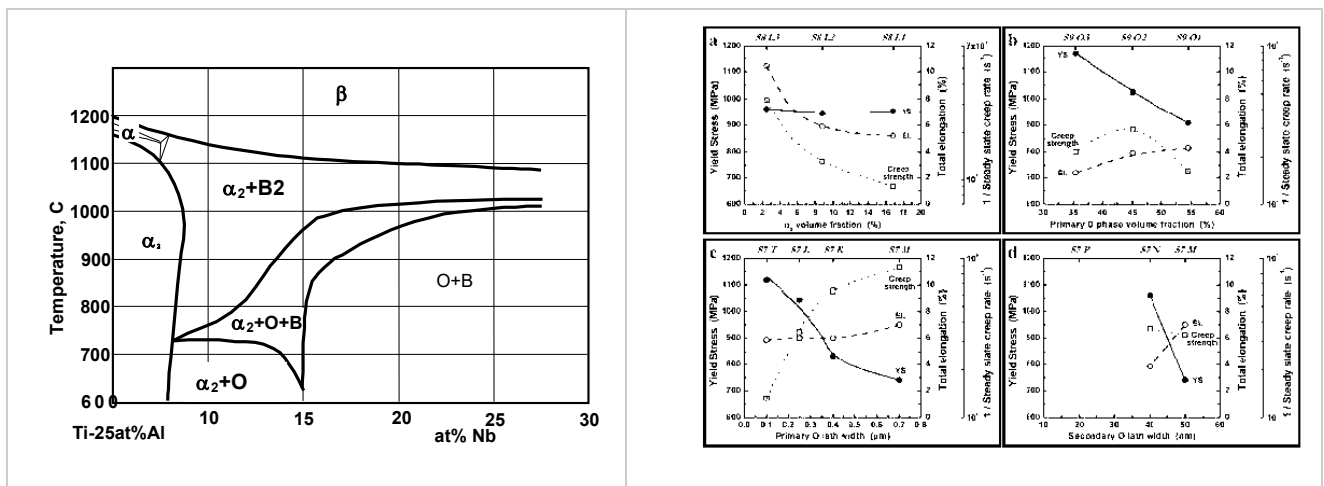
Figure 1: A vertical section in the Ti-Al-Nb ternary section. The disordering of the B2 phase is not indicated	Fig. 2: Effect of microstructural parameters in high Nb alloys on tensile properties at room temperature and on creep rate at: a-b) 650°C / 300MPa, (c) 550°C / 500MPa, (d) 650°C / 400MPa.

References

[1] D. Banerjee, "The Intermetallic Ti_2AlNb", *Progress in Materials Science,* 42(1997), No.1, 135, Pergamon,

[2] A.K.Gogia et al., "Microstructure and Mechanical Properties of Orthorhombic Alloys in the Ti-Al-Nb System", *Intermetallics*, 6 (1998), 741-748.

[3] L. Germann et al., "Effect of Composition on the Mechanical Properties of Newly Developed Ti_2AlNb-based Titanium Aluminide", *Intermetallics*, 13(2005), 920-924.

O–IT 12

Oxidation behavior or TiAl alloy in the atmospheres containing water vapor at 650 °C

Shigenari Hayashi[1], Ali Shaaban[2], Masao Takeyama[3] and Jun Sato[4]

[1]Hokkaido University, N13, W8, Kitaku, Sapporo Hokkaido, Japan,
hayashi@eng.hokudai.ac.jp

[2]Tokyo Institute of Technology, 1-2-1, Ookayama, Meguroku, Tokyo, Japan,
shaaban.a.aa@m.titech.ac.jp

[3]Tokyo Institute of Technology, 1-2-1, Ookayama, Meguroku, Tokyo, Japan,
takeyama@mtl.titech.ac.jp

[4]Mitsubishi Hitachi Power Systems, 1-1-3, Miyukityo, Hitachi, Ibaraki, Japan,
jun3_sato@mhps.com

Introduction

Higher efficiency of power generation in coal-fired power plants can be achieved by higher operation temperatures. However, the high temperature capability of current heat registrant steels for steam turbine has been already reached the limit. In order to increase the steam temperatures up to more than 650°C, temperature capability of materials used for components must be increased.

TiAl alloys are light-weight material and have higher mechanical strength at higher temperatures. Those alloys have already used for low-pressure turbine blades of aero engines [1, 2]. Thus, TiAl alloys can be one of the candidate of alternative materials for steam turbine blades, too. However, one of the critical issues of TiAl alloys is their poor high temperature oxidation resistance. Moreover, the effect of steam on oxidation behavior of TiAl alloy has not been clarified yet. In this study, we investigated the oxidation behavior of commercial TiAl alloy, TNM, in water vapor containing atmospheres.

Materials and Methods

Material used in this study was as-HIPed commercial TNM alloy with the nominal composition of Ti-43.5Al-4.0Nb-1.0Mo-0.1B, (in at.%). The oxidation tests were performed at 650 °C for up to 500 h in air or Ar with/without 30vol.%H_2O.

Results and Discussion

The oxidation mass gains of the samples oxidized in atmospheres containing water vapor were two to three-times higher than those in dry atmospheres as shown in Fig .1. The oxidation mass gain in Ar was about five-times higher than that in air regardless of the presence of H_2O. The result of oxidation tests indicates that water vapor accelerates but nitrogen decreases the oxidation rate of TNM alloy at 650 °C.

TEM observation revealed that a duplex TiO_2 + Al_2O_3 mixed oxide scale consisting of an outer layer rich in Al_2O_3 and an inner layer rich in TiO_2 were developed in all atmospheres after 500 h of oxidation. Below this duplex oxide, a thin Al-rich oxide layer was confirmed to form in dry atmospheres, but Al was internally oxidized in the atmospheres with a presence of H_2O. Since this Al-rich oxide layer is more continuous in air and a Ti(O)N layer was also formed in the subsurface region of the alloy in air and air + H_2O, an Al-rich oxide layer is considered to provide the oxidation resistance in dry condition and the Ti(O)N layer would prevent internal oxidation of Al_2O_3, promoting the formation of an Al-rich oxide layer.
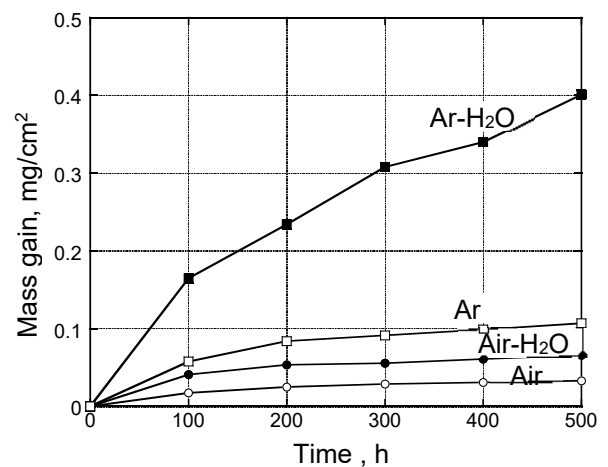
References

[1] H. Clemens, S. Mayer, Design, Processing, Microstructure, Properties, and Applications of Advanced Intermetallic TiAl Alloys, Advanced Engineering Materials, **2013**, *15*, 191–215.

[2] J. Aguilar, A. Schievenbusch, O. Kättlitz, Intermetallics **2011**, *19*, 757-761.

O–IT 13

Oxidation and creep behavior of novel intermetallic Mo-Si-Ti alloys

M. Heilmaier, D. Schliephake, A. Kauffmann, C. Gombola, X. Cong

Mo-based silicides consisting of the three phases Mo_{ss}, Mo_5SiB_2 and Mo_3Si have been considered promising candidates for structural applications at elevated temperatures. Recently, it was found that macro-alloying of Mo-Si-B alloys by Ti allows for replacing Mo_3Si by the more creep and oxidation resistant phase Mo_5Si_3. Furthermore, Ti causes a significant reduction in density of such alloys.

An alternative approach in the ternary Mo-Si-Ti system focusing on two-phase alloys with different ratios of Mo solid solution and 5-3 type silicides also shows very encouraging results regarding oxidation and creep behavior at elevated temperatures. As a consequence, this talk will focus on two alloy familiess with different – eutectic and eutectoid – phase equilibria in the ternary Mo-Si-Ti system. Microstructure evolution for both reactions was experimentally tracked regarding composition, temperature and time as well as compared to thermodynamic calculations. For annealed (optimized) microstructures the isothermal and cyclic oxidation and compressive creep behavior was characterized at temperatures between 800 and 1200°C and finally assessed against state-of-the-art ternary and quaternary Mo-Si-B(-Ti) alloys as well as Ni-base single crystalline alloys.

O–MB 01

Low temperature ductility of B2 structured transition metal intermetallic compounds YCu and YAg

Werner Skrotzki[1], Rolf Schaarschuch[1], Carl-Georg Oertel[1], Guanghui Cao[2] and Jens Freudenberger[3]

[1]Institute of Solid State and Materials Physics, Dresden University of Technology,
D-01062 Dresden, Germany
werner.skrotzki@tu-dresden.de, rolf.schaarschuch@tu-dresden.de,
carl-georg.oertel@tu-dresden.de,

[2]Department of Materials Engineering, Shanghai University, Shanghai 200072, P.R. China
ghcao@shu.edu.cn

[3]IFW Dresden, Institute for Metallic Materials, Helmholtzstraße 20, D-01069 Dresden, Germany
j.freudenberger@ifw-dresden.de

Introduction

Intermetallic compounds in general are brittle at low temperatures due to insufficient independent slip systems or low grain boundary cohesion. The present paper reports on the deformation of YCu and YAg known to be highly ductile at room temperature [1]. It is shown that despite of violating the von Mises criterion these B2-structured intermetallic transition metal compounds are extremely ductile down to 130 K and 4 K, respectively. Based on a thorough thermal activation analysis the reasons for this unexpected behavior are discussed, including low elastic anisotropy, low Peierls stress and martensitic transformation.

Materials and Methods

Master alloy ingots of almost stoichiometric composition YCu and YAg were produced by induction melting of high purity Y, Cu and Ag in Ar atmosphere followed by casting into a graphite mould. To get a defined homogeneous microstructure and texture, in addition the ingots were hot extruded. To decrease friction during extrusion, the cylindrical ingots (35 mm length, 30 mm diameter) were canned in copper. The extrusion processing was done at 875K with a stem speed of 6 mm/s and an extrusion ratio of 5.3. After extrusion the rods were air-cooled. YAg single crystals were grown by the Bridgman method.

The grain structure was investigated by electron backscatter diffraction (EBSD) in a scanning electron microscope (Zeiss Ultra 55). Texture measurements were done by neutron diffraction. Phase transformations were detected by X-ray diffraction (XRD). XRD was performed with an X-ray micro diffraction system D8 DISCOVER (Bruker AXS GmbH) equipped with a micro focus X-ray tube iMOXS (Cu-Kα radiation) with a spot size of 50 μm on the sample and an area detector Vantec-2000. The dislocation structure was analyzed with a Tecnai G2 transmission electron microscope (TEM) operated at an acceleration voltage of 200 kV.

To carry out tensile tests from room temperature down to 4 K at a strain rate of about 10^{-4}/s, a deformation apparatus with He cryostat for temperature adjustment was used [2]. The low temperature deformation system consists of an Instron 4502 electromechanical 2-spindle testing machine with an MTS ReNew Elite controller and a He cryostat type CryoVac 3-06-2516B with CryoVac TIC 304-MA. Dog-bone shaped samples for tensile deformation were cut by spark erosion from the extruded rods and from the single crystals. The strain measurement was carried out by precision correction of the sample elongation through calibration with Ni single crystals. This procedure was especially necessary for the sensitive stress relaxation measurements used for the thermal activation analysis.

Results and Discussion

The hot extruded rods of both intermetallics were dynamically recrystallized and had an average grain size of a few microns. The texture was a weak <110> fibre texture. The stress - strain curves

reveal a pronounced ductility of a few percent slightly decreasing with decreasing temperature. YCu becomes brittle below 130 K due to a martensitic phase transformation from B2 to B27. In contrast, YAg does not show any phase transformation and stays ductile down to 4 K. The yield stress is constant for YCu down to the brittle-to-ductile transition temperature, while for YAg it slightly increases with decreasing temperature (Fig. 1). The Peierls stress estimated from the extrapolated thermal part of the flow stress at 0 K is <40 MPa, much lower than that of NiAl which is 535 MPa [3]. This is in agreement with the low unstable stacking fault energy reported for $\frac{1}{2}\{110\}<100>$ slip: YCu 325 mJ/m^2, YAg 315 mJ/m^2, NiAl 1290 mJ/m^2 [4]. The experimental rate sensitivity linearly depends on stress (Fig. 2) typical for the Cottrell-Stokes behavior [5] indicating forest dislocation cutting as the rate controlling process. TEM contrast analysis of the dislocation structure only reveals dislocations with <100> Burgers vector. This type of Burgers vector only provides 3 independent slip systems, thus violating the von Mises criterion for homogeneous deformation of polycrystals.

Based on these results, the following explanation is given for the high ductility of YCu and YAg. Both intermetallic compounds predominantly deform by <100> slip violating the von Mises criterion. As the yield stresses determined by forest dislocation cutting are very low, also internal stresses developing from strain incompatibilities at the grain boundaries are low. Moreover, these internal stresses are isotropic, because the elastic anisotropy $A = 2c_{44}/(c_{11} - c_{12})$ is almost one: YCu 0.99, YAg 1.54, in comparison to NiAl 3.27. In conclusion, the deformation behavior of these two intermetallic compounds is more similar to that of face-centered than body-centered cubic metals.
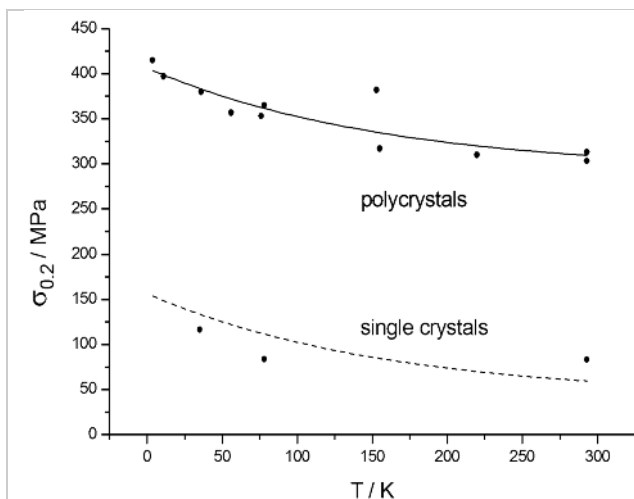
Fig. 1: Temperature dependence of the yield stress of YAg <931> single crystals and polycrystals
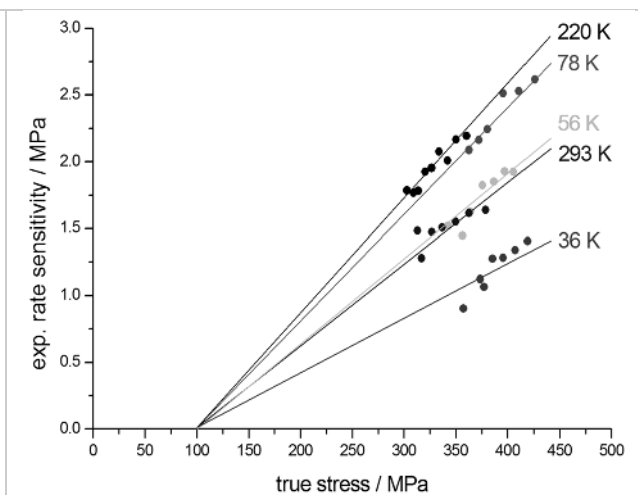
Fig. 2: Experimental rate sensitivity of YAg polycrystals as a function of true stress at different temperatures

References

[1] K.A. Gschneidner Jr., A.M. Russel, A. Pecharsky, J. Morris, Z. Zhang, T.A. Lograsso, Nature Materials. **2003**, *2*, 587-590.

[2] D. Brunner, J. Diehl, Zeitschrift für Metallkunde. **1992**, *83*, 828-834.

[3] D. Brunner, P. Gumbsch, Zeitschrift für Metallkunde. **2002**, *93*, 672-680.

[4] J.R. Morris, Y. Ye, Y. Lee, B.N. Harmon, K.A. Gschneidner Jr., A.M. Russel, Acta Materialia. **2004**, *52*, 4849-4857.

[5] L. Hollang, E. Hieckmann, D. Brunner, C. Holste, W. Skrotzki, Materials Science and Engineering A. **2006**, *424*, 138-153.

O–MB 02

In-situ micro-cantilever tests to study the fracture properties of phases in a NiAl-Cr eutectic system

S. Gabel[1], S. Giese[1], I. Sprenger[2], M. Heilmaier[2], S. Neumeier[1], M. Göken[1]

[1]Department of Materials Science & Engineering, Institute I: General Materials Properties, Friedrich-Alexander-University of Erlangen-Nuremberg, Erlangen, Germany, e-mail address: stefan.s.gabel@fau.de

[2]Institute for Applied Materials, Karlsruhe Institute of Technology (KIT), Karlsruhe, Germany

Nanomechanical testing is nowadays important for studying the material properties at the micron or even sub-micron scale. For example, pre-notched micro-cantilever fracture tests are suitable to determine the local fracture toughness [1,2]. By investigating the fracture toughness of individual phases and the influence of toughening mechanisms, the macroscopic fracture behaviour of eutectic materials with a multiphase microstructure like directionally solidified NiAl-Cr can be understood. Eutectic NiAl-Cr consists of, the brittle intermetallic β-NiAl and the more ductile reinforcing α-Cr phase. Depending on the solidification rate and the composition, either α-Cr fibers or α-Cr lamellae are present in the β-NiAl matrix [3]. Regardless of the microstructure of these directionally solidified eutectics, they exceed the fracture toughness of their constituting pure phases. This is achieved by different toughening mechanisms, which increase the fracture toughness after initial crack nucleation [4].

In order to investigate the influence of different microstructures and lamellae orientations on the fracture toughness of NiAl-Cr eutectic composites, in-situ micro cantilever tests on notched samples were carried out, see Fig. 1. In-situ composites based on the NiAl-Cr eutectic system were produced by directional solidification with cellular growth. Replacement of Cr by Mo was used to change the eutectic microstructure. The NiAl-(Cr,Mo) alloys with 0,5 at.% Mo had a fibrous microstructure, while the NiAl-(Cr,Mo) with 3 at.% Mo had a lamellar structure. The chemical compositions of the α-Cr and β-NiAl phase were analyzed by EDX measurements. Using micro cantilever beams, produced by FIB milling, the local fracture toughness of the phases was measured. A fiber containing and a lamellar NiAl-Cr eutectic, with different positioning of the notch and sizes of the cantilevers, were studied. This shows the versatility of the micro-cantilever deflection technique. Testing of the cantilevers was either performed in-situ in an electron microscope with a micromanipulator or, depending on their size, ex-situ with a nanoindenter.

Apparently the α-Cr phase has with 8–10 MPa√m a higher fracture toughness than β-NiAl of about 1.6–2.1 MPa√m. Due to the high purity of the α-Cr phase, the fracture toughness of α-Cr is high and in good consistency with the macroscopic fracture toughness of pure Cr [5]. The relatively low fracture toughness of β-NiAl is a result of a non-stoichiometric, Al-rich composition. Furthermore the fracture toughness of the interface was measured and is about 2.8-3.7 MPa√m. Therefore, toughening mechanisms with a crack deflection at the interface are assumed to be less important for the macroscopic fracture toughness of the composite.
However, the measured fracture toughness correlates with the early stages of crack initiation, which has a limited impact on the macroscopic fracture toughness. The ex-situ experiments, as shown in Fig 2, revealed that crack deflection, renucleation and bridging take place after the crack grows in the range of the thickness of a lamella. Hence, cantilevers containing multiple phase boundaries show the first stages of the transition from single phase fracture to the fracture toughness increasing mechanisms, which influence crack resistance of the eutectic system on the macroscopic scale.

Fig. 1: Micro-cantilever with a crack at the α-Cr/β-NiAl interface

Fig. 2: NiAl-Cr fracture surface of an ex-situ cantilever
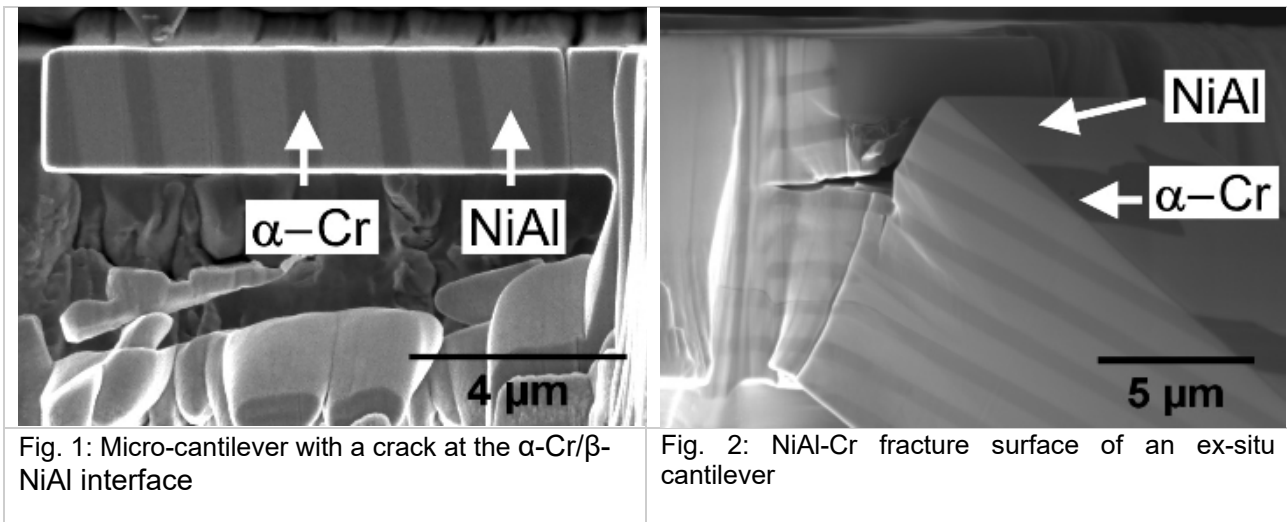
References

[1] J. Ast, T. Przybilla, V. Maier, K. Durst, M. Göken, *Journal of Material Research*, **2014**, *29*, 2129-2140.

[2] K. Matoy, H. Schönherr, T. Detzel, T. Schöberl, R. Pippan, C. Motz, G. Dehm, *Thin Solid Films*. **2009**, *518*, 247–256.

[3] H.E. Cline and J.L. Walter, *Metallurgical Transactions. 1970, 1,* 2907–2917.

[4] D.R. Johnson, S.F. Chen, B.F. Oliver, *Intermetallics. 1995, 3,* 99–113.

[5] H. Stamm, M. Bonansinga, F.D.S. Marques, P. Hähner, H. Kolbe, A. Volcan, *Journal of Nuclear Materials.* **1998**, *258*, 1756-1761.

O–MB 03

Microstructure control and plastic deformability of two-phase heat resistant alloys based on E2$_1$-type Co$_3$AlC$_{1-x}$

Yoshisato Kimura[1], Mami Kasakura[2], and Yaw Wang Chai[3]

[1]Tokyo Institute of Technology, School of Materials and Chemical Technology, Department of Materials Science and Engineering, J3-19, 4259 Nagatsuta-cho, Midori-ku, Yokohama 226-8502, Japan, kimura.y.ac@m.titech.ac.jp

[2]Tokyo Institute of Technology, Interdisciplinary Graduate School of Science and Engineering, Department of Materials Science and Engineering, J3-19, 4259 Nagatsuta-cho, Midori-ku, Yokohama 226-8502, Japan, kasakura.m.ab@m.titech.ac.jp, *now with* Nissan Motor Corporation.

[3]Tokyo Institute of Technology, School of Materials and Chemical Technology, J2-56, 4259 Nagatsuta-cho, Midori-ku, Yokohama 226-8502, Japan, chai.y.aa@m.titech.ac.jp

Introduction

The E2$_1$ type intermetallic compound Co$_3$AlC$_{1-x}$ can be an attractive strengthener of Co-base heat resistant alloys, since the E2$_1$ type ordered crystal structure is similar to that of the L1$_2$ type Ni$_3$Al which is a well-known strengthener of Ni-base superalloys. The ordered structures of E2$_1$ and L1$_2$ can be differentiated by an interstitial carbon atom occupying at the cell center of E2$_1$. In the chemical formula of Co$_3$AlC$_{1-x}$, x stands for the deficiency of a carbon atom as a vacancy at the carbon-site of the E2$_1$ ordered structure. Authors' group reported that Co$_3$AlC$_{1-x}$ shows excellent ductility and strength using poly- and single-crystal alloys[1,2]. It is possible to comtrol the two-phase microstructure consisting of the fcc (Co) matrix and Co$_3$AlC$_{1-x}$ precipitates, however, a relatively large lattice mismatch, exceeding 2.5%, between these two phases induces the formation of nodular type discontinuous precipitation (DCP) lamellar microstructure. Since the formation of DCP lamellar is locally distributed, the overall morphology of microstructure tends to become inhomogeneous. We have proposed heat treatments [3] and unidirectional solidification to control or to avoid DCP lamellar microstructure. The objectives of the present work are to evaluate the thermal stability of two-phase microstructure based on E2$_1$ Co$_3$AlC$_{1-x}$ phase and fcc solid solution (Co) phase, and to understand the relationship between morphology of microstructure and plastic deformability as well as the strength of the alloys. Mechanical properties at high temperatures should be important factors of heat resistant alloys, and at the same time, the better understanding of plastic deformability and strength at ambient temperature is also important for the heat resistant alloy design.

Materials and Methods

Several Co-Ni-Al-C quaternary two-phase alloys based on E2$_1$ Co$_3$AlC$_{1-x}$ were fabricated using arc melting and consecutive directional solidification using the optical floating zone melting in an argon gas atmosphere. The Ni addition is aimed to enlarge the two-phase field consisting of E2$_1$ (Co,Ni)$_3$AlC$_{1-x}$ phase and fcc solid solution (Co,Ni) phase, since Ni atoms substitute for Co atoms in both phases. Depending on the chemical compositions, B2 (Co,Ni)Al coexists as a third phase. Microstructure control using heat treatments was applied on alloy A (62.4Co-16.6Ni-17.0Al-4.0C in at%), and using unidirectional solidification on alloy B (65.1Co-11.9Ni-16.0Al-7.0C). Microstructure was observed and characterized by means of scanning electron microscopy using backscattered electron image (BEI) and transmission electron microscopy. Chemical compositions of each phase were quantitatively measured using the electron probe micro-analysis. Mechanical properties of the alloys were measured by tensile test at room temperature, and compression test at room temperature and 1123 K, at the initial strain rate of 10^{-4} s^{-1}.

Results and Discussion

Microstructure
Typical two-phase microstructure consisting of E2$_1$ (Co,Ni)$_3$AlC$_{1-x}$, κ phase, and fcc (Co,Ni), α phase, of alloy A is shown in Fig. 1, in which κ phase is observed in dark contrast and α phase in bright

contrast, respectively. In the solidification sequence of alloy A, α phase solidifies as a primary phase in the dendritic morphology, then, the eutectic α and κ lamellar microstructure is formed as the final product of solidification. Consecutively, κ phase precipitates having fine cuboidal morphology in the dendrite α matrix during cooling. After annealing, the DCP lamellar nodules of α and κ form locally in the α matrix with fine κ precipitates region. The DCP lamellar nodules initiate at the boundaries of α dendrite regions and they grow locally by replacing those regions. The driving force of DCP is to lower the Gibbs energy due to supersaturation of solute carbon atoms and the interfacial energy according to the lattice mismatch between α and κ phases. The inter-lamellar spacing and nodular region size of the DCP lamellar nodules become larger with increasing heat treatment temperature. The DCP lamellar spacing can be estimated as ranging from 0.4 to 1 μm at 973 K annealing, from 3 to 7 μm at 1173 K, and from 10 to 20 μm at 1373 K. As heat treatment temperature increases higher, the frequency of the nucleation increases larger while the growth rate becomes slower since the diffusion rate is lower. On the other hand, directionally solidified microstructure of alloy B is shown in Fig. 2. α and κ phases are well aligned along the growth direction, and κ phase precipitates in α phase as shown in (a). A cellular type growth is indicated by the morphology of two-phase microstructure observed in (b). Note that the DCP can be avoided by the directional solidification partly because the supersaturation of carbon is suppressed due to the slow solidification rate.

Fig. 1: Typical two-phase microstructure consisting of E2$_1$ (Co,Ni)$_3$AlC$_{1-x}$ and fcc (Co, Ni); alloy A (a) as-cast and (b) annealed at 1173 K for 96 h.

Fig. 2: Microstructure of directionally solidified alloy B at 20 mm/h; the cross-section (a) parallel and (b) perpendicular to the growth direction.
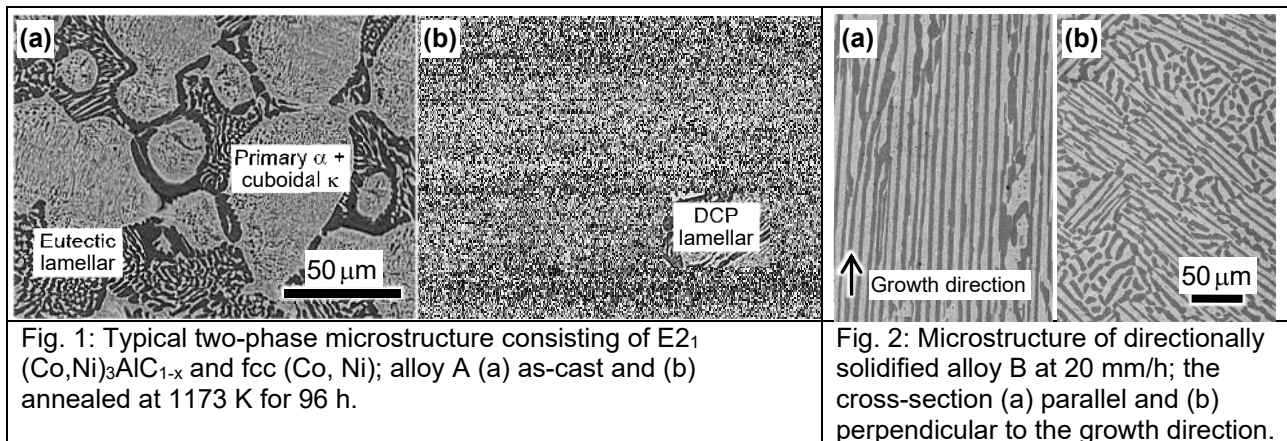
Mechanical properties

Compression and tensile tests were conducted to measure mechanical properties of alloys which have two-phase microstructure with three different morphologies; primary α matrix dendrite with fine cuboidal κ precipitates, $\alpha+\kappa$ eutectic lamellar, and $\alpha+\kappa$ DCP lamellar. As-cast of alloy A exhibits high yield strength of about 975 MPa in compression, and the excellent ductility of about 4.4 % in tension at 300 K. Annealed counterparts also show high yield strength at 300 K in compression, from about 750 MPa (annealed at 1173 K for 96 h) up to 1.2 GPa (at 973 K for 96 h) depending on the volume fractions of DCP lamellar and its spacing. Corresponding tensile ductility of these alloys is excellent 13 % (1173 K, 96 h) and poor 2.5 % (973 K, 96 h). High temperature strength of alloy A is 486 MPa at 1123 K in compression. It was anticipated that the DCP lamellar reduces the strength of alloys, however, the fine DCP lamellar formed at 973 K makes the alloy even stronger. Two-step heat treatment, annealing at 973 K for 96 h followed by at 1173 K for 96 h, was applied to control the DCP lamellar nodule finer. As a result, the ductility is excellent 11% in tension, while the yield strength is reduced down to 830 MPa at 300 K and 405 MPa at 1123 K. On the other hand, directionally solidified alloy B shows fairly high yield strength of 629 MPa at 300 K and 452 MPa at 1123 K. Consequently, the best balance of strength between ambient temperature and elevated temperature can be achieved in the directionally solidified microstructure.

References

[1]   Y. Kimura, K. Sakai, Y. Mishima, Phase Equilibria and Diffusion. **2006**, 27, 14-21.

[2]   Y. Kimura, K. Sakai, F.G. Wei, Y. Mishima, Intermetallics. **2006**, 14, 1262-1269.

[3]   M. Kasakura, Y. Kimura, Proc. of the 9th Pacific Rim Intl. Conf. on Advanced Materials and Processing (PRICM-9), **2016**, 770-775.

O–MB 04

Deformation behavior of Fe-Al single crystals containing Ni₂Al(Ti,V) precipitates

Hiroyuki Y. Yasuda[1], Hirofumi Otani[1] and Ken Cho[1]

[1]Division of Materials and Manufacturing Science, Graduate School of Engineering,

Osaka University, 2-1, Yamada-oka, Suita, Osaka 565-0871, Japan

hyyasuda@mat.eng.osaka-u.ac.jp, k_cho@mat.eng.osaka-u.ac.jp

Introduction

Ferritic heat-resistant steels are widely used for steam turbine of thermal power plants due to their low thermal expansion coefficient, high thermal conductivity and low cost, compared with Ni-based superalloys [1]. However, the application limit temperature is around 630°C. Thus, extensive efforts have been made to develop new ferritic heat-resistant alloys with high application limit temperature. It is well known that precipitation hardening is one of the effective ways to increase material strength. In ternary Fe-Al-Ni phase diagram, there is a two-phase field composed of the bcc phase and the NiAl phase with the B2 structure. The precipitation of the NiAl phase leads to a huge increase in strength in the wide temperature range [2,3]. Recently, our research group carried out a systematic study on the strengthening mechanism of Fe-Al-Ni alloys using the single crystals and found that the difference in primary slip system between the bcc matrix and the NiAl precipitates is closely related to the strong precipitation hardening [4]. The primary slip systems of the bcc matrix and the NiAl precipitates are {101}<111> and {110}<001>, respectively. For example, at <149> orientation, {101}<111> slip occurs, which is favorable for the bcc matrix. However, the NiAl precipitates are also sheared by <111> slip, resulting in strong hardening. On the other hand, at <557> orientation, {110}<001> slip occurs, though <001> slip is generally impossible to take place in bcc metals. This also leads to strong hardening. Thus, we call this type of precipitation hardening "slip frustration hardening (SFH)". SFH is very effective in increasing high temperature strength in Fe-Al-Ni alloys. In the present study, Ti and V were doped to improve the mechanical properties of Fe-Al-Ni alloys at high temperatures. Ti or V doping led to the formation of the Ni₂Al(Ti, V) precipitates with the L2₁ structure. In general, the Ni₂Al(Ti,V) precipitates have the high dissolution temperature, which is favorable for high temperature strength. It is also noted that Ti and V were co-doped to control the characteristics of the L2₁ precipitates and to improve high temperature strength.

Materials and Methods

Fe-23Al-6Ni and Fe-21Al-6Ni-3(Ti, V) (at.%) alloys were prepared by arc melting and the single crystals were grown by a floating zone method at a growth rate of 5 mm/h. After homogenization at 1100°C for 48 h, these crystals were furnace-cooled to room temperature at 80°C /h. Compression specimens with <149> orientation favorable for {101}<111> slip were cut from the single crystals. Compression tests were performed in the temperature range between room temperature to 950°C at a constant cross-head speed of 0.5 mm/min corresponding to an initial strain rate of 1.7×10^{-4} /s. The slip planes after compression were determined by a two-surface trace analysis using an optical microscope. The microstructure and dislocation structure were observed by a transmission electron microscope (TEM) operated at 300 kV.

Results and Discussion

Fig. 1 shows TEM micrographs of undoped, 3Ti-doped and 3V-doped single crystals. In undoped crystals, fine NiAl precipitates with the B2 structure are densely distributed in the bcc matrix (Fig. 1 (a)). In contrast, 3Ti-doped crystals have coarse L2₁ precipitates with the rectangular shape of which habit plane is {001} (Fig. 1 (b)). It is also noted that small B2-type precipitates are observed between coarse L2₁ precipitates. In contrast, fine L2₁ phase is precipitated in 3V-doped crystals (Fig. 1 (c)). A dissolution temperature (Tc) of the precipitates and a misfit strain (δ) between the bcc matrix and the precipitates depend strongly on the crystals, also shown in Fig. 1. 3Ti-doped crystals exhibit high

Tc and large δ. In contrast, δ of 3V-doped crystals is small, though Tc is the almost same as that of undoped crystals. The data for 2.5Ti-0.5V-doped crystals are also shown in Fig. 1 (d). The size, Tc and δ of the $L2_1$ precipitates are intermediate between those of 3Ti- and 3V-doped crystals. This means that the characteristics of the $L2_1$ precipitates can be controlled by co-doping with Ti and V.

Fig. 2 shows temperature dependence of yield stress in undoped, 3Ti- and 3V-doped crystals. 3Ti-doped crystals demonstrate higher strength than undoped crystals, especially at high temperatures above 600°C. Higher Tc of 3Ti-doped crystals results in high strength at high temperatures. However, the dislocations bypassed coarse $L2_1$ precipitates due to high δ. This also means that SFH never takes place in 3Ti-doped crystals. On the other hand, the yield stress of 3V-doped crystals is almost the same as that of undoped crystals. In 3V-doped crystals, fine $L2_1$ precipitates were cut by paired 1/2[111] dislocations in bcc matrix, and therefore, SFH occurred. However, lower Tc of 3V-doped crystals is unfavorable for high temperature strength. In contrast, co-doping of Ti and V is effective in increasing strength in the wide temperature range, as shown in Fig. 2. 2.5Ti-0.5V-doped crystals also exhibit high strength at high temperatures, similar to 3Ti-doped crystals. Moreover, the $L2_1$ precipitates in co-doped crystals were sheared by 1/2[111] dislocations at room temperature. This means that SFH occurs in co-doped crystals due to low δ.
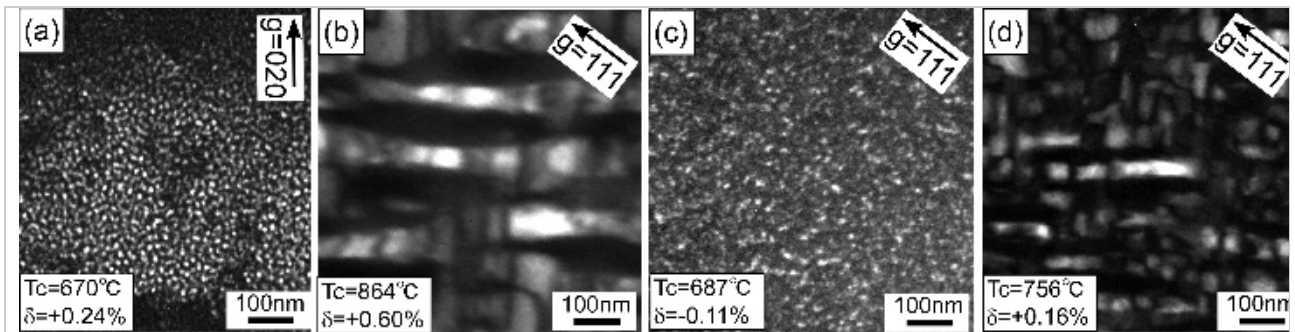
Fig. 1: Microstructure of undoped (a), 3Ti- (b), 3V- (c) and 2.5-0.5V-doped (d) crystals.
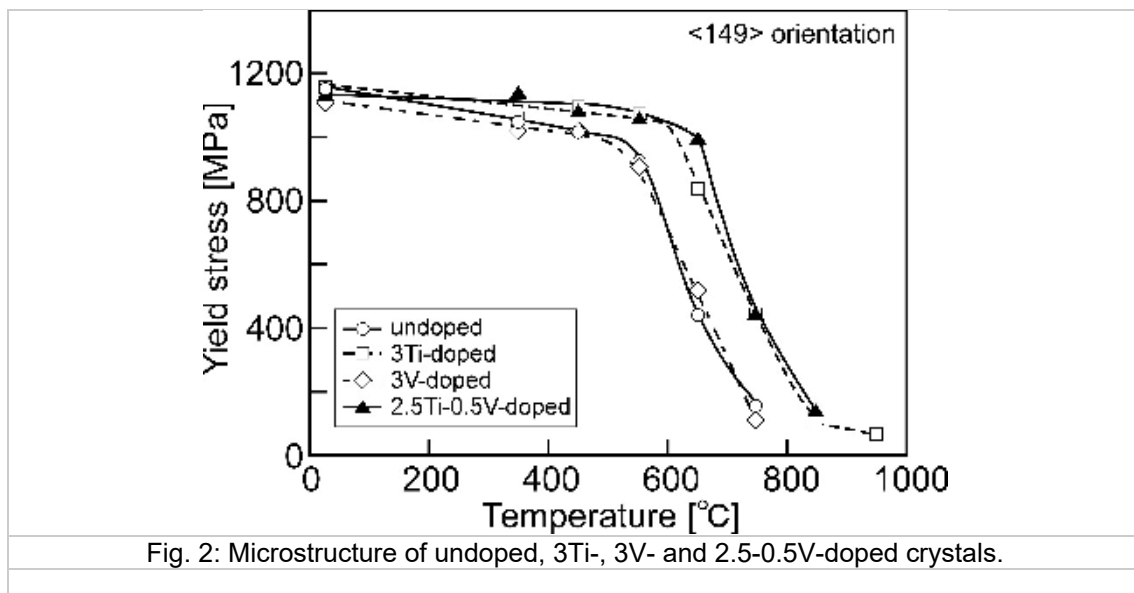
Fig. 2: Microstructure of undoped, 3Ti-, 3V- and 2.5-0.5V-doped crystals.

References

[1]   H. K. D. H. Bhadeshia, ISIJ International. **2001**, *41*, 626–640

[2]   R. Taillard, A. Pineau, Mater. Sci. Eng. **1982**, *56*, 219-231.

[3]   C. Stallybrass, A. Schneider, G. Sauthoff, Intermetallics. **2005**, *13*, 1263-1268.

[4]   T. Edahiro, K. Kouzai, H.Y. Yasuda, Acta Mater. **2013**, *61*, 1716-1725.

O–MB 05

Stacking faults in C14 Fe_2Nb Laves phase

Michaela Šlapáková[1,2], <u>Christian Liebscher</u>[2], Sharvan Kumar[3], Frank Stein[2]

[1]Charles University in Prague, Faculty of Mathematics and Physics, Department of Physics of Materials, Ke Karlovu 5, Prague, 121 16, Czech Republic, slapakova@karlov.mff.cuni.cz

[2]Max-Planck-Institut für Eisenforschung, Structure and Nano-/Micromechanics of Materials, Max-Planck-Strasse 1, Düsseldorf, 402 37, Germany, liebscher@mpie.de, stein@mpie.de

[3]Brown University, School of Engineering, 182 Hope St., Providence, RI 02912 USA, Sharvan_Kumar@brown.edu

Introduction

Laves phases AB_2 are intermetallic materials with three main structural variants – cubic C15 and hexagonal C14 and C36. Their structural unit is composed of a single layer of smaller atoms B and a triple layer of ABA atoms [1]. The sequence of the successive triple layers determines the structural variant.

The main deformation mechanism of Laves phases was reported to be slip – on {111} planes in the cubic structure [2] and on (0001) plane in hexagonal structures [3]. During the deformation, perfect dislocations split into partial dislocations which bind stacking faults [4]. The motion of the partial dislocations was described by a model of Synchroshear [5] – a synchronous motion of two adjacent atomic layers within the triple layer in two different directions.

Materials and Methods

Single phase Fe_2Nb with hexagonal C14 structure was fabricated by levitation melting in laboratory conditions [6]. Three compositions were cast – 29.7 at.% Nb, 33 at.% Nb and 35 at.% Nb. The materials were subjected to compression tests at elevated temperatures (1100-1400 °C). The deformed microstructure was investigated by means of conventional transmission electron microscopy (Philips CM 20) and high-resolution scanning transmission electron microscopy (FEI Titan Themis).

Results and Discussion

The microstructure of the deformed materials depends on both the composition and deformation temperature. Stacking faults are the most dominant feature. In both the Nb-lean and stoichiometric material the stacking faults lie on the basal plane (0001) and are bound by partial dislocations with **b** = 1/3 $<10\bar{1}0>$ type Burgers vector. In the Nb-rich material, the stacking faults lie not only on the basal plane but also on pyramidal planes $\{10\bar{1}1\}$ and prismatic planes $\{10\bar{1}0\}$ (Figure 1).

The width of the stacking faults strongly depends on the temperature of the deformation. After deformation at 1200 °C the stacking faults are very long and can extend over a whole grain (grain size ~100 µm) – their bounding partial dislocations are trapped in the grain boundaries. Some of the stacking faults overlap. With increasing temperature their width decreases and after deformation at 1400 °C the spacing of the partials reduces to ~50 nm.

On the atomic scale, the basal stacking faults are formed by a shift of one triple layer (Figure 2) where locally a cubic C15 stacking is formed. Moreover, in the Nb-rich material other stacking fault variants on basal, pyramidal and prismatic planes were observed. A few atomic layers of µ-phase Fe_7Nb_6, which is another stable phase in the Fe-Nb phase diagram [7], were found to form being coherent with the Laves phase. The excess Nb atoms segregate to the stacking faults inducing a phase formation to reduce the off-stoichiometry of the Nb-rich Laves phase. Such structural change was also observed in the as-cast Nb-rich material. This second phase formation might directly impact the mechanical properties since higher stresses are required to deform the Nb-rich material compared to the stoichiometric and Nb-lean ones [8], as moving dislocations have to overcome a change in the structure.
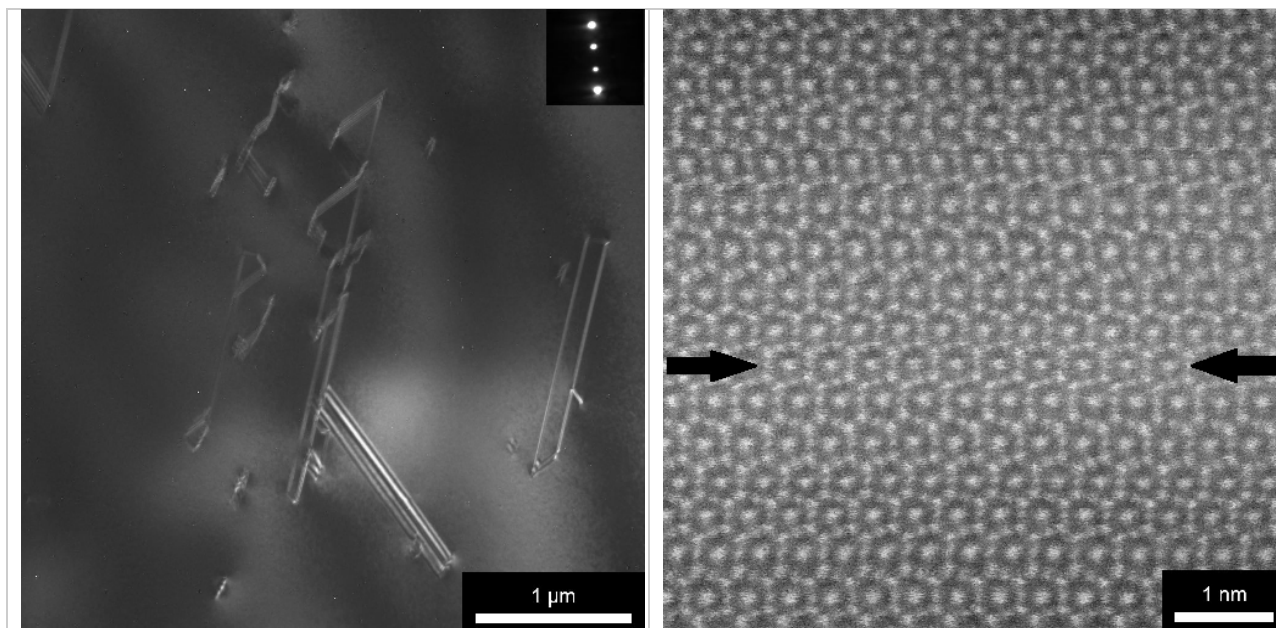
Fig. 1: Stacking faults on basal, pyramidal and prismatic planes in Nb-rich material after deformation at 1200 °C. B = [0001], g = [1$\bar{1}$00].

Fig. 2: HAADF STEM image of a basal stacking fault in Nb-lean material after deformation at 1300 °C.. B = [1$\bar{2}$10].

References

[1] D.J. Thoma, Intermetallics: Laves phases, in Encyclopedia of Materials: Science and Technology, Elsevier, Amsterdam, **2001**, 4205-4213.

[2] M. Yoshida, T. Takasugi, TEM observation for deformation microstructures of two C15 $NbCr_2$ intermetallic compounds, Intermetallics. **2002**, *10*, 85-93.

[3] N. Takata, H. Ghassemi-Armaki, M. Takeyama, S. Kumar, Nanoindentation study on solid solution softening of Fe-rich Fe_2Nb Laves phase by Ni in Fe–Nb–Ni ternary alloys, Intermetallics. **2016**, *70*, 7-16.

[4] A.V. Kazantzis, M. Aindow, I.P. Jones, G.K. Triantafyllidis, J.Th.M. De Hosson, The mechanical properties and the deformation microstructures of the C15 Laves phase Cr_2Nb at high temperatures, Acta Materialia. **2007**, *55*, 1873-1884.

[5] M.F. Chisholm, S. Kumar, P. Hazzledine, Dislocations in Complex Materials, Science. **2005**, *307*, 701-703.

[6] S. Voß, F. Stein, M. Palm and D. Raabe, Synthesis of defect-free single-phase bars of high-melting Laves phases through modified cold crucible levitation melting. Materials Science and Engineering: A. 2010, 527, 7848–7853.

[7] S. Voß, M. Palm, F. Stein and D. Raabe, Phase equilibria in the Fe-Nb system, Journal of Phase Equilibria and Diffusion. **2010**, *32*, 97–104.

[8] S. Voß, M. Palm, F. Stein and D. Raabe, Compositional dependence of the compressive yield strength of Fe-Nb(-Al) and Co-Nb Laves phases, Materials Research Society Symposium Proceedings. **2011**, 1295, 311–316.

O–MB 06

Chemical order in plastically deformed 18 carat red gold alloy

Marina Garcia Gonzalez[1,2], Nadine Baluc[2], Fanny Lalire[3], Helena Van Swygenhoven[1,2]

[1]Paul Scherrer Institute, Switzerland, marina.garcia-gonzalez@psi.ch

[2]Ecole Polytechnique Federale de Lausanne, Switzerland, nadine.baluc@epfl.ch

[3] Varinor SA, Switzerland

Introduction

An 18 carat red gold alloy is an age-hardenable alloy. Above the critical temperature ($T_c \approx 350^\circ C$ [1]) the alloy has a chemically disordered FCC structure. Below this temperature, chemical ordering takes place and the harder $Au_{50}Cu_{50}$ phase is formed. Chemical ordering involves diffusion of gold and copper atoms to distinct {001} planes within the disordered matrix. This causes a tetragonal distortion of the initial cubic lattice and induces strong misfit strains [2-3].

The kinetics of the ordering process depends on the temperature at which previous disordering was done. It has been observed that the presence of short-range order prior to cooling increases the time required for a full ordering transformation [4]. This implies that the final microstructure in terms of grain size and ordering will depend on the history of annealing temperatures and cooling time. Additionally, there are indications that plastic deformation of a partially ordered microstructure can change the disorder kinetics during annealing and the microstructure obtained after subsequent cooling will be different from the one obtained without plastic deformation. This study is to investigate how plastic deformation affects degree of ordering and the morphology of precipitates in a partially ordered sample which is subjected to a further annealing.

Materials and Methods

The alloys were prepared by continuous casting from fine metal precursors (Au, Ag, Cu) melt in a graphite crucible to form 18 carat red gold ($Au_{75}Cu_xAg_{(1-x)}$ for $x \geq 20$ in %wt.). They were rolled in the form of strips, well homogenized and recrystallized. Partial ordering is present after heat treatment. Some of the samples were additionally subject to a bending deformation to induce both compressive and tensile strain states, representative of complex deformation states that happen during processing. The deformed and non-deformed specimens were annealed well above the ordering critical temperature ($\approx 0.6 T_m$) for a few minutes followed by rapid cooling. Electron microscope investigations are carried out in thin foils prepared by mechanical polishing and electrolytic thinning with the double-jet technique in a Tenupol-5. The electrolyte used for this thinning is a mixture of 50%HCl – 30% ethanol-10% glycerol at $3^\circ C$. Observations are made in a FEI Talos microscope operating at 200kV. Both bright-field and dark-field observations are made combined with selected area diffraction patterns. The degree of ordering, the morphology of ordered domains and dislocation distribution are analysed and discussed in terms of the plastic deformation applied before annealing.

References

[1] J. Henning, Phase Transformations in 18-Carat Gold Alloys Studied by Mechanical Spectroscopy, EPFL Doctoral Thesis, Lausanne, **2010**, doi:10.5075/epfl-thesis-4635

[2] L. Nowack, Zeitschrift für Metallkunde, **1930**, 22, 84.

[3] Harker, Transactions of American Society of Metals, **1944**, 32, 210.

[4] G.C. Kuczynski, R.F. Hochman, M. Doyama, Journal of Applied Physics, **1955**, 26, 871.

O–MB 07

Diffraction based determination of single crystalline elastic constants on polycrystalline alloys

Alexander E. Heldmann[1], Markus Hoelzel[1], Michael Hofmann[1], Wolfgang W. Schmahl[2]

[1] Forschungs-Neutronenquelle Heinz Maier-Leibnitz (MLZ), Lichtenbergstr. 1, 85748 Garching near Munich, Germany, alexander.heldmann@frm2.tum.de

[2]Department für Geo- und Umweltwissenschaften, LMU München, Theresienstraße 41 80333 Munich

Introduction

Through heating, phase transitions and applying stresses, strains appear in any material. The strains proceed through the object interacting with all grains. In general the stress is described as a tensor of second rank σ and is connected to the occurring strains ε through the general form of Hook's law:

$$\sigma = c\varepsilon, \qquad \text{or the inverse} \qquad \varepsilon = s\sigma, \qquad \text{where} \qquad s = c^{-1}. \qquad (1)$$

Where in the above equations c and s is the stiffness and compliance tensor of fourth rank, respectively [1].

The tensor components of c or s are directly related to material parameters such as the shear-, Young's- and Bulk modulus. But also non-mechanical properties such as the Debye temperature can be calculated using the tensor components [2]. One major field of application is the stress analysis by diffraction, where from measured strains residual stresses are determined with use of the elastic constants.

However, for many materials the derivation of the single-crystalline elastic constants is complicated. Most of the established methods like ultra-sound techniques, can only be performed on single crystals. However, the fabrication of single-crystalline specimen of most engineering-alloys is either difficult or even impossible. In such cases these methods are unable to determine the single-elastic constants properly.

Different diffraction techniques allow the investigation of poly-crystalline and multi-phase materials due to its outstanding possibility to visualize the different strains of all phases averaged over all orientations. Combining this with the knowledge of the occurring stresses enables a type of reversal of the classical stress analysis calculation with c or s as result [3].

Materials and Methods

For the derivation of the stiffness-constants c the exact knowledge of the lattice-plane distances, $d(hkl)$, is necessary. Through Bragg's law $d(hkl)$ can be calculated directly from the diffraction pattern. From these the elastic strain tensor ε can be obtained. With the known stress tensor σ a system of equations for the elastic constants can be derived. To derive this set of equations, (1) can be rewritten as given in equation (2) [3]. Here $S_1(hkl)$ and $S_2(hkl)$ are the diffraction elastic constants and φ and ψ are the orientation angles of the specimen in sample system with respect to the measurement system [3].

$$\begin{aligned}
\varepsilon(\varphi, \psi, hkl) = {} & S_1(hkl)[\sigma_{11} + \sigma_{22} + \sigma_{33}] \\
& + \frac{1}{2}S_2(hkl)[\sigma_{11}\cos^2(\varphi)\sin^2(\psi) + \sigma_{22}\sin^2(\varphi)\sin^2(\psi) + \sigma_{33}\cos^2(\psi)] \\
& + \frac{1}{2}S_2(hkl)[\sigma_{12}\sin(2\varphi)\sin^2(\psi) + \sigma_{13}\cos(\varphi)\sin(2\psi) + \sigma_{23}\sin(\varphi)\sin(2\psi)].
\end{aligned} \qquad (2)$$

The diffraction patterns were measured from samples positioned into a rotatable tensile-rig [4] for different orientations and applied stresses. This specialized setting sets all stress-tensor components to zero, except σ_{33} which can be calculated from the applied load.

Under these conditions equation (2) simplifies to (3) where $\frac{\varepsilon(\psi,hkl)}{\sigma_{33}}$ and $\cos^2(\psi)$ is known.

$$\frac{\varepsilon(\psi,hkl)}{\sigma_{33}} = S_1(hkl) + \frac{1}{2}S_2(hkl)\cos^2(\psi). \tag{3}$$

$S_1(hkl)$ and $S_2(hkl)$ can then be either calculated from the data collected in the different diffraction patterns (3) or from the components of the elastic tensor (4), with the orientation parameter Γ which depends on the lattice-plane (hkl) [3]. The components of the elastic tensor are then fitted to minimize the difference between the measured and the calculated $S_1(hkl)$ and $S_2(hkl)$.

There have been many approaches to calculate the diffraction-elastic constants from either the stiffness or the compliance tensor. For samples with an equal orientation-distribution e.g. non textured, the five most important models are Voigt [3], Reuss [3] (example for the cubic symmetry is shown in equation (4)), Hill [3], Kroener [5] and DeWitt [5]. These models can be extended also for textured materials with the model developed by Eshelby [6].

Fig. 1: Shows how the diffraction elastic constants are calculated from the measurements. These are the constants for the (2,2,0) plane of V2A Steel.

$$S_1(hkl) = s_{12} + s_0\Gamma, \text{and } \frac{1}{2}S_2(hkl) = s_{11} - s_{12} - 3s_0\Gamma, \text{with } s_0 = s_{11} - s_{12} - 0.5s_{44}. \tag{4}$$

The validation of this technique was done on different types of Iron S 235 JR (BCC), V2A (FCC) and Duplex Steel (BCC and FCC). In additionwe also investigated different Ti-alloys, α-Ti, β-Ti and α,β-Ti.

Results and Discussion

The steel samples were used to validate the method and the obtained results. For this purpose the calculated stiffness constants were compared directly to literature data and were found to match within their standard deviation. For the Ti-alloys there only a few comparable literature data exists and therefor the correctness was mainly ensured by calculating macroscopic values and comparing them to either literature data and/or own experiments.

References

[1] L. Spieß, G. Teichert, R. Schwarzer, H. Behnken, C. Genzel, Moderne Röntgenbeugung. **2005**.

[2] H. M. Ledbetter, N. V. Frederick and M. W. Austin. J. Appl. Phys. *51(1):*305-309, **1980**

[3] H. Behnken: RWTH, Habil.-Schr. RWTH Aachen. **2002**. Bercihte aus der Werkstofftechnik. Shaker, Aachen 2003. ISBN 3-8322-1384-8

[4] Hoelzel, M. , Gan, W.M., Hofmann, M., Randau, C., Seidl, G., Jüttner, Ph., Schmahl, W.W.: Nucl. Instr. **2013**, A711, 101-105

[5] R. De Witt.: J. Appl. Cryst. , **1997,** 30(4):510-511

[6] J. D. Eshelby. In Proceedings of the Royal Society of London A: Mathematical Physical and Engenerring Sciences, *241*, 376-396. The Royal Society, **1957**

O–TA 01

Application of a forged γ-TiAl alloy as low pressure turbine blade in an aircaft engine

Ulrike Habel[1], Falko Heutling[1], Dietmar Helm[1], Claudia Kunze[1], Wilfried Smarsly[1], Helmut Clemens[2]

[1]MTU Aero Engines AG, Munich, Germany, ulrike.habel@mtu.de

[2]Montanuniversität Leoben, Leoben, Austria, helmut.clemens@unileoben.ac.at

Introduction

Intermetallic titanium aluminide alloys based on γ-TiAl are distinguished by their high specific strength and stiffness at temperatures up to 900°C resulting from their low density as well as good retention of properties at elevated temperatures [1,2]. A drawback is their very moderate capability to accommodate plastic deformation, which has required extensive research efforts prior to their transitioning into service [2,3]. One area of application of γ-TiAl alloys is in jet engines, where weight savings and their resistance to titanium fire are key advantages.

The first application of a TiAl-based alloy as turbine blades in jet engines utilizes a cast TiAl-alloy [4]. A relatively new application of a TiAl part is in the geared turbofan jet engine, where a forged version of γ-TiAl-based TNM alloy is used [5]. A schematic cross-section of the geared turbofan jet engine is shown in Figure 1. Characteristic of this engine is a gear box decoupling fan and low pressure turbine, which allows both components to run at their respective optimum speed resulting in reductions in fuel burn as well as pollutant and noise emissions. The high rotational speed of the low pressure turbine requires high strength and creep resistance, which are supplied by the forged TNM alloy. Figure 2 shows assembly of the TNM low pressure blades prior to engine testing.

Preceeding alloy selection, extensive testing of different alloy variants and heat treatments has been conducted. This presentation discusses some properties observed during that work.
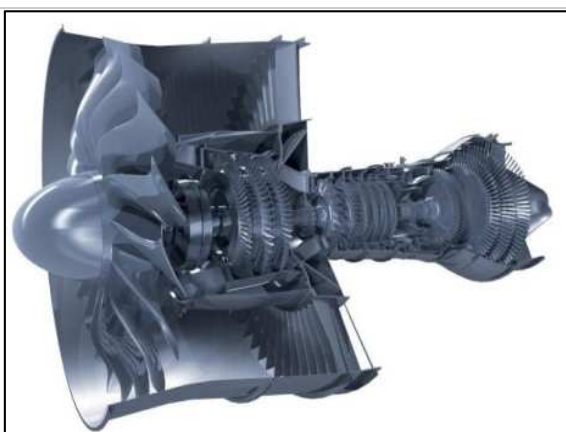
Figure 1: Cross-section of the geared turbofan jet engine (schematic)

Figure 2: Low-pressure blade assembly of the geared turbofan instrumented for testing

Materials and Methods

The TNM alloy is based on the γ-TiAl phase, but contains the β-stabilizing alloying elements Nb and Mo. The alloy design ensures solidification through the β-phase, a prerequisite for grain refinement and suppression of formation of highly textured columnar grains [6]. A cast and forged version of the TNM alloy (Ti-43.5Al-4Nb-1Mo-0.1B, in at%) was subjected to a two-step heat treatment consisting of a recrystallization anneal followed a stabilization anneal. Two different temperatures were selected for the recrystallization step to obtain either a triplex microstructure or a nearly lamellar (NL) microstructure. Experimental details are reported in [5].

Results and Discussion

The triplex microstructure consists of recrystallized lamellar colonies, globular γ-grains, β-phase with a B2-structure (β_o), each not exceeding a size of 20 μm, and a small fraction of non-recrystallized lamellar colonies. The NL microstructure is fully recrystallized, containing lamellar colonies with a size of 50 μm and only small amounts of globular γ- and β_o-phases.

Tensile tests were conducted at temperatures ranging from room temperature to 800°C. In this temperature range, the NL microstructure exhibits higher degrees of work hardening and higher strength levels than the triplex microstructure. The lower strength of the triplex microstructure can be attributed to the presence of non-recrystallized lamellar colonies exhibiting coarse lamellae and to its lower content of α_2-phase. In γ-TiAl-based intermetallics, the strength has been found to decrease with increasing lamellar spacing, and it has been proposed that the α_2-phase increases strength in γ-TiAl-based alloys [7, 8, 9].

Creep tests were conducted at temperatures of 700 and 800°C and stresses ranging from 100 to 250 MPa. At 700°C, primary, secondary, and tertiary creep regimens exist and a nearly steady-state creep regimen is observed. At 800°C, the TNM alloy does not exhibit a secondary (steady-state) creep. This type of creep behavior is frequently noted for TiAl alloys containing β-stabilizing elements [10]. Plots of creep rate $\dot{\varepsilon}$ vs. creep strain ε were used to obtain the minimum creep rate $\dot{\varepsilon}_{min}$. A stress exponent of around 3 was determined from $\log\dot{\varepsilon}_{min}$–$\log\sigma$ plots. This value agrees well with literature [11]. Activation energies for creep for the test conditions of the present study were estimated using minimum creep rates and a power-law relationship [10] to be 400 kJ/mol for the NL microstructure and 430 kJ/mol for the triplex microstructure. These values of activation energy agree well with the results derived from internal friction measurements and results obtained for other TiAl-alloys [10, 11,12].

Literature References

[1] Y.-W. Kim, D.M. Dimiduk, M.H. Loretto (eds), Gamma Titanium Aluminides 1999, TMS, Warrendale, PA, USA, **1999**

[2] H. Clemens, S. Mayer, Adv. Eng. Materials **2013**, 15, 191-215.

[3] B.P. Bewlay, S. Nag, A. Suzuki, M.J. Weimar, Materials at High Temperatures **2016**, 33 (4-5), 549-555

[4] B.P. Bewlay, M. Weimer, T. Kelly, A. Suzuki, P.R. Subramanian, in I. Baker, M. Heilmaier, S. Kumar, K. Yoshimi (eds), MRS Proc. Vol. 1516, 1993, MRS, Warrendale, PA, USA, 49-58

[5] U. Habel, F. Heutling, D. Helm, C. Kunze, W. Smarsly, G. Das, H. Clemens, in: V. Venkatesh, A. L. Pilchak, J. E. Allison, S. Ankem, R. Boyer, J. Christodoulou, H. L. Fraser, M. A. Imam, Y. Kosaka, H. J. Rack, A. Chatterjee, A. Woodfield (eds): 13th Titanium World Conf. 2015, Wiley, Hoboken, NJ, USA, **2016**, ch208

[6] H.F. Chladil, H. Clemens, A. Otto, V. Güther, S. Kremmer, A. Bartels, R. Gerling, Berg- und Hüttenmännische Monatshefte, **2006**, 151 (9), 356-361

[7] W. Wallgram, T. Schmölzer, L. Cha, G. Das, V Güther, H. Clemens, Int. J. Mat. Res. **2009**, 100 (8), 1021-1030

[8] CT. Liu, H. Schneibel, P.J. Masziaz, J.L. Wright, D.S. Easton, Intermetallics, **1996**, 4, 429-440

[9] J.D.H. Paul, F. Appel, R. Wagner, Acta Mater **1998**, 46, 1075-1085

[10] P. Simas, T. Schmoelzer, M.L. No, H. Clemens, J.S. Juan, MRS Proc. Vol. 1295, **2011**, MRS, Warrendale, PA, USA, 139-144

[11] F. Appel, J.D.H. Paul, M. Oehring, Gamma Titanium Aluminides Science and Technology, **2011**, Wiley VCH, Weinheim, Germany, 316-320

[12] J.G. Wang, T.G. Nieh, Intermetallics, **2000**, 8, 737-748

O–TA 02

In situ synchrotron X-ray diffraction study on the room temperature tensile behaviour of γ-TiAl based sheets

Petra Erdely[1], Emad Maawad[2], Peter Staron[2], Norbert Schell[2], Joachim Klose[3], Helmut Clemens[4], and Svea Mayer[4]

[1]Recipient of a DOC Fellowship of the Austrian Academy of Sciences at the Department of Physical Metallurgy and Materials Testing, Montanuniversität Leoben, Roseggerstr. 12, A-8700 Leoben, Austria; petra.erdely@unileoben.ac.at.

[2]Institute of Materials Research, Helmholtz-Zentrum Geesthacht, Max-Planck-Str. 1, D-21502 Geesthacht, Germany; emad.maawad@hzg.de; peter.staron@hzg.de; norbert.schell@hzg.de.

[3]GfE Fremat GmbH, Lessingstr. 41, D-09599 Freiberg, Germany; joachim.klose@gfe.com.

[4]Department of Physical Metallurgy and Materials Testing, Montanuniversität Leoben, Roseggerstr. 12, A-8700 Leoben, Austria; helmut.clemens@unileoben.ac.at; svea.mayer@unileoben.ac.at.

Introduction

Sheets made of intermetallic γ-TiAl based alloys possess promising engineering properties for light-weight high-temperature applications. They have been implemented as skin material and tested in thermal and acoustic protection systems, gas leading parts, and exhaust nozzles in propulsion systems for hypersonic air- and spacecraft [1,2]. However, γ-TiAl based sheets have not yet been fully commercialised due to the complexity of their manufacturing process and, most importantly, their low ductility and toughness at room temperature [3,4]. In the present work, the response of γ-TiAl based sheets to tensile loading at room temperature is explored in an in situ manner by means of high-energy X-ray diffraction (HEXRD). Thus, the elastic and plastic behaviour of all constituent phases is revealed in detail. Investigations on sheets of different chemical compositions and processing history disclose the interplay of the various phases, i.e. γ (L1$_0$ structure), α$_2$ (D0$_{19}$ structure), and for some sheets also β$_o$ (B2 structure), during loading. Valuable insights are gained on the factors that limit the room temperature ductility of γ-TiAl based sheets. Furthermore, the broad existing knowledge in this field is extended to novel multi-phase TNM sheets with a nominal composition of Ti-43.5Al-4Nb-1Mo-0.1B (at.%).

Materials and Methods

In the present work, three primary-annealed γ-TiAl based sheet materials are compared: a low-alloyed and distinctly textured sheet made of Ti-47Al-2Cr-0.2Si (at.%) as described in Ref. [5], a powder-metallurgically produced, high-Nb containing TNB (Ti-46Al-9Nb (at.%)) sheet [6], and a TNM sheet produced by hot rolling of cast ingots without a preceding ingot breakdown [7].

Following a thorough basic characterisation of all sheets including the analysis of the microstructure by means of scanning electron microscopy and texture as described in Ref. [7], in situ tensile loading experiments were conducted at the HZG-run P07 high-energy materials science (HEMS) beamline at PETRA III, DESY, Germany. The tensile tests were set up as described in Ref. [8] using a mean photon energy of 87 keV and a fast Perkin-Elmer XRD 1622 area detector to capture complete diffraction patterns (Debye-Scherrer rings) during loading with a reasonable time resolution. Two sectors of the diffraction patterns parallel as well as perpendicular to the loading direction were integrated over 10° using the software programme Fit2D [9]. Subsequently, the lattice spacings d_{hkl} of selected planes were determined from Gaussian fits. From these values, the volume averaged strains ε_{hkl} were calculated considering the positional shift of the diffraction peaks selected for evaluation. Analysing the macroscopic stress versus hkl-dependent strain (σ–ε_{hkl}) curves, the Young's moduli E_{hkl} and Poisson's ratios v_{hkl} were evaluated to characterise the materials' elastic response, while the hkl-dependent yield stresses and peak evolutions within the γ, α$_2$, and, if present, the β$_o$ phase offered information on the plastic behaviour.

Results and Discussion

Figure 1 exemplarily illustrates the evaluation of the elastic properties of the (200)γ planes in the nominal TNM sheet from the measured σ–ε_{200} curves parallel and perpendicular to the loading direction. The experimental values E_{200} (129±3 GPa) and v_{200} (0.26±0.02) reflect the influences of the chemical composition, microstructure, and texture of the material in distinct ways. By performing a targeted comparison of numerous lattice planes within the different materials, these influences can be discriminated.

Fig. 1: σ–ε_{200} curves for the (200)γ planes of the nominal TNM sheet parallel and perpendicular to the loading direction (LD). E_{200} is determined from the slope in LD, while v_{200} is given by the negative ratio of the slopes in both directions.

Fig. 2: Room temperature σ–ε_{hkl} curves for the (200)γ, (002)γ, (112)γ, and (201)γ planes of the nominal TNM sheet along LD. The onset of plastic deformation is indicated by the deviation from Hooke's law.

In Fig. 2 room temperature σ–ε_{hkl} curves of several lattice planes of the γ phase in the nominal TNM sheet are presented as a selected example. From the deviation from Hooke's law, the onset of plastic deformation becomes apparent. Upon yielding, each lattice plane responds to the external load in a distinct way, which correlates with the activated deformation mechanisms.

The respective evaluation of all phases within the three investigated materials revealed various differences between the sheets. For example, the α_2 phase showed a varied but reproducible behaviour upon yielding, which proved characteristic of each type of sheet. It can be interpreted in the context of the characterisation of the microstructure and the phase fractions present in the sheets. The β_o phase in the TNM alloy, which exhibits an ordered cubic B2 structure, does not yield at room temperature. However, the plastic deformation of the γ phase was found to influence the σ–ε_{hkl} curves of the β_o phase and, thus, impact the elastic deformation of this brittle phase.

References

[1] S.L. Draper, D. Krause, B. Lerch, I.E. Locci, B. Doehnert, R. Nigam, G. Das, P. Sickles, B. Tabernig, N. Reger, K. Rissbacher, Mater. Sci. Eng. A. 2007, 464, 330–342.

[2] H. Clemens, S. Mayer, Mater. High Temp. 2016, 33, 560–570.

[3] G. Das, H. Kestler, H. Clemens, P.A. Bartolotta, JOM. 2004, 4, 42–45.

[4] F. Guo, L'influence de la microstructure sur des propriétés mécaniques et des contraintes internes d'un alliage intermétallique biphasé à partir de TiAl, Ph.D. Thesis, Arts et Métiers ParisTech, France, 2001.

[5] H. Clemens, W. Glatz, F. Appel, Scripta Mater. 1996, 35, 429–434.

[6] R. Gerling, A. Bartels, H. Clemens, H. Kestler, F.-P. Schimansky, Intermetallics. 2004, 12, 275–280.

[7] P. Erdely, P. Staron, E. Maawad, N. Schell, J. Klose, S. Mayer, H. Clemens, Acta Mater. 2017, 126, 145–153.

[8] E. Maawad, H.-G. Brokmeier, Z.Y. Zhong, N. Al-Hamdany, M. Salih, L. Wagner, N. Schell, Mater. Sci. Eng. A. 2014, 594, 62–67.

[9] A.P. Hammersley, S.O. Svensson, M. Hanfland, A.N. Fitch, D. Häusermann, High Press. Res. 1996, 14, 235-248.

O–TA 03

Thermodynamic database for multicomponent Ti- and TiAl-based alloys

Hai-Lin Chen[1], Yang Yang[1], Qing Chen[1], Anders Engström[1] and Andreas Markström[1]

[1]Thermo-Calc Software AB, Råsundavägen 18, 16967 Solna, Sweden, hailin@thermocalc.se, yang@thermocalc.se, qing@thermocalc.se, anders@thermocalc.se, andreas@thermocalc.se

Introduction

Calphad-type calculations have been widely employed to computationally design materials and optimize their processing conditions. The reliability of Calphad calculations by large depends on the quality of the database being used. In this work, we present the development of a new titanium database, TCTI1, that contains 23-elements: Ti, Al, B, C, Co, Cr, Fe, Hf, Mn, Mo, N, Nb, Ni, O, Re, Ru, Si, Sn, Ta, V, W, Y, and Zr. It consists of 236 assessed binary systems and more than 70 assessed Ti-containing ternary systems. It is the first thermodynamic database which covers both Ti-based alloys and TiAl-based materials, and, moreover, it can be employed to design light alloys based on the Al_3Ti and $AlTi_3$ intermetallic phases.

Database and Applications

The TCTI1 database has been developed in a systematic way in order to cope with the complexity in the phase relations and phase transformations in titanium alloy systems. The common solution phases, such as liquid, Bcc_A2 (βTi) and Hcp_A3 (αTi and α'), are treated as substitutional solutions [1]. Most intermetallic compounds and their solutions, including the ordered structure $L1_2$, are described with sublattice models [1]. The phase transformations among variant ω phases, including the simple solid solution based on ω-Ti, and the ordered compounds of the C32 type, the $B8_2$ type, the $D8_8$ type and the Ti_5Ga_4 type, have been examined carefully from a crystallographic viewpoint, so that reasonable thermodynamic models could be adopted for them. The ordered B2 phase is, however, described with the so-called partitioning model [2, 3], which connects B2 with its disordered counterpart Bcc_A2. This treatment is necessary for the A2/B2 second-order transition, which has been observed in many Ti-based alloys [4, 5].

In systems where experimental data are sparse or controversial, high throughput density function theory (DFT) calculations are employed to compute thermodynamic quantities for intermetallic compounds and solid solutions (including those based on intermetallics). Regarding the calculations for the α, β and ω solutions, Special Quasirandom Structures (SQSs) [6, 7], Small Sets of Ordered Structures (SSOSs) [8], and supercells have been used to approximate the random substitutional solution phases in both binary and ternary systems.

All the binary systems and most ternary systems in TCTI1 have been assessed over the entire compositional ranges and include all the stable phases (e.g. Fig. 1). TCTI1 can not only account for the phase formation in existing experimental and industrial alloys but also be employed to design new alloys within the 23 element framework. For instance, it well describes the structure transformation of Al_3Ti from $D0_{22}$ to $L1_2$ with the addition of transition metals such as Co, Cr, and Mn, so it may be used for searching potential Al_3Ti ($L1_2$)-based light alloys with high strength and reasonable ductility. TCTI1 also includes a good number of well-assessed carbide systems C-Ti-X (X = Al, Cr, Mo, Nb, Ta, V, W and Zr) (e.g. Fig. 2) and boride systems B-Ti-X (X = Al, Co, Cr, Mo, Nb, Ni, Sn, Ta, V, W and Zr).

The TCTI1 database can be used to predict not only stable phase equilibria but also metastable or non-equilibrium phase transformations associated with ω and α'. Figure 3 compares the calculated T_0 line between β-Ti and α' with the experimentally determined martensitic transformation temperatures in Ti-Zr alloys. As an empirical rule, the T_0 line is approximately equivalent to the average temperatures of A_s and M_s or A_f and M_f. The comparison indicates a reasonable agreement between the T_0 line and the values of $0.5*(A_s + M_s)$. Figure 4 presents the calculated T_0 lines of β-

Ti/α' and β-Ti/ω in the Ti-Nb system. It is interesting to note that the A_s temperatures are barely higher than the M_s temperatures in this system. In such cases, these temperatures can be directly accounted for by the calculated T_0 lines.
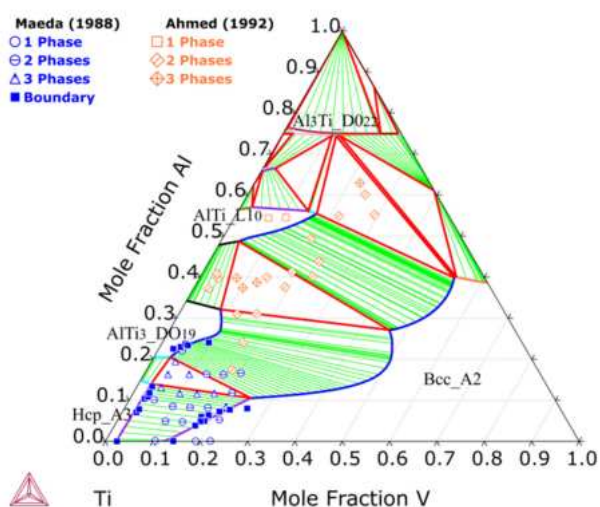
Fig. 1: Al-Ti-V isothermal section at 700 °C
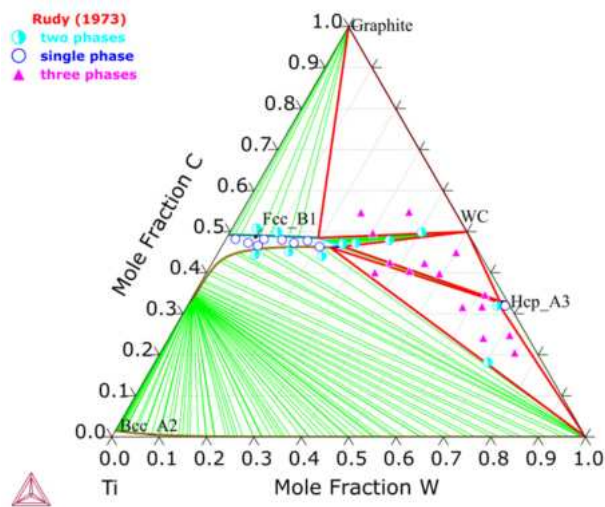
Fig. 2: C-Ti-W isothermal section at 1500 °C
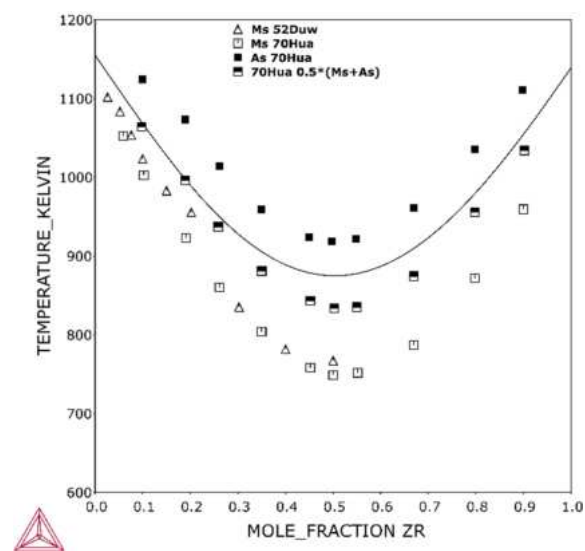
Fig. 3: Calculated β/α' T_0 line in the Ti-Zr system
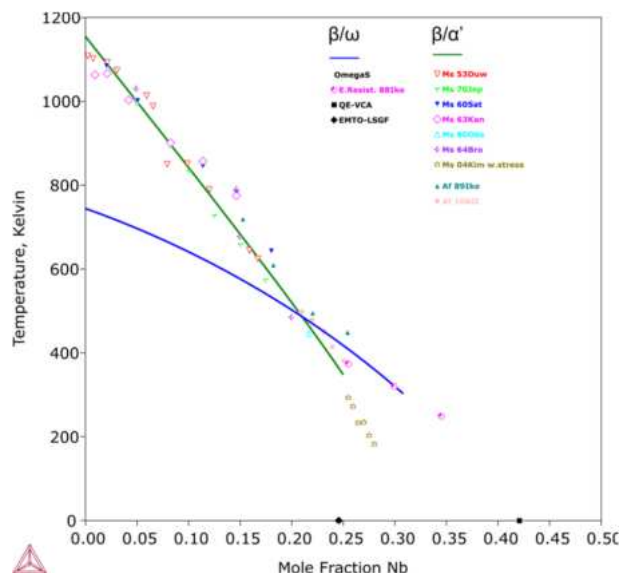
Fig. 4: Calculated T_0 lines of β/α' and β/ω in the Ti-Nb system

References

[1] H.L. Lukas, S.G. Fries, B. Sundman, Computational thermodynamics: The Calphad Method, Cambridge University Press. **2007**.

[2] I. Ansara, N. Dupin, H.L. Lukas, B. Sundman, J. Alloys Comp. **1997**, 247, 20-30.

[3] N. Dupin, I. Ansara, B. Sundman, Calphad. **2001**, 25, 279-298.

[4] R. Kainuma, M. Palm; G. Inden, Intermetallics. **1994**, 2, 321-332.

[5] J.C. Schuster, M. Palm, J. Phase Equilib. Diff. **2006**, 27, 255-277.

[6] D. Shin, A. van de Walle, Y. Wang, Z. Liu, Phys. Rev. B. **2007**, 76, 144204.

[7] C. Jiang, Acta Mater. **2009**, 57, 4716-4726.

[8] C. Jiang, B.P. Uberuaga, Phys. Rev. Lett. **2016**, 116, 105501.

O–TA 04

Effect of oxygen on phase equilibria among β/α/γ phases in TiAl alloys using soft X-ray spectroscopy

Arata Kinouchi, Hirotoyo Nakashima and Masao Takeyama

School of Materials and Chemical Technology, Tokyo Institute of Technology,
2-12-1-S8-8, Meguro-ku, Tokyo, Japan,
email: kinouchi.a.aa@m.titech.ac.jp

Introduction

γ-TiAl alloys are promising for high temperature jet engine applications due to their low density and high specific strength. Based on our phase diagram studies on Ti-Al-M ternary systems (M: β-Ti former elements), microstructure of the alloys can be designed through a unique transformation pathway of $\beta+\alpha\text{-Ti}\rightarrow\alpha\rightarrow\alpha+\gamma\rightarrow\beta+\alpha+\gamma$, which does not exist in the binary system [1]. This microstructure control makes it possible to produce wrought and cast alloys with required properties. Although the effect of substitutional elements M on the phase equilibria among $\beta/\alpha/\gamma$ phases has been well-established, little information on the interstitial element effect, especially oxygen, is available. This is because of difficulty in quantitative analysis of a small amount of oxygen in each phase by conventional WDS and EDS analyses. Since TiAl alloys inevitably contain a certain amount of oxygen (0.1~0.2 at.%) from the starting materials and some pick-ups in process, the phase boundaries shift among the phases by oxygen cannot be neglected for microstructure control along the transformation pathways. Atom Probe (AP) is useful for quantitative analysis of impurity elements and in fact revealed higher enrichment of oxygen in α phase than γ phase [2], indicating that oxygen stabilizes α phase against γ phase. Thus, it is believed that oxygen in solution shifts the phase boundaries of the $\alpha/\alpha+\gamma$ and $\alpha+\gamma/\gamma$ toward higher aluminum side in Ti-Al system. However, the AP method is destructive and the analyzed region is very limited. Recently, soft X-ray spectroscopy useful to detect emitted characteristic x-rays of lighter elements in the energy level less than 200 eV has been developed, and allows us to analyze the oxygen content of each phase in nondestructive manner, just like a conventional fluorescent x-ray analysis. In this study, thus, we prepared a series of Ti-Al binary and Ti-Al-Nb ternary alloys with various oxygen content up to 1.0 at.%, and have attempted to identify the effect of oxygen on phase equilibria among the three phases in terms of the soft X-ray spectroscopy.

Materials and Methods

The alloys studied have nominal compositions of Ti-43Al-xO and Ti-43Al-9Nb-xO (x=0.1, 0.4, 0.6, 1.0) (in at.%). These alloys are arc-melted to 120 g button ingot. The oxygen content in the alloys was adjusted with a Ti-O mother alloy, and the total amount of oxygen in each ingot was analyzed by inert gas fusion method. All of the alloys were first homogenized in α single-phase region and then equilibrated at temperatures from 1273 K to 1723 K for up to 1.2 Ms. The homogenization treatment was conducted by specially designed vertical furnace capable to heat up to 1773 K with evacuation system. The sample wrapped with Ta foil were hung in the upper chamber of the furnace, and rolled down to the heat available zone adjusted to a given temperature under backfilled Ar after evacuation down to 5.3×10^{-3} Pa. After holding there for a given time, then it was water quenched by dropping it into water by opening the gate valve. The subsequent equilibrated heat treatment was conducted by encapsulating the sample wrapped with Ta foil in silica tube under backfilled Ar after evacuation down to 1.3×10^{-3} Pa. After the heat treatment, sample was water quenched by breaking the capsule. Microstructure and composition analysis were conducted by FE-EPMA equipped with WDS (Wavelength-dispersive spectrometer), EDS (Energy-dispersive spectrometer) and SXES (Soft x-ray emission spectroscopy). The major constituent elements (Ti, Al and Nb) in each phase present in the samples after the equilibration were examined by WDS and also by EDS. The oxygen concentration of the phases present was quantitatively identified by a calibration method obtained using the homogenized α single-phase samples analyzed by the SXES with the third order reflection of the oxygen-K_α emission at 175 eV.

Results and Discussion

One of the examples of the oxygen peaks obtained by SXES is shown in Fig. 1. The height of the oxygen peaks between the homogenized samples containing oxygen of 0.6 at.% and 1.0 at.% in the alloys can be clearly distinguished. This peak height is sensitive not only to the sample surface preparation but also analyzing conditions, and the detailed of this analysis will be described in the presentation. Figure 2 shows the microstructure of Ti-43Al without and with oxygen equilibrated in the $\alpha+\gamma$ two phases at 1473 K. Note that the alloy without oxygen contains a level of 0.1 at.% O (500 ppm by weight), which is inevitable impurity level. The microstructure of both alloys basically shows lamellar microstructure consisting of α (brighter) and γ (darker) phases, and it should be noted that the volume fraction of the γ phase is apparently increased. Since oxygen is preferentially partitioned into α phase rather than γ phase (Fig. 3), the volume fraction of the α phase is expected to increase with increasing oxygen content, but unlike the expectation the results are completely the other way around. In order to confirm the results, the compositions of the constituent elements of the phases present in the alloys shown in Fig. 2, together with those of alloys containing Nb without and with oxygen equilibrated at 1473 K, was analyzed, and they are plotted in the isothermal section of Ti-Al-Nb ternary system in Fig. 4. Regardless of the presence of Nb, Al concentration in the α phase in equilibrium with γ phase is decreased by 1.0 at.% by the addition of 1.0 at % oxygen. In contrast, Al concentration in the γ phase in equilibrium with α phase remains unchanged in the alloy without Nb, whereas it increases by 1.0 at % in the alloy with Nb by the oxygen, indicating that presence of Nb affects the solubility and partitioning of oxygen in γ phase. The oxygen effect on the phase equilibria including β phase will be discussed in terms of the partitioning behavior based on thermodynamics.

Fig. 1 Third order peaks of oxygen in ultra-soft X-ray region detected by SXES in the α single-phase alloys with different oxygen content.
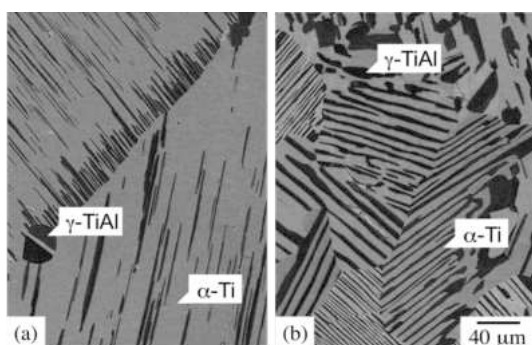
Fig. 2 BESs of Ti-43Al alloys containing oxygen of (a) 0.1 at.% and (b) 1.0 at % after equilibration at 1473 K/1.2 Ms.
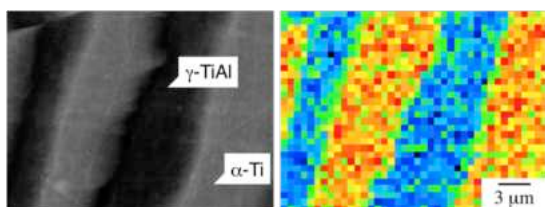
Fig. 3 Oxygen mapping by SXES in α and γ phases in Ti-43Al containing 1.0 at% O equilibrated at 1473 K/1.2 Ms.
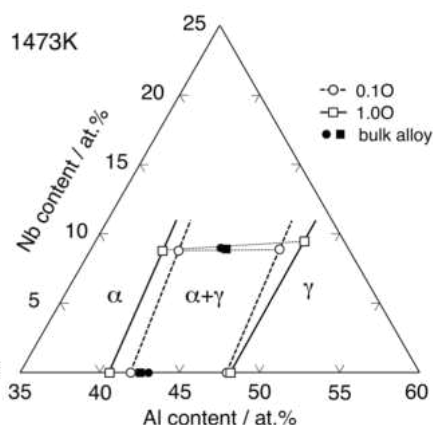
Fig. 4. Isothermal section of Ti-Al-Nb system, showing the change in Al and Nb content in the α and γ phases in Ti-43Al and Ti-43Al-9Nb alloys without and with oxygen equilibrated at 1473 K.

References

[1] M. Takeyama et al., Intermetallics, **2005**, *13*, 993-999

[2] A. Menand et al., Acta materialia, **1996**, *44*, 4729–4737.

O–TA 05

The order/disorder transformation of β/βo phase in binary and ternary γ-TiAl based alloys studied by synchrotron and neutron diffraction

Victoria Kononikhina[1], Andreas Stark[1], Weimin Gan[2], Andreas Schreyer[3] and Florian Pyczak[1]

[1]Helmholtz-Zentrum Geestacht, Geesthacht, Germany, Victoria.Kononikhina@hzg.de

[2]German Engineering Materials Centre at MLZ, Garching, Germany

[3]European Spallation Source ERIC, Lund, Sweden

Introduction

Due to their high melting point, low density, and good oxidation resistance, γ-TiAl based alloys have recently started to replace Ni-based superalloys as a material for turbine blades in aircraft engines [1]. Conventional TiAl alloys usually contain the ordered phases γ-TiAl and α_2-Ti_3Al at lower temperatures and disordered α-Ti(Al) phase at higher temperatures. Additional alloying elements like Nb, Mo, Ta, Cr or Fe, can stabilize the disordered β-Ti(Al) phase (A2 structure), which can transform at lower temperatures to ordered β_o-TiAl (B2 structure) or even to more complex phases. The ductile body centred cubic β phase is important for processing because it significantly improves the hot forming behaviour of the material. Otherwise the ordered low temperature β_o phase is said to embrittle the material at service temperature. Unfortunately little is known about the exact order/disorder transformation temperatures of β/β_o in several ternary alloy systems and the influence of β stabilizing elements is still under research. Additionally, even for the binary TiAl phase diagram the existence of an ordered β_o phase field at high temperatures has yet not been finally proofed or rebutted [2].

With conventional *in situ* investigation methods like differential scanning calorimetry (DSC) an unambiguous assignment of a certain peak to the β_o↔β transformation is not possible in TiAl alloys. X-ray diffraction (XRD) measurements are also not suitable because the superstructure reflections are very weak due to the small electron density differences of the different atom sites in the ordered crystal structures. However *in situ* neutron diffraction (ND) measurements are best suited to study order/disorder transformations in titanium aluminides [3,4]. The neutron scattering lengths of Ti and Al are almost equal in magnitude but of opposite sign. Thus disordered phases, with a Ti:Al ratio close to one, yield only very weak diffraction peaks, because the average scattering length is almost zero. The fundamental reflections in ordered TiAl crystal structures are also very weak because the scattering lengths of Al sites and Ti sites with their opposite sign add up. However the superstructure reflections of these ordered TiAl crystal structures become rather large, because they contain the difference of the scattering lengths of each site.

Materials and Methods

We studied three binary TiAl alloys (Ti-xAl with x = 39, 42 and 45) and five alloys with additional alloying elements (Ti-42Al-2y with y = Nb, Mo, Ta, Cr and Fe). The alloys were produced by arc melting under Ar atmosphere. The melt buttons were remelted 5 times to ensure chemical homogeneity and subsequently heat-treated at 1100°C for 5 days in order to homogenize the microstructure.

In situ ND measurements were performed in the materials science diffractometer STRESS-SPEC at FRM II in Garching near Munich (Germany). We used a gauge volume of 390 mm^3 (for cylindrical samples of 20 mm length and 5 mm diameter) and a wavelength of 2.1 Å. The detector covered the q-range of 1.7-2.3 2πÅ^{-1} which enables to monitor superstructure reflections of all three ordered phases simultaneously, namely α_2-101, β_o-100 and γ-110. A vacuum high temperature furnace was used for the heat treatments and the samples were stepwise heated in a range from 1100°C up to 1440°C with a minimum step width of 10°C in ranges of special interest. The exposure time was varied from 20 minutes to 1 hour in order to have a small peak to background ratio.

Complementary *in situ* synchrotron XRD measurements were performed in the High Energy Material Science (HEMS) beamline at DESY in Hamburg, Germany. In order to penetrate the 5 mm thick

samples high-energy X-rays with a photon energy of 100 keV, corresponding to a wave length of 0.124 Å, were used. The gauge volume was 5 mm^3. The heat treatments were performed in a DIL805A/D dilatometer with a heating rate of 5 K/min from 1000-1250 °C and 20 K/min from 1250-1450 °C. Complete Debye-Scherrer diffraction rings up to a q-value of 5.5 2πÅ^{-1} were continuously recorded on a PerkinElmer XRD 1621 flat panel detector with a frame rate of 0.15 Hz and an exposure time of 3 s.

Results and Discussion

During the *in situ* ND measurements the superstructure reflection β_o-100 was never observed in the binary TiAl alloys [5]. However the *in situ* high-energy XRD experiments clearly show the formation of disordered β phase at about 1360 °C and 1400 °C for Ti-42Al and Ti-45Al respectively. These results proof the direct transformation of disordered α to disordered β in the binary Ti-Al phase diagram without the formation of a high temperature ordered β_o-TiAl phase.

In three alloys with β-stabilizing elements, namely with Fe, Mo and Cr, the superstructure β_o reflection was observed by ND [5]. The synchrotron experiments show that after the order/disorder transformation β is stable up to the highest temperatures in these alloys.

The ternary alloys with Nb and Ta behave similar to the binary alloys. No superstructure β_o reflection was observed by ND, but the high-energy XRD measurements show the formation of disordered β at the highest temperatures. This indicates that Nb and Ta are significantly weaker β-stabilizing elements than Fe, Mo and Cr. At the moment the analysis of the synchrotron experiments is still under progress and more detailed results will be published soon.

References

[1] F. Appel, J.D.H. Paul, M. Oehring, Gamma Titanium Aluminide Alloys: Science and Technology, Wiley-VCH, Weinheim, **2011**.

[2] V.T. Witusiewicz, A.A. Bondar, U. Hecht, S. Rex, T.Y. Velikanova, Journal of Alloys and Compounds. **2008**, 465, 64.

[3] I.J. Watson, K.-D. Liss, H. Clemens, W. Wallgram, T. Schmoelzer, T.C. Hansen, M. Reid, Advanced Engineering Materials. **2009**, 11, 932.

[4] P. Erdely, T. Schmoelzer, E. Schwaighofer, H. Clemens, P. Staron, A. Stark, K.-D. Liss, S. Mayer, Metals. **2016**, 6,10.

[5] V. Kononikhina, A. Stark, W. Gan, A. Schreyer, F. Pyczak, MRS Advances. **2017**, 1-6.

O–TA 06

Elemental redistribution during formation and growth of the ω_o phase in β_o phase containing TiAl alloys

Thomas Klein, Michael Schachermayer, David Holec, Boryana Rashkova, Helmut Clemens and Svea Mayer

Department of Physical Metallurgy and Materials Testing, Montanuniversität Leoben, Roseggerstr. 12, 8700 Leoben, Austria, e-mail address: thomas.klein@unileoben.ac.at

Introduction

Intermetallic structural materials based on γ-TiAl are today implemented increasingly in modern aero and automotive propulsion systems. The expanding industrialization and concomitant market penetration of TiAl alloys can be ascribed, among other aspects, to fundamental research strategies of the past years, which yielded reliable alloys processible via robust manufacturing routes. A representative is the so-called TNM alloy with the nominal composition of Ti-43.5Al-4Nb-1Mo-0.1B (at.%) [1]. However, through the incorporation of the essential β-stabilizing elements additional phases, such as the ω_o phase, are introduced to the microstructure. In this study we report on the effects of the strong β-stabilizing element Mo on the formation and growth mechanisms of the ω_o phase in the TNM alloying system. Thereby, microstructural analysis of different material conditions was conducted by scanning and transmission electron microscopy. The elemental redistribution phenomena occurring during growth were quantified by atom probe tomography corroborated by *ab initio* calculations to deepen the understanding of alloying related effects on the phase stability. Finally, all data are merged to elucidate the complex formation sequence of ω_o particles in β_o phase containing TiAl alloys.

Materials and Methods

The sample material investigated in this study is based on the TNM alloying concept and was produced via arc remelting and centrifugal casting. Different specimen conditions were adjusted using a Carbolite RHF 1600 furnace under atmospheric conditions. The creep tests were performed at 750 °C and 150 MPa for ≈ 300 h. Scanning electron microscopy (SEM) was conducted using a focused ion beam (FIB) workstation Versa 3D DualBeam™ from FEI at an acceleration voltage of 20 kV. Transmission electron microscopy (TEM) investigations were carried out on a Philips CM12 operated at 120 kV on electrolytically thinned specimens prepared using the A3-electrolyte (Struers). Atom probe tomography (APT) was performed using a local electrode atom probe (LEAP™) 3000X HR from Cameca. For details on specimen preparation and measurement of TiAl samples by APT see Ref. [2]. The stability of the phases involved with respect to the Mo concentration was assessed by *ab initio* calculations conducted using the Vienna Ab initio Simulation Package (VASP).

Results and Discussion

The microstructure of the TNM alloy in all material conditions investigated comprises of γ, α_2 and β_o phases of different morphologies. In case of the TNM alloy, the ω_o phase was reported to form from the β_o phase below ≈ 825 °C ($T_{\omega_o,solv}$) [3]. Thus, the following analysis focuses on this microstructural constituent (Fig. 1). The first specimen was rapidly cooled in air from a temperature above $T_{\omega_o,solv}$ (state A, Fig. 1(a)). While diffraction spots belonging to the ω_o phase were observed by TEM and a weak substructure is visible in the bright field (BF) image, no elemental redistribution could be evidenced by APT in agreement with Ref. [4]. Upon furnace cooling from a temperature above $T_{\omega_o,solv}$ (state B, Fig. 1(b)) diffraction spots of ω_o could be observed and the phase separation is visible clearly in the BF image and the atom map. In the crept material condition (state C, Fig. 1(c)) the prevalence of two phases (β_o and ω_o) can be visualized clearly by TEM as well as APT. During slow cooling or creep exposure below $T_{\omega_o,solv}$ a redistribution of Mo is discernible, which suggests that the diffusion of Mo influences the formation kinetics of ω_o particles. In states B and C Mo isoconcentration surfaces were utilized to separate the adjacent phases.

In order to rule out the prevalence of nano-scaled clustering, the nearest neighbor distribution of Mo-Mo pairs was calculated from the APT data. In this analysis the actual distribution of the chemical species is compared to a random allocation of the chemical species on the reconstructed lattice. The latter condition resembles thermal fluctuations present in any material. As no differences could be evidenced between these curves of state A, the initial stages of phase separation are assumed to elapse without diffusive chemical redistribution.

As determined by APT analysis a destabilization of the ω_o phase by Mo may prevail. Thus, *ab initio* calculations were conducted in order to compare the energies of formation of the pure phases with those obtained after the incorporation of Mo on its preferred lattice site. While the β_o phase is stabilized by Mo, a substantial destabilization of the ω_o phase is determined in agreement with the theoretical analysis by Hu et al. [5]. This phenomenon accounts for the pronounced elemental redistribution observed experimentally.
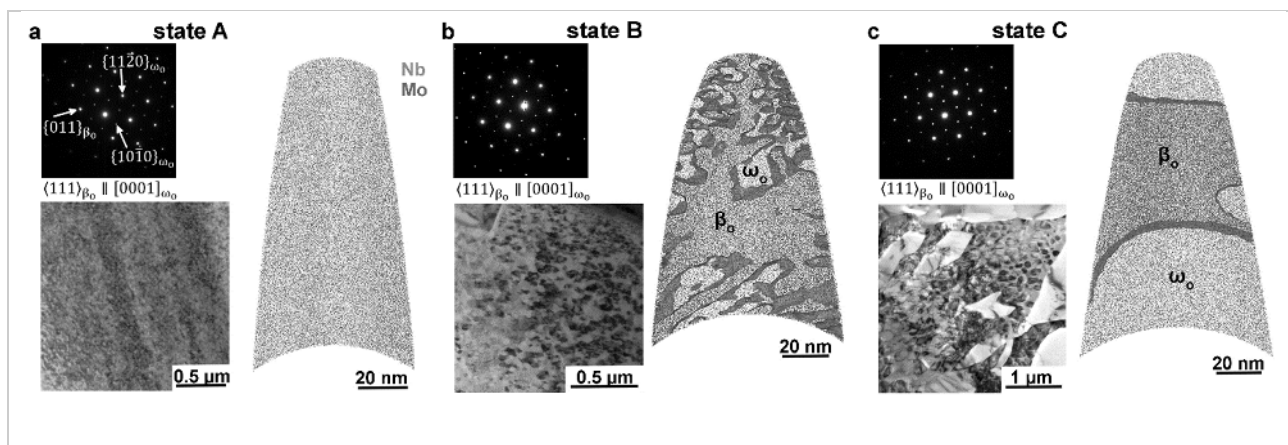
Fig. 1: Elemental distribution and TEM analyses of differently heat-treated TNM specimens [6]. In all specimen conditions diffraction spots belonging to the ω_o phase are discernible. In the furnace cooled as well as the crept specimen condition (b and c) phase separation can be identified clearly by strong partitioning of Mo. During air cooling (a) no partitioning prevails, evidencing that the initial stages of phase formation occur without the diffusion of Nb and Mo.

Summary

Intermetallic alloys based on γ-TiAl have become decisive in advanced propulsion systems, but their broad introduction necessitates an in-depth understanding of the underlying mechanisms of phase formation. In particular the crucial alloying element Mo modifies transformation pathways.

This study reports on the effects of Mo on the formation of the ω_o phase in the TNM alloy. Results obtained by SEM, TEM, APT and *ab initio* calculations allow to conclude that the ω_o phase is destabilized by Mo, which in turn affects the formation kinetics by diffusional redistribution in the parent phase. Initial stages of phase formation evolve without the redistribution of Mo, while the subsequent growth sequence is controlled diffusively.

References

[1] S. Mayer, P. Erdely, F.D. Fischer, D. Holec, M. Kastenhuber, T. Klein, H. Clemens, Advanced Engineering Materials. **2017**, DOI: 10.1002/adem.201600735.

[2] M. Schachermayer, T. Klein, H. Clemens, S. Mayer, Practical Metallography. **2016**, 53 (2), 73-85.

[3] M. Schloffer, B. Rashkova, T. Schöberl, E. Schwaighofer, Z. Zhang, H. Clemens, S. Mayer, Acta Materialia. **2014**, 64, 241-252.

[4] L. Song, X.J. Xu, J. Sun, J.P. Lin, Materials Characterization. **2014**, 93, 62-67.

[5] Q.-M. Hu, L. Vitos, R. Yang, Physical Review B. **2014**, 90, 54109.

[6] T. Klein, M. Schachermayer, D. Holec, B. Rashkova, H. Clemens, S. Mayer, Intermetallics. **2017**, 85, 26-33.

O–TA 07

Influence of W on the high temperature properties of the TNM alloy

Melissa Allen[1], Volker Güther[2], Janny Lindemann[3], Michael Kastenhuber[4], Helmut Clemens[5], Svea Mayer[6], and Martin Schloffer[7]

[1]GfE Metalle und Materialien GmbH, Höfener Str. 45, Nuremberg, Germany;
melissa.allen@gfe.com

[2]GfE Metalle und Materialien GmbH, Höfener Str. 45, Nuremberg, Germany;
volker.guether@gfe.com

[3]GfE Fremat GmbH, Lessingstr. 41, 09599 Freiberg, Germany,
janny.lindemann@gfe.com

[4]Montanuniversität Leoben, Franz-Josef-Str. 18, 8700 Leoben, Austria
michael.kastenhuber@unileoben.ac.at

[5]Montanuniversität Leoben, Franz-Josef-Str. 18, 8700 Leoben, Austria
helmut.clemens@unileoben.ac.at

[6]Montanuniversität Leoben, Franz-Josef-Str. 18, 8700 Leoben, Austria
svea.mayer@unileoben.ac.at

[7]MTU Aero Engines, Dachauer Str. 665, 80995 Munich, Germany
martin.schloffer@mtu.de

Introduction

The objective of the work was to improve the high temperature capability of the TNM alloy (nominal composition: Ti-43.5Al-4Nb-1Mo-0.1B, in at % [1]) by alloying with W, which is mentioned as an alloying element capable to increase tensile strength at very high temperatures due to solid solution hardening [2]. In order to keep the balance of alloying elements of the TNM alloy unchanged, Mo was partly or entirely replaced by W via metallurgical alloying techniques.

Materials and Methods

Materials manufacturing was based on single Vacuum Arc Remelting (VAR) using compacted consumable electrodes which consist of Ti sponge, Al granules and master alloys. Resulting VAR ingot has been remelted and homogenized in an Induction Skull Melter and subsequently centrifugally cast in steel molds. In summary 4 different TNM based alloy compositions containing 0.1 at % W, 0.3 at % W, 0.5 at % W, and 1.0 at % W have been manufactured. Cast parts were subject to HIP for closing remaining casting porosity and 3 different heat treatments (HT) for creating appropriate microstructures. For being able to add W to the alloy, a ternary NbWAl masteralloy without high melting phases was developed. Chemical analyses have been carried out by XRF, ICP and LECO combustion techniques. Phase transition temperatures were determined by DSC measurements. The microstructural analysis was done by metallography and SEM. The tensile tests were done under standard test conditions at room temperature, 700 °C and 800 °C. In addition, creep properties have been determined at 750 °C and 800 °C at 150 MPa for all 4 alloy compositions but just for the heat treatment which resulted in the most promising tensile properties.

Results and Discussion

DSC measurements show that the replacement of Mo by W does not significantly influence the phase transition temperatures. Thus, the resulting microstructures after thermal treatments of all 4 experimental alloys are very similar to the microstructure of the original TNM alloy. It can be concluded that the β-stabilizing effect of Tungsten is more or less equivalent to that of Molybdenum. Moreover, semi-quantitative EDX analyses indicate that Tungsten is being placed on the Molybdenum lattice sites. The density of Mo atoms in the β-phase of the TNM alloy and of W atoms in the β-phase of the TNM type alloy without Mo is almost the same. The heat treatments which have

been applied (exposure slightly below and above the gamma-solvus transition temperature followed by air cooling (AC) and ageing at 850 / 900 °C with subsequent furnace cooling (FC)) result in a remarkable increase of hardness and tensile strength. Most promising properties are being reached with the sequence 1300 °C for 1h / AC / 850 °C for 6h / FC (HT 2). The microstructure consists of lamellar colonies with very fine lamellar spacing and remaining globular β-phase, for example see alloy Ti-43.5Al-4Nb-0.5Mo-0.5W-0.1B (at %) in Figure 1.
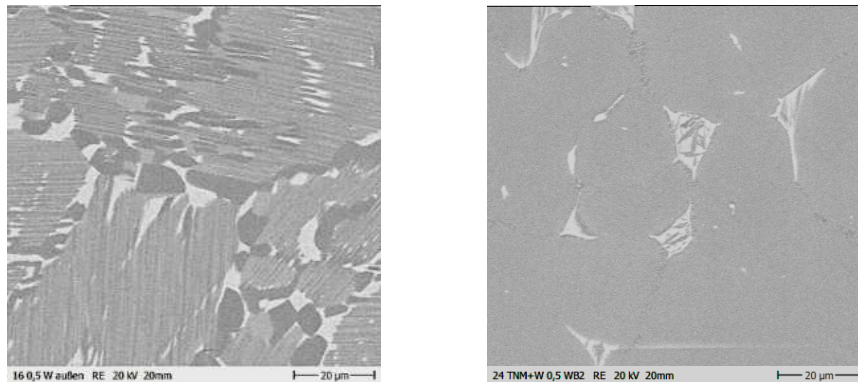
Figure 1: Microstructure of the Ti-43.5Al-4Nb-0.5Mo-0.5W-0.1B alloy after HIP (left image) and after a subsequent heat treatment (right image). SEM images were taken in BSE mode.

The heat treatments improve remarkably the tensile properties at room temperature and at elevated temperatures as well, whereas an influence of the W content on the yield strength could not be determined (see data summarized in Figure 2, based on HT 2).
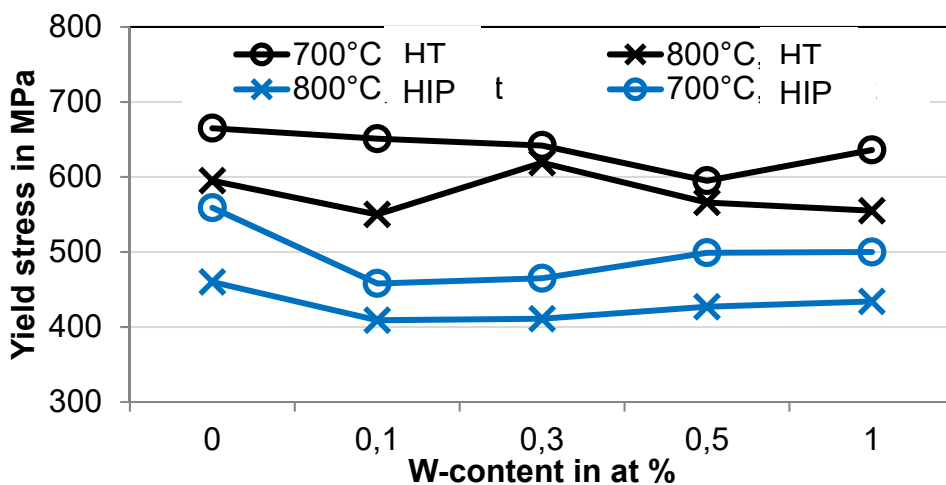
Figure 2: Tensile yield strength at 700 °C and 800 °C of a TNM based alloy with different W-contents

In summary, it can be stated that alloying of TNM with W results in very similar mechanical properties compared to the original alloying with Mo. Moreover, W exhibits the same β-stabilizing equivalent as Mo in the TNM alloy. An appropriate heat treatment has a stronger influence on properties than the alloying effect.

References

[1] H. Clemens, S. Mayer, Design, Processing, Microstructure, Properties, and Applications of Advanced Intermetallic TiAl Alloys, Advanced Engineering Materials 15-4 (2013) 191-215.

[2] T. Voisin, J.-P. Monchoux, M. Thomas, C. Deshayes, A. Couret, Mechanical Properties of the TiAl IRIS Alloy, Metallurgical and Materials Transactions A, 12/2016.

O–TA 08

Near surface residual stress in TiAl before and after elevated temperature exposure

J.D.H. Paul[1], M Oehring[1], F Appel[1] and F Pyczak[1]

[1]Helmholtz-Zentrum Geesthacht, Max-Planck-Str. 1, D-21502 Geesthacht, Germany.
Contact: jonathan.paul@hzg.de

Introduction

It has been well documented in the TiAl literature that exposure to elevated temperature results in a reduction of the ductility on subsequent testing at room temperature [1-3]. Recently it has been suggested that the development of tensile stress at the surface of exposed material could be the underlying cause for this reduction in ductility [4]. The aim of this study was to gain an insight into the development of near-surface stress in the γ phase of the TiAl, as a function of depth, both before and after exposure.

Materials and Methods

Depth resolved stress measurements were performed on two sets of materials in the as-polished condition and after subsequent heat treatment for one hour at 700°C in air. One set of specimens (as polished and as-exposed) were prepared from pre-alloyed Ti-49Al powder that had been HIPed at 1200°C/4 h/200 MPa. The second set of specimens were taken from an extruded bar (extruded at 1250°C to a 7:1 reduction) of Ti-45Al-5Nb-0.2B-0.2C. Both wavelength and angle dispersive x-ray diffraction were used to determine the variation of residual stress as a function of depth from the surface. The stress (within the γ phase) is determined from the variation of crystal lattice d-spacing as a function of orientation with regard to the surface. The Kröner model was used to determine the stress from the variation of lattice spacing. Further details of the investigation are described in [5].

Results and Discussion

The variation of residual stress as a function of depth for the HIPed Ti-49 alloy and the extruded Ti-45Al-5Nb-0.2B-0.2C bar in the as-polished condition and after exposure for 1 h at 700°C can be seen in Fig. 1. It is clear that a significant compressive residual stress is present close to the surface for both materials in the as-polished state. This probably results from surface work hardening that developed during the specimen preparation and reduces in magnitude with distance from the surface. It is interesting that the residual stress in the high strength Ti-45Al-5Nb-0.2B-0.2C alloy is somewhat lower than that in the softer Ti-49Al alloy. This may be a reflection of the difference in strength levels of the two alloys. After elevated temperature exposure a tensile residual stress has developed within the initial 0.6 μm from the outer surface. Maximum measured residual stress levels of +300 to +350 MPa are present at about 0.15 μm from the surface. The development of tensile stress is in agreement with the finding in [4]. Compressive residual stress is present at depths below around 0.6 μm but at reduced levels compared to the as-polished specimens. There are at least two possible reasons for the development of tensile stress including i) a nanometer thick oxygen enriched outer layer (that is in compression) imposing a tensile stress on the underlying material (as proposed in [4]), ii) a reduction in the aluminum content of the material due to the formation of an (aluminum rich) alumina layer (discussed in [5]). The reduction of overall compressive stress compared to the as-polished condition is possible to ascribe to the annealing out of deformation induced defects that resulted from surface work hardening of the as-polished specimens.

With regard to room temperature ductility, the presence of significant compressive residual stress is certainly beneficial and thus its reduction after exposure and the development of near-surface tensile stress is in consequence potentially detrimental. However, fracture mechanic considerations would seem to indicate that such short range tensile stress would have little, if any, impact on crack propagation [5]. Thus although it seems a short range tensile stress is developed after exposure, in

agreement with previous work [4], the extent to which this actually contributes to the so called environmental embrittlement remains unclear.

Fig. 1: Graphs that compare the near-surface residual stress profiles in un-exposed (as-polished) and exposed (700°C/1 h) specimens of (a) Ti-49Al and (b) Ti-45Al-5Nb-0.2B-0.2C. As indicated at the top of the figure, stresses for points on the left hand side of the graphs were determined using angle-dispersive diffraction and those on the right using energy-dispersive diffraction.

References

[1]   W.E. Dowling, W.T. Donlon, Scripta Metall Mater. **1992**, 27, 1663-1668.

[2]   C.M. Austin, T.J. Kelly. In: R Darolia, J.J. Lewandowski, C.T. Liu, P.L. Martin, D.B. Miracle, M.V. Nathal (Eds.): Structural Intermetallics. Warrendale (PA): TMS, **1993**, 143-150.

[3]   M. Thomas, O. Berteaux, F. Popoff, M-P. Bacos, A. Morel, B. Passilly, V. Ji, Intermetallics. **2006**, 14, 1143-1150.

[4]   X. Wu, A. Huang, D. Hu, M.H. Loretto, Intermetallics. **2009**, 17, 540-552.

[5]   J.D.H. Paul, M. Oehring, F. Appel, F. Pyczak, Intermetallics. **2017**, 84, 1-9.

O–TA 09

Time and space resolved HEXRD study during transient liquid phase bonding of a γ-TiAl alloy with a Ti-29Fe solder

Katja Hauschildt, Andreas Stark, Martin Müller, Florian Pyczak

Helmholtz-Zentrum Geesthacht, Max-Planck-Straße 1, 21502 Geesthacht, Germany,
katja.hauschildt@hzg.de

Introduction

Transient liquid phase bonding (TLPB) is a promising method to close cracks (in noncritical or non-highly loaded areas) in aero engine vanes and thus extend their service life. Recently, intermetallic γ-TiAl based alloys, which are promising candidates for replacing the twice as dense Ni-based superalloys in high-temperature applications, are increasingly used in aero engine and automotive applications [1]. Therefore, the development of suitable repair methods is a topic that requires investigation.

For TLPB a solder with a lower melting point than the substrate material (melting point of γ-TiAl alloys > 1450 °C) is used. The solder contains a melting point depressing element (MPD), in our case Fe. During a holding time at the brazing temperature (above the melting point of the solder), the MPD diffuses into the substrate material and the melting point of the material in the brazing zone increases continuously until it is fully solidified. In the ideal case, this leads to a microstructure in the brazed zone similar to the microstructure in the substrate material with similar mechanical properties [2].

During brazing several phase transformations at different chemical compositions take place in the brazing zone. However, only little is known about this phase evolution and its influence on microstructure formation [3]. To get insight into the phase evolution the TLPB process was monitored by *in-situ* measurements with high energy X-ray diffraction (HEXRD).

Materials and Methods

For the experiments, two cylindrical γ-TiAl specimens of 5 mm diameter and 10 mm length were used. The alloy has a composition of Ti-45Al-5Nb-0.2B-0.2C (in at. %) and has been hot extruded. The brazing solder with a composition of Ti-29Fe (in at. %) was applied as a thin foil with a thickness of 300 µm and was positioned between the two γ-TiAl blocks.

The *in-situ* HEXRD measurements were performed with an induction furnace using the HZG-run materials science beamline HEMS at the synchrotron radiation facility at DESY in Hamburg, Germany. An energy of 100 keV (corresponding to a wavelength of 0.124 Å) and a beam size of 400 µm in width and 25 µm in height was used. While the sample is being heated (at 1110 °C), it was repeatedly scanned over the joint region in several steps with a step width of 25 µm. In order to increase the number of grains in reflection condition the stacked specimens were rotated continuously while heating with a rotation speed of about 5 seconds per rotation.

Results and Discussion

The Debye-Scherrer diffraction rings were integrated for each step. Afterwards, the single diffractograms were stacked next to each other, which leads to an overview of the joint region, fig. 1. Thus, the grayscale indicates the intensity. Here, three scans over the joint region from substrate to substrate of a Ti-29Fe joint are shown after 3 min, 2 h, and 14.5 h of brazing.

The substrate material contains of γ and α_2 phase. Initially, after 3 min, a diffuse region is present in the middle of the joint, which indicates the joint region as liquid. Only two small peaks are visible in the diffuse background (at 2Θ of 3.1° and 4.4°) indicating already a small amount of β phase in the liquid joint region. After 2 h, the material has fully solidified. Furthermore, the amount of the disordered β phase (A2 structure) increased. Additionally, an ordered FeTi phase (B2 structure) has occurred next to the β phase with a smaller lattice parameter. Only these two phases are present in the joint region. In detail, the FeTi phase is only detected in the middle of the joint region. In contrast, the β phase decreases slightly in the transition region into the substrate, where the amount of γ and α_2 increase. It is clearly visible, that the lattice parameter of the β phase changes over the joint

region. It decreases from substrate to the middle of the joint. This effect is also visible for the FeTi phase. After 14.5 h the joint region widens significantly. Still, there exist only β and FeTi phase in the joint region. Additionally, small peaks in the joint region are visible, which display oxides. Furthermore, the shift of the lattice parameter of the β phase increases in comparison to the scan after 2 h. In the middle of the joint region, the ordered FeTi phase shows almost the same lattice parameter as the disordered β phase. This indicates, that the two different β structures adapt to each other with increasing brazing time. Furthermore, the occurrence of all these phases fits well with the ternary phase diagram of Al-Fe-Ti at 1000 °C [4].

Fig. 2 shows the microstructure of a joint region after 15 h of brazing with additional furnace cooling. Here, the substrate is fine grained and the joint region appears with a symmetric structure with a transition zone between the substrate and the middle of the joint. The transition zone consists of β phase with small globular α_2 grains and smaller γ grains. In the middle of the joint region, big β grains are visible with additional γ phase in form of needles in the β grains and globular grains at the grain boundaries.

The existence of α_2 and β fits well with the HEXRD results. The FeTi phase could not be assigned anymore. Besides, the γ phase occurs while cooling, which is additionally confirmed by the morphology of the γ grains [5].
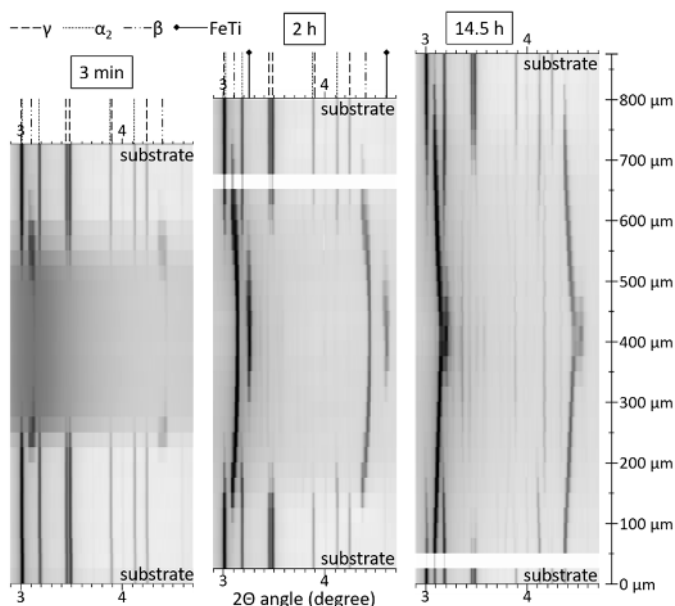
Fig. 1: Three scans over the joint region of a Ti-29Fe joint: after 3 min, 2 h, and 14.5 h, the three present phases are related to the single reflections.
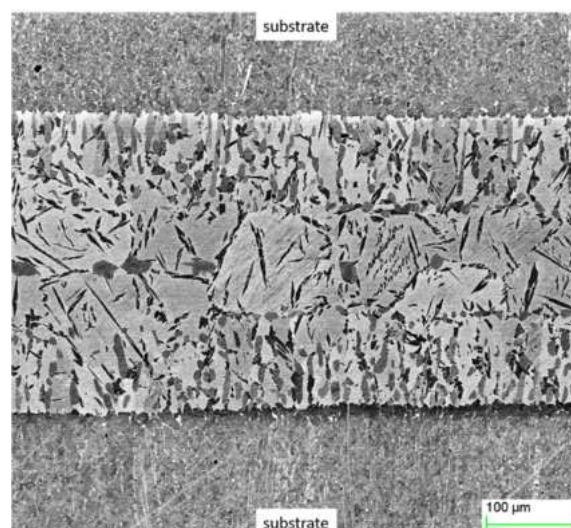
Fig. 2: Microstructure of a Ti-29Fe joint (BSE mode) after 15 h brazing and additional furnace cooling.

Acknowledgements

References

[1]   F. Appel, J. D. H. Paul, M. Oehring: Gamma Titanium Aluminide Alloys, Wiley-VCH, Weinheim, Germany, **2011**

[2]   W. F. Gale, D. A. Butts, Science and Technology of Welding and Joining, **2004**, 9, 283-300.

[3]   K. Hauschildt, A. Stark, U. Lorenz, N. Schell, T. Fischer, M. Blankenburg, M. Müller, F. Pyczak, MRS Symposium Proceedings, **2013**, 1516, 215-220.

[4]   M. Palm, J. Lacaze, Intermetallics, **2006**, 14, 1291-1303.

[5]   M. Schloffer, B. Rashkova, T. Schöberl, E. Schwaighofer, Z. Zhang, H. Clemens, S. Mayer, Acta Materialia, **2014**, 64, 241-252.

O–TA 10

Laser additive manufacturing of titanium aluminides

Silja-Katharina Rittinghaus[1], Andreas Vogelpoth[1]

[1] Fraunhofer Institute for Laser Technology ILT, Steinbachstr. 15, D-52074 Aachen, Germany

Introduction

Lightweight titanium aluminides (TiAl, $\rho = 3.9 – 4.1$ g/cm^3) are becoming increasingly interesting as high temperature structural materials. Advantageous properties like high strength and creep resistance combined with high corrosion and wear resistance [1] increase their attractiveness for aircraft applications like e.g. low pressure turbine blades [2]. Additive manufacturing (AM) technologies provide the possibility for near-net-shape production as well as repair of worn parts and therefore can contribute to reduction of consumption and costs of material, tooling and finishing [3]. The typical high brittleness and oxygen affinity of TiAl cause special requirements for processing with AM [4, 5]. In this work the defect free workability of TiAl alloy TNM with both Laser Metal Deposition (LMD) and Selective Laser Melting (SLM) is demonstrated.

Materials and Methods

Powder material of the β-solidified TNM-B1 of the nominal composition Ti-43.5Al-4Nb-1Mo-0.1B (at.-%) was processed by LMD and SLM. Similar precision cast material was used for reference. Produced samples were analyzed by means of optical (LOM) and scanning electron microscopy (SEM) regarding microstructure and phases. Micro hardness was measured according to Vickers. Oxidation measurements were performed by means of carrier gas hot extraction.

Results and Discussion

With both technologies it is possible to produce defect free parts by using preheating of approximately 800°C. Bulk samples of an approximate size of 10x10x10 mm³ (SLM) and 10x10x60 mm³ (LMD) can be built as well as thin-walled specimens of 1 mm (LMD) down to 0.13 mm (SLM) width. Dependent on the process parameters, the gain in oxygen is about +300-1000 ppm for LMD and +200-600 ppm for SLM, respectively. The as-built microstructure consists out of lamellar ($\alpha_2 + \gamma$) colonies and nearly globular γ as well as β/β_0 at the grain boundaries (Fig.1, 2) which is typical for cast material as well [1, 6].
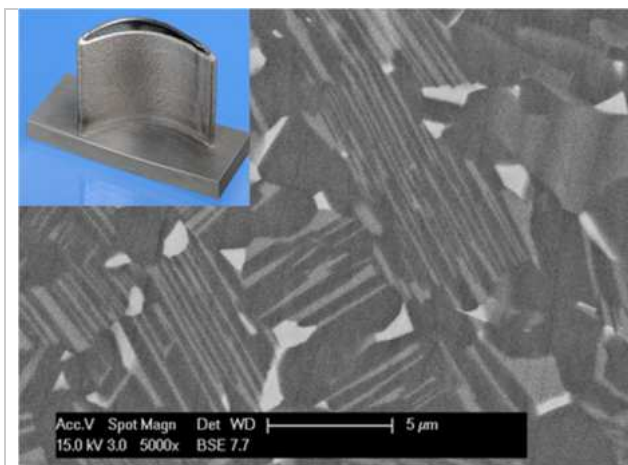
Fig. 1: LMD sample out of TiAl alloy TNM and SEM micrograph of corresponding microstructure
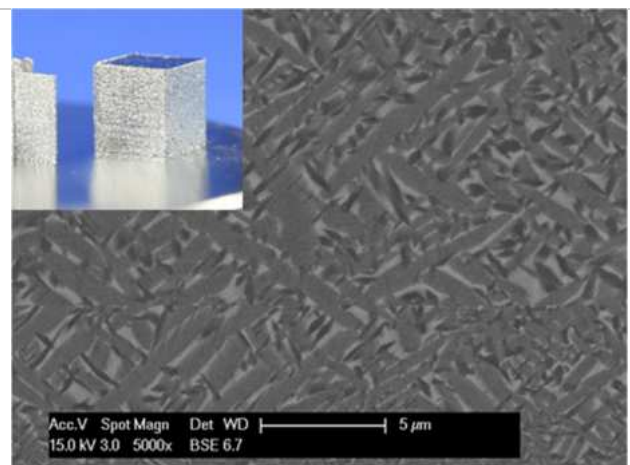
Fig. 2: SLM samples out of TiAl alloy TNM and SEM micrograph of corresponding microstructure

High cooling rates in the magnitude 10^5-10^6 K/s provide small grain sizes of 5-15 µm (LMD) and 1-7 µm (SLM), respectively. Measured β_0-fraction is approx. 1.5% (LMD) compared to 9-12% (SLM). In LMD samples lamellar spacing is to be found averaging well below 1 µm, while lamellar spacing in SLM samples is too small to measure at the same magnification. Hardness measurements reveal

an increased hardness in SLM samples (515-560HV0.3) compared to LMD (490-520HV0.3). These values are significantly higher compared to the reference cast material (390HV0.3) and can be attributed to both small grain sizes in accordance with Hall-Petch relationship and embrittlement caused by increased oxygen content. Differences between SLM and LMD material can be explained by different process conditions such as melt pool size and overheating, cooling and solidification rate, re-melting ratio and process duration. For functional characteristics the response of AM material to post heat treatment has to be considered as well. Refinement of the microstructure has a detrimental effect on creep resistance and can influence the velocity of solid-phase transition reactions crucially. In addition, even small increase in O_2 can stabilize the α-phase and shift the lamellar transition to higher Al-contents [7].

Acknowledgement

References

[1] Appel, F., Paul, J. D. H., Oehring, M.: Gamma Titanium Aluminide Alloys. Science and Technology. Weinheim: Wiley 2012

[2] Loria, E.A.: Quo vadis gamma titanium aluminide. Intermetallics 2001, vol9, p997-1001

[3] Gasser, A., Backes, B., Kelbassa, I., Weisheit, A., Wissenbach, K.: Laser additive manufacturing - Laser Metal Deposition (LMD) and Selective Laser Melting (SLM) in Turbo-Engine Applications. Laser Technik Journal 7, 2 (2010), p58-63

[4] Gussone, J., Hagedorn, Y.-C., Gherekhloo, H., Kasperovich, G., Merzouk, T., Hausmann, J.: Microstructure of γ-titanium aluminide processed by selective laser melting at elevated temperatures. Intermetallics 2015, vol66, p133–40.

[5] Rittinghaus, S.-K., Weisheit, A., Mathes, M., Garcia Vargas, W.: Laser Metal Deposition of Titanium Aluminides – A Future Repair Technology for Jet Engine Blades?. Proceedings of the 13th World Conference on Titanium, Wiley 2016

[6] Schwaighofer, E., Clemens, H., Mayer, S., Lindemann, J., Klose, J., Smarsly, W., Güther, V.: Microstructural design and mechanical properties of a cast and heat-treated intermetallic multi-phase γ-TiAl based alloy. Intermetallics 2016, vol44, p128-140

[7] Zhong, H.; Yang, Y.; Li, J.; Wang, J.; Zhang, T.; Li, S.; Zhang, J.: Influence of oxygen on microstructure and phase transformation in high Nb containing TiAl alloys: Materials Letters 83 (2012), p198–201

O–TA 11

α_2/O-phase domains in Nb containing lamellar gamma-TiAl

Heike Gabrisch[1], Uwe Lorenz[1], Marcus Rackel[1], Florian Pyczak[1], Andreas Stark[1]

[1]Helmholtz-Zentrum Geesthacht, Max-Planck-Str.1, 21502 Geesthacht, Germany
e-mail: heike.gabrisch@hzg.de

Introduction

γ-based intermetallic TiAl-alloys exhibit excellent high-temperature strength, low density and good corrosion resistance, which qualify them for applications as structural components in aero-engines. The addition of niobium to binary TiAl alloys improves not only corrosion resistance but also increases the alloys' high-temperature yield stress and room temperature ductility [1]. Microstructural investigations of niobium containing γ-TiAl alloys indicated the presence of an orthorhombic phase that was thought to be responsible for the improved mechanical properties [2, 3]. The nature, shape and arrangement of this phase were not fully understood at the time.

Recently we identified the orthorhombic O-phase in a niobium containing alloy Ti-42Al-8.5Nb by high energy X-ray diffraction (HEXRD) [4]. In-situ heating HEXRD experiments verified that the O-phase forms from the hexagonal α_2 phase and that it reproducibly forms between 500-700°C and dissolves as the temperature exceeds 700°C. The finding of orthorhombic O-phase in γ-based TiAl-alloys is new. On the other hand, the formation of O-phase from α_2 and/or β_o phase grains has been reported before for α_2-based alloys that are Al-lean and niobium-rich [5, 6]. In the present study, the spatial arrangement of α_2 and O-phase within the alloy's lamellar microstructure is characterized by transmission electron microscopy. Furthermore, in-situ heating TEM experiments illustrate that internal stresses are responsible for the stability of the O-phase at this alloy composition.

Materials and Methods

The alloy Ti-42Al-8.5Nb has been produced from powder by hot-isostatic pressing (HIP) at 1250°C under 200 MPa. Details on the processing route have been published in [7]. The HIPed specimens were annealed at 550°C and 650°C between 8 hours and 672 hours (4 weeks). Specimens for Transmission Electron Microscopy were prepared from 400µm thick slices cut from the HIPed material. Discs of 2.3 mm diameter were drilled out of the slices and were ground manually to about 100 µm thickness. TEM foils were polished electrolytically at -39 °C using a solution of 18 ml perchloric acid in a mixture of 430 ml methanol and 250 ml 2-buthanol. TEM investigations were performed at the Helmholtz-Zentrum in Geesthacht using a Philips CM 200 TEM operated at 200 kV and a Cs image corrected FEI Titan 80-300 TEM operated at 300 kV.

For TEM observations by image, diffraction and high resolution imaging lamellar ($\alpha_2+\gamma$) colonies were tilted to low indexed zone axis directions. The experimentally observed diffraction patterns and high resolution images were compared to simulated images and diffraction patterns that were generated using the software package JEMS. Some TEM foils were investigated by in-situ heating in the CM 200 using a Gatan double tilt heating holder.

Results and Discussion

The geometry of lamellar ($\alpha_2+\gamma$) colonies facilitates TEM observations parallel to the α_2/γ interfaces in edge-on projections of the lamellae. Simulations show that it is possible to identify the orthorhombic O-phase by diffraction and high resolution imaging in the edge-on viewing direction along α_2 <10-10> directions. An example for co-existing α_2 and O-phase is given in the bright-field image in Fig. 1. The contrast modulation in Fig. 1 is due to lattice strain within the α_2/O-phase lamellae and indicates the presence of multiple phases. In the corresponding diffraction pattern reflections are observed that are typical of the O-phase (not shown here).

In the α_2 [0001] viewing direction the α_2 lamellae consist of facets having rhomboid or rectangular shapes as shown in Fig. 2. These are differently tilted regions of the crystal lattice. High-resolution imaging shows that within the facets small nm sized regions exist that are characterized by hexagonal and orthorhombic atomic ordering. No segregation of niobium is observed in these regions. Combining the information of edge-on and plan view projections it appears that the former α_2 lamellae are populated by columnar α_2 and O-phase crystallites. These crystallites are based at the interface between α_2 and γ.

During in-situ heating of a thin TEM foil the orthorhombic phase irreversibly transforms to the hexagonal α_2 phase. This observation is in contrast to observations during in-situ heating HEXRD experiments on bulk material and suggests that internal stress states stabilize the observed O-phase.

Figures
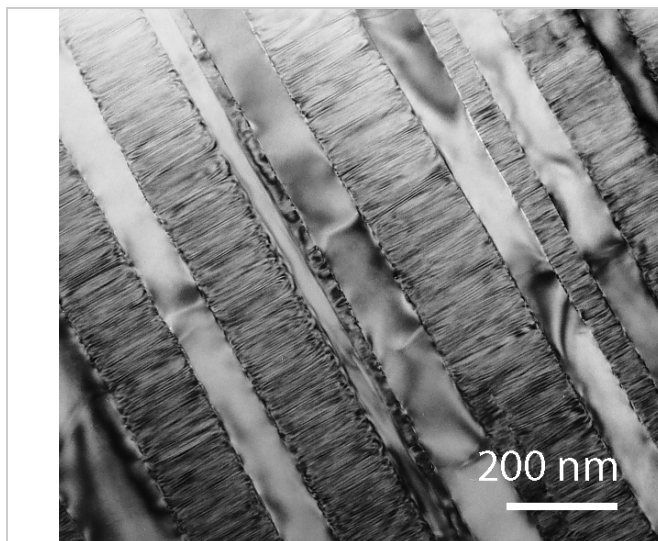
Fig. 1: Lamellar colony in α_2 [01-10] viewing direction
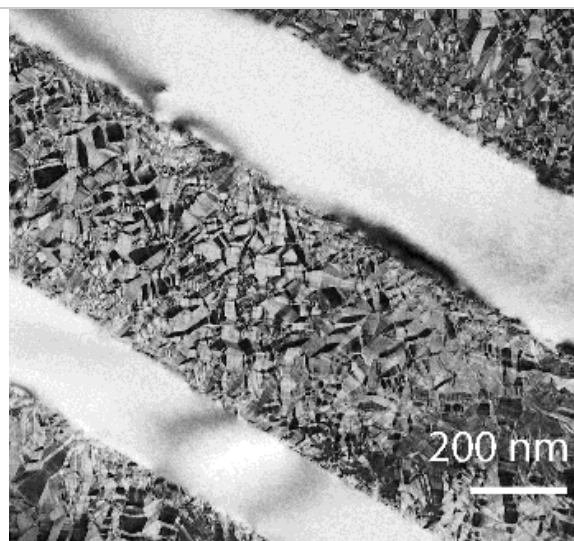
Fig. 2: Lamellar colony in α_2 [0001] viewing direction.

References

[1] F. Appel, M. Oehring, and R. Wagner, Intermetallics 8 1283-1312 (2000).

[2] F. Appel, M. Oehring, and J.D.H. Paul, Advanced Engineering Materials 8 371-376 (2006).

[3] L. Song, et al., Journal of Alloys and Compounds 618 305-310 (2015).

[4] M.W. Rackel, et al., Acta Materialia 121 343-351 (2016).

[5] D. Banerjee, et al., Acta metall. 36 871-882 (1988).

[6] L.A. Bendersky and W.J. Boettinger, Acta metall. mater. 42 2337-2352 (1994).

[7] R. Gerling, H. Clemens, and F.P. Schimansky, Advanced Engineering Materials 6 23-38 (2004).

O–TA 12

Study of the NbTiAl system: influence of the Al-content and Si-doping

Laurence Sikorav[1,2], <u>Zhao Huvelin</u>[1] , Phillippe Vermaut[2,3] , Anne Denquin[1] , Agnès Bachelier-Locq[1]

[1]ONERA – The French Aerospace Lab, F-91761 Palaiseau, France – Laurence.sikorav@onera.fr / zhao.huvelin@onera.fr

[2]PSL Research University, Chimie ParisTech – CNRS, Institut de Recherche de Chimie Paris, 75005, Paris, France – philippe.vermaut@chimie-paristech.fr

[3]Sorbonne Université, UPMC Univ Paris 06, UFR926, F-75005, Paris, France

Introduction

Niobium based refractory intermetallic alloys are considered as having great potentials for high temperature applications based on a good balance of high temperature strength and low-temperature damage tolerance [1]. Moreover this family of alloys also exhibits a high melting point and a low density; hence they are good candidates for low pressure turbine blade applications over the temperature range of 800 – 1000 °C. The specificity of the study is to explore the Nb-Ti-Al system along the $Nb_{50-x}Ti_{50-x}Al_{2x}$ pseudo-binary diagram, and to dope the alloys with a small amount of Si to maintain high-temperature properties while keeping good ductility at room temperature. The Si content is limited to 1% to maximize the solid solution effect [2]. A number of heat treatments at 800 and 1000°C were applied to the solution-treated alloys in order to assess the Al and Si contents influence on the microstructure evolutions, such as the silicides or the orthorhombic phase precipitation, β phase ordering. Finally the influence of the microstructure on the micro-hardness and compression tests at various temperatures will be discussed**.**

Materials and Methods

The alloys were prepared by arc-melting starting from pure elements (99.99%) in a laboratory vacuum arc melting furnace, using a non-consumable tungsten electrode. Each ingot was re-melted several times to ensure a complete mixing of the constituents. The nominal chemical composition of each alloy is presented in Table 1. At first, the four alloys were homogenized at 1420°C for 24h under vacuum to erase the microstructure of solidification, then the samples were subsequently aged at 800 or 1000°C for 168h, followed by oil-quenching. These treatments aim to identify the phases in equilibrium in these alloys at this range of temperature. The kinetics of precipitation of the orthorhombic phase has been investigated by different aging time at 800°C (1h, 15h and 168h), followed by oil quenching (OQ).

Table 1: Nominal chemical composition of the studied alloys (at.%)

Alloy designation	Nb	Ti	Al	Si
10Al-0Si	45	45	10	0
10Al-1Si	44.5	44.5	10	1
15Al-0Si	42.5	42.5	15	0
15Al-1Si	42	42	15	1

The microstructure of the studied alloys after solidification and subsequent heat treatments was characterized by scanning electron microscopy (SEM), and transmission electron microscopy (TEM) techniques. ImageJ software was adopted to measure and quantitatively analyze the average thickness/width and the volume fraction of O-phase precipitates in SEM images. Vickers microhardness was measured using a Buehler Omnimet MTH machine.

Results and Discussion

Homogenized samples have been aged at 800°C/168h/OQ, the SEM micrographs of the four alloys after aging are presented in Fig. 1.
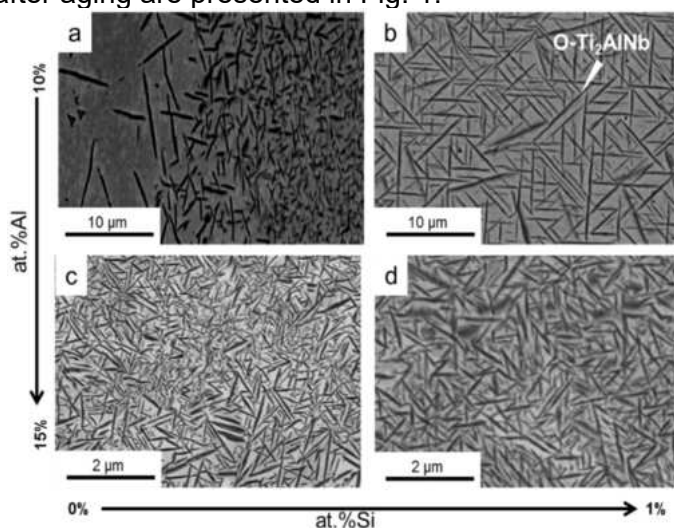
Figure 1: SEM/BSE micrographs of alloys homogenized + aged 800°C/168h+OQ, a) 10Al-0Si, b)10Al-1Si, c) 15Al-0Si, d) 15Al-1Si

The microstructural features such as size and precipitation rate of the O-Ti_2AlNb precipitates depend strongly on the contents of Aluminum and Silicon. Firstly, a minimum Al content is required to order the system from β to β_0. This minimum is between 10 at.% and 15 at.%. The ordering of the matrix induces a strengthening of the mechanical properties of the alloy as shown in Fig. 2. Encircled points show clearly that 15Al-0Si alloy presents a higher microhardness than 10Al-0Si alloy. At homogenized state such increase of hardness is probably due to the ordering of the matrix in 15Al-0Si alloy.
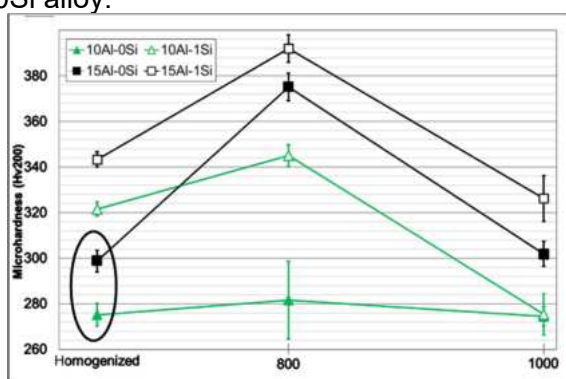
Figure 2: Microhardness Hv200 evolution of the alloys after homogenization, homogenized + 800°C/168h+OQ and homogenized + 1000°C/168+OQ

Furthermore, the Al content impacts also on the orthorhombic phase (O-phase) precipitation. As shown in Fig.1, an increase of Al content leads to a more homogeneous precipitation of O-phase with smaller Ti_2AlNb platelets thus is beneficial to the microhardness of the alloy (Fig. 2).

Concerning the Si doping, it does not show any effects on the ordering of the system, but it has a great impact on the kinetic of precipitation of the O-phase especially at 800°C (Fig. 1). Consequently, the strength of the alloys is significantly improved by addition of 1 at.% of Si (Fig. 2).

References

[1] S. Naka, M. Thomas, T. Khan, Ordered Intermetallics – Physical Metallurgy and Mechanical Behaviour, C.T. Liu, R.W. Cahn, G.Sauthoff (Eds.), **1992**, vol 213, pp. 645-662

[2] B. Kong, L. Jia, H. Zhang et al., International Journal of Refractory Metals and Hard Materials, **2016**, vol. 58, pp. 84-91

O–PS 01

Ab initio thermodynamics and kinetics of precipitate formation in Al-Sc alloys

Tilmann Hickel[1,*], Ankit Gupta[1], Biswanath Dutta[1], Bengü Tas Kavakbasi[2], Yulia Buranova[2], Vladislav Kulitcki[2], Sergiy V. Divinski[2], Gerhard Wilde[2], Jörg Neugebauer[1]

[1]Max-Planck-Institut für Eisenforschung GmbH, D-40237 Düsseldorf, Germany
*t.hickel@mpie.de

[2]Institute of Materials Physics, University of Münster, D-48149 Münster, Germany

Introduction

In view of a continuously rising demand for high strength and light-weight materials Al-based alloys are important industrial materials for structural applications. One of the most promising strategies to improve their mechanical performance is a tuning of precipitate chemistry, morphology and size. In particular, the addition of Sc to Al yields elastically strong and highly stable (up to 1320°C) Al_3Sc precipitates. Experimentally it is known that they remain coherent at small sizes up to about 20 nm due to a relatively small lattice misfit of about 1.25% at room temperature [1] and further alloying can even reduce it. However, the chemo-thermo-mechanical coupling, i.e. how chemical composition, temperature, and local strain fields interact during precipitates nucleation and growth, has not yet been explored. With the present contribution, we provide ab initio insights into some key thermodynamic and kinetic aspects underlying this process.

Methods

The local stress in the matrix during precipitate formation is caused by the lattice mismatch between the host and precipitate phase. To determine the temperature dependence of the mismatch, we have performed density functional theory (DFT) calculations, taking all relevant entropy contributions to the free energy into account [2]. The electronic structure has been determined within the projector augmented-wave (PAW) method as implemented in the VASP code [3]. By comparing the generalized-gradient (GGA) and the local-density (LDA) approximation, we reveal a small sensitivity of the thermodynamic properties on the exchange correlation functional. While our electronic and quasiharmonic free energy calculations follow established routes [2], we obtain the electron-phonon coupling parameter using density functional perturbation theory (DFPT) as implemented in the ABINIT code [4]. Further, the impact of explicitly anharmonic lattice vibrations is considered with the upsampled thermodynamic integration using Langevin dynamics (UP-TILD) [5]. In order to investigate the modification of the solute kinetics due to the presence of the precipitate, the climbing image nudged elastic band method has been employed. The precipitate formation and growth has been investigated with kinetic Monte-Carlo simulations using the in-house python based workbench pyiron.

Results and Discussion

The quality of our temperature dependent free energy calculations has first been checked by comparing the resulting heat capacities with accurate calorimetric measurements (Fig. 1) [2]. We achieve a perfect agreement for all measured temperatures (0 – 400 K), including remarkable non-Debye features in the low-temperature regime (below 50 K). We were able to attribute them to low-lying flat regions in the phonon spectrum and to electronic excitations described by the Sommerfeld model and corrected by nonadiabatic electron-phonon coupling. Due to the stronger Al-Sc bonds in the precipitate phase, these effects are more pronounced in the Al matrix. Hence, we validated that our ab initio description of the thermal expansion of both phases is highly reliable from T=0K up to the melting point and can be used to predict the local stress state at the interface.
Based on these insights the kinetics of precipitate formation has been evaluated. On the one hand, the strain dependence of the migration barrier [6] and elastic constants [7] caused by the growing

precipitates has been determined. For the sake of comparison with experimental tracer diffusion measurements [6], this evaluation has been performed for Co atoms (Fig. 2). On the other hand, kinetic Monte-Carlo simulations have been performed to derive time-temperature-transformation (TTT) diagrams [8]. For the analysis, we employed thermodynamic concepts about the temperature dependent Sc solubility. Furthermore, we have defined the critical nucleation size of the precipitates as a temperature dependent quantity. We convinced ourselves that the maximum precipitate size at high temperatures is limited by the configurational entropy in the solid solution, yielding an upper asymptotic temperature for the formation of precipitates. Furthermore, we investigate the effect of binding energy between the solute particles on the TTT diagrams. As a result of our investigations, a linear relationship between the asymptotic temperature and the nose temperature of the TTT diagrams has been obtained. This allows a computationally highly efficient description of the impact of chemical bonding on nucleation behavior by employing simple scaling laws.
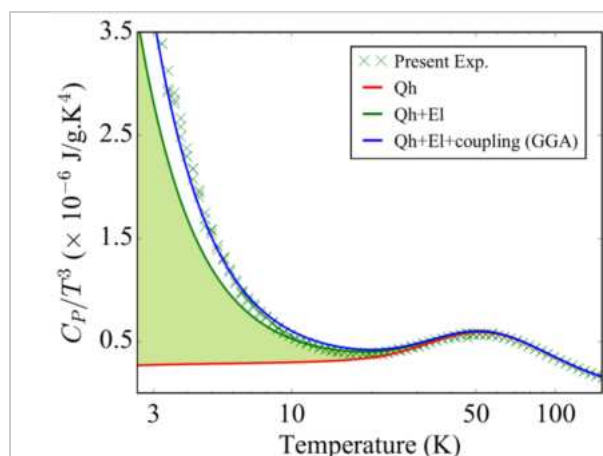
Fig. 1: Experimentally measured (green crosses) and ab initio calculated (lines) isobaric heat capacity for Al_3Sc. Quasiharmonic results (Qh), the addition of electronic excitations (El) and the further addition of electron-phonon coupling (coupling) are shown. The renormalization allows one to visualize the competition of these three contributions. [2]	Fig. 2: Variation of the energy profile (for a Co atom making a diffusion jump into the nearest neighbor vacancy) along the minimum energy path for different strain states in the Al matrix. The respective initial state corresponds to the Gibbs energy of a vacancy formation next to a Co atom. [6]
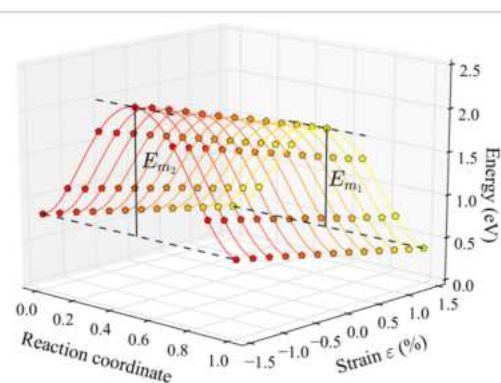
References

[1] Yu. Buranova, V. Kulitskiy, M. Peterlechner, A. Mogucheva, R. Kaibyshev, S.V. Divinski, G. Wilde, Acta Materialia. **2017**, *124*, 210-224.

[2] A. Gupta, B. Tas Kavakbasi, B. Dutta, B. Grabowski, M. Peterlechner, T. Hickel, S.V. Divinski, G. Wilde, J. Neugebauer, Phys. Rev. B. **2017**, *95*, 094307.

[3] G. Kresse and J. Hafner, Phys. Rev. B. **1993,** *47*, 558(R).

[4] X. Gonze, et al., Comput. Mater. Sci. **2002**, *25*, 478.

[5] B. Grabowski, L. Ismer, T. Hickel, and J. Neugebauer, Phys. Rev. B. **2009**, *79*, 134106.

[6] S.V. Divinski, V. Kulitskiy, B. Tas Kavakbasi, A. Gupta, Y. Buranova, T. Hickel, G. Wilde, J. Neugebauer; https://arxiv.org/abs/1701.06694 [cond-mat.mtrl-sci]

[7] C. Schwarze, A. Gupta, T. Hickel, R. Darvishi Kamachali, Phys. Rev. B. **2017**, *95*, 174101.

[8] A. Gupta, master thesis (Ruhr University Bochum, Bochum, 2015).

Acknowledgement

O–PS 02

Structural units in intermetallics: a topological study

Tatiana Akhmetshina[1], Vladislav Blatov[1,2] and Alexander Shevchenko[1]

[1]Samara Center for Theoretical Materials Science (SCTMS), Samara University, Ac. Pavlov St.1, Samara 443011, Russia, e-mail: akhmetshina.tanya@yandex.ru

[2]School of Materials Science and Engineering, Northwestern Polytechnical University, Xi'an, Shaanxi 710072, People's Republic of China, blatov@samsu.ru

Introduction

Traditionally, intermetallics are described in terms of coordination polyhedra (CP), close-packed atomic layers or clusters assembling, and it is usually a manual and routine work. Recently [1], we proposed a nanocluster method, which represents any intermetallic structure as an assembly of multi-shell nanoclusters. The main advantage of this approach is that it is strict and excludes human's subjectivity when considering intermetallics of any composition and complexity. In this study, we perform a comparison of all these methods. Moreover, we provide the comprehensive statistical data on how many types of CP are realized in intermetallics, which atomic nets are the most widespread and how many nanoclusters can assemble the crystal structure.

Materials and Methods

For topological and geometrical analysis we have used crystallographic data on more than 38,000 intermetallics from the Inorganic Crystal Structure Database (ICSD, release 2015/2) and Pearson's Crystal Data (version 2014/15). With the ToposPro program package [2] we have analyzed types of nanoclusters in intermetallics, types of CP in intermetallics and types of close-packed layers. To decompose crystal structure to the building blocks (primary nanoclusters) we have used the Nanoclustering procedure, which is implemented in the ToposPro program package and described in details in [2]. All possible nanoclusters were revealed with the nanoclustering procedure; then we found their occurrence in intermetallics. Thus, we have created the collection of Topological Types of Nanoclusters (TTN) [3]. For the automatic analysis of the shape of CPs we have used the Voronoi approach, which is also realized in ToposPro [4]. The layers in intermetallics were found using a unique ToposPro capability to search for a finite graph in an infinite periodic net [2].

Results and Discussion

Analysis of the statistical data shows that 12- and 14-coordinated polyhedra prevail in intermetallics – 33% and 13%, respectively. Note that in 59% of cases the polyhedra with coordination number (CN) 12 have an icosahedral shape. Almost 97% of CPs have coordination numbers from six to 18, while other CNs are not widespread. Besides the data about nanocluster topology and occurrence in the TTN collection we have added the information of how many intermetallics can be assembled with only one non-equivalent nanocluster and what type of underlying nets this nanocluster forms. We have revealed that 926 out of 3681 topological types of the intermetallics can be represented as a *monocluster* assembly. In total, 15,534 (about 40%) intermetallic crystal structures belong to these topological types. The size of the polyhedral building blocks varies from five to 25 atoms. We have found the following dominating topologies of the underlying net: **pcu, hex, bcu-x, bct, fcu, hcp, feb, eca, chb** and **dia**. We believe that such strategy to study of intermetallics from local atomic configuration to global arrangement in crystals can help in design and prediction of new structures. Therefore, we have analyzed the nanoclusters models in different types of intermetallics: icosahedron- (1528 crystal structures), Mackay- (60) and Bergman-based (41) [3,5,6]. Moreover, we have found strong correlations between chemical composition of nanoclusters and topological descriptors such as local and overall topologies. A peculiarity is that the homogeneous (consisting of just one sort of atoms) first shell of Mackay and Bergman clusters is realized in all cases. The information obtained about preferred ways of binding the nanoclusters is included into the knowledge database of the ToposPro program package. In addition, we have generated 509 atomic plane nets and examined their occurrence in intermetallics in an automatic mode. Thus, we have demonstrated

that any description of intermetallics can be automatized. Thus, the nanocluster method of analysis can be considered suitable for the development of knowledge database and the modeling of new crystal structures.

References

[1] V. A. Blatov, Structural Chemistry. **2012**, *23,* 955-963.

[2] V. A. Blatov, A. P. Shevchenko, D. M. Proserpio, Crystal Growth & Design. **2014**, *14,* 3576-3586.

[3] A. A. Pankova, T. G. Akhmetshina, V. A. Blatov, D. M. Proserpio, Inorganic Chemistry. **2015**, *54,* 6616-6630.

[4] A. P. Shevchenko, I. A. Blatov, E. V Kitaeva, V. A. Blatov, Crystal Growth and Design. **2017**, *17,* 774-785.

[5] T. G. Akhmetshina, V. A. Blatov, Structural Chemistry. **2017**, *28,* 133-140.

[6] T. G. Akhmetshina, V. A. Blatov, Structural Chemistry. **2016**, *27,* 1685-1692.

O–PS 03

Relative stability of intermetallic compounds in the AMn_2Al_{20} alloys (where A = lanthanide/actinide/rare earth)

Gili Yaniv, David Fuks and Louisa Meshi

Department of Materials Engineering, Ben Gurion University of the Negev, Beer-Sheva 84105, Israel, gilisha@post.bgu.ac.il, fuks@bgu.ac.il, louisa@bgu.ac.il

Introduction

In the last few years, in the framework of materials genome initiative, the discovery of new materials with unique properties was accelerated. An example of such researches is search for heavy fermion compounds exhibiting magnetic ordering and unconventional superconductivity. A-T-Al aluminides, where A = actinide, lanthanide or rare earth elements with $4f$- or $5f$-shells and T=transition metal, are representatives of these compounds. Till now the information about these systems` phase diagrams is not complete since most of the experimental researches are performed using "trial and error" approach, which could be time consuming. It would be of clear benefit to formulate a rule that could predict the relative stability of the structures that may form in the ternary Al-richest phases in the A-T-Al systems. First steps towards achieving this goal were performed through investigation of the ThT_2Al_{20} system (where T=3d transition metal) [1]. It was proved both experimentally and theoretically that the symmetry of the Th-based ternary aluminides` structure changes abruptly as a function of atomic number, Z_T, of T. At T=Mn the symmetry decreases from cubic (structure that crystallizes with $Z_T<25$) to orthorhombic (structure of aluminides crystallizing with $Z_T>25$). This change inevitably imposes modification of magnetic and electrical properties. Although in the $ThMn_2Al_{20}$ alloy, the orthorhombic $YbFe_2Al_{10}$-type structure was found to be the stable one, other AMn_2Al_{20} might present different behavior. For example, UMn_2Al_{20} compound crystallizes in the cubic $CeCr_2Al_{20}$-type structure [2].

Current research focuses on the AMn_2Al_{20} systems with an aim to understand the influence of A type atoms on the formation of the stable structures. The work was performed systematically, investigating several AMn_2Al_{20} alloys, with different electronic structures, both experimentally and by Density Functional theory (DFT) calculations.

Materials and Methods

Experimental
High purity (99.99%) A (A=Y, Gd, Th), Mn and Al were used for the preparation of the alloys. The nominal composition of the alloys was 87at%Al-8at%Mn-4at%A. The alloys were prepared by arc melting in UHP Ar atmosphere. The melt was cast into Cu molds. Final ingot shape was rod, 6mm in diameter. Following the preliminary analysis of the alloys, they were wrapped in Ta foil and encapsulated in quartz capsule under Ar atmosphere. Thermal treatment at 800°C for 300 hours was performed for homogenization.
The characterization of the homogenized alloys was performed by Scanning Electron Microscopy (SEM), Transmission Electron Microscopy (TEM) and powder X-ray diffraction method (XRD). Rietveld analysis was used for the refinement.

DFT calculations
For interpreting the trends in the changes of the relative stability of the Al-richest A-Mn-Al phases DFT was used [3]–[5]. Full Potential with Linearized Augmented Plane Waves (FP-LAPW) method as implemented in the WIEN2k code (Version 10.1) [6] was applied. The exchange-correlation potential was calculated within the Perdew-Burke-Ernzerhof (PBE) generalized gradient approximation (GGA) [7]. The muffin-tin radii (R_{mt}) were taken equal to 2.5 Bohr for A (A=Y, Gd, Th, U) and Mn atoms, and equal to 2.2 Bohr for Al atoms. It was found that the number of k-points in the first Brillouin zone was equal to 300 which is enough to obtain the accuracy of the self-consistent calculations for the energy of the system not less than $\sim 10^{-3}$ Ryd, in all cases. To check the quality

of calculations, the equilibrium volume of the unit cell for all considered phases was obtained by fitting the data to Murnaghan equation of state [8].

Results and Discussion

For the experimental part of this work, A-Mn-Al alloys (where A=Gd, Y, Th) were cast in the AMn_2Al_{20} stoichiometry in order to check if the cubic phase (with the $CeCr_2Al_{20}$ structure type) will form. It should be noted that the alloy with A=U was not cast since in [2], cubic UMn_2Al_{20} phase was already reported to exist. Following characterization of alloys with A=Gd and Y, it was found that the cubic AMn_2Al_{20} phase was not formed, despite the adequate quantity of Al that was provided. Instead, the tetragonal AMn_2Al_{10} phase (with the $CaCr_2Al_{10}$ type) was formed and excess of Al resulted in formation of Al-matrix. The characterization of the $ThMn_2Al_{20}$ alloy revealed a similar situation, the cubic phase did not form, but in this case, the orthorhombic $ThMn_2Al_{10}$ phase (with the $YbFe_2Al_{10}$ type) crystallized in the Al matrix.

DFT calculations were performed for the cubic ($CeCr_2Al_{20}$ type), tetragonal ($CaCr_2Al_{10}$ type) and orthorhombic ($YbFe_2Al_{10}$ type) structures in considered systems. The equilibrium state of each structure in each system was found by plotting the total energy of the corresponding structures as a function of the unit cell volume. Fitting the calculated energies to Murnaghan equation of state was performed to obtain equilibrium lattice parameters. The preference of one structure over the other was determined according to the energy differences with respect to the cubic structure (ΔE). Thus, more negative ΔE magnitude points to the most stable structure. ΔE values for each of considered systems are presented in Table 1.

Table 1: Energy differences ΔE (Ry) with respect to the cubic structure

	Y-Mn-Al	Gd-Mn-Al	Th-Mn-Al	U-Mn-Al
Orthorhombic	-0.102	-0.069	-0.254	0.037
Tetragonal	-0.139	-0.106	-0.207	0.031
Cubic	0	0	0	0

It can be seen that tetragonal structure is the most stable in the YMn_2Al_{20} and $GdMn_2Al_{20}$ alloys. For the $ThMn_2Al_{20}$ alloy orthorhombic structure is favorable, whereas in the UMn_2Al_{20} alloy the cubic structure is the most stable one. These results coincide with the experimental data. The calculated and experimentally determined lattice parameters were compared and an excellent agreement was found.

References

[1] A. Uziel, A. I. Bram, A. Venkert, A. E. Kiv, D. Fuks, L. Meshi, Journal of Alloys and Compounds, **2015**, 648, 353–359.

[2] P. Wiśniewski, P. Swatek, A. Gukasov, and D. Kaczorowski, Physical Review B, **2012**, 86, no. 5, 054438.

[3] W. Kohn and S. L. J., Physical Review, **1965**, 140, 1133–1138.

[4] P. Hohenberg and W. Kohn, Physical Review, **1964**, 136, 864–871.

[5] J. P. Desclaux, Computer Physics Communications, **1969**, 1, 216–222.

[6] P. Blaha, K. Schwarz, G. Madsen, D. Kvasnicka , J. Luitz, An augmented plane wave plus local orbitals program for calculating crystal properties, **2001**, 2, 237.

[7] J. P. Perdew, K. Burke, M. Ernzerhof, Physical Review Letters, **1996**, 77, no. 18, 3865–3868.

[8] F. D. Murnaghan, Proceedings of the National Academy of Sciences, **1944**, 30, no. 9, 244–247.

O–PS 04

Bi-Rh and Bi-Mn-Rh: phase equilibria

Peter Kainzbauer, Klaus Richter and Herbert Ipser

Department of Inorganic Chemistry – Functional Maerials, University of Vienna
Althanstraße 14 (UZA II), 1090 Wien, Austria

peter.kainzbauer@univie.ac.at, klaus.richter@univie.ac.at, herbert.ipser@univie.ac.at

Introduction

The intermetallic phase α-BiMn with NiAs-type structure has been suggested as an interesting ferromagnetic material with the major advantage of not containing rare earth elements [1]. Unfortunately, it has not been possible to synthesize this phase as single-phase bulk material despite several decades of intensive research (see e.g. [2,3]). A possible approach to circumvent the difficulties of synthesizing it was considered the addition of a third element, which forms an intermetallic phase with Bi that is iso-typic to α-BiMn, as for example BiRh [4].
Stabilization of BiMn by Rh was described by Lee et al. [5], however, it was the high-temperature modification β-BiMn that was stabilized down to lower temperatures. A similar observation was made more recently by Taufour et al. [6] who described a ferromagnetic BiMn compound $BiMn_{1.05}Rh_{0.02}$. A ferromagnetic ternary compound $Bi_4Mn_5Rh_2$ was identified by Street et al. [6] though with a Curie temperature of -7°C. On the other hand, Suits [7] discovered ferromagnetism in Bi-substituted MnRh with the composition $Mn_{0.8}Bi_{0.2}Rh$. Based on these observations, a systematic study of the ternary Bi-Mn-Rh system was considered of interest, with the potential of finding additional intermetallic phases, which might possibly exhibit ferromagnetism. During this study it was found that the binary Bi-Rh phase diagram was still not fully known; in particular, nothing was known about the accurate homogeneity range of the NiAs-type phase BiRh [8,9]. Thus a new and thorough investigation of the binary Bi-Rh phase diagram was initiated, too.

Materials and Methods

For sample preparation, calculated amounts of the element powders (total amount 0.5-1 g) were mixed and pressed into pellets. Samples containing less than about 50 at.% Bi were melted in an arc furnace on a water-cooled copper plate under Ar atmosphere, using Zr as getter material, and sealed into evacuated silica glass tubes. All other pellets were immediately sealed into evacuated silica glass tubes and melted over an oxyhydrogen flame under shaking. All samples were annealed at different temperatures for at least two weeks and quenched in cold water.
Phase identification was performed by powder X-ray diffraction (XRD), electron probe microanalysis (EPMA) and scanning electron microscopy (SEM) as well as differential thermal analysis (DTA). A few selected samples were also analyzed by high-temperature powder XRD. For evaluation and Rietveld refinement of all diffraction patterns the TOPAS® 4.2 Software [10] was used. All binary Bi-Rh samples between 42.5 and 52.5 at% Rh were investigated by EMPA using wavelength dispersive X-ray spectroscopy (WDS). For all other samples, SEM was used with energy-dispersive X-ray spectroscopy (EDX). Backscattered electrons served for surface visualization. DTA measurements were performed in evacuated silica glass crucibles. The temperature program included two heating/cooling cycles at a rate of 5 K/min starting from 200°C up to about 30°C above the estimated liquidus temperature, not exceeding a maximum temperature of 1040°C.

Results and Discussion

Binary Bi-Rh Phase Diagram
The results of the present study confirm the main features of the phase diagram as described earlier in the literature [4,8,9]. The phase BiRh is formed in a peritectic reaction (L + Rh → BiRh) at 979±2°C. Its homogeneity range at 750°C was determined to extend from 47 to 53.5 at% Rh based on the concentration dependence of the lattice parameters. The phase Bi_2Rh was found to exist in two different modifications: β-Bi_2Rh forms in a peritectic reaction (L + BiRh → β-Bi_2Rh) at 785±1°C and

transforms between 433 (Bi-rich side) and 448 (Rh-rich side) into the low-temperature modification α-Bi_2Rh. The phase Bi_4Rh forms also in a peritectic reaction from liquid and β-Bi_2Rh at about 460°C. The phase Bi_3Rh, stable between 336 and 433°C according to Weitzer et al. [8], could not be found in the present study. This is in agreement with the observation by Ross and Hume-Rothery [4], it might indicate that Bi_3Rh is a metastable compound. Weitzer et al. reported also the existence of a metastable compound $Bi_{14}Rh_3$ which was not identified here as no samples had been placed in this composition range.

Ternary Bi-Mn-Rh Phase Diagram
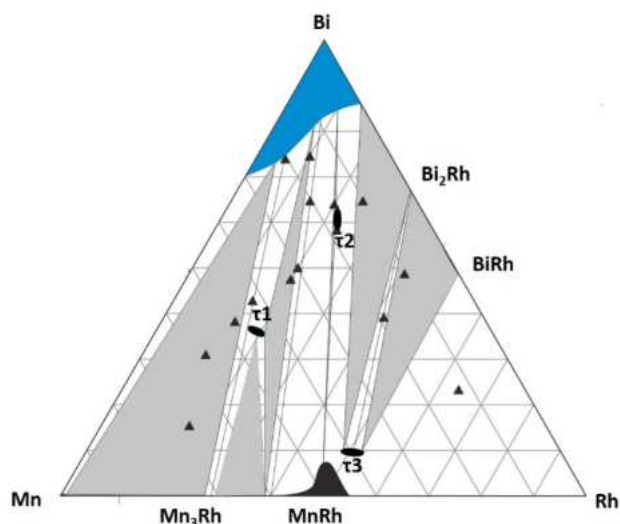
Fig. 1. Isothermal section of the ternary Bi-Mn-Rh phase diagram (still incomplete)

Fig. 1 shows an isothermal section, though still incomplete, of the ternary Bi-Mn-Rh phase diagram at 600°C. As can be seen, there is certainly no solid solution between the two NiAs-type phases BiMn and BiRh. Quite contrary, no significant solid solubility of Mn in the phases BiRh and β-Bi_2Rh and, on the other side, no stabilization of BiMn up to this temperature could be observed. The ternary phase τ1 corresponds to the compound $Bi_4Mn_5Rh_2$, already earlier reported in the literature [6]; the newly discovered phases τ2 and τ3 correspond to $Mn_{38}Rh_{52}Bi_{10}$ and $Mn_{16}Rh_{22}Bi_{62}$, respectively, where the latter compositions are from SEM-EDX only. The ternary compound τ3 shows possibly ferromagnetism.

Acknowledgement

References

[1] M.J. Kramer, R.W. McCallum, I.A. Anderson, S. Constantinides, JOM **2012**, *64*: 752-763.

[2] J. Cui, J.-P. Choi, E. Polikarpov, M.E. Bowden, W. Xie, G. Li, Z. Nie, N. Zarkevich, M.J. Kramer, D. Johnson, Acta Mater. **2014**, *79*, 374-381.

[3] Y.-Ch. Chen, G. Gregori, A. Leineweber, F. Qu, Ch.-Ch. Chen, T. Tietze, H. Kronmüller, G. Schütz, E. Goering, Scripta Mater.**2015,** *107,* 131-135.

[4] R.G. Ross and W. Hume-Rothery, J. Less-Comm. Met. **1962**, *4,* 454-459.

[5] K. Lee, J.C. Suits, and G.B. Street, Appl. Phys. Lett. **1975**, *26*, 27-29.

[6] V. Taufour, S. Thimmaiah, S. March, S. Saunders, K. Sun, T. N. Lamichhane, M. J. Kramer, S. L. Budko, P. C. Canfield, Phys. Rev. Applied **2015**, *4*, 014021.

[7] J.C. Suits, IBM J. Res. Dev. **1975**, *19*, 422-423.

[8] F. Weitzer, W. Schnelle, R.C. Gil, S. Hoffmann, R. Giedigkeit, Y. Grin, Calphad **2009**, *33*, 27-30.

[9] H.J. Okamoto, J. Phase Equilib. Diff. **2010**, *31*, 204.

[10] TOPAS 4.2, Bruker AXS Inc., Karlsruhe, Germany, **2011**.

O–PS 05

Effect on Al and Cr substitution on TCP structure of Fe_2Nb Laves phase

Ryosuke Yamagata[1], Masao Takeyama[1] and Kyosuke Yoshimi[2]

[1] Department of Materials Science & Engineering, School of Materials and Chemical Technology, 2-12-1-S8-8, Meguro-ku, Tokyo, Japan.   e-mail: yamagata.r.aa@m.titech.ac.jp

[2] Department Materials and Science, School of Engineering, Tohoku University, 6-6-02 Sendai, Miyagi, Japan.

Introduction

Ferritic creep-resistant steels are the most candidate material for heavy wall components in next generation coal-fired power plants due to their low cost and low thermal expansion coefficient compared to austenitic steels and Ni-based alloys. Unfortutately, their high-temperature (creep) strength has not fulfilled the demands yet. Conventional ferritic steels have been strengthened by carbides and nitrides. However, their strengthening effects have reached a ceiling because of their thermal instability in the operating temperature range. Laves phase intermetallic compounds have been considered as one of effective precipitation-strengtheners in ferritic steels. Especially, Fe_2Nb Laves phase has attracted a great deal of attention because it has high thermal stability better than carbides [1]. In order to achieve high-temperature strength for long service time, precipitations should be finely and stably dispersed in matrix, and the particle size should be kept during operation time. Laves phase has three-types of crystal structure:i.e., hexagonal C14, cubic C15 and dihexagonal C36, and all they have topologically close-packed (TCP) structures. It is expected that there is close relationship between geometrical factors such as lattice parameter and axial ratio and phase stability. Recently, the effect of atomic size ratio on the formation enthalpies was studied for the C15 structure [2]. However, there has been few reports about the phase stability of the C14 structure that mainly precipitates in steels. In this study, the structure of C14-type Fe_2Nb Laves phase equilibrated in a ferritic steel containing Al and Cr is refined by the Rietveld technique in order to relate the geometrical factors of the C14-type structure to the phase stability. The effect of Al and Cr substitution in Fe_2Nb on the geometrical factors is discussed.

Materials and Methods

The nominal composition of the alloys employed were Fe-(27-33.3)Nb-(0-16.67)Al or Cr. These alloys were prepared by a conventional Ar arc-melting technique. Homogenization heat-treatment was carried out at 1300°C for 70 h under a vacuum of about 1.0×10^{-4} Pa. Quantitative compositional analysis was carried out by the Field Emission-Electron Probe Micro Analysis (FE-EPMA) equipped with the Wavelength Dispersive Spectroscopy (WDS). Pure metals were used as standards for the analyses of Fe, Cr and Nb, and AlN for Al. Structural analyses were performed by the Rietveld refinement. Powder X-ray diffractometry (XRD) was conducted using the Cu-$K\alpha$ radiation under the Bragg-Brentano focusing optical system. The Rietveld refinement was run on the TOPAS® software by Bruker AXS. The fundamental parameter method was applied on the profile function calculation. In order to investigate micro-hardness change by Al and Cr substitution, nano-indentation tests were carried out with the loading force of 10 mN.

Results and Discussion

From the results of the Rietveld refinement, the effect of Al and Cr substitution in Fe_2Nb on the lattice parameter and atomic coordinate of each element were clarified. Based on the lattice parameter and atom coordinate, effective atom radii in each crystallographical atom site in Laves phase of 6h (Fe1), 2a (Fe2) and 4f (Nb) sites were calculated as shown in Fig. 1. The effective atom radius of two Fe-atom sites showed different values even though in the case of the stoichiometric composition. From the results of packing ratio estimation using effective atom radii and unit cell volume, it was revealed that packing ratio increased with Al and Cr addition. Therefore, it was suggested that the element-substitution behavior in C14-type Fe_2Nb Laves phase is based on the increase in packing ratio. It

was found that micro-hardness of the Laves phase increased with increasing the packing ratio as shown in Fig. 2. Because the hardness and melting-point have a positive correlation [3], it was expected that geometrical factors and phase stability also show correlativity in C14-type Fe_2Nb Laves phase.
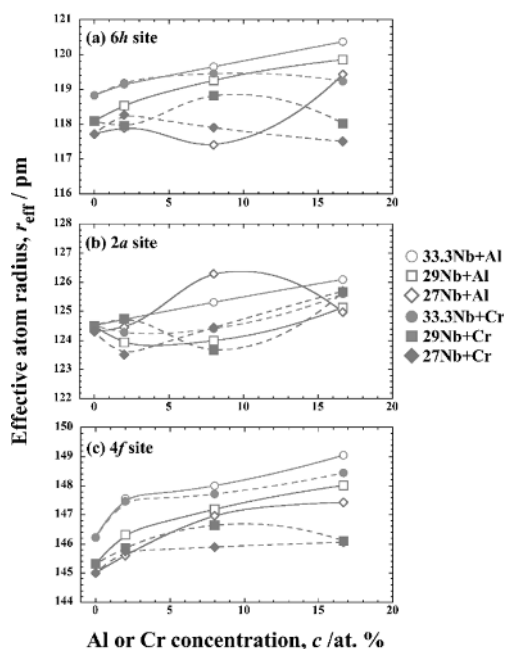
Fig. 1: Effective atom radius of Laves phase in (a) 6h site, (b) 2a site and (c) 4f site, as a function of Al or Cr concentration in alloy.
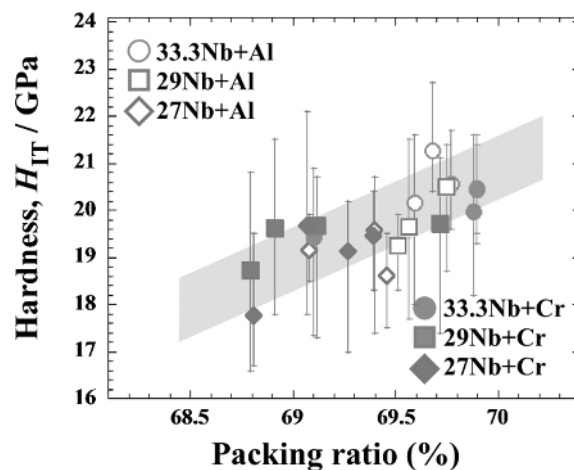
Fig. 2: Nano-hardness of Laves phases as a function of estimated packing ratio of each Laves phases.

References

[1]   J. Hald and L. Korcakova, ISIJ int. **2003**, *43*, 420-427.

[2]   J. H. Zhu, C. T. Liu, L. M. Pike and P. K. Liaw, Intermetallics. **2002**, *10*, 579-595.

[3]   R. L. Fleisher in: J. H. Westbrook and R. L. Fleischer (Eds.): Structural Applications of Intermetallic Compounds. Wiley, United States, **2000**. Chapter 11, pp. 257.

O–PS 06

Impact of magnetism on the stability of topologically close-packed (TCP) phases in Fe-Nb alloys

A. Zendegani[1], M. Šlapáková[1,2], C. Liebscher[1], F. Stein[1], A.N. Ladines[3], T. Hammerschmidt[3], R. Drautz[3], F. Körmann[1], T. Hickel[1], J. Neugebauer[1]

[1]Max-Planck-Institut für Eisenforschung GmbH, Max-Planck-Straße 1, 40237 Düsseldorf, Germany, zendegani@mpie.de

[2]Charles University in Prague, Czech Republic, slapakova@karlov.mff.cuni.cz

[3]ICAMS, Ruhr-Universität Bochum, 44801 Bochum, Germany

Introduction

Ferritic steels containing Fe-Nb topologically close-packed (TCP) phases (e.g. Laves Fe_2Nb and μ Fe_7Nb_6) have a number of industrially relevant high-temperature applications, e.g., for the automotive industry. These alloys have been studied in several previous works [1-9]. To tailor in particular the high-temperature strength of these materials, e.g., via heat treatments, a precise knowledge of the thermodynamic stability of the TCP phases, their interfaces and defects, is essential. In the present work, we demonstrate the role of temperature, magnetism, and chemical composition in this context.

Materials and Methods

We have investigated the phase stability of the most relevant TCP phases in Fe-Nb alloys, i.e. the hexagonal μ and Laves (C14, C36) phases, and the cubic Laves (C15) phase, by combining density functional theory (DFT) and thermodynamic concepts. The DFT calculations were performed utilizing plane-wave basis sets as implemented in the Vienna ab initio simulation package (VASP) [10] and the Perdew-Burke-Ernzerhof (PBE) [11] exchange-correlation functional in the generalized gradient approximation (GGA).

The ground state energy as well as finite temperature entropy contributions of these structures are evaluated for various magnetic configurations, ranging from non-magnetic simulations over selected ferro/ferri-magnetic ones to fully paramagnetic calculations (Fig. 1). The spin-space averaging (SSA) method [12] is utilized to average forces over many magnetic configurations determined from special-quasirandom structures (SQS) to simulate disordered magnetic states.

We used the direct method for phonon calculations. The vibrational contribution to the free energy is treated within the quasi-harmonic approximation and evaluated employing the S/PHI/nX program library [13].

Results and Discussion

The calculation of phonons is of central importance for temperature dependent phase stabilities. It is therefore important that the vibrations of Fe-Nb alloys, which are paramagnetic at room temperature, cannot be treated with non-magnetic (non-spin-polarized) calculations. Such a treatment would not only affect quantitative values, but can even result in dynamical instabilities, e.g. in C36. We have therefore carefully analysed the magnetic structure of these phases.

It can be seen in Fig. 1 that at T=0 K the ferrimagnetic C15 (UD) structure is more stable than ferrimagnetic C14 (DUD) structure. Finite temperature calculations showed that C15 UD became even more stable than C14 DUD at higher temperatures. However, in the experimental phase diagram, the stable phase is C14 at finite temperature. Therefore, performing only ferrimagnetic calculations would contradict experimental results. Only when we employed the paramagnetism explicitly for these phases, we obtained agreement with experiment and better insight into the phase stability. Most importantly, our simulations correctly reproduced the transition from the ferrimagnetic to the paramagnetic regime.

The simulations revealed that paramagnetic Fe_2Nb Laves phases C15 and C14 exhibit a very shallow energy landscape, with energy differences of ~10 and ~5 meV per atom for different magnetically disordered systems, respectively. Hence constrained spin DFT [14] is necessary to

make magnetic disorder calculations feasible. We have carefully evaluated the application of constraining fields in standard DFT code for phonon calculations of paramagnetic Fe-Nb alloys and have derived an efficient computational scheme for this purpose.

This scheme paved the way for further atomistic investigation of the microstructure of these alloys. We investigated point and extended defects such as the intrinsic stacking fault (Fig. 2), which plays an important role for the mechanical properties. Our simulations revealed that the basal stacking fault shown in Fig. 2 shows remarkable structural and chemical properties, which can explain the distribution of these defects in experimental microstructures.
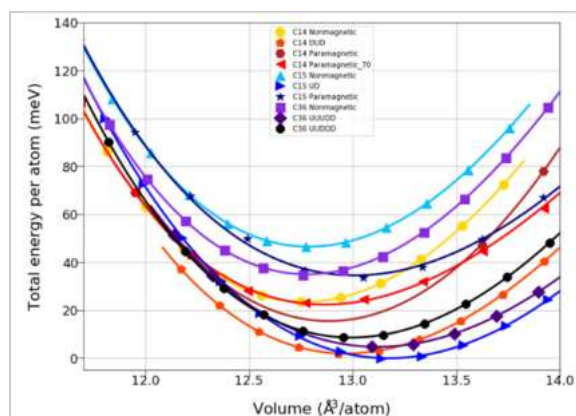
| Fig. 1: Energy vs volume curves for the Laves phases for various magnetic configurations, e.g. C15 UD (Fe↑16d, Nb↓8a), C14 DUD (Fe↓2a, Fe↑6h, Nb↓4f), and C36 UUUDD (Fe↑ 6h, Fe↑ 6g, Fe↑ 4f, Nb↓4f, Nb↓4e). | Fig. 2: Basal stacking fault in Fe-Nb alloy. The Fe and Nb atoms are shown in brown and green, respectively. While the bulk phase has a C14 crystal structure, the stacking fault plane has a different symmetry and composition. |
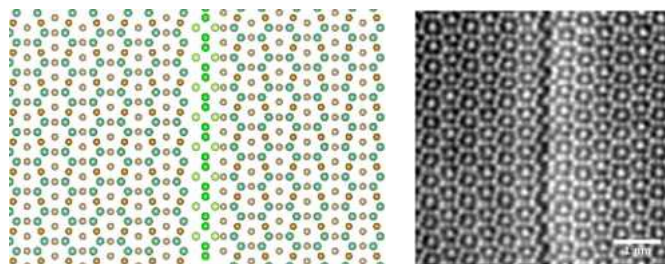
References

[1] K. Wetzig, physica status solidi (b), **1969**, *34*, K79-K81.

[2] D. A. Read, G. C. Hallam, M. S. Sahota and A. Mustaffa, Physica B+C, **1977**, *86-88*, 66-68.

[3] S. Ishida, S. Asano and J. Ishida, J. of the Physical Society of Japan, **1985**, *54*, 3925-3933.

[4] Y. Yamada and A. Sakata, J. of the Physical Society of Japan, **1988**, *57*, 46-47.

[5] D. Moroni-Klementowicz, M. Brando, C. Albrecht, et al., PRB, **2009**, *79*, 224410.

[6] S. Voß, M. Palm, F. Stein and D. Raabe, J. of Phase Equilibria and Diffusion, **2011**, *32*, 97-104.

[7] T. D. Haynes, I. Maskery, M. W. Butchers, et al., PRB, **2012**, *85*, 115137.

[8] A. Jacob, C. Schmetterer, D. Gruner, et al., J. of Alloys and Compounds, **2015**, *648*, 168-177.

[9] A. N. Ladines, R. Drautz and T. Hammerschmidt, J. of Alloys and Compounds, **2017**, *693*, 1315-1322.

[10] G. Kresse and J. Furthmüller, PRB, **1996**, *54*, 11169-11186.

[11] J.P. Perdew, K. Burke and M. Ernzerhof, PRL, **1996**, *77*, 3865-3868.

[12] F. Körmann, A. Dick, B. Grabowski, T. Hickel and J. Neugebauer, PRB, **2012**, *85*, 125104.

[13] S. Boeck, C. Freysoldt, A. Dick, L. Ismer and J. Neugebauer, Computer Physics Communications, **2011**, *182(3)*, 543-554.

[14] P. W. Ma and S. L. Dudarev, PRB, **2015**, 91, 5.

O–FI 01

Intermetallic compound $Al_{13}Fe_4$ as a platform or precursor for catalysis materials

Satoshi Kameoka[1], Tsunetomo Yamada[2], Eiji Abe[3] and An Pang Tsai[4]

[1]IMRAM, Tohoku University, Sendai, 980-8577, Japan, kameoka@tagen.tohoku.ac.jp

[2]IMRAM, Tohoku University, Sendai, 980-8577, Japan, tntmymd@tagen.tohoku.ac.jp

[3]The University of Tokyo, 7-3-1 Hongo, 113-8656, Japan, abe@material.t.u-tokyo.ac.jp

[4]IMRAM, Tohoku University, Sendai, 980-8577, Japan, aptsai@tagen.tohoku.ac.jp

Introduction

On conventional preparation of catalysts (*e.g.*, impregnation, co-precipitation etc.), a solution of one or more metal compounds is used to obtain the metal dispersed catalysts with metal oxides such as SiO_2, Al_2O_3 or TiO_2 as supports [1]. Several thermal processes (drying, calcination, reduction) are needed to remove ligands of precursors' and/or activate metals at high temperatures. Therefore, an increase in grain size, a reduction in catalyst dispersion and a deterioration of the size-dependent properties such as catalytic activity and selectivity are inevitable. On the other hand, it is well known that supported transition metal (TM) catalysts with monodispersed TM have shown to excellent catalytic properties for several reactions. Recently, monodispersed TM catalysts have been prepared by multi-step chemical processes [2-4]. However, it is difficult to prepare supported TM catalysts with monodispersed TMs by means of the conventional preparation methods. Other potential alternative facile methods for preparation of TM catalysts are strongly required. Most recently, we suceeded the one-step preparation method of monodispersed Pt-Fe_3O_4 with high catalytic performance using the caustic leaching for an intermetallic compound $Al_{13}Fe_4$ [5]. In this presentation, we will report $Al_{13}Fe_4$ as a platform or precursor for catalysis materials.

Materials and Methods

Alloys with compositions of $Al_{76.5-x}Fe_{23.5}TM_x$ (at%; TM = Pt, Pd, Cu etc.; x = 0 - 1) were prepared from elemental raw materials with purities of 99.9 wt.% in an arc furnace under an Ar atmosphere. $Al_{76.5-x}Fe_{23.5}TM_x$ means that Al sites in $Al_{76.5-x}Fe_{23.5}$ ($Al_{13}Fe_4$) intermetallic compound are partly replaced by TM atoms. These alloys were subsequently crushed to powders with particle sizes in the desired range (<125 μm). The sample powders were leached in a 10 wt.% NaOH aq. for 4h at rt, and then filtered out and thoroughly washed with distilled water until no alkali was detected in the filtrate. These samples before and after leaching treatment are designated by AlFe-TM (BL) and AlFe-TM (AL), respectively. The reaction was carried out in a standard fixed-bed flow reactor by passing a gaseous mixture of CO (1 vol. %) and O_2 (0.5 vol. %) in He flow at a total flow rate of 50 cm^3 min^{-1} over 50 mg of catalyst (total pressure: 1 atm; space velocity (SV) : 20,000 h^{-1}). The samples were characterized by XRD, SEM, TEM etc..

Results and Discussion

Fig. 1 shows the XRD patterns for different AlFe-TM alloys before (BL) and after leaching (AL) in the 10%NaOH aqueous solutions. The diffraction peaks responsible for the $Al_{13}Fe_4$ phase of the each alloy sample were observed before leaching (Fig.1 BL). The original diffraction peaks of all samples disappeared completely after leaching (Fig.1 AL). Only broad diffraction peaks from Fe_3O_4 came up after leaching. Surprisingly, the peaks corresponding to TM were not visible in the XRD patterns, while the diffraction peaks of TM on conventional supported TM catalysts can be observed even at those moderate loading region (*e.g.*, 5.2 wt% Pt). This suggests that the TM species on Fe_3O_4 form very small crystallite and/or particle size. According to the ICP analysis of

the leaching solution, no TM ions were detected, indicating that selective dissolution of Al from AlFe-TM alloys took place during the leaching (Table 1). The BET surface areas of these samples were drastically increased which compared with before leaching (< 1 m^2/g). Mesopores around 10 nm were observed for those samples after leaching. Consequently, it is indicated that monodispersed TM-Fe_3O_4 catalysts can be prepared readily by one-step process using the caustic leaching treatment for the bulk $Al_{76.5-x}Fe_{23.5}TM_x$ intermetallic compound.

Fig. 2 shows the CO conversion as a function of reaction temperatures for each sample. The catalytic activity of the AlFe-Pt is the highest among these samples. The CO oxidation is promoted by the presence of TM. The order of the catalytic activity is as follows: Pt > Pd > Cu > none. The monodispersed TM-Fe_3O_4 obtained from $Al_{76}Fe_{23.5}TM_{0.5}$ exhibited high catalytic performance for the CO oxidation due to the TM nanoparticles in the porous Fe_3O_4 matrix, which is compared with other TM-Fe_3O_4 as well as a conventional impregnated TM/Fe_3O_4 catalyst. Interestingly, Pt is found to promote the CO oxidation even in the $Al_{76.5-x}Fe_{23.5}TM_x$ ($Al_{13}Fe_4$-TM) intermetallic compound itself without leaching treatment, i.e., $Al_{13}Fe_4$ itself plays as a platform of catalyst.

In conclusion, we developed a novel one-step process to prepare TM-Fe_3O_4 catalysts with monodispersed TM using the caustic leaching for the bulk $Al_{76}Fe_{23.5}TM_{0.5}$ (at%) intermetallic compounds. This one-step process is a promising method to apply to various Al-based intermetallic compounds including catalytic active 8-11 groups metals (< 5 at.%).

References

[1] J.A. Schwarz, C. Contescu and A. Contescu, Chem. Rev., **1995**, *95*, 477-510.
[2] C. Wang, H. Daimon and S. Sun, Nano Lett., **2009**, *9*, 1493-1496
[3] M.R. Buck, J.F. Bondi and R.E. Schaak, Nature Chem., **2012**, *4*, 37-44.
[4] D.A. Robinson and K.J. Stevenson, J. Mater. Chem. A, **2013**, *1*, 13443-13453.
[5] S. Kameoka, S. Wakabayashi, E. Abe and A.P. Tsai, Catal. Lett., **2016**, *146*, 1309-1316.
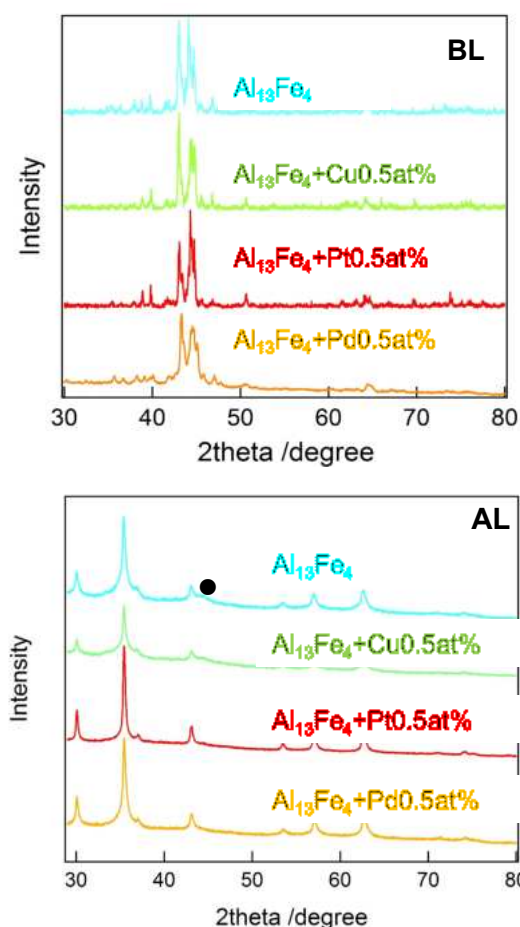
Figure 1. XRD for various AlFe-TM alloys.
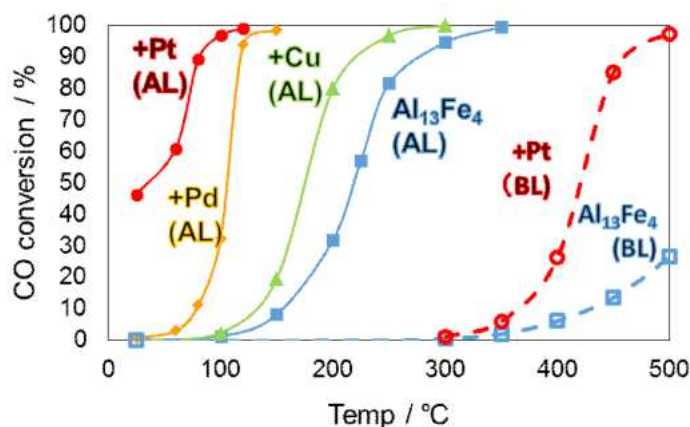
Figure 2. CO conversion of CO-ox over various AlFe-TM

Table 1. Summary of $Al_{76}Fe_{23.5}TM_{0.5}$ (at%) (AL) catalysts.

Sample	as TM/Fe_3O_4	S_{BET}	Al dissolv.
AlFe-TM	(TM wt.%)	(m^2 g^{-1}-cat)	(%)
AlFe	0	35.4	94.8
AlFe-Pt	5.2	41.0	98.8
AlFe-Pd	2.9	44.3	99.2
AlFe-Cu	1.7	49.8	99.2

O–FI 02

Microstructures and crystal structures of Ni-Sn and Cu-Sn intermetallics grown by solid-state diffusion

Andreas Leineweber**,** Philipp Kalanke, Mykhaylo Motylenko, Christian Schimpf, Alexander Walnsch, Constantin Wolf

Institute of Materials Science, TU Bergakademie Freiberg, Gustav-Zeuner-Straße 5, 09599 Freiberg, Germany, andreas.leineweber@iww.tu-freiberg.de, philipp.kalanke@de.bosch.com, schimpf@iww.tu-freiberg.de, alexander.walnsch@iww.tu-freiberg.de, cwolfc@web.de

Introduction

The intermetallics forming upon reaction of tin-based solders with underlying metal substrates play an important role in the reliability of solder joints. Thereby, current research activities are, in particular, driven by the introduction of lead-free solders and the ongoing miniaturization of electronic assemblies [1,2]. While a lot research is devoted to microstructure formation during reflow and solidification, reactive diffusion leading to intermetallics also occurs in the pure solid state, i.e. at temperatures below the solidus temperature of the solder, even at ambient temperature, like with many other systems [3]. The often quite thin reaction zones containing one or several intermetallic phases constitute a special challenge in the course of microstructure characterization and phase identification, in particular, if metastable or highly defective intermetallics are formed at the sub-solidus temperatures.

Materials and Methods

Different Cu and Ni base metal substrates were polished, etched anodically and covered by Sn layers of a thickness of about 5 μm using galvanic electrodeposition at 35°C. For that a commercial electrolyte based on 150 g/l methanesulfonic acid (MSA), 360 g/l MSA tin solution (HS 20) and 100 g/l Niveostan SL (ATOTECH, Berlin, Germany) was employed. After annealing at temperatures $\leq$ 200 °C the microstructure of the reaction zone was investigated by optical microscopy, scanning-electron microscopy (SEM, including electron-backscatter diffraction, EBSD and electron dispersive X-ray spectroscopy, EDX) on cross sections, or, alternatively, in plain view on the intermetallic after removal of the residual Sn using alkaline o-nitrophenole solution at 60 °C. The latter specimens were also investigated by X-ray diffraction in reflection geometry as well as by transmission electron microscopy.

Results and Discussion

Cu substrates covered by Sn were annealed at 50 °C, 100 °C and 200 °C for different times followed by quenching giving rise to a double-layer microstructure consisting from ε-Cu_3Sn and η-Cu_6Sn_5 intermetallic phases (see Figure 1). In line with the literature [4], as shown by X-ray powder diffraction patterns, the η phase is disordered hexagonal if generated at 200°C, whereas it exhibits monoclinic [5] long-range order (η') if generated at 50 °C or 100 °C. Quantitative evaluation of the reflection positions indicates that, although there are 4 independent lattice parameters a, b, c and β for the monoclinic η'-phase structure [5], these four values can be traced back to two independent pseudo-hexagonal lattice parameter a_h and c_h. This is surprising since first-principles calculations indicate that the metric of ordered η'-Cu_6Sn_5 should significantly deviate from the pseudo-hexagonal one [6]. Likely the twin-domain microstructure in Cu_6Sn_5 leads to internal stresses avoiding that the equilibrium lattice parameters are established.

Ni substrates covered by Sn develop after annealing at temperatures from ambient to 120 °C the stable Ni_3Sn_4 phase and metastable $NiSn_4$. The relative fraction of Ni_3Sn_4 increases with increasing annealing temperature; at higher annealing temperatures, the $NiSn_4$ phase is absent. X-ray diffraction analysis on $NiSn_4$ grown at ambient temperature allowed resolving the confusion caused by different structure models present in the literature [7]: the crystal structure consists of quadratic $NiSn_4$ layers stacked in a partially random fashion so that the powder diffraction patterns cannot be

reconciled with any type of perfectly ordered crystal structure. The $NiSn_4$ which had been generated at temperatures of 60°C or above shows additional narrow reflection, which imply formation of a twelve-$NiSn_4$-layer polytype (see Figure 2). Transmission electron microscopy techniques were used to further clarify the stacking order and disorder.

Moreover, the crystal structure data obtained from the phases will be discussed in view of efficient phase identification using EBSD on the corresponding microstructures.
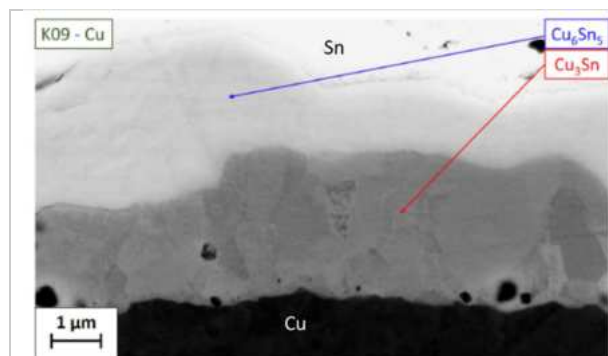
Fig. 1: SEM image (BSE contrast) of a double layer of Cu-Sn intermetallic phases consisting from disordered η-Cu_6Sn_5 and ε-Cu_3Sn which was generated in an Cu-Sn double layer after annealing at 200 °C for 25 h.	Fig. 2: Parts of diffraction patterns (Co-$K_{\alpha 1}$ radiation) from Ni-Sn intermetallic phases ($NiSn_4$ and Ni_3Sn_4) formed in Ni-Sn double layers annealed at the indicated temperatures T for 255 h or 1440 h (room temperature; RT) after removal of the remaining Sn. The diffuse scattering observed after annealing at RT and 40 °C being characteristic for the stacking disorder in $NiSn_4$ [7] is superposed after annealing at 60 °C and 80 °C, respectively, by narrow reflections implying long-period stacking order of the $NiSn_4$ layers.
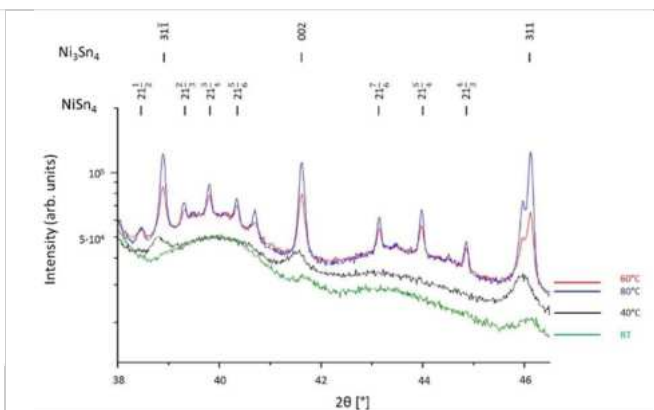
References

[1] K.N. Reeve, J.R. Holaday, S.M. Choquette, I.E. Anderson, C.A. Handwerker, Journal of Phase Equilibria and Diffusion **2016**, *37*, 369-386.

[2] K. Zeng, K. N. Tu, Materials Science and Engineering R **2002**, *38*, 55-105.

[3] V. Simic, Z. Marinkovic, Journal of Materials Science **1998**, *33*, 561-624.

[4] K.N. Tu, Acta Metallurgica **1973**, *21*, 347-354.

[5] A.K. Larson, L. Stenberg, S. Lidin, Acta Crystallographica B **1994**, *50*, 636-643.

[6] S. Ramos de Debiaggi, C. Deluque Toro, G.F. Cabeza, A. Fernández Guillermet, Journal of Alloys and Compounds **2012**, *542*, 280-292.

[7] C. Schimpf, P. Kalanke, S.L. Shang, Z.K. Liu, A. Leineweber, Materials and Design **2016**, *109*, 324-333.

O–FI 03

Size effect on superelasticity in Cu-Al-Ni shape memory intermetallics

J. San Juan[1], J.F. Gómez-Cortés[1], I. López-Ferreño[1], A. Chuvilin[2], J. Hernández-Saz[3], S. Molina[3] and M.L. Nó[4]

[1]Dpt. Fisica Materia Condensada, Facultad de Ciencia y Tecnologia, Universidad del Pais vasco, Aptdo 644, 48080 Bilbao, Spain. jose.sanjuan@ehu.es

[2]CIC nanoGUNE, Tolosa Hiribidea 76, 20018 Donostia-San Sebastian, Spain. a.chuvilin@nanogune.eu

[3]Dpt. Ciencia de los Materiales e I.M., Facultad de Ciencias, Universidad de Cádiz, Campus Río San Pedro, 11510 Puerto Real, Cádiz, Spain. sergio.molina@uca.es

[4]Dpt. Fisica Aplicada II, Facultad de Ciencia y Tecnologia, Universidad del Pais vasco, Aptdo 644, 48080 Bilbao, Spain. maria.no@ehu.es

Introduction

Shape memory alloys (SMAs) are considered as functional intermetallics because of their properties of shape memory and superelasticity associated to a reversible thermoelastic martensitic transformation. At present, SMAs are firm candidates to be incorporated into micro electro-mechanical systems (MEMS), to work as sensors and actuators at small scale. Good properties of superelasticity as well as ultra-high mechanical damping at nano-scale and a very fast response along thousand of cycles have been reported in Cu-Al-Ni SMAs [1-4], whose high temperature phase is a Heusler $L2_1$ intermetallic. However there is a lack of a quantitative characterization of the observed size effects at small scale in SMA, with view to their applications in wearable healthcare and flexible electronic technologies.

The goal of this work I to offer such quantitative characterization and analysis by presenting the evolution of the superelastic behaviour of a series of pillars covering a broad range of size diameters from few hundred of nanometers to some microns.

Materials and Methods

In the present work a Cu-27.6Al-3.6Ni (at%) SMA exhibiting the martensitic transformation below room temperature, Ms=252 K and Af=285 K, has been used to study the superelastic effect at small scale. Single crystals of this alloy were growth on [001] axis direction, from which 2 mm slides were cut and polished for nano-compression tests. Many pillars with diameters ranging from 2 μm down to 260 nm were milled by focused ion beam technique on previous slides. Then, nano-compression tests, following the method described in references [1-3], were performed in a Hysitron TI-950 equipment.

Results and Discussion

An example of the milled nano pillars is presented in Fig. 1 for a pillar of 275 nm in diameter, and in Fig. 2 the stress-strain curve obtained during nano-compression test is presented. In Fig. 2 it has been marked the critical stress for the stress-induced martensitic transformation, taking place during the superelastic effect in SMA. In addition, the line corresponding to the elastic modulus has been plotted. The results obtained on the complete set of pillars show that above approximately 1 μm diameter there is no significant size effect on the critical stress for superelasticity. On the contrary, in the nano-scale range, there is a dramatic increase of the critical stress for the stress-induced martensitic transformation, when decreasing the diameter of the pillar. So, a remarkable size-effect has been found for the critical stress of superelasticity below 1 μm diameter.

The results have been also analyzed in order to find the scaling power law for superelasticity at small scale, following the same criteria used in plasticity at small scale [5]. A surprising power law exponent of $n=2$ (in plasticity n range from 0.3 to 0.8) has been found and an atomic and elastic model for the size effect on superelasticity has been proposed [6]. This model not only predicts an exponent of $n=2$, according the experimental results, but allow a remarkable good fitting of all series of pillars in the complete range of diameters from 2 μm down to 260 nm.

Conclusions

A remarkable size-effect on the critical stress for superelasticity has been found in Cu-Al-Ni SMA pillars below 1 μm diameter. This behaviour has been explained through an atomistic and elastic model of homogeneous nucleation of martensite by shearing of the austenite atomic lattice.
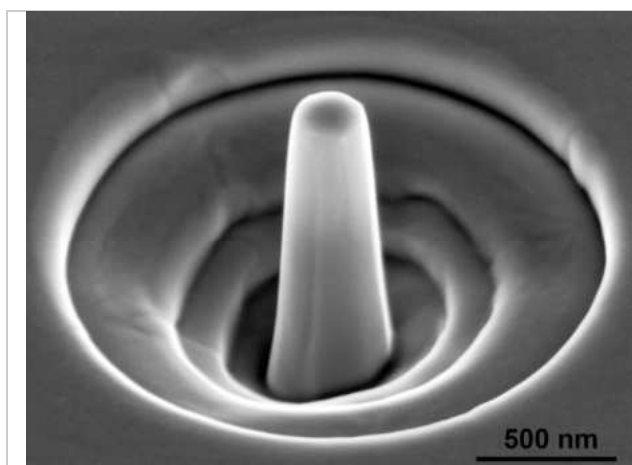
Fig. 1: Nanopillar of 275 nm in diameter milled by FIB on a [001] oriented single-crystal of Cu-A-Ni SMA.	Fig. 2: Nano-compression test on the presented pillar, where the critical stress for superelasticity is indicated, as well as the elastic modulus line.
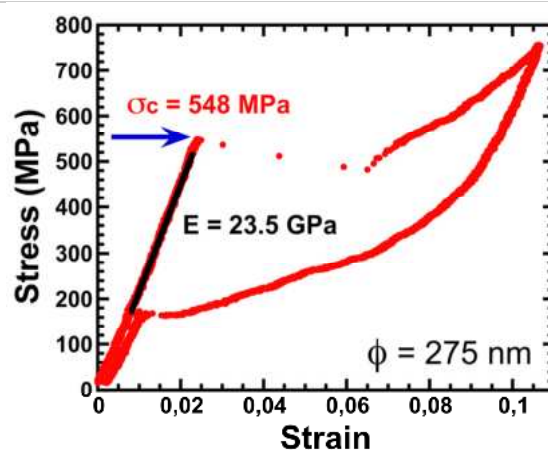
Acknowledgements

References

[1] J. San Juan, M.L. Nó & C.A. Schuh. Superelasticity and shape memory in micro- and nanometer-scale pillars. *Adv. Mater.* **20**, 272-278 (2008).

[2] J. San Juan, M.L. Nó & C.A. Schuh. Nanoscale shape-memory alloys for ultrahigh mechanical damping. *Nature Nanotechnology* **4**, 415-419 (2009).

[3] J. San Juan, M.L. Nó & C.A. Schuh. Superelastic cycling of Cu-Al-Ni shape memory alloy micropillars. *Acta Mater.* **60**, 4093-4106 (2012).

[4] J. San Juan, J.F. Gómez-Cortés, G.A. López, C. Jiao & M.L. Nó. Long-term superelastic cycling at nano-scale in Cu-Al-Ni SMA micropillars. *Appl. Phys. Lett.* **104**, 011901 (2014).

[5] J.R. Greer & J.T.M. De Hosson. Plasticity in small-sized metallic systems: Intrinsic versus extrinsic size effect. *Progress in Materials Science* **56**, 654-724 (2011).

[6] J.F. Gómez-Cortés, M.L. Nó, I. López-Ferreño, J. Hernández-Saz, S.I. Molina, A. Chuvilin & J. San Juan. Size-effect and scaling power-law for superelasticity in Shape memory Alloys at small-scale. *Nature Nanotechnology*, in Press, DOI: nnano.2017.91.

O–FI 04

Alloy design and microstructure of refractory Mo-V-Nb-W-Ti$_x$ HEAs

Georg Hasemann[1], Markus Wilke[2], Thorsten Halle[2], Manja Krüger[1]

[1] Forschungszentrum Jülich, Institute of Energy and Climate Research (IEK-2), Jülich, Germany, g.hasemann@fz-juelich.de; m.krueger@fz-juelich.de

[2] Otto-von-Guericke University Magdeburg, Institute of Materials and Joining Technology, Magdeburg, Germany, markus.wilke@ovhu.de; thorsten.halle@ovgu.de

Introduction

Roughly speaking, HEAs are solid solution alloys containing at least 5 elements in equiatomic or near-equiatomic composition. In the present study we report on an alloy design route for refractory high-entropy alloys (HEAs) based on equimolar Mo-V-Nb alloys with additions of W and Ti. In general, our work was motivated by Senkov et al. [1, 2] who investigated refractory HEAs based on Mo-Nb-W-Ta and Mo-V-Nb-W-Ta and the US Patent published by Bei [3] in which a multi-component solid solution alloy with high mixing entropy, namely Mo-V-Nb-W-Ti, have been mentioned. Senkov et al. investigated their alloys experimentally and showed that they have a single-phase body-centered cubic (bcc) structure. It is assumed that the patented alloy Mo-V-Nb-W-Ti also consists of a single-phase bcc structure. However, no experimental evidence can be found in Bei's patent. We used a systematic alloy design involving four- and five-element compositions to show, that Mo-V-Nb-W-Ti$_x$ is indeed a HEA with a bcc dendritic structure. By carrying out these experiments the Ti-concentration was varied within the composition interval between 5 at.% and 35 at.% defined by Yeh [4] for each principle elements in HEAs.

Materials and Methods

For the alloy design of the present study, three four-element alloys Mo$_{25}$-V$_{25}$-Nb$_{25}$-W$_{25}$, Mo$_{25}$-V$_{25}$-Nb$_{25}$-Ti$_{25}$, Mo$_{30}$-V$_{30}$-Nb$_{30}$-Ti$_{10}$, and two five-element alloys Mo$_{20}$-V$_{20}$-Nb$_{20}$-W$_{20}$-Ti$_{20}$, Mo$_{22.5}$-V$_{22.5}$-Nb$_{22.5}$-W$_{22.5}$-Ti$_{10}$ very chosen for investigation (all concentrations are given in atomic fractions). The alloys were prepared from high-purity metals chips or granules via vacuum arc-melting. Buttons of 5 g were re-melted and flipped five times to ensure good homogeneity. To characterize the as-cast microstructure, the buttons of each alloy were cut and prepared for metallographic examination. After initial grinding, the samples were polished using a 3 mm and a 1 mm diamond suspension, and finally polished with colloidal silica (Struers OP-S). The microstructural observations were carried out using a SEM microscope FEI ESEM XL30 FEG equipped with BSE and EDS detector.

The hardness of the alloys Mo$_{25}$-V$_{25}$-Nb$_{25}$-Ti$_{25}$ and Mo$_{20}$-V$_{20}$-Nb$_{20}$-W$_{20}$-Ti$_{20}$ was tested using a Hysitron TriboIndenter with a Berkovich tip and maximum applied loads of 3000 μN.

Results and Discussion

First experimental results of alloy Mo$_{20}$-V$_{20}$-Nb$_{20}$-W$_{20}$-Ti$_{20}$ are presented in Figure 1. The alloy consists of a dendritic microstructure. The EDS analysis revealed that the elements Mo, Nb and W preferentially segregate to the dendrites, while the inter-dendritic regions are enriched with V and Ti. For comparison, investigations on a four-element alloy Mo$_{25}$-V$_{25}$-Nb$_{25}$-Ti$_{25}$ showed a similar dendritic microstructure where Mo, V and Nb form a mostly short-branched dendritic microstructure, where Ti was also preferentially found in the inter-dendritic regions. Presently the effect of W is under further investigation using Mo$_{25}$-V$_{25}$-Nb$_{25}$-W$_{25}$ and Ti-alloyed materials as described above to find evidence for the strong formation of Ti-rich inter-dendritic areas.

First investigations on the hardness of alloys Mo$_{25}$-V$_{25}$-Nb$_{25}$-Ti$_{25}$ and Mo$_{20}$-V$_{20}$-Nb$_{20}$-W$_{20}$-Ti$_{20}$ revealed values of 5.7 GPa and 7.6 GPa, respectively, which are comparable to those of Senkov et al. [1] for refractory Mo-Nb-W-Ta (4.4 GPa) and Mo-V-Nb-W-Ta (5.2 GPa) HEAs. Consistent with Senkov et al.'s experiments the five-element alloy Mo$_{20}$-V$_{20}$-Nb$_{20}$-W$_{20}$-Ti$_{20}$ exhibits higher hardness values than its four-element counterpart, which can be attributed to the severe lattice distortion effect of HEAs [4].

Fig. 1: Element distribution in the alloy Mo_{20}-V_{20}-Nb_{20}-W_{20}-Ti_{20} in the as-cast condition.
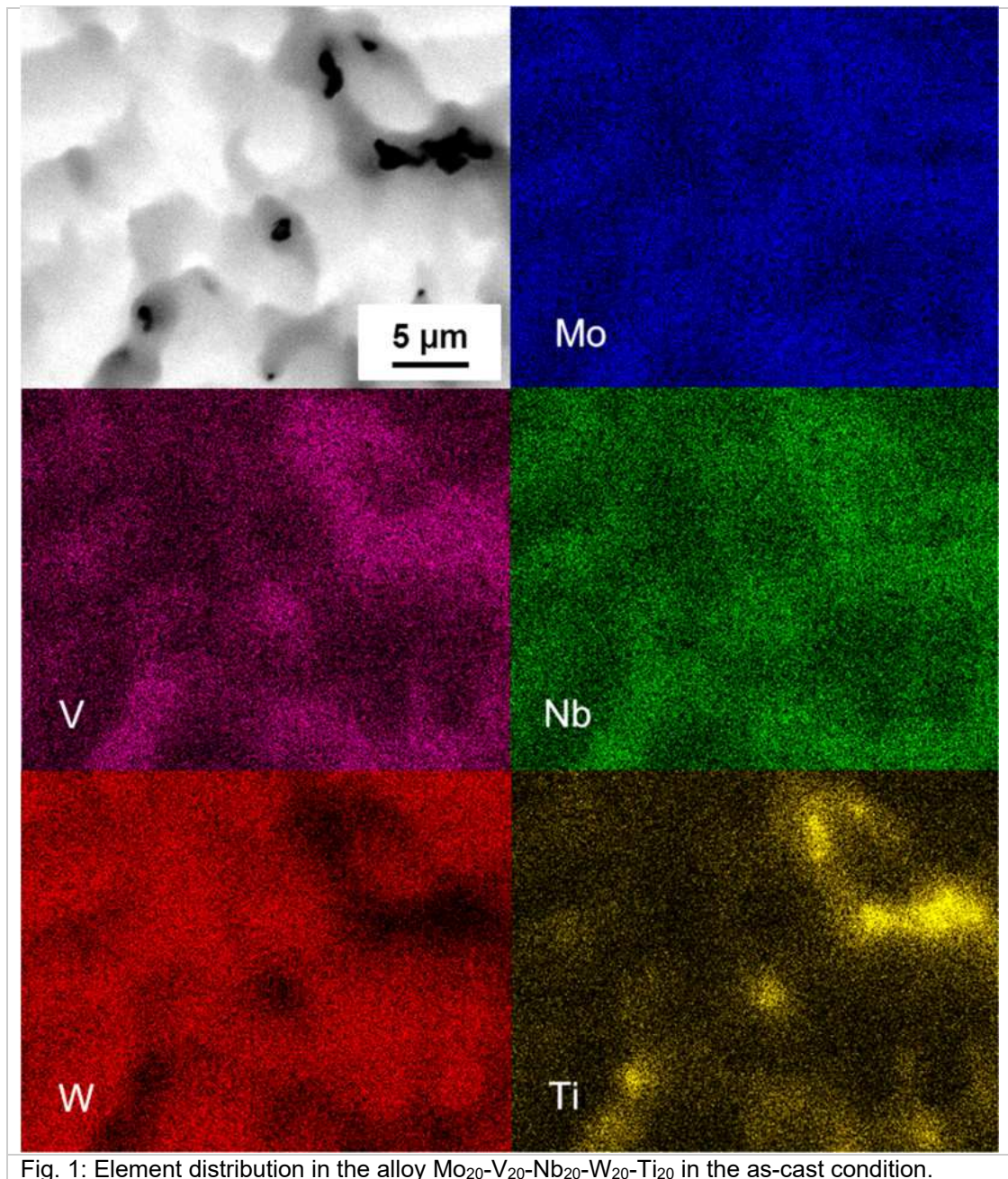
References

[1] O.N. Senkov, G.B. Wilks, D.B. Miracle, C.P. Chuang, P.K. Liaw, Intermetallics. **2010**, *18*, 1758-1765.

[2] O.N. Senkov, G.B. Wilks, J.M. Scott, D.B. Miracle, Intermetallics. **2011**, *19*, 698-706.

[3] H. Bei, US Patent 2013/0108502 A1**. 2013**.

[4] J.W. Yeh, JOM**. 2013**, *65*, 1759-1771.

O–PR 01

Microstructural shaping & viscoplastic behavior of a TiAl alloy obtained by powder metallurgy

P. Serrano[1], L. Toualbi[1], P. Kanouté[1], M. Thomas[1], A. Couret[2]

[1]ONERA DMAS, 29 Avenue de la Division Leclerc, BP 72, 92322 Châtillon cedex, France

[2]CNRS, CEMES (Centre d'Elaboration de Matériaux et d'Etudes Structurales), BP 94347, 29 rue J. Marvig, F-31055 Toulouse, France

Technological advances in aircraft engine design require the use of lightweight materials at increasing high temperatures. It is against this background that studies on intermetallic titanium aluminide alloys based on γ-(TiAl) have been multiplied, leading to their introduction in the most recent civil turbo-engines. These alloys, characterized by their high specific strength and stiffness, turn out to be extremely dependent on the processing and thermal history [1,2]. Hence, for a same composition, diverse microstructures can be achieved leading to scatter mechanical properties. The aim of this study is to link directly the macroscopic viscoplastic behavior to the microstructure, and thus optimize the processing route for a specific need. To this end, several microstructures are chosen to be characterized and tested. Those mechanical tests are used to identify parameters of a multi-scale model.

The material used is the G4 alloy (Ti-47Al-1Re-1W-0.2Si at%) obtained by powder metallurgy and hot isostatic pressing [3, 4]. The powder is produced by argon gas atomization from ingots originally casted at Howmet Casting facilities. All microstructures are characterized with a scanning electron microscope using back scattered electron imaging to measure phase fraction, grain size and lamellar spacing when possible. An optical microscope is also used to quantify thermally induced porosity and grain size.

Three distinct microstructural states, near-γ, duplex and lamellar, are investigated to observe the impact of microstructural parameters. For each state, one microstructure is chosen as reference. Then, specific thermal treatments are chosen to create other microstructures (of the same state), in which only one microstructural parameter differs. Thereby, those parameter impacts on mechanical properties are clearly exposed. For near-γ and duplex states, we study respectively the impact of phase fraction γ/β_0 and $\gamma/(\alpha_2 + \gamma)$, whereas for the lamellar state, we study the impact of lamellar spacing and grain size.

The near-γ microstructures are mostly composed by γ globular grains, but also by α_2 and β_0 grains. The duplex microstructures contain γ globular grains and $(\alpha_2 + \gamma)$ lamellar grains, surrounded by a γ matrix in which β_0 precipitates are observed. Finally, in the lamellar microstructures, lamellar grains have the largest volume fraction but are still surrounded by a $(\gamma + \beta_0)$ matrix. Those results are compared to recent works on the so-called IRIS alloy (Ti-48Al-2W-0.08B at%) elaborated by Spark Plasma Sintering, where a similar $(\gamma + \beta_0)$ matrix is observed [5, 6].

A test campaign is then performed to investigate the viscoplastic behavior of each microstructure. The reference temperature is 750°C, i.e. above the ductile to brittle transition temperature (DBTT). This campaign includes room temperature tensile tests, relaxation after tensile tests at two strain rates, multilevel cyclic tests at three successive strain rates and cyclic tests involving hold periods. Microstructural parameter's influence on classic mechanical properties like yield stress, elongation or ultimate tensile stress is discussed. Especially, strain rate sensitivity is shown to be strongly dependent to the microstructural state. Observations made on the $(\gamma + \beta_0)$ matrix role over the deformation by Voisin et al. are thus confirmed [6]. Fig. 1 shows the results of the tensile tests at two strain rates performed on four microstructures.

Finally, a numerical analysis is performed with the so-called three-scale model developed at ONERA [7]. This model, specifically developed for TiAl alloys, takes into account the microstructure, i.e. the deformation mechanisms, to represent the macroscopic behavior. The first scale transition between

the macroscopic length scale and the scale of an individual grain (α_2, γ, lamellar) is made using elastically self-consistent transformation field analysis with anisotropic elasticity. The second transition between the lamellar grain and the lamellae is derived from a system of linear equations for a multilayer. The constitutive equations of the α_2 and γ phase are obtained through the framework of crystal plasticity. The different hypothesis and transitions are resumed in Fig. 2 and detailed in [7]. This model is compared to the two-scale model developed by Cornec et al. which uses periodic unit cells and a multilevel finite element method (FE²) [8]. Those multi-scale models imply a large amount of parameters to identify (at least eighteen for lamellar grains). Therefore, the methodology developed in [8] and the results obtained are used to simplify greatly the identification process.

Lastly, with the model calibrated on our reference microstructures, numerical experiments are made to check our approach consistence. By varying numerical microstructural parameters accordingly to our comparison microstructure for each state, the viscoplastic behavior observed during the test campaign is reproduced.
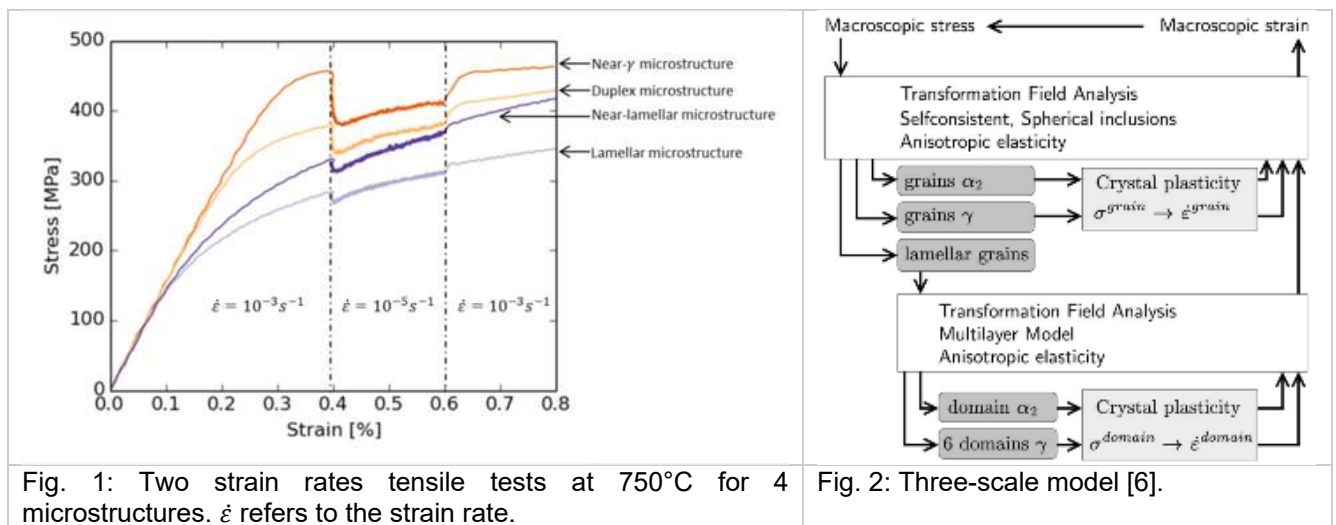
Fig. 1: Two strain rates tensile tests at 750°C for 4 microstructures. $\dot{\varepsilon}$ refers to the strain rate.

Fig. 2: Three-scale model [6].

References

[1] F. Appel, Encyclopedia of Aerospace Engineering, 2010, John Wiley & Sons, Ltd.

[2] M. Thomas, Techniques de l'Ingénieur, 2011.

[3] S. Naka, M. Thomas, T. Khan, A. Bachelier-Locq : 'Alliage Intermétallique à base d'Aluminiure de Titane pour la Fonderie', Brevet France N°95 03 511 du 24/03/1995, N°publication 2 732 038 (6 Juin 1997). US Patent N° 5,846,345 8/12/1998.

[4] M. Grange, J.-L. Raviart, M. Thomas, Met Mater Trans A, 2004;35A:2087.

[5] T. Voisin, J.-P. Monchoux, M. Perrut, A. Couret, Intermetallics 71 (2016) 88-97.

[6] T. Voisin, J.-P. Monchoux, M. Thomas, C. Deshayes, A. Couret, Metallurgical and Materials Transactions A, 2016, 10.1007/s11661-016-3801-3.

[7] A. Roos, J.-L. Chaboche, L. Gélébart, J. Crépin, International Journal of Plasticity 20, 2004, 811-830.

[8] A. Cornec, M.R. Kabir, N. Huber, Materials Science & Engineering A 620, 2015, 273-285.

O–PR 02

Structural and phase transformations occurring during fabrication of TiAl-based composite reinforced by TiB$_2$ particles

Daria Lazurenko[1], Vyacheslav Mali[2], Andreas Stark[3], Maksim Esikov[4], Adelya Kashimbetova[5], Florian Pyczak[6]

[1]630073, Russia, Novosibirsk, Karl Marks str. 20, pavlyukova_87@mail.ru

[2]630090, Russia, Novosibirsk, Lavrentiev av. 15, vmali@mail.ru

[3]21502, Germany, Geesthacht, Max Plank Str. 1, andreas.stark@hzg.de

[4]630090, Russia, Novosibirsk, Lavrentiev av. 15, esmax@ya.ru

[5]630073, Russia, Novosibirsk, Karl Marks str. 20, k.yaleda@mail.ru

[6]21502, Germany, Geesthacht, Max Plank Str. 1, florian.pyczak@hzg.de

Introduction

The development of new materials for the energy-conversion aircraft systems remains an important topic over the last decades. TiAl-based alloys are widely recognized to have the potential to meet the design requirements (higher service temperatures, lower weight, and higher operational speeds) of gas-turbine engines. They possess outstanding physical, chemical, and mechanical properties such as high melting point, high strength and stiffness, good structural stability, good oxidation, and corrosion resistance in combination with low density. To improve properties of titanium aluminides, e.g. creep resistance, plasticity, fracture toughness, the addition of different alloying elements is a typical approach [1]. In this study, we consider an alternative possibility to improve the properties of titanium aluminides by fabrication of TiAl-based multilayer composites reinforced by ceramic particles. The efficiency of formation of multilayer materials has been shown in studies of Vecchio and our previous research [2, 3]. For instance, fracture toughness and fatigue properties of lamellar structures is higher compared to bulk materials due to the positive influence of interfaces which induce deflection and blunting of cracks. Moreover, the combination of dissimilar layers with strongly distinguished properties can provide a unique combination of mechanical properties. Introduction of stiff and hard layers can promote higher strength and stiffness in particular directions. The aim of this paper is the investigation of structural and phase transformations and the study of the formation processes of multilayer materials consisting of TiAl and TiB$_2$ layers.

Materials and Methods

The samples were produced in Lavrentyev Institute of Hydrodynamics (SB RAS, Novosibirsk) using a Labox 1575 spark plasma sintering machine. Before sintering, workpieces consisting of titanium, aluminum and TiB$_2$ layers were packed in titanium shells to prevent leakage of aluminum during heating. The procedure of workpiece preparation was described elsewhere [3]. Samples were sintered in two stages. In the first stage, they were heated up to 830 °C and held at this temperature for 10 minutes. Then the temperature was increased to 1250 °C and samples were sintered at this temperature for 2 minutes. The pressure varied from 40 MPa at 830 °C to 10 MPa at the maximum temperature.
The structure of materials after both stages of sintering was investigated at Helmholtz Zentrum Geesthacht (HZG), Germany, using scanning electron microscopy (SEM) equipped with energy dispersive X-ray (EDX) and transmission electron microscopy (TEM). Phase transformations were studied at the HZG run beamlines at the Deutsches Elektronen-Synchrotron (DESY) in Hamburg, Germany.

Results and Discussion

Initially workpieces consisting of Ti and Al foils with a thickness of 50 µm were stacked alternately as shown in Fig. 1. TiB$_2$ powder was homogeneously distributed on every second layer. Sintering at 830 °C led to an interaction between Al and Ti and the formation of an Al$_3$Ti compound. At this stage,

Al was expended for the formation of an Al-rich intermetallic phase. At the borders between Ti and Al_3Ti thin interlayers were observed. It was published previously [3] that these interlayers consisted of intermediate phases: Ti_3Al, TiAl and Al_2Ti. It was expected that a γ-TiAl-based alloy would form when the reaction proceeded longer or at a higher temperature. Structural investigations of a sample which has been held at 1250 °C for 2 minutes approved this assumption. SEM and TEM investigations revealed the formation of a lamellar structure of intermetallic layers. They consisted of γ-TiAl and $α_2$-Ti_3Al phases.
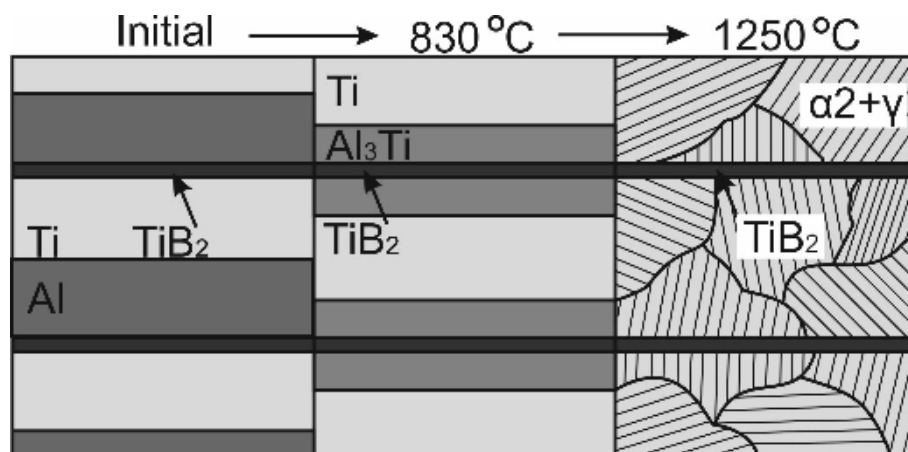
Fig. 1. Scheme of the reactions occurring during formation of the TiAl-TiB_2 multilayer composite.

TiB_2 particles were recrystallized during a high-temperature sintering process which was proved by modification of their shape; it transformed from equiaxed to elongated (Fig. 2). However, no reaction between intermetallic phases and the reinforcing material was observed. TEM studies showed that ceramic particles were distributed in the intermetallic matrix and formed a dense layer consisting mainly of TiB_2 and a small quantity of TiAl and Ti_3Al.
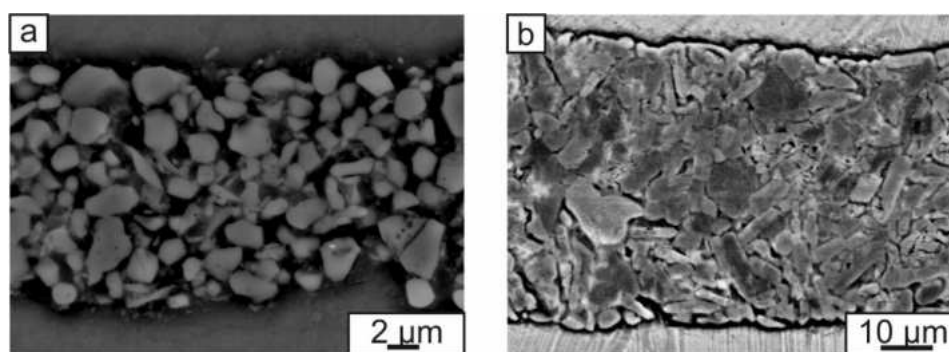
Fig. 2. Transformation of the reinforcing particle structure during sintering at: a – 830 °C; b – 1250 °C.

References

[1] F. Appel, J. D. H. Paul, M. Oehring: Gamma Titanium Aluminide Alloys: Science and Technology. Wiley-VCH Verlag GmbH & Co. KGaA, **2011**, 465-478.

[2] K. S. Vecchio, JOM. Journal of the minerals, metals and materials society. **2005**, *57 (3)*, 25–31.

[3] D.V. Lazurenko, V. I. Mali, I. A. Bataev, A. Thoemmes, A. A. Bataev, A. I. Popelukh, A. G. Anisimov, N. S. Belousova, Metallurgical and Materials Transactions A, **2015**, *46 (9)*, 4326-4334.

Acknowledgement

O–PR 03

Features of complex technology (PREP + HIP) for obtaining intermetallic alloys

A.I. Logacheva, M.S. Gusakov, I.A. Logachev, Zh.A. Sentyurina

OJSC «Kompozit», 141076, Russian Federation, Korolev, Pionerskaya St. 4
info@kompozit-mv.ru

Introduction

We discuss the experience of production of intermetallic alloys of the Ni-Al-Cr system by Plasma Rotating Electrode Process (PREP) and Hot Isostatic Pressing HIP. The complex technology PREP + HIP allows to form a different kind of microstructure, including fine grains. This is very important for intermetallic alloys which tend to embrittlement at room temperature. The paper shows the choice of parameters for PREP process, which avoid contamination of the powder with impurities during atomization and allow to get intermetallic granules, which have predominantly a spherical shape, and less than 100 μm granulometric size. The problem of selecting parameters for HIP process for preserving a small-grained, defect-free structure in a compact state is also considered. Based on the study of the mechanical properties of the intermetallic alloys and calculated data of the diffusion path of vacancies in the alloys, the optimum values of the temperature and pressure of HIP process were received. In conclusion, data on the microstructure, mechanical and functional characteristics of the granular alloy based on the Ni-Al-Cr system are presented.

Materials and Methods

The composition of the alloy was 40 at. % Ni, 40 at. % Al, 20 at. % Cr. The initial ingots for the PREP process were manufactured by the VIM + VAR method. Atomization (PREP) was carried out at the upgraded equipment - PREP-9I (OJSC «Electromechanica», OJSC Komposite, Russia). The HIP process was carried out in an ABRA equipment (Sweden).

The granulometric appearance of the powder was investigated by laser diffraction (Analysette 22, Fritsch GmbH). The phase composition was determined by X-ray diffraction analysis on a DRON-3 setup (Russia) using Co-Kα radiation at $2\theta = 10\text{-}140°$. The microstructure of the experimental samples was studied with optical microscopy (OM) using an Axiovert 200 MAT/M inverted metallographic microscope and with scanning electron microscopy (SEM) on a Hitachi S-3400N microscope equipped with an energy dispersive X-ray spectrometer NORAN. Mechanical tests of experimental samples were carried out using the universal testing machine Schenk-Trebel RMC-100.

Results and Discussion

We used granules with granulometric size distribution from 40 to 100 μm, obtained by the PREP method at an electrode rotation speed of 20,000 rpm. Granules are characterized by a spherical shape, a low level of gas porosity and the absence of satellites (Figure 1) and have a fine-grained dendritic structure with a uniform distribution of all alloying components.

To optimize the mechanical properties of the intermetallic alloy, it is very important to avoid grain growth during the HIP process. When selecting the parameters for HIP process, we used handling based on the fact that it is necessary to keep the pressure value at a preset temperature not higher than the level $\sigma_{0.02}$(0.02 proof stress) of the corresponding material. At the same time, the maximum conditions for the vacancy diffusion mechanism must be created. Based on the results of

experimental studies, the role of our assumptions in the formation of the small-grained structure of the intermetallic alloy was evaluated.

Based on the data on the mechanical properties of the intermetallic Ni-Al-Cr system, a series of HIP experiments were performed with varying pressure and temperature. Based on the results two-stage HIP mode parameters were proposed: the first stage realizes the mechanism of plastic deformation and is characterized by short duration. The second stage, in which the vacancy diffusion mechanism is realized to a greater extent, is carried out at a pressure not higher than $\sigma_{0.02}$ at a given temperature and with a duration of at least 3 hours. At all stages of compaction, the microstructure of the alloy was monitored.

This approach to the HIP process made possible to obtain compact samples with a relative density of 99.9% and an average grain size of 40 μm. The compacts have a uniform microstructure (Figure 2), in which three basic structural components can be identified: an intermetallic matrix of NiAl with dissolved chromium (amount of 7-9% at); fine precipitates based on α-Cr and intergranular Ni-Cr interlayers (the ratio Ni / Cr ~ 2/1).
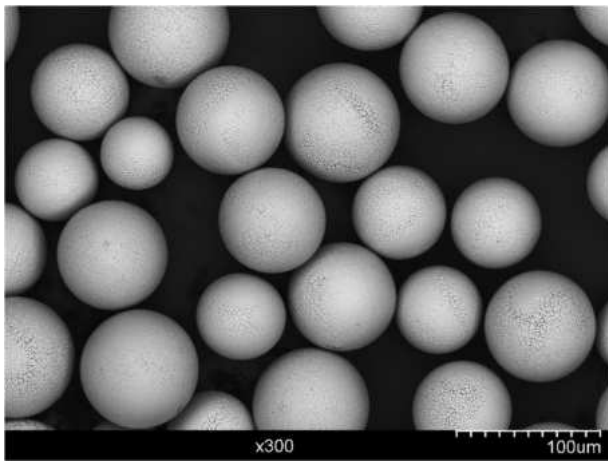
Fig. 1: Morphology of the initial granules from the Ni-Al-Cr system alloy
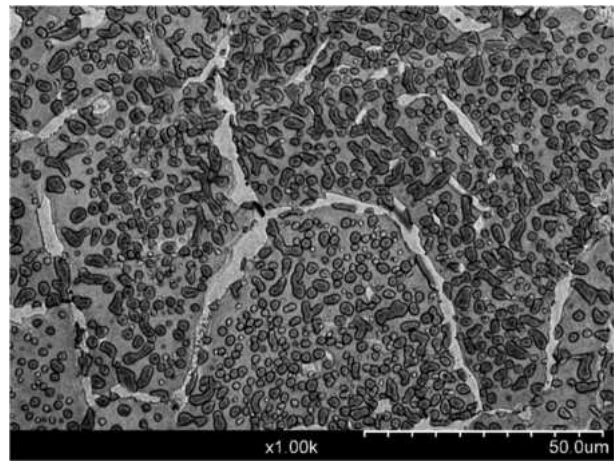
Fig. 2: Microstructure of the Ni-Al-Cr system alloy obtained by HIP pellets

The formation of a small-grained microstructure of intermetallic Ni-Al-Cr system provides a growth of mechanical and functional high temperature properties compared to cast samples. The properties of this alloy at room temperature, as well as in the range of 800-1400 °C, are also studied in the paper.

O–PR 04

Development of a reliable hybrid joining between steel and aluminum

Xiangfan Fang

Institute of Automotive Lightweight Design, University of Siegen, Germany
Breite Strasse 11, D-57076 Siegen, Germany
email: xiangfan.fang@uni-siegen.de

Introduction

Hybrid casting is a well known technology to join steel and Aluminum. It has been applied in the production of non-structural parts of automotive such as engines or transmissions, when steel inserts are embedded into Al-cast to enhance the friction resistance. The joining is based on force and form locking connections. Since the material based connection is very brittle, no structural application in body or chassis could be realized up to now [1-2]. In order to enable a better and ductile material connection between steel and Al, a new metal coating has been now developed [3] based on the recent development of intermetallic alloys/phases (IMP) and surface coatings of Fe-Al-X-systems [4-7].

According to [4] and other works before, the formation of Fe-Al-Intermetallic phases is determined by their kinetics rather than thermodynamics. The very brittle Al-rich phases such as orthorhombic $\eta - Al_5Fe_2$, or monoclinic $\theta - Al_3Fe$ phases can be built faster than the cubic $\alpha_c - AlFe$ phase. During a inter-diffusion test between steel and pure Al or Al alloy with 5 % Si, a very complex phase building process has been observed. The IMPs formed hereby are all brittle phases with low crystal symmetry.

Hybrid casting tests using uncoated steel and different Al alloys were all unsuccessful. Zn coated steel may sometimes enable a material based joining between steel and Al. However, the joinings are instable, inhomogeneous and their strength scatters in a large range.

Since different alloy elements may increase the ductility of Fe-Al IMPs as described in [7], the idea of this work was to use alloy coatings to improve the ductility of the inter-diffusion layer between steel and Al. One of the possible element is Si, which has been already applied in industrial AlSi coatings and investigated in [5,6]. Welding experiments with AlSi5 filler materials also showed some positive results [2]. Another issue is the fact, that reducing the thickness of the IMPs may also increase its ductility. Since Si may reduce the IMP thicknesses in any case [6], it should be considered in this work.

Materials and Methods

Based on these findings of the state of the art, a coating system consisting Al and Si should be developed which can be applied on steel substrate in order to obtain a thin ductile intermetallic layer to join steel parts with Al during the hybrid casting process. By the formation of this kind of material joining with a ductile layer property, the joining properties in such hybrid casted parts should be improved.

In addition of the industrial Al-Si-coating a new PVD Al-Si coating has been investigated in this work. In comparison to the existing coatings, this coating consists of two sub-layers: a first thin 1-3 μm layer consisting of 40-45 wt. % Fe, 45 wt. % Al and 12 wt. % Si. The IMP of this first layer can thus be approximately written as $Al_{57}Fe_{27}Si_{15}$ and according to the Fe-Al-Si phase diagram [5] it should have a ordered cubic crystal structure of type α_2 and some orthorhombic $\eta - Fe_2Al_5$. The thickness of 1-3 μm is also small in comparison to the industrial coating of > 5 μm. Above this thin layer a second thicker layer of approx. 20 μm is applied (Fig. 1).

In order to create this type of coating on a DC04 steel, a high energy PVD coating process (7000 W and 4h time) was selected.

An AlSi9MgMn alloy was used for the high pressure die casting process, when a steel shear tensile sample (DC04 with PVD and 22MnB5 steel with industrial AlSi coating as well as CPW1000 steel with EG coating) was hybrid casted by Al. The investigated casting conditions can be found in [3].

Results and Discussion

Using the industrial AlSi coating no material based joining could be achieved for any casting conditions. For EG Zn coated steels a very strong material connection could be obtained when certain casting conditions were used. However, the shear strength of this type of materials scatters in a large range of 14-18 MPa and the fracture surface is clearly brittle. SEM investigations shows an Al-Zn mixture in some areas of the sample of the fracture surface, while in other areas Fe-Al connections could be detected. Since Al-Zn mixture is a brittle material, the lack of the ductility of this kind of joining may be explained.

When the new PVD coating was used for hybrid casting, a strong ductile material based joining could be generated. Aside from a shear strength of more than 11 MPa, which is comparable with the lower limit values of the automotive structure adhesives, the ductility of the connection is high. This can be revealed by the shear force-displacement curves in Fig. 2. After reaching a certain force level, the shear force remains almost constant for a certain time. This implicates a plastic deformation within the joining layer between steel and Al. This assumption can be confirmed by the SEM micro structural analysis on fractured shear samples. The fracture surface shows a honeycomb structure almost everywhere.

Further analysis shows that well controlled casting die and process parameters must be used to enable the steel-Al inter-diffusion on one side and restrict this diffusion in an appropriate range in the other side. The possible failure mechanism in the new layer of material joining was discussed as well.
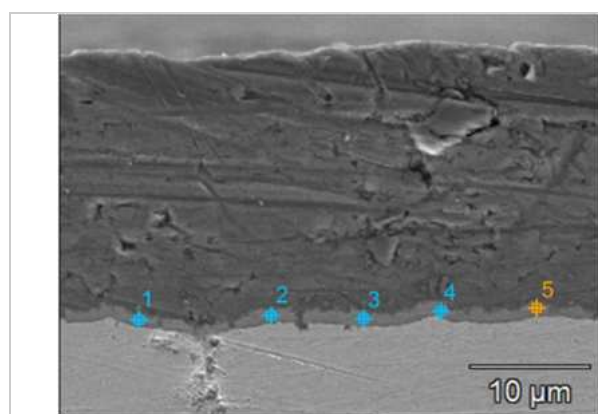
Fig. 1: The new PVD Al-Si coating with two sub-layers	Fig. 2: Shear force and displacement curve of a PVD Al-Si coated steel in hybrid casted shear samples
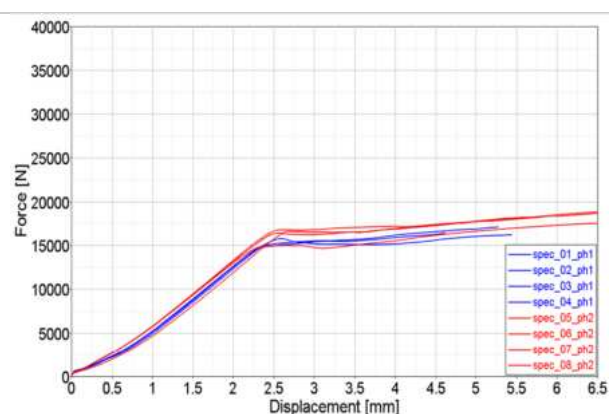
References

[1] T. Watkins, D. Erdman, P. Joshi, G. Ludtka, B. Murphy, A. Sabau, H. Yin, W. Zhang, T. Skszek, X. Niu, "DOE Vehicle Technologies Annual Merit Review and Peer Evaluation meeting", **2013**

[2] L. Jacome, S. Weber, E. Leitner, E. Arenholz, J. Bruckner, H. Hackl, A. Pyzalla, Advanced Engineering Materials 11 (5), **2009,** 350-358.

[3] X.F. Fang: accepted by Journal of Material Science and Engineering, 2017.

[4] H. Springer, A. Kostka, E.J. Payton, D. Raabe, A. Kaysser-Pyzalla, G. Eggeler, Acta Materialia 59, **2010,** 1586-1660.

[5] M. Suehiro, K. Kusumi, T. Miyakoshi, J. Maki, M. Ohgami, Nippon Steel Report No. 88. **2003**.

[6] R.W. Richards, R.D. Jones, P.D. Clements, H. Clarke, International Materials Reviews 39 (5) **1994**, 191-212.

[7] D.J. Alexander, P.J. Maziasz, J.L. Wright, Material Science and Engineering A 258 (1-2), **1998**, 276-284.

O–PR 05

Additive manufacturing of iron aluminide alloys

Alena Michalcová[1], Lucia Senčekova[1], Gesa Rolink[2], Andreas Weisheit[2], Josef Pešička[3], Martin Palm[1]

[1] Max-Planck-Institut für Eisenforschung GmbH, D-40237 Düsseldorf, Germany; palm@mpie.de

[2] Fraunhofer Institute for Laser Technology ILT, Steinbachstr. 15, D-52074 Aachen, Germany

[3] Department of Physics of Materials, Faculty of Mathematics and Physics, Charles University Prague, Ke Karlovu 5, 121 16 Prague 2, Czech Republic

Introduction

Additive Manufacturing (AM) is a near-net-shape processing technology. It is specifically well-suited for the production of parts from intermetallic alloys, which may be expensive to machine as they have a high hardness and wear resistance. In case of iron aluminides the high cooling rates associated with AM should also yield a fine-grained microstructure, which possibly could enhance ductility [1]. The aim of this study was to check whether iron aluminide alloys can be processed by AM and if concepts developed for strengthening of cast Fe–Al alloys are also effective for AM processed alloys.

Materials and Methods

Gas atomized powders of a binary Fe–Al alloy and three Fe–Al–Ti(–B) alloys were processed by Selective Laser Melting (SLM) and by Laser Metal Deposition (LMD) [2, 3]. Reference alloys of the same compositions were produced by induction melting and casting into cold copper molds. Initial powders and produced samples were examined by light optical and scanning electron microscopy (LOM, SEM). Images in the SEM were taken in electron backscatter diffraction (EBSD) mode. Compositions of individual phases and homogeneity of the samples were established by wavelength-dispersive spectrometry (WDS) on an electron probe microanalyzer (EPMA). Fine precipitates were identified by transmission electron microscopy (TEM). X-ray diffraction (XRD) was employed to determine the structures and lattice constants of phases as well as for the determination of residual stresses. Tensile and compressive yield stress and 4-point bending tests were carried out on a universal testing machine. The creep behavior in air at 600 and 700 °C was established in compression by stepwise increasing the load.

Results and Discussion

By adjusting the process parameters, it was possible to produce defect-free samples from all alloys. However, preheating was necessary for all alloys, 200 °C (LMD) or 600 °C (SLM) in case of binary Fe–Al and 400–700 °C (LMD) or 600–800 °C (SLM) for Fe–Al–Ti(–B) [2, 3].
The microstructure of the binary Fe–28Al alloy (in at.%) consisted of large grains (mm) which were elongated in growth direction [2]. EBSD showed that grains grew preferentially in [001] direction, i.e. the direction of the highest heat flow in α-Fe,Al (A2). The grain size decreased with increasing preheating temperature, i.e. with decreasing temperature gradient. Individual grains showed a continuous change in the crystallographic orientation of up to 20° between bottom and top of the grain. These misorientations developed during cooling between the built up of the next layer. TEM revealed very high dislocation densities of 2.0×10^{13} m^{-2} (LMD) and 2.2–3.5×10^{14} m^{-2} (LMD), which are one respectively two magnitudes higher than in the as-cast alloy (3.8×10^{12} m^{-2}). The higher dislocation density after SLM correlates with the higher cooling rate compared to LMD.
At 700 °C no marked difference in the compressive yield strength between SLM and LMD samples was observed [2]. Also no difference was observed between the yield strength of the AM samples and a rolled alloy of about the same Al content [4]. The LMD samples show an improved ductility compared to SLM and as-cast samples [5]. Apparently, the strong crystallographic texture and high dislocation density have no influence on ductility. Local stress measurements by XRD showed that in general the stresses are higher in the – faster cooled – SLM samples than in the LMD samples.

However the XRD measurements yield no explanation why the LMD samples show an improved ductility compared to the as-cast alloy of the same Al content.
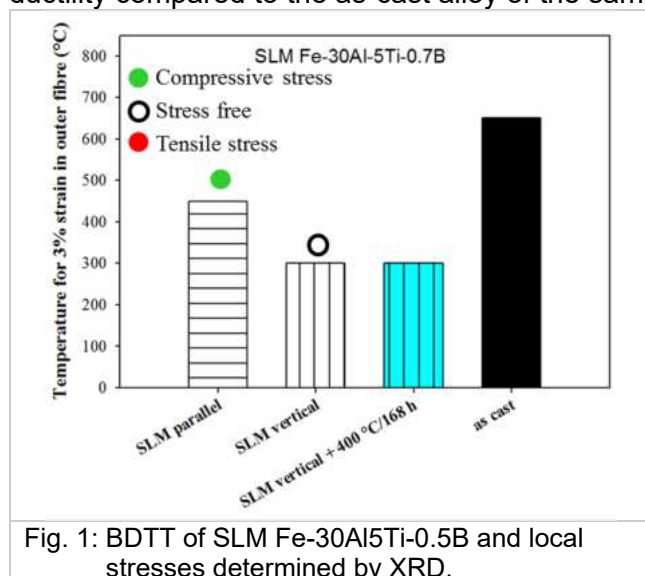
Fig. 1: BDTT of SLM Fe-30Al5Ti-0.5B and local stresses determined by XRD.	Fig. 2: BDTT of LMD Fe-30Al5Ti-0.5B and local stresses determined by XRD.
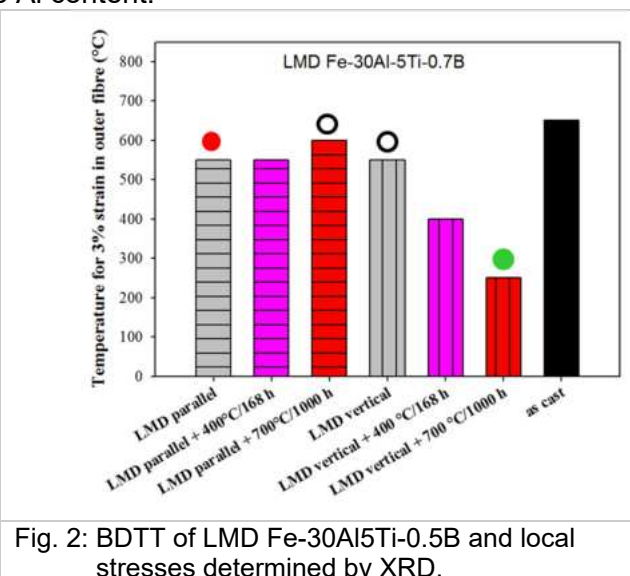
The microstructure of Fe-30Al5Ti-0.5B after SLM or LMD consists of equiaxed Fe–Al grains (< 5 μm) and TiB$_2$ precipitates (50 nm) in the Fe–Al grains and at grain boundaries, which is about the same microstructure as in the as cast condition. The grains show no preferred orientation and no changes of the crystallographic orientation within individual grains are observed [3]. No difference in the compressive and tensile yield strength and the creep resistance is observed between SLM, LMD or as cast samples. However, there are again marked differences in ductility (Fig. 1, 2). Such differences are observed if samples are tested parallel or vertical to the build direction (Fig.1) or after a certain heat treatment (Fig. 2). Local stress measurements by XRD again revealed quite different stress states in various samples, though no relation between stresses and ductility is apparent (Fig. 1, 2).

The microstructure of the single-phase L2$_1$-ordered alloy Fe–30Al–10Ti is below 5 μm in the SLM and LMD samples, which is substantially lower than in the as-cast alloy (> 100 μm) [3]. Despite this substantial reduction of the grain size, the ductility of the SLM and LMD samples did not improve.

TEM of Fe–22Al–5Ti revealed that the alloy had a coherent L2$_1$ + A2 microstructure with a particle size of 30 nm after SLM, which is comparable to the as cast microstructure. Marked differences in the compressive yield strength exist whether SLM samples are tested horizontal or vertical to the building direction. These differences may be due to different size and distance of the precipitates and the crystallographic mismatch between them, which may result in varying coherency stresses between matrix and precipitates [3].

Acknowledgement

References

[1]   D.G. Morris, M.A. Morris-Munoz: Intermetallics. **1999**, *7*, 1121–1129.

[2]   G. Rolink et al.: Journal of Materials Research. **2014**, *29*, 2036–2043.

[3]   A. Michalcová et al.: Materials and Design. **2017**, *116*, 481–494.

[4]   C.G. McKamey et al.: "Development of Iron Aluminides for Coal Conversion Systems". **1988**. *ORNL Report 10793*, 1-55.

[5] D. Risanti et al.: Intermetallics **2005**.*13*, 1337–1342.

O–PR 06

Processing of iron aluminides using selective electron beam melting

Lucas Adler[1], Fuad Osmanlic[1] and Carolin Körner[2]

[1]FAU, ZMP Dr. Mack-Straße 81, 90762 Fürth, Germany, lucas.adler@fau.de

[2]FAU, WTM, Martensstraße 5, 91058 Erlangen, Germany, carolin.koerner@fau.de

Introduction

Iron aluminides are investigated since the early 1930s as promising high temperature material for demanding environments [1]. This is mainly due to their high resistance to oxidation and sulfidation in combination with the low prices of the constituents [2]. Since technical alloys on the basis of Fe_3Al iron aluminides still show high brittle to ductile transition temperatures (BDTT) combined with a high hardness, subtractive manufacturing routes are not applicable [3, 4, 5]. A near net shape processing route which can process iron aluminide is provided by laser based additive manufacturing (AM) [6, 7]. In this contribution AM processing by selective electron beam melting (SEBM) of the binary Fe_3Al as well as the technical more relevant alloy Fe28Al5Ti1.3B [at.%] is investigated. The feasibility to process iron aluminides via SEBM is shown via processing windows for the production of dense specimens. Furthermore, the influence of processing parameters on microstructure and Al-evaporation are discussed. Eventually, mechanical and high temperature properties are presented and compared to those of comparable laser based AM-studies.

Materials and Methods

The used iron aluminide alloy has a composition of Fe28Al5Ti1.3B and is used in powder form with a particle size distribution form 45 µm to 106 µm with a mean particle diameter of 70 µm. The powder was processed on an Arcam A2X SEBM machine. For evaluation of the relative density microsections were analyzed via light optical microscopy. The resulting microstructure of SEBM built iron aluminides is examined regarding the grain size via light optical microscopy and regarding the involved phase via electron microscopy and XRD measurements. The Al-content is measured via electron dispersive spectroscopy and electron microprobe examination. For mechanical and high temperature properties compression tests are conducted over a temperature range from room temperature to 900 °C. Furthermore creep tests at 700 °C and 800 °C under varying stresses were carried out. The oxidative properties of iron aluminides processed by SEBM are evaluated using static oxidation testing in synthetic air under 800 °C and 900 °C for up to 50 h.

Results and Discussion

Light optical examination of the prepared microsections shows that the processing route of SEBM is capable of producing iron aluminides without any problems regarding the formation of cracks during fabrication. Since the building temperature of 1050 °C exceeds the BDTT the absence of cracks is not surprising. The evaluation of the relative density revealed a broad processing window for dense specimens with a relative density higher than 99,5 %, which is shown exemplary for the alloy Fe28Al5Ti1.3B for a line offset of 100 µm in Figure 1. The resulting microstructure of a specimen built with a deflection speed of the electron beam of 4000 mm/s and an area energy for melting of 1.4 J/mm² is depicted in Figure 2. The SEM image shows globular grains with a mean size of 5 µm-10 µm. XRD-analysis showed that this Fe-Al matrix is $L2_1$ ordered, also depicted in Figure 2. At the grain boundaries needle like precipitations can been seen in Figure 2. The elemental distribution within and around these precipitations strongly suggests TiB_2 as precipitated phase. Hereby, TiB_2 pins the grain boundaries and prevents significant ripening at these high building temperatures, Figure 3. First tests show compression strengths comparable to laser based AM-studies [6], see Figure 4. From the gathered results it becomes clear that SEBM is a suitable route for processing intermetallic iron aluminide alloys.
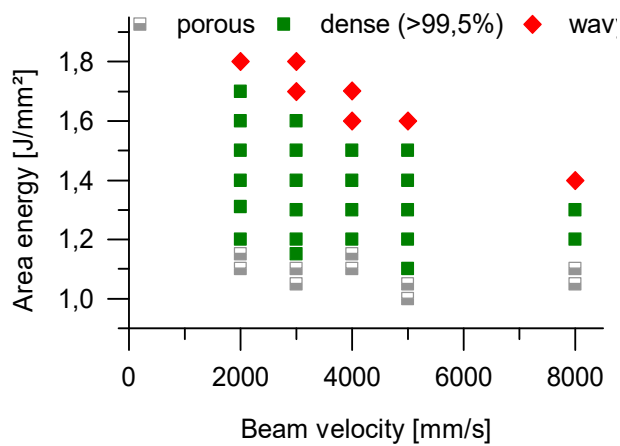
Fig. 1: Processing window of Fe28Al5Ti1.3B processed via SEBM with a Line Offset of 100 µm.
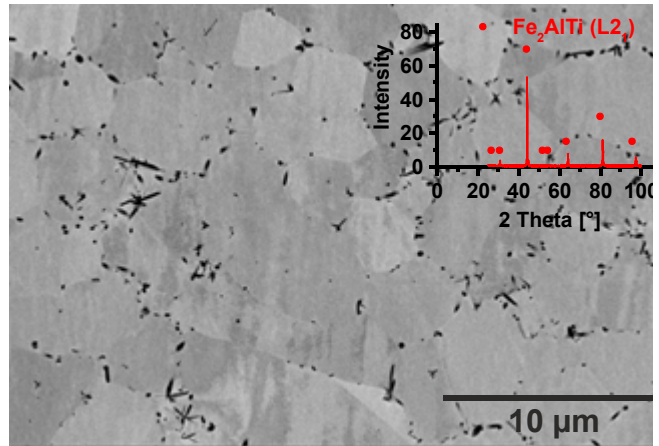
Fig. 2: Microstructure of the SEBM built iron aluminide alloy Fe28Al5Ti1.3B.
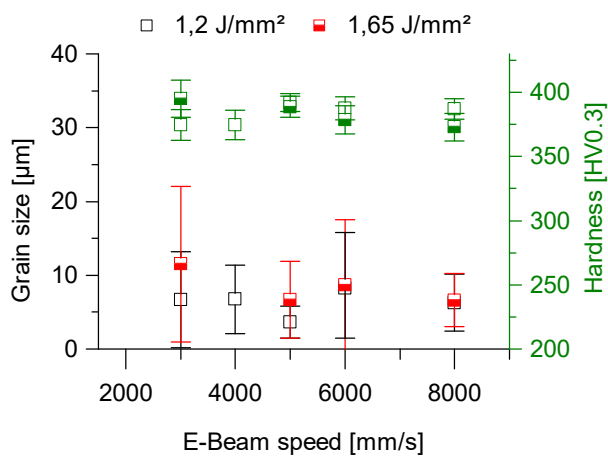
Fig. 3: Influence of processing parameters on grain size and micro hardness.
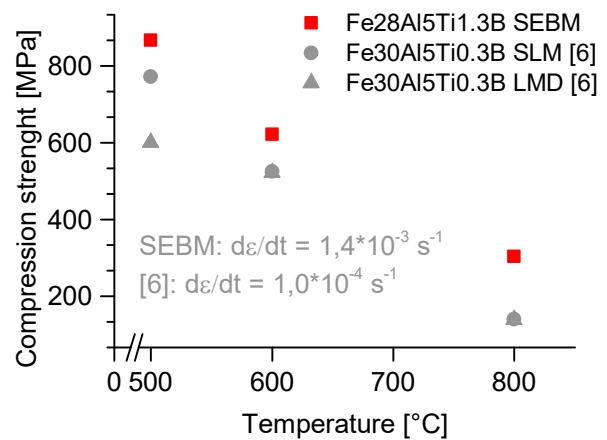
Fig. 4: Compression strength of the SEBM built alloy in comparison to similar AM-studies [6].

References

[1]   C. G. McKamey, J. H. DeVan, P.F. Tortorelli, V. K. Sikka: Journal of Materials Research. **1991**, Vol. *6*, No. 8, 1779-1805.

[2]   M. Zamanzade, A. Barnoush, C. Motz: Crystals. **2016**, Vol. 6, No. 10, 1-29.

[3]   P. Prokopcakova, M. Svec, M. Palm: International Journal of Materials Research. **2016**, 107, 396-405

[4]   M. Palm, G. Sauthoff: Intermetallics. **2004**, 12, 1345-1389

[5]   X. Li, P. Prokopcakova, M. Palm: Materials Science & Engineering A. 2014, 611, 234-241

[6]   A. Michalcova, L. Sencekova, G. Rolink, A. Weisheit, J. Pesicka, M. Sobik, M. Palm: Materials and Design, **2017**, 116, 481-494

[7]   T. Durejko, M. Zietala, M. Lazinska, S. Lipinski, W. Polkowski, T. Czujko, R. A. Varin: Materials Science & Engineering A. **2016**, 650, 374-381

O–HT 01

Alloy design concept for bcc-T2 silicide-B2 aluminide multi-component alloys in conjunction with Laves phase

Seiji Miura [1], Takuya Yamanouchi[2], Satoshi Takizawa[3],
Ken-ichi Ikeda[4] and Toshiaki Horiuchi[5]

[1] Division of Materials Science and Engineering, Faculty of Engineering, Hokkaido University, Kita13 Nishi 8, Kita-ku, Sapporo 060-8628, Japan, miura@eng.hokudai.ac.jp

[2] Department of Materials Science and Engineering, Hokkaido University, Kita13 Nishi 8, Kita-ku, Sapporo 060-8628, Japan, takuyaimf@gmail.com

[3] Division of Materials Science and Engineering, Faculty of Engineering, Hokkaido University, Kita13 Nishi 8, Kita-ku, Sapporo 060-8628 Japan, takizawa@lms4-ms.eng.hokudai.ac.jp

[4] Division of Materials Science and Engineering, Faculty of Engineering, Hokkaido University, Kita13 Nishi 8, Kita-ku, Sapporo 060-8628 Japan, ikeda.ken-ichi@eng.hokudai.ac.jp

[5] Department of Mechanical Engineering, Faculty of Engineering, Hokkaido University of Science, Sapporo 006-8585, Japan, horiuchi@hus.ac.jp

Abstract

Refractory-metal based materials have attracted attentions for many years because of the demand for high temperature components. In order to obtain materials with superior properties for high temperature use (high toughness, high strength and good oxidation resistance), multicomponent-multiphase alloys are required. Authors have conducted studies mainly on Nb-based materials; mechanical and physical properties of bcc solid-solution phase, M_5Si_3 silicide phase and B2 aluminide phase and phase equilibrium among these constituent phases [1-8].

For the improvement of strength, dispersion of $(Nb, Mo)_5(Si, B)_3$ phase in Nb-Mo bcc solid-solution matrix has been studied by many groups. Although silicide phases show superior oxidation resistance, we focused on B2 aluminides as an oxidation-resisting coating material because B2-NiAl has been used for commercial Ni-based superalloys. However, ternary compounds such as $Nb(Ni, Al)_2$ Laves phase might be formed at the interphase boundary between NiAl and Nb-based alloys during high temperature heat-treatment. Therefore, phase equilibrium between Nb-Mo bcc solid-solution phase and B2 aluminides were examined as the first step. To avoid the formation of Laves phase, both the B2 phase composition and the bcc alloy composition were optimized based on the phase diagrams such as Nb-Al-Pd [9] and Nb-Mo-NiAl [2], and a composition area at which bcc solid-solution phase equilibrates with B2 aluminide was found in Nb-Mo-Ni-Al-Pd quinary system. However, for the further improvement of oxidation resistance of Nb-based alloys and B2 compound, alloy design including Cr is quite important, while it may introduce Laves phase $NbCr_2$.

A systematic investigation revealed that there is a continuous solid-solution between $NbCr_2$ and $Nb(Ni, Al)_2$ in the Nb-Cr-Ni-Al quaternary system. It is quite Interesting that Cr tends to be substituted by Ni and Al, i.e., $NbCr_{(2-2x)}Ni_xAl_x$ [10]. It has been repeatedly confirmed that the atomic size ratio of constituent elements is one of the key to understand the stability of Laves phases, however, Al has much larger atomic size than Ni and Cr. It is suggest that the size of Al atom seemingly much smaller in B2 aluminides than that in pure Al [11]. To understand the substitutional behavior of the compound, electronic structure calculations based on the density functional theory (DFT) was performed. It is found that the lattice constants of the $NbCr_2$ compound with Ni and Al atoms in Cr-site are almost the same with that of $NbCr_2$, suggesting the size of Al is similar to that of Ni and Cr. Such information will be utilized to establish rules for the selection and amount of additive elements for obtaining high performance refractory-based materials.

Acknowledgement

References

[1] S. Miura, T. Hatabata, T. Okawa, T. Mohri, Metall.Mater.Trans.A, **2014**, 45A, 1136-1147.

[2] S. Miura, Y. Sekito, T. Okawa, T. Yamanouchi and T. Mohri, Materials Science Forum, **2014**, Volumes 783-786, 1171-1175.

[3] T. Yamanouchi, S. Miura, MRS Proceedings, Editors: I. Baker, M. Heilmaier , K. Kishida, M. Mills and S. Miura, **2015**, 1760, yy05-38.

[4] S. Suzuki, N. Sekido, T. Ohmura, S. Miura, MRS Proceedings, Editors: I. Baker, M. Heilmaier , K. Kishida, M. Mills and S. Miura, **2015**, 1760, yy05-08.

[5] T. Yamanouchi and S. Miura, 123HiMAT2015, Sapporo, **2015.**

[6] T. Yamanouchi and S. Miura, The proceedings of The 9th Pacific Rim International Conference on Advanced Materials and Processing (PRICM9), ed. by T. Furuhara, M. Nishida and S. Miura, The Japan Institute of Metals and Materials, **2016**, 784-787.

[7] T. Yamanouchi, S. Miura, M. Ohno and K. Ikeda, MRS Advances, **2017**.

[8] N. Matsuzaki, K. Ikeda, S. Miura, N. Sekido, T. Ohmura, MRS Advances, **2017**.

[9] P. Cebra, M. Vilasi, B. Malaman, J.Steinmetz, Journal of Alloys and Compounds. **1993**, 201, 57-60.

[10] T. Yamanouchi and S. Miura, submitted to Materials Transactions, **2017**.

[11] M. Ellner, K. Kolatschek, and B. Predel: J. Less-Common Met. **1991**, 170, 171-184.

O–HT 02

Effect of microstructure on room-temperature fracture toughness of ZrC-added Mo-Si-B alloys

Shunichi Nakayama[1] and Kyosuke Yoshimi[2]

[1] Department of Materials Science and Engineering, Tohoku University, 6-6-02, Aramaki Aza Aoba, Aoba-ku, Sendai, 980-8579, Japan, shunichi.nakayama.q5@dc.tohoku.ac.jp

[2] Department of Materials Science and Engineering, Tohoku University, 6-6-02, Aramaki Aza Aoba, Aoba-ku, Sendai, 980-8579, Japan, yoshimi@material.tohoku.ac.jp

Introduction

The development of ultrahigh-temperature materials (UHTMs) beyond Ni-based superalloys are critical for high pressure turbine (HPT) blades in gas turbines and jet engines to improve their energy efficiency. Mo-Si-B-based alloys have been considered as one of leading candidate UHTMs because of their high melting point (>1800 °C) and good creep strength. Nevertheless, industrial applicaitons of Mo-Si-B-based alloys have suffered from several drawbacks including high density, poor room-temperature fracture toughness, poor oxidation resistance and so on. Recently, it has been found in our previous studies that adding lightweight carbides such as TiC and ZrC can effectively reduce the density and improve room-temperature fracture toughness of Mo-Si-B-based alloys [1,2]. However, the toughnening mechanism due to brittle TiC and ZrC phases is still unclear at present. In this study, the correlation between microstructure and room-temperature fracture toughness is systematically investigated for a series of ZrC-added Mo-Si-B alloys with various compositions. The effect of microstructural morphology on room-temperature fracture toughness is discussed.

Materials and Methods

Several ZrC-added Mo-Si-B alloys were prepared using a conventional arc-melting technique in Ar atmosphere. The nominal compositions of the alloys were Mo-(3.2-7.0)Si-(6.5-14.0)B-(4.7-12.9)ZrC (at.%). Si, B, Zr and C concentrations were fixed at Si/B=0.5 and Zr/C=1. Button ingots with the weight of ~90 g and diameter of ~50 mm were produced from Mo rods, Si grains, B grains and ZrC powder. The ingots were heat-treated at 1800°C for 24 h in Ar atmosphere. Microstructures of the heat-treated alloys were observed by scanning electron microscopy (SEM) in a backscattered electron (BSE) mode. Constituent phases were identified using both X-ray diffractometry (XRD) and energy dispersive X-ray diffractometry (EDX). Moreover, microstructures were characterized by the electron backscatter diffraction patterns (EBSD)-orientation imaging microscopy (OIM) method.
 4-point bending tests with a Chevron notch were employed at room temperature to evaluate the room-temperature fracture toughness of the alloys. Bending specimens had a final dimension of 1.5 ± 0.05 × 2.0 ± 0.05 × 25 mm^3 after polished with sandpapers to #400. The 4-point bending tests were performed using an Instron 5982 at room temperature with a crosshead speed of 0.3 μm/s. Fracture toughness value K_Q was evaluated based on the Irwin's similarity relationship [2].

Results and Discussion

A BSE image in Fig. 1 shows the representative microstructure of a heat-treated ZrC-added Mo-Si-B alloy with the nominal composition of 64.5Mo-3.2Si-6.5B-12.9Zr-12.9C (at.%). The ZrC-added Mo-Si-B alloys were mainly composed of molybdenum solid solution (Mo_{ss}) (bright), Mo_5SiB_2 (T_2) (dark gray) and ZrC (dark) whereas Mo_2B (bright gray) of less than 5 vol.% was observed in a few alloys. The room-temperature fracture toughness value of the investigated alloys ranged from 12 to 20 MPa(m)$^{1/2}$ depending on alloy composition. According to literature [3], the fracture toughness value of Mo-Si-B ternary alloys ranged 5 to 15 MPa(m)$^{1/2}$. Several ZrC-added Mo-Si-B alloys showed significantly higher fracture toughness values than the Mo-Si-B ternary alloys. Considering from microstructure formation, the microstructure of the Mo-Si-B ternary alloys was composed of Mo_{ss}+T_2 eutectic and Mo_{ss}+T_2+Mo_3Si eutectics which had brittle-phase matrices. In contrast, the microstructure of the ZrC-added Mo-Si-B alloys was composed of not those eutectics but Mo_{ss}+ZrC eutectic which had ductile Mo_{ss} matrix. Thus, it suggested that ductile phase toughening by Mo_{ss} was

efficiently worked on the ZrC-added Mo-Si-B alloys. To verify this suggestion, the percolation of Mo_{ss} in the ZrC-added Mo-Si-B alloys was analyzed using the EBSD-OIM method. As shown in Fig. 1, Mo_{ss} was taken as ductile phase and the other phases as brittle phases, and phase maps obtained by EBSD-OIM were binarized to ductile and brittle phases. Then, continuous ductile or brittle phases were defined as a cluster. Next, in order to eliminate the difference in volume fraction between ductile and brittle phases, the area of a ductile or brittle phase cluster was divided by the overall area of the ductile or brittle phase. This ratio was defined as the occupancy of a cluster n, and the obtained n distributions were shown in graphs in Fig. 1. For example, a 64.5Mo-3.2Si-6.5B-12.9Zr-12.9C alloy which showed the fracture toughness value of 19 $MPa(m)^{1/2}$ contained a >95%-continued ductile phase cluster and a lot of <4%-continued brittle phase clusters. From this result, this alloy was categorized as a brittle-phase-dispersed ductile-phase-matrix alloy. From the experimental results and percolation evaluation, it was ascertained that the alloys with the room-temperature fracture toughness value of 18-20 $MPa(m)^{1/2}$ had almost fully continued Mo_{ss} even if containing 16 vol.%T_2 and 23 vol.%ZrC. Therefore, it was considered that the high tougheness of the ZrC-added Mo-Si-B alloys results from high Mo_{ss} percolation.
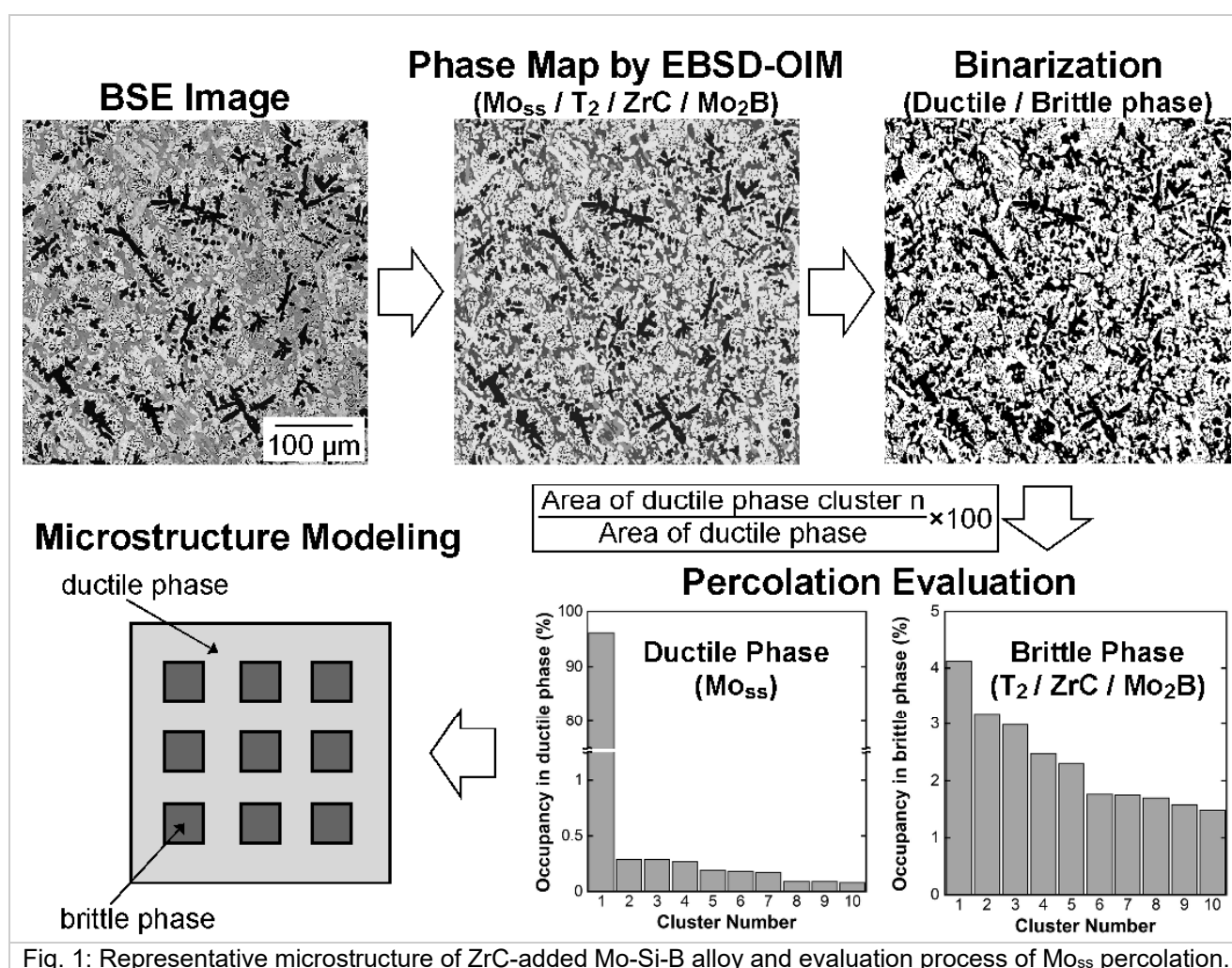
Fig. 1: Representative microstructure of ZrC-added Mo-Si-B alloy and evaluation process of Mo_{ss} percolation.

References

[1] S. Miyamoto, K. Yoshimi, S.H. Ha, T. Kaneko, J. Nakamura, T. Sato, K. Maruyama, R. Tu, T. Goto, Metallugical and Materials Transactions A. **2014,** *45*, 1112–1123.

[2] T. Moriyama, K. Yoshimi, M. Zhao, T. Masnou, T. Yokoyama, J. Nakamura, H. Katsui, T. Goto, Intermetallics. **2017**, *84*, 92–102.

[3] J.A. Lemberg, R.O. Ritchie, Mo-Si-B alloys for ultrahigh-temperature structural applications, Advanced Materials. **2012,** *24*, 3445–3480.

O–HT 03

Creep properties of the Mo_3Si and Mo_5SiB_2 phases in the Mo-Si-B alloy system

Olha Popovych[1], Iurii Bogomol[2], Konstantin Naumenko[3] and Manja Krüger[4]

[1]Institute of Materials and Joining Technology, Otto-von-Guericke University Magdeburg, Universitätsplatz 2, 39106 Magdeburg, Germany, olha.popovych@ovgu.de

[2]High Temperature Materials and Powder Metallurgy Department, National Technical University of Ukraine "I. Sikorsky KPI", Peremogy Av. 37, Kiev 03056, Ukraine, ubohomol@iff.kpi.ua

[3]Institute of Mechanics, Otto-von-Guericke University Magdeburg, Universitätsplatz 2, 39106 Magdeburg, Germany, konstantin.naumenko@ovgu.de

[4]Forschungszentrum Jülich GmbH, 52425 Jülich, Germany, m.krueger@fz-juelich.de

Introduction

The use of new materials realizes more effective engines thanks to increased working temperature. In gas turbines, structural materials for the blades have to withstand static and dynamic tensile stresses, as well as variable thermal and other complex loads. In addition, the operating temperatures of the materials are above 1000 °C. In modern gas turbines up to 40% of the engine weight falls on the high-temperature alloys [1]. Currently single-crystal Ni-base superalloys are used for the blades, which operate at temperatures above 1000 °C, but their development has already reached a limit, restricted by the melting temperature [2–4].

For a long service life these materials should have firstly a high melting temperature, secondly limited reactivity with environment and, at the same time, good compatibility with coatings which are resistant to oxidation. In addition, it is essential to regulate micro-structural changes at high temperatures and the creep properties. A further important aspect is the phase equilibrium of all components in the system; in the case of phase transformation kinetic data have to be considered and integrated.

Through the beneficial physical and mechanical properties at high temperatures, Mo-Si-B alloys are considered as promising candidates for the substitution of Ni base alloys, which can increase the thermodynamic efficiency of engines. This means a significant reduction of fuel costs and emissions due to 20 – 40 % decreasing of the fuel consumption [5], as well as increased performance due to oxidation resistant alloy composites, usable in air up to 1370 °C [5]. Published reviews of numerous investigations to develop Mo-based alloys containing Si and B [3, 4, 6, 7] have shown, that the best combination of high temperature properties provide alloy compositions which are located in the so-called "Berczik triangle" (a three-phase microstructure with a ductile molybdenum solid solution phase and the two intermetallic phases Mo_3Si (A15) and Mo_5SiB_2 (T2). These materials dispose high temperature strength, good oxidation behavior and acceptable room temperature toughness. Since these materials are designed for use at high temperatures, creep properties are very important. A number of studies on the creep behavior of these materials has already been published. The creep properties of different molybdenum solid solutions have already been published by Jain and Kumar [8], the creep properties of T2 phase were studied by Hayashi, Ito et al. [9] only at 1500 °C, the creep properties of the individual phase Mo_3Si haven`t been studied, yet. Due to these reasons our actual research focuses on completing the creep data for Mo_3Si and T2 phases at different temperatures aiming in the development of a model based creep description of multi-phase Mo-Si-B alloys.

Materials and Methods

Two processing routines were used to produce single phase Mo_3Si and T2 materials. The first is conventional arc-melting (AM) of elemental starting materials in an argon atmosphere. They were weighed in from high purity Mo (99.95 wt.%), Si (99.999 wt.%) and B (99.5 wt.%). For the Mo_3Si single phase specimens the Mo – 23 at.% Si alloy composition was used. T2 specimens were molten from the mechanically alloyed stoichiometric powder mixtures of Mo, Si and B of 99.95%,

99.6% and 98% purity, respective (20 h milling by 200 rpm and 1 h heat treatment at 1400 °C). To ensure good homogeneity, each button was flipped and re-molten five times.

The second routine was a directional solidification (DS) process using a crucible-free float-zone technique at a growth velocity of 30 mm/h. Mo_3Si specimens were produced from a powder mixture with Mo – 23 at.% Si alloy composition, T2 specimens from the mechanically alloyed stoichiometry powder mixture (same as for previous processing routine) of Mo, Si and B powders of 99.95%, 99.6% and 98% purity, respectively. After cold pressing the green samples were compacted in an induction heated zone melting device "Crystal 206" (Ukraine). Zone melting was performed in a high purity He atmosphere.

To investigate the phase composition XRD powder measurements were performed using an X'pert powder X-ray diffractometer with a Cu-K$_\alpha$ beam. The phase identification was obtained using the quantitative phase analysis software TOPAS.

To investigate the microstructures, specimens were cut via electrical discharge machining (EDM). specimens of DS materials were cut transverse and longitudinal to the crystal growth direction. All specimens were embedded in a cold hardening epoxy, subsequently grind and polished. The microstructural observations were carried out using a SEM microscope FEI ESEM XL30 FEG. The SEM images were obtained in the backscattered electron (BSE) mode.

To perform compressive creep tests prismatic creep specimens with a typical square cross-sections of 2,5 mm each and a height of 4 mm were prepared by EDM. Specimens of DS materials were cut transverse, longitudinal and at 45° to the crystal growth direction. The creep tests were conducted in a flowing Ar/H_2 atmosphere using a Zwick/Roell Z100 electro-mechanical testing machine equipped with a Maytec furnace. Creep testing was carried out by applying a constant true stress to the specimen. After attaining a constant, i.e. steady-state creep rate, at a particular constant stress level the stress was increased until a new steady-state was established. This involved a careful and continuous monitoring of the creep strain during the entire test.

The creep properties of Mo_3Si and T2 were described by the power law creep relationship (Eq. 1):

$$\dot{\varepsilon} = A\sigma^n \exp\left(-\frac{Q}{RT}\right), \tag{1}$$

where $\dot{\varepsilon}$ is the minimum or steady-state creep rate, A a pre-exponential factor, σ the applied stress, n the creep stress exponent, Q the characteristic activation energy for creep, R the gas constant and T the absolute temperature. The stress exponent n is then expressed as the slope in the Norton-plot (Eq. 2).

$$n = \frac{\Delta \log \dot{\varepsilon}}{\Delta \log \sigma} \tag{2}$$

A detailed description of the results and analyses will be given at the conference.

References

[1] Reed, R. C.: The superalloys: Fundamentals and applications, Cambridge University Press, Cambridge, UK, New York, **2006**.

[2] Dimiduk, D. M.; Miracle, D. B.; Ward, C. H., Mater. Sci. Tech., **1992**, 8 (4), 367–375.

[3] Perepezko, J. H.; Sakidja, R.; Kumar, K. S., Advanced Structural Materials: Properties, Design Optimization, and Applications, CRC Press, **2006**.

[4] Lemberg, J. A.; Ritchie, R. O., Adv. Mater., **2012**, 24 (26), 3445–3480.

[5] David Shifler, NAVY STATEMENT A. ONR Approval # 43-2203-16, **2017**.

[6] Heilmaier, M.; Rösler, J.; Mukherji, D.; Krüger, M., Microstructural design of advanced engineering materials, Wiley-VCH. Weinheim, **2013**.

[7] Perepezko, J. H.; Pint, B. A.; Forrest, D. R., Advanced Materials and Processes, **2014**, 172 (9), 22–26.

[8] Jain, P.; Kumar, K. S., Acta Materialia, **2010**, 58 (6), 2124–2142.

[9] Hayashi, T.; Ito, K.; Ihara, K.; Fujikura, M.; Yamaguchi, M., Intermetallics, **2004**, 12 (7-9), 699–704.

O–HT 04

Formation of silicides in mechanically alloyed V-Si solid solution powders

Janett Schmelzer[1], Christoph Daniel Günther[2] and Manja Krüger[3]

[1] Institute of Materials and Joining Technology, Otto-von-Guericke-University Magdeburg, Magdeburg, Germany, Janett.schmelzer@ovgu.de

[2] Otto-von-Guericke-University Magdeburg, Magdeburg, Germany, Christoph-Daniel-Guenther@gmx.de

[3]Forschungszentrum Jülich, Institute of Energy and Climate Research (IEK-2), Jülich, Germany, m.krueger@fz-juelich.de

Introduction

To increase the efficiency of thermodynamic processes, nowadays high temperature materials are required to withstand temperatures beyond the potential of conventional nickel-based superalloys or heat resistant steels. Especially refractory metal silicides based on elements with ultra-high melting points like molybdenum (T_m = 2623°C) or niobium (T_m = 2467°C) are currently under development and investigation [1-3]. Beside a high melting point also the weight of the components is of importance to achieve the target of increased thermodynamic efficiency. Vanadium points out with good strength values, even at high temperatures up to 1430 °C [4], combined with a low density (ρ = 6.11 g/cm^3) in comparison to other high-melting metals. To enhance the high temperature strength and creep resistance of a V solid solution material strong and creep-resistant phases, for example V_3Si or V_5Si_3, incorporated homogenously in the solid solution matrix, may cause a significant contribution [5]. In the present work a powder metallurgical route for the production of silicide-reinforced V-Si alloys is introduced.

Materials and Methods

V-Si powder mixtures with Si concentrations of 2 at.%, 4 at.%, 15 at.% and 25 at.%, respectively, were prepared under protective argon atmosphere using pure V (purity: > 99.9 %) and Si powders (purity: 99.9 %). Mechanical alloying (MA) was carried out in a planetary ball mill (Retsch PM 400) at a rotational speed of 200 rpm to form supersaturated V(Si) solid solution powders. Subsequently an argon protected thermal treatment of the V(Si) solid solution powders, at temperatures ranging from 1000 up to 1400°C, for 1 hour was conducted. For all alloys an X-ray diffraction analysis (XRD) using Cu-Kα radiation (PANalytical X'Pert Pro) was performed. To determine the microhardness of the powder particles a Vickers pyramid was indented with a force of 0.1 N (HV 0.01) for 5 s in the V(Si) solid solution single phase. All milling conditions and analytical methods are described in more detail in [6].

Results and Discussion

The X-ray diffraction analyses of different mechanically alloyed V-Si compositions (before thermal treatment) show that the elemental silicon was dissolved completely due to the formation of a V(Si) solid solution phase. Depending on the amount of the Si concentration the milling time needed to form supersaturated solid solutions varies from 2 h for 2 at.% Si and 4 at.% Si up to 50 h for 25 at.% Si. Si appears to be an effective solid solution strengthener for V and leads to an improved hardness caused by the distortion of the lattice structure. The microhardness measurements of the powder samples approved a steady enhancement of the microhardness with increasing Si concentration from 7 GPa (2 at.% Si) to 16 GPa (25 at.% Si) for the example of 10 h milling time. Additionally, the contributions of the grain refinement (Hall-Petch strengthening) and the work hardening effect during

MA also have a strong impact on the entire hardening and have to be considered in addition to the solid solution strengthening effect. To transfer the V(Si) solid solution from the non-equilibrium to the equilibrium state, an argon protected heat treatment was conducted. As expected, the X-ray diffractograms show a peak shift towards the initial peak position of pure vanadium due to the depletion of Si in the V solid solution (i.e. a change of the lattice parameter). Fig. 1 shows that increased Si concentrations in case of alloyed V-15Si and V-25Si powders lead to the formation of the intermetallic V_3Si phase. The composition V-15Si is located midway between the V solid solution phase and the intermetallic V_3Si phase, depicted by an approximately 60% proportion of the strong intermetallic phase embedded in the ductile V solid solution matrix, shown in Fig 1a. The alloy composition V-25Si matches the stoichiometry of the V_3Si phase and forms a single phase V_3Si microstructure after the heat treatment (Fig. 1b). Both highly alloyed V-Si materials (15 at.%, 25. at% Si) exhibit a significant increase of microhardness after the annealing procedure. According to the volume fraction and the distribution of the V_3Si phase, depending on the heat treatment temperature, values from 2000 GPa to 2300 GPa for the 15 at.% alloyed V-Si composition and 2200 GPa to 3100 GPa for the 25 at.% alloyed V-Si composition can be observed.
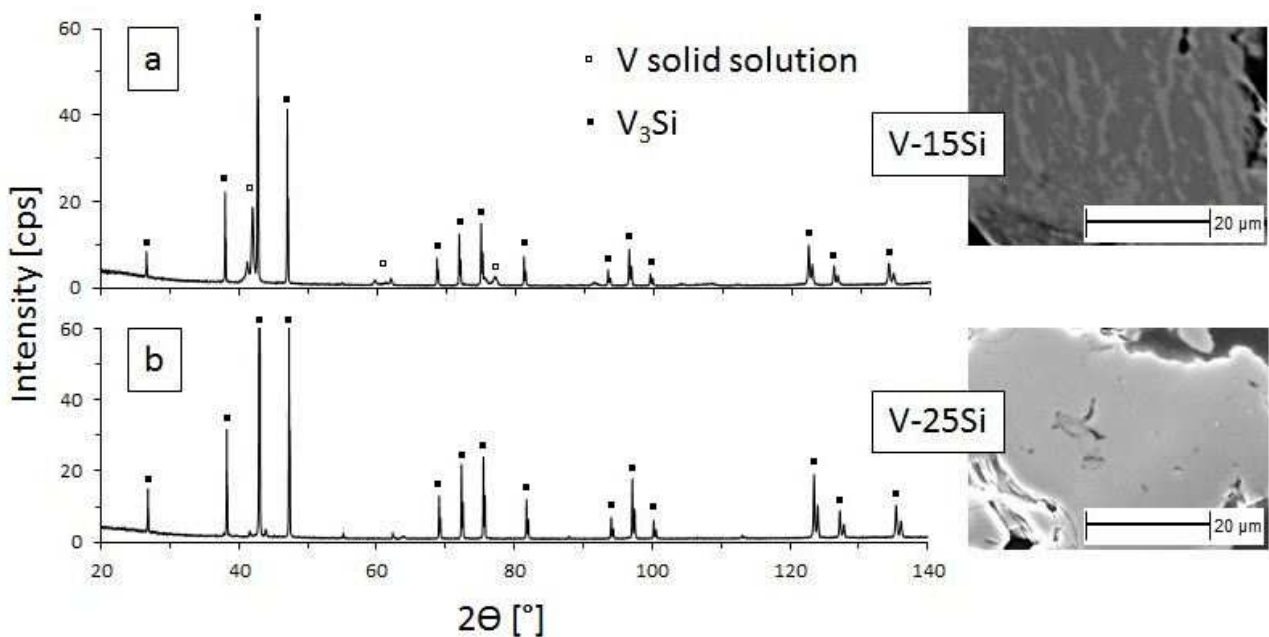
Fig. 1: X-ray diffractogram and microstructure of a) V-15Si and b) V-25Si in equilibrium conditions

References

[1] H. Saage, M. Krüger, D. Sturm, M. Heilmaier, J.H. Schneibel, E. George, L. Heatherly, Ch. Somsen, G. Eggler, Y. Yang, Acta Materialia, **2009**. 57. 3895-3901.

[2] M. Heilmaier, M. Krüger, H. Saage, Trans Tech Publications, **2010**. 549-558.

[3] Z. Yao, J. Stiglich, T.S. Sudarshan, Journal of Materials Engineering and Performance, **1999**. 8. 291-304.

[4] V.V. Shyrokov, C.B. Vasyliv, O.V. Shyrokov, Journal of Nuclear Materials, **2009**. 394. 114-122.

[5] M. Krüger, Scripta Materialia, **2016**. 121. 75-78.

[6] J. Schmelzer, T. Baumann, S. Dieck, M. Krüger, Powder Technol., **2016**. 294. 493.

O–HT 05

Microstructure and creep properties
of near-eutectic Mo-Zr-B and Mo-Hf-B alloys

Volodymyr Bolbut[1], Manja Krüger[1,2]

[1]Institute of Materials and Joining Technology, Otto-von-Guericke University Magdeburg, Universitätsplatz 2, 39106 Magdeburg, Germany, volodymyr.bolbut@ovgu.de

[2]Forschungszentrum Jülich (IEK-2), 52425 Jülich, Germany, m.krueger@fz-juelich.de

Introduction

In our previous work [1,2] we showed the existence of two new phases Mo_2ZrB_x and Mo_2HfB_x in the respective Mo-Zr-B and Mo-Hf-B phase diagrams, which were not described in the literature before. It was shown that each of these phases form a eutectic microstructure with the molybdenum solid solution phase Mo_{SS}. In this work we present microstructural features and creep properties of Mo_{SS} - Mo_2ZrB_x and Mo_{SS} - Mo_2HfB_x eutectic alloys.

Materials and Methods

The alloys were melted from pure molybdenum (99.95 at. %), zirconium (99.2 at. %), hafnium (98 at. %) and boron (99 at.%) pieces in an arc-melting furnace (Buehler mini arc-melting system type 'MAM-1') under an argon atmosphere upon five flipping and re-melting stages to ensure homogeneity. The eutectic compositions were found empirically by the variation of chemical compositions. After melting specimens were cut for compressive creep tests and for microstructural investigation using electrical discharge machining (EDM). Samples for microstructural analyses were embedded in a cold hardening epoxy (Demotec 15). After manually grinding from 80 down to 1200 grit size the specimens were finished by automatically polishing with a 3 and 1 µm diamond suspension. The microstructure observations were conducted by using a SEM microscope (FEI ESEM XL30 FEG) equipped with EDX (energy dispersive X-ray spectroscopy). The SEM images were typically obtained in the backscattered electron (BSE) mode. For creep tests rectangular specimens with the geometry 2x2x3.5 mm were manufactured. The creep strength was evaluated in a flowing Ar/H_2 atmosphere at 1100 °C using a Zwick/Roell Z100 electro-mechanical testing machine equipped with a Maytec furnace under constant applied stress of 100 MPa, 200 MPa, 300 MPa and 400 MPa.

Results and Discussion

The eutectic point between the phases Mo_{SS} and Mo_2ZrB_x was found at the chemical composition of 59.2 at. % Mo, 14.8 at. % Zr and 26 at. % B. The eutectic microstructure of the alloy Mo-14.8Zr-26B is shown in the Fig. 1. Eutectic colonies with typically fine lamellae are visible with Mo_{SS} as the light grey phase. The eutectic point in the quasi binary system Mo_{SS} - Mo_2HfB_x lies at the chemical composition 63 at. % Mo, 14 at. % Hf and 23 at. % B. The microstructure of this alloy is very similar compared to the microstructure of alloy Mo-14.8Zr-26B shown in Fig.1. The fraction of Mo_{SS} in both eutectic alloys is about 50 vol. %.

The high temperature creep behavior of the alloys Mo-14.8Zr-26B and Mo-14Hf-23B was compared with the single-crystalline Ni-based superalloy CMSX-10 [3] and a ternary near-eutectic directionally solidified Mo-17.5Si-8B alloy [4], at temperatures of about 1100 °C (Fig.2). Compared to the single-crystalline alloy CMSX-10 the eutectic alloys Mo-14.8Zr-26B and Mo-14Hf-23B provide substantially enhanced creep behavior, which is improved by several orders of magnitude. Furthermore, it is noticeable that the alloys Mo-14.8Zr-26B and Mo-14Hf-23B show almost similar creep resistance compared to the ternary eutectic alloy Mo-17.5Si-8B, which incorporates the phases Mo_3Si, Mo_5SiB_2 and Mo_{ss}, but has only half of the volume fraction of the weakest constituent Mo_{SS} [4]. In the Norton plot (Fig. 2) the stress exponents n for Mo-14.8Zr-26B and Mo-14Hf-23B are evaluated to be 0.9 and 1.8 respectively. Stress exponents in this range indicate diffusion controlled creep mechanisms [5] and demonstrate the potential of the Mo-14.8Zr-26B and Mo-14Hf-23B alloys as creep resistant high temperature materials for possible ultra-high temperature applications.
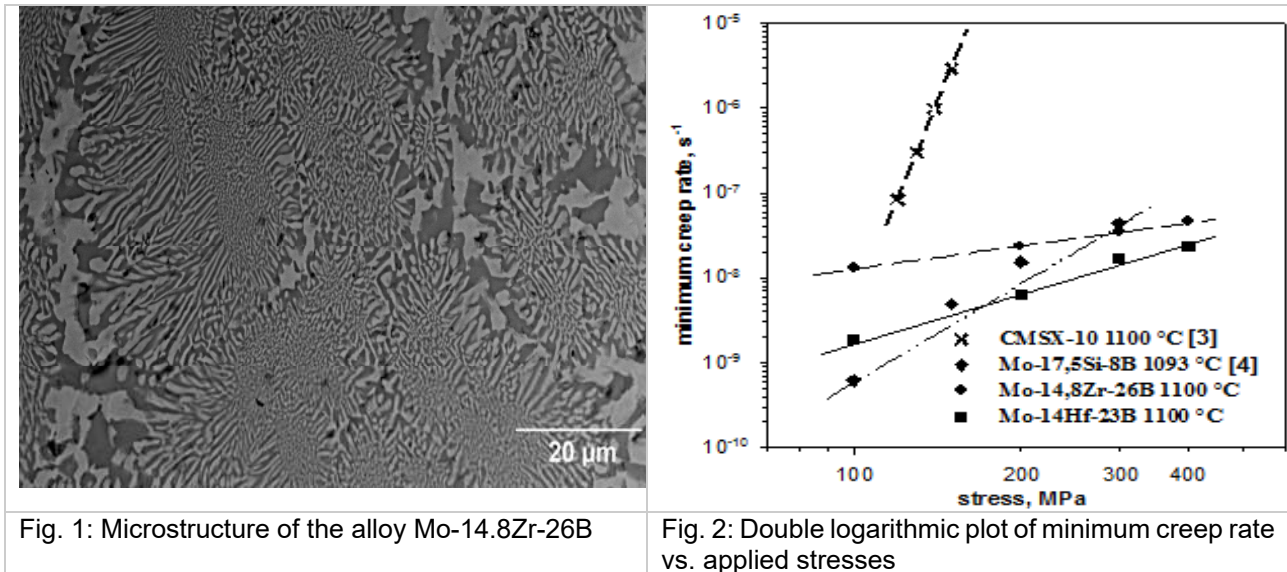
Fig. 1: Microstructure of the alloy Mo-14.8Zr-26B	Fig. 2: Double logarithmic plot of minimum creep rate vs. applied stresses

References

[1] V. Bolbut, I. Bogomol, C. Bauer, M. Krüger: submitted to Journal of Material Science and Engineering Technology. **2017**.

[2] V. Bolbut, I. Bogomol, P. Loboda, M. Krüger: submitted to Journal of Alloys and Compounds. **2017**.

[3] N.K. Sinha, Materials Science and Engineering: A. **2006**, *432*, 129–141.

[4] G. Hasemann, I. Bogomol, D. Schliephake, P.I. Loboda, M. Krüger, Intermetallics. **2014**, *48*, 28–33

[5] J. Rösler, H. Harders, M. Bäker, Mechanisches Verhalten der Werkstoffe, 4th ed. Springer Vieweg, Wiesbaden, **2012**.

O–HT 06

High-entropy alloys under high-pressure high-temperature

Kirill V. Yusenko

College of Engineering, Swansea University, SA2 8EN, UK, k.yusenko@swansea.ac.uk

Introduction

High-entropy alloys (HEAs) were proposed for applications where high temperature stability (including mechanical and chemical stability) and high mechanical impact are required. HEAs are also attractive for special applications due to the absence of ductile to brittle transition, their high strength, and unusual magnetic behaviour. Nowadays, HEA is a rapidly developing field, which will affect the basis and applications of materials science. While originally proposed as consisting of one or two solid solutions (mainly *fcc* or *bcc*), most HEAs were later found to contain ordered or partially ordered secondary phases and inclusions [1]. Nevertheless, careful analysis of their crystal structures and local composition suggests that nearly all HEAs consist of phase mixtures. Only few multicomponent alloys can be considered single-phase HEAs. At the same time, phase composition strictly determines mechanical and functional features. For example, it has been shown that Al content in Al_xCoCrFeNi alloys plays an important role for phase stability and mechanical properties. Since HEAs were proposed as materials with outstanding high-temperature stability, detailed knowledge about phase composition, stability and possible local structure under extreme conditions is required. Recently, several systems were investigated under heating *ex situ* and *in situ* up to their melting using neutrons and X-ray diffraction. It has been found that phase instability above 800-1000°C limits HEAs application. Nevertheless, high-pressure properties of HEAs were never investigated in details. Pilot high-pressure experiments suggest pressure stability of HEAs under moderate (below 20 GPa) pressures. In [2-3], two-phase HEAs were investigated in diamond-anvil cells at RT up to 20 GPa. These data are to be considered preliminary, as they give only a partial overview of the phase stability and the equation of state of HEAs. They should be complemented by systematic studies considering the synergic effect of pressure and temperature. HEA's high-pressure (up to 11 GPa) stability has been recently confirmed by shock compression of *fcc*-CoCrFeMnNi and *bcc*-AlCoCrFeNi [4].

Here, recent experimental *in situ* investigations of HEAs under high-temperature high-pressure conditions up to 55 GPa and 2000°C are reported. Stabilization of single-phase compositions under high-pressure was found which opens new perspectives for preparation of new HEAs with outstanding properties for extreme applications. Several model refractory binary and ternary systems were investigated to support an investigation of HEAs systems.

Materials and Methods

High-entropy and multicomponent *fcc*- and *bcc*-structured alloys were prepared from pure Al, Fe, Co, Ni, Cr and Sc powders using induction melting with further high-temperature homogenization. Refractory *fcc*- and *hcp*-structured high-entropy alloys were prepared using a single-source precursors strategy [1]. In brief, 5- and 6-component salts were co-crystallized from water solution: $a[Ir(NH_3)_5Cl]Cl_2 + b[Rh(NH_3)_5Cl]Cl_2 + (1-a-b)[Ru(NH_3)_5Cl]Cl_2 + c(NH_4)_2[IrCl_6] + d(NH_4)_2[OsCl_6] + e(NH_4)_2[PtCl_6] + (1-c-d-e)(NH_4)_2[ReCl_6] \rightarrow [Ir(NH_3)_5Cl]_a[Rh(NH_3)_5Cl]_b[Ru(NH_3)_5Cl]_{(1-a-b)}[IrCl_6]_c[OsCl_6]_d[PtCl_6]_e[ReCl_6]_{(1-c-d-e)} + 2NH_4Cl$. Thermal decomposition in a hydrogen flow follows the general scheme, forming a multicomponent alloy [6-8]:
$[Ir(NH_3)_5Cl]_a[Rh(NH_3)_5Cl]_b[Ru(NH_3)_5Cl]_{(1-a-b)}[IrCl_6]_c[OsCl_6]_d[PtCl_6]_e[ReCl_6]_{(1-c-d-e)} + 7/2H_{2(gas)} \rightarrow Ir_{0.5(a+c)}Rh_{0.5b}Ru_{0.5(1-a-b)}Os_{0.5d}Pt_{0.5e}Re_{0.5(1-c-d-e)} + 5NH_4Cl_{(gas)} + 2HCl_{(gas)}$.
High-pressure high-temperature response was investigated using a piston-cylinder press (up to 2 GPa and 1000°C), multi-anvil large-volume press (up to 20 GPa and 2000°C) and laser-heated diamond-anvil cells (up to 50 GPa and 1500°C) [6, 9]. Phase transformations were monitored *in situ* using synchrotron X-ray diffraction on ID06-LVP and ID15B beam-lines based at the ESRF. High-temperature transformations at ambient pressure were investigated in inert atmosphere at the I11 beam-line at the DIAMOND LS. Microstructure and hardness were used for a characterization of macroscopic properties before and after high-pressure high-temperature treatment.
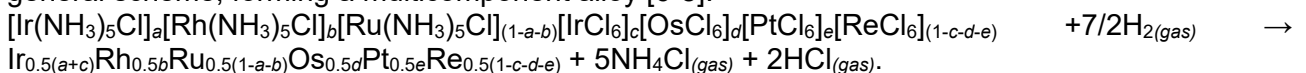
Results and Discussion

Addition of small quantities of Sc into the light *bcc*- and *fcc*-structured Al$_x$CoCrFeNi alloys results in a precipitation of hexagonal *W*-phase (MgZn$_2$-type intermetallic compound). Sc-doped alloys show higher hardness and higher high-temperature stability. Al-Sc-*M* (*M* = Co, Cr, Fe) ternary *W*-phase seems to be an ideal secondary phase candidate for co-precipitation and rational properties design. Such ternary phase shows extraordinary thermodynamic stability and can be easily formed as pinning centres for improvement mechanic and functional properties.

High-pressure high-temperature treatment results in dissolution of *W*-phase in the HEA matrix with the formation of a single-phase Sc-doped alloy and significantly enhances its hardness. An adequate high-pressure high-temperature treatment could thus be functional in dissolving the analogous AlCuSc *W*-phase in Al-Cu alloys, while retaining the benefits of scandium additions upon quenching. Here we show that the application of high pressure and the precipitation of a homogeneously dispersed Sc-based intermetallic efficiently inhibits the phase transformation occurring in Al$_2$CoCrFeNi at high temperature. The dissolution of the intermetallic in the main phase at high pressure suggests a brand new strategy in the design and optimization of HEAs.

In contrast, the first single-phase *hcp*-structured PGM-based 5-component HEA shows extraordinary stability under extreme conditions. The alloy has higher thermal expansion and lower bulk modulus in comparison with individual PGMs, an unexpected result, which requires further investigation. *Hcp*-structured HEA shows significant electrocatalytic activity in methanol oxidation The high electro-catalytic activity of the investigated HEA systems can be associated with the electronic effects often associated with alloys, or to the synergic effect inherent to HEAs and often referred to as "*cocktail effect*". So far, a deeper understanding of the catalytic activity of HEAs has been hindered by the sensitivity of the alloy to its production route. The synthetic pathway herein reported, on the other hand, leads to highly reproducible results.

Here, we show first successful synthesis of single-phase *hcp*-structured HEA from a single-source precursor and detailed investigation its properties under extreme conditions. We also show dissolution of stable intermetallic phase under high-pressure. Both approaches seem to be very productive for preparation of new HEAs with outstanding stability under extreme conditions.
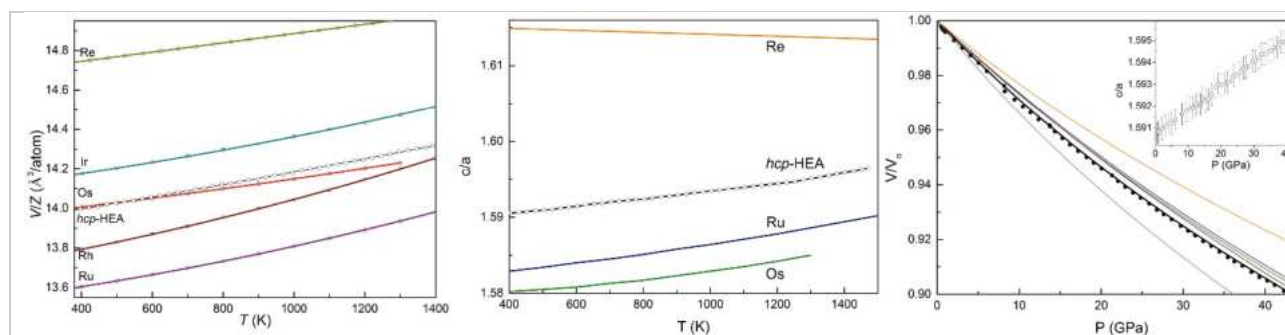
Fig. 1. Thermal expansion curve for *hcp*-IrOsReRhRu (*hcp*-HEA) (*left*); temperature dependence of *c/a* ratio (*middle*); room temperature compressibility curve for *hcp*-Ir$_{0.19}$Os$_{0.22}$Re$_{0.21}$Rh$_{0.20}$Ru$_{0.19}$ HEA in comparison with PGMs (*orange* – Os, *blue* – Ir, *green* – Re, *red* – Ru, *grey line* – Rh) (*right*).

References

[1] D.B. Miracle, O.V. Senkov, Acta Materialia. **2017**, *122*, 448-511;

[2] Li *et al.* (2015): JOM 67(10) 2310;

[3] Yu *et al.* (2016): Intermetallics 70 82;

[4] Z.J. Jiang *et al.*, Materials Research Letters, **2016**, DOI: 10.1080/21663831.2016.1191554;

[5] C.L. Tracy, S. Park, D.R. Rittman, S.J. Zinkle, H. Bei, M. Lang, R.C. Ewing, W.L. Mao, https://arxiv.org/abs/1611.00876, **2016.**

[6] K.V. Yusenko *et al.*: *submitted to Acta Materialia*. **2017**.

[7] K.V. Yusenko *et al.*, Journal of Alloys and Compounds. **2015**, *622*, 155-161.

[8] K.V. Yusenko *et al.*, Journal of Alloys and Compounds. **2017,** *700*, 198-207.

[9] S. Riva, K.V. Yusenko *et. al.*: *submitted to Scientific Reports*. **2017**

O–IA 01

Theory-guided design of novel Fe-Al-based superalloys

M. Friák[1*], D. Holec[2], Y. Jirásková[1], M. Palm[3], F. Stein[3], D. Janičkovič[4],
N. Pizúrová[1], P. Dymáček[1], F. Dobeš[1], P. Šesták[1,5,6], J. Fikar[1], J. Šremr[1,6],
L. Nechvátal[1,6], S. Oweisová[7], V. Homola[7], A. Titov[1,8], A. Slávik[1,7],
I. Miháliková[1,7], J. Pavlů[9,7,1], V. Buršíková[7], J. Neugebauer[3], D. Boutur[1,10],
Y. Lapusta[10] and M. Šob[9,1,7]

[1] Institute of Physics of Materials, Academy of Sciences of the Czech Republic, v.v.i., Brno, Czech Republic

[2] Department of Physical Metallurgy and Materials Testing, Montanuniversität Leoben, Leoben, Austria

[3] Max-Planck-Institut für Eisenforschung GmbH, Düsseldorf, Germany

[4] Institute of Physics, Slovak Academy of Science, Bratislava, Slovak Republic

[5] Central European Institute of Technology, Brno University of Technology, Brno, Czech Republic

[6] Faculty of Mechanical Engineering, Brno University of Technology, Brno, Czech Republic

[7] Faculty of Science, Masaryk University, Brno, Czech Republic

[8] VSB-Technical University of Ostrava, Ostrava-Poruba, Czech Republic

[9] Central European Institute of Technology (CEITEC MU), Masaryk University, Brno, Czech Republic

[10] SIGMA Clermont, Campus des Cézeaux, Aubière cedex, France

[*] friak@ipm.cz

Our modern industrialized society increasingly requires new structural materials for high-temperature applications in automotive and energy-producing industrial sectors. Iron-aluminides are known to possess excellent oxidation and sulfidation resistance as well as sufficient strength at elevated temperatures (see, e.g., Refs. [1-4]). New Fe-Al-based materials will have to meet multiple casting, processing and operational criteria including high-temperature creep strength, oxidation resistance and room-temperature ductility. Such desirable combination of materials properties can be achieved in multi-phase multi-component superalloys with a specific type of microstructure (the matrix contains coherent particles of a secondary phase as in, e.g., Ref. [5]).

In case of Fe-Al-based materials, Fe matrices with less than 15 at. % Al are ductile at low temperatures at which shape-forming processes take place. Those with more than 18 at. % Al are extremely corrosion-resistant due to the formation of thin Al_2O_3 films on the surface and the desirable strength is achieved by the thermodynamically stable second-phase nano-particles. Unfortunately, the thermodynamic stability of the second-phase particles and, consequently, the strength related to their existence, may significantly decrease at higher temperatures and depends very sensitively on the composition. Therefore, in order to design new Fe-Al-based superalloys, we employ a state-of-the-art theory-guided materials design concept [6,7] to identify suitable combinations of solutes.

With the help of quantum-mechanical (*ab initio*) methods we analyzed 64 combinations of seven different transition-metal elements (plus Fe) occupying Fe-sublattice atomic positions in both Fe_3Al-$D0_3$-like compounds (Fig. 1a) with the stoichiometry $Fe_8Al_4X_1Z_3$ (X, Z = Ti, V, Mn, Fe, Zr, Nb, Mo, and Ta) as a model for the ordered phase in Fe-Al based superalloys, and in special quasi-random structures (SQS, Ref. [8], Fig. 1b) with the stoichiometry $Fe_9Al_3X_1Z_3$ used as a model for the disordered phase. Using the above mentioned methodology, a wealth of results was obtained. First, the thermodynamic stability of both ordered and disordered phase was approximatively assessed by computing their formation energies at T = 0 K using the energies of elemental constituents in the ground-state crystal structures as references. Importantly, a number of tested solute combinations lead to negative formation energies (Figs. 1c,d) and thus represent possible candidates for stable

phases (subject, of course, to complex thermodynamics of other competing phases which may possibly appear in multi-component phase diagrams of studied materials).
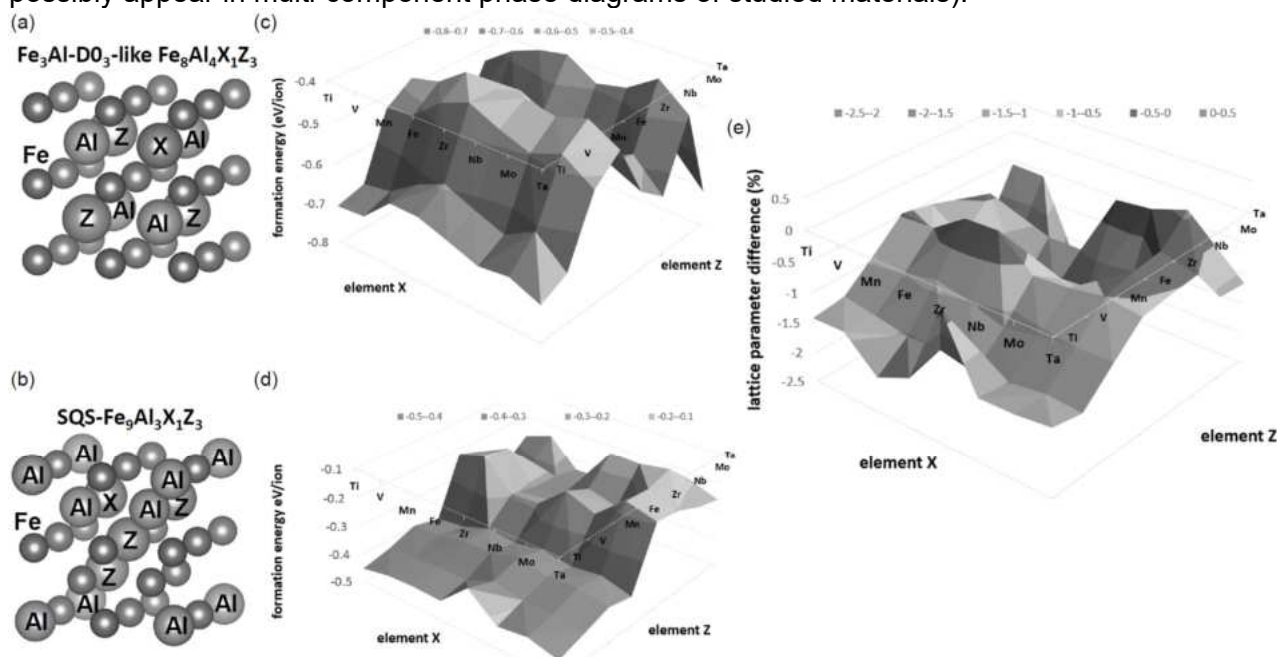
Fig. 1: Quantum-mechanical (ab initio) calculations were applied to analyze a number of properties of different configurations of transition-metal elements occupying atomic positions in both Fe3Al-D03-like compounds (see the periodically repeated computational supercell in part (a) and in special quasi-random structures (SQS, Ref. [8], see it in part (b)) which were used as models for the disordered phase. The thermodynamic stability was checked by computing the formation energies of both ordered (c) and disordered phases (d). As a critical parameter for the formation of a superalloy microstructure with the two phases coherently co-existing, the lattice parameters of phases were determined and their relative difference is shown in part (e).

Next, the lattice parameters of different ordered and disordered phases were calculated and compared. As it may be seen in Fig. 1e, our study identifies a number of solute combinations leading to only a very small lattice parameter difference. These findings are among our most important results as the lattice parameter difference is a materials-design aspect which is critically important for the existence of coherent superalloy microstructures. Lastly, our *ab initio* calculations and other theoretical approaches (atomistic modeling, CALPHAD) were supported experimentally by microstructure and phase characterization (electron-microscopy methods) of selected samples, mechanical testing including a novel mathematical analysis (rheological modeling of creep processes) as well as measurements of other crucial materials properties (e.g., magnetic ones).

References

[1] C.G. McKamey, J.H. DeVan, P.F. Tortorelli, V.K. Sikka, J. Mat. Res. **1991,** *6,* 1779.

[2] D.G. Morris, M.A. Munoz-Morris, L.M. Requejo, Acta Mater. **2006**, *54*, (2006) 2335.

[3] C.H. Liebscher *et al.*, Acta Mater. **2015**, *92*, 220.

[4] R. Krein, M. Palm, M. Heilmaier, J. Mat. Res. **2009**, *24*, 3412.

[5] R. Krein, M. Friák, J. Neugebauer, M. Palm, M. Heilmaier, Intermetallics **2010**, *18*, 1360.

[6] D. Raabe, B. Sander, M. Friák, D. Ma, J. Neugebauer, Acta Mater. **2007**, *55*, 4475.

[7] M. Friák, D. Raabe, J. Neugebauer, In: D. Lehmhus, M. Busse, A. S. Herrmann, K. Kayvantash (Eds.): Structural Materials and Processes in Transportation, Wiley-VCH Verlag, **2013**, 481-495.

[8] S.-H. Wei, L.G. Ferreira, J. Bernard, A. Zunger, Phys. Rev. B **1990**, *42*, 9622.

O–IA 02

Fe-Al-Ni-Ti strengthened by L2$_1$-(Fe,Ni)$_2$TiAl precipitates

Flora Godor[1], Martin Palm[2], Christian Liebscher[2], Frank Stein[2],
Christoph Turk[1], Boryana Rashkova[1], Svea Mayer[1], Helmut Clemens[1]

[1]Department of Physical Metallurgy and Materials Testing, Montanuniversität Leoben,
Roseggerstr. 12, 8700 Leoben, Austria
e-mail address: Flora.Godor@unileoben.ac.at

[2]Max-Planck-Institut für Eisenforschung GmbH, Max-Planck-Str. 1, 40237 Düsseldorf, Germany

Introduction

In the last few years, Fe-Al-Cr-Ni alloys with disordered ferritic matrix (A2 structure) strengthened by intermetallic precipitates (B2 structure) were investigated regarding their high-temperature applicability [1–4]. However, their creep resistance and strength above 700 °C are insufficient due to a rather low precipitate volume fraction and not optimized lattice mismatch between the matrix and B2-precipitates [3,4]. One way to control the lattice parameter misfit and to generate two-phase precipitates is alloying these alloys with Ti to form coherent Heusler-based precipitates (L2$_1$ structure) within the ferritic matrix [5,6]. In the present study, a Fe-Al-Ni-Ti alloy was investigated. Compared to previously investigated Fe-Al-Cr-Ni-Ti alloys [5,6] Cr was eliminated to further reduce the density and the Ti-content was significantly increased to obtain a high volume fraction of coherent Heusler precipitates within this alloy.

Materials and Methods

The alloy with a nominal composition of 60Fe-20Al-10Ni-10Ti (in at.%) was produced by high-frequency remelting and spin casting into copper molds. For an in-depth understanding of the microstructural evolution, specimens in the as-cast condition and after different heat treatments were analyzed employing scanning electron microscopy (SEM), transmission electron microscopy (TEM), atom probe tomography (APT) along with hardness measurements (Vickers HV10). Using APT data, phase compositions were determined. The phase transition temperatures were obtained from differential thermal analysis (DTA) measurements. As the oxidation resistance is an important issue for high-temperature applications, thermogravimetric analysis (TGA) and oxidation heat treatments were conducted.

Results and Discussion
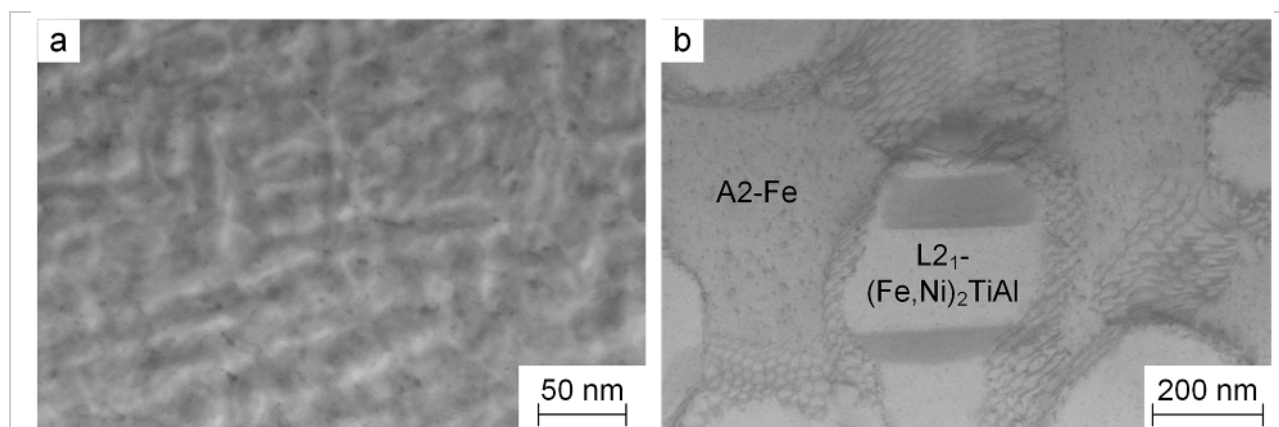
Fig. 1: STEM-BF images showing the microstructures of the alloy after homogenization at 1200 °C for 24 h followed by (a) water quenching and (b) furnace cooling.

For the microstructural characterization special emphasis was laid on two sample conditions: water quenching (WQ) and furnace cooling (FC). For both conditions, the alloy was homogenized at 1200 °C for 24 h followed by either water quenching (WQ) or furnace cooling (FC). This temperature

was chosen, because the DTA measurements indicated that precipitation of the $L2_1$ Heusler phase in the A2 matrix occurs below this temperature at about 1020 °C. Nevertheless, even after WQ the microstructure already consisted of coherent Heusler precipitates embedded in a disordered ferritic matrix (Fig. 1a). The precipitates in the WQ state are aligned along certain crystallographic orientations and were identified as off-stoichiometric $L2_1$-(Fe,Ni)$_2$TiAl precipitates with Fe being the major constituent. In the slowly cooled state (FC) the microstructure also consisted of a ferritic matrix and $L2_1$-(Fe,Ni)$_2$TiAl precipitates (Fig. 1b). Interfacial dislocations are formed during the slow cooling process at the phase boundary between matrix and precipitate causing a relaxation of misfit strains. As a consequence, the resulting microstructures are semicoherent. Additionally, the precipitates are much coarser, they are not aligned anymore and start to coalesce.

The APT measurements prove that in both states the matrix is continuous, though the volume fraction of the $L2_1$-(Fe,Ni)$_2$TiAl precipitates is > 50 %. However, the cooling rate has a strong effect on the morphology of the precipitates: they change from a cuboidal, in the water-quenched state, to spherical or polygonal shape in the furnace-cooled state. The cooling rate also influences the hardness values, as the size and morphology of the precipitates change. The hardness values vary from 699 HV10 after rapid cooling to 463 HV10 after furnace cooling.

For the characterization of the oxidation behavior TGA measurements were conducted at 900 °C for 24 h and the mass gain was recorded. Supplementary oxidation treatments were performed at 900 °C for up to 500 h, in order to investigate the oxide layers in the SEM. Fig. 2 shows that there is only a little change in mass within the first 24 h. Only after 500 h a very thin, but dense oxide layer can be clearly seen in the SEM. Therefore, it is concluded that the alloy possesses a favorable oxidation resistance.
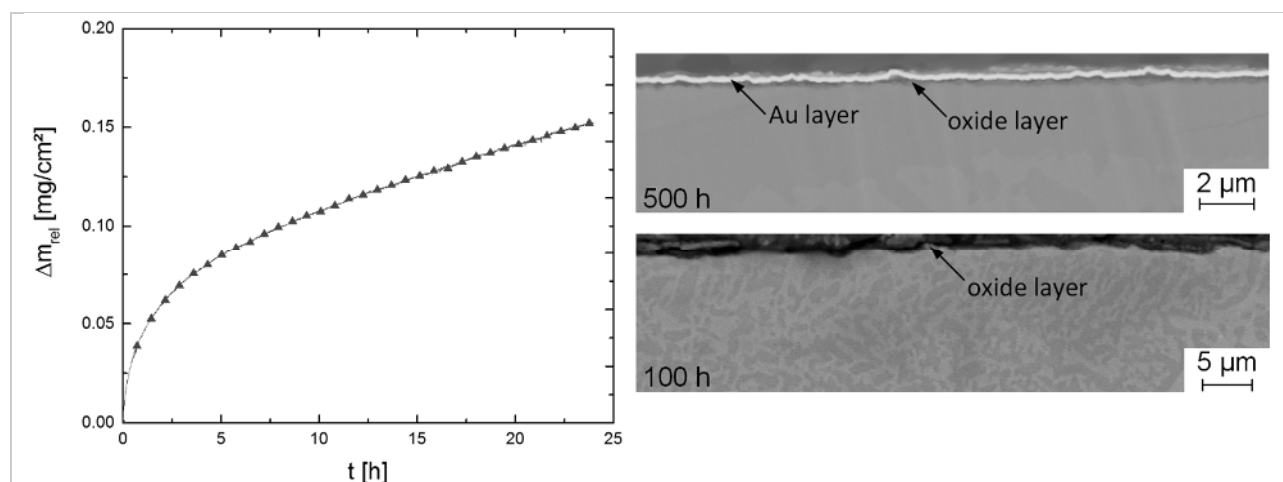
Fig. 2: Relative mass gain obtained from TGA measurements at 900 °C for 24 h. Additionally, SEM images in back-scattered electron mode were taken from the oxide layers of specimens heat-treated at 900 °C for 100 or 500 h. For a better visibility of the oxide layer, the specimen heat-treated for 500 h was sputtered with a thin Au layer before metallographic preparation, which shows a bright contrast.

References

[1] Z. Sun, C.H. Liebscher, S. Huang, Z. Teng, G. Song, G. Wang, M. Asta, M. Rawlings, M.E. Fine, P.K. Liaw, Scripta Materialia. **2013**, 68, 384–388.

[2] Z.K. Teng, F. Zhang, M.K. Miller, C.T. Liu, S. Huang, Y.T. Chou, R.H. Tien, Y.A. Chang, P.K. Liaw, Intermetallics. **2012**, 29, 110–115.

[3] N.Q. Vo, C.H. Liebscher, M.J.S. Rawlings, M. Asta, D.C. Dunand, Acta Materialia. **2014**, 71, 89–99.

[4] C. Stallybrass, A. Schneider, G. Sauthoff, Intermetallics. **2005**, 13, 1263–1268.

[5] C.H. Liebscher, V. Radmilovic, U. Dahmen, M. Asta, G. Ghosh, Journal of Materials Science. **2013**, 48, 2067–2075.

[6] G. Song, Z. Sun, J. Poplawsky, Y. Gao, P.K. Liaw, Acta Materialia. **2017**, 127, 1–16.

O–IA 03

Structural properties and room temperature mechanical properties of ultrafine eutectic $Fe_{50}Al_{50-n}Nb_n$ alloys

Mehmet Yildirim[1], M.Vedat Akdeniz[2] and Amdulla O. Mekhrabov[2]

[1] Department of Metallurgical and Materials Engineering, Selcuk University, Konya, Turkey, ymehmet@selcuk.edu.tr

[2] Novel Alloys Design and Development Laboratory (NOVALAB), Department of Metallurgical and Materials Engineering, Middle East Technical University, Ankara, Turkey, akdeniz@metu.edu.tr and amekh@metu.edu.tr

Introduction

Fine-scaled eutectic Fe–Al–Nb alloys can be considered as potential candidates for structural applications at high temperatures due to their extraordinary mechanical properties at ambient temperatures because of their bimodal microstructure. Their microstructure is consisted of relatively soft micrometer-scale Fe-Al based dendrites and a hard fine-scaled eutectic mixture [1-5]. Fe–Al–Nb alloys with such a bimodal solidification microstructure exhibit high compressive plasticity and ultrahigh strength. In this study, we report on a systematic investigation of the microstructures, phase relationships, room-temperature mechanical properties, and deformation mechanisms of off-eutectic and eutectic $Fe_{50}Al_{50-n}Nb_n$ alloys (n=1, 3, 5, 7, and 9 at.%) after solidification and subsequent heat-treatment. Moreover, an emphasis was placed on establishing a strong correlation between the structural properties and room-temperature mechanical properties.

Materials and Methods

Details on materials, production method, heat-treatment and relevant characterization techniques can be found in [6].

Results and Discussion

The $(Fe, Al)_2Nb$ Laves phase is found to form even at 1 at.% Nb addition due to the limited sloid solubility of Nb in FeAl (Fig. 1). Microstructures of the all the investigated ternary alloys consisted of a relatively softer Fe–Al-based phase and hard $(Fe, Al)_2Nb$ Laves phase. The volume fraction of the Laves phase increased with increasing Nb content. Based on the results of EDS analysis and microstructural investigations, the Nb solubility of the Fe–Al-based phase and eutectic composition were 3 and 9 at:% Nb, respectively. In addition, the eutectic phase transition temperature was approximately 1265 °C.
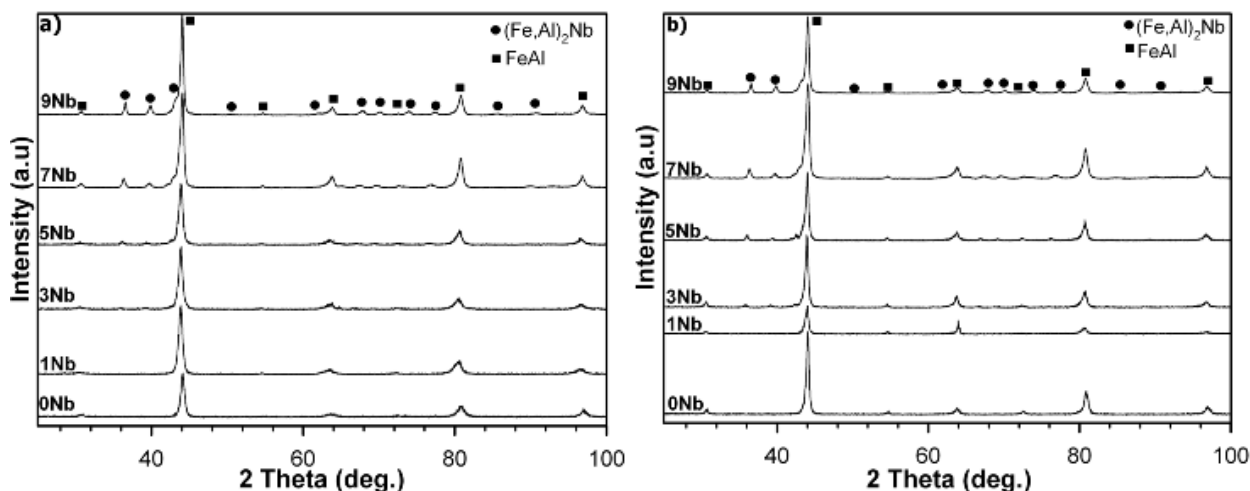
Fig. 1: XRD patterns of $Fe_{50}Al_{50-n}Nb_n$ alloys (a) as-cast and (b) heat-treated.

The room temperature mechanical properties of as-cast and heat-treated $Fe_{50}Al_{50-n}Nb_n$ alloys were investigated by means of compression tests (Fig. 2). Among the as-cast alloys, the near-eutectic $Fe_{50}Al_{43}Nb_7$ and eutectic $Fe_{50}Al_{41}Nb_9$ alloys exhibited higher compressive strength and reasonable compressive fracture strain. Compared with the as-cast state, all the heat-treated alloys exhibited ultrahigh compressive strength and considerably increased compressive fracture strains. Among the heat-treated alloys, the hypoeutectic $Fe_{50}Al_{47}Nb_3$ alloy exhibited the highest compressive strength and fracture strain of 3.02 GPa and 33.1 %, respectively. The eutectic $Fe_{50}Al_{41}Nb_9$ alloy exhibited the lowest compressive strength and fracture strain of 2.66 GPa and 21.8 %, respectively, because of the absence of the relatively softer Fe–Al-based primary dendrites. The improved compressive plasticity of the heat-treated alloys can be understood based on the elimination of solidification artifacts and lattice defects, bimodal distribution of the microstructure, and structural incoherency between the crystalline phases
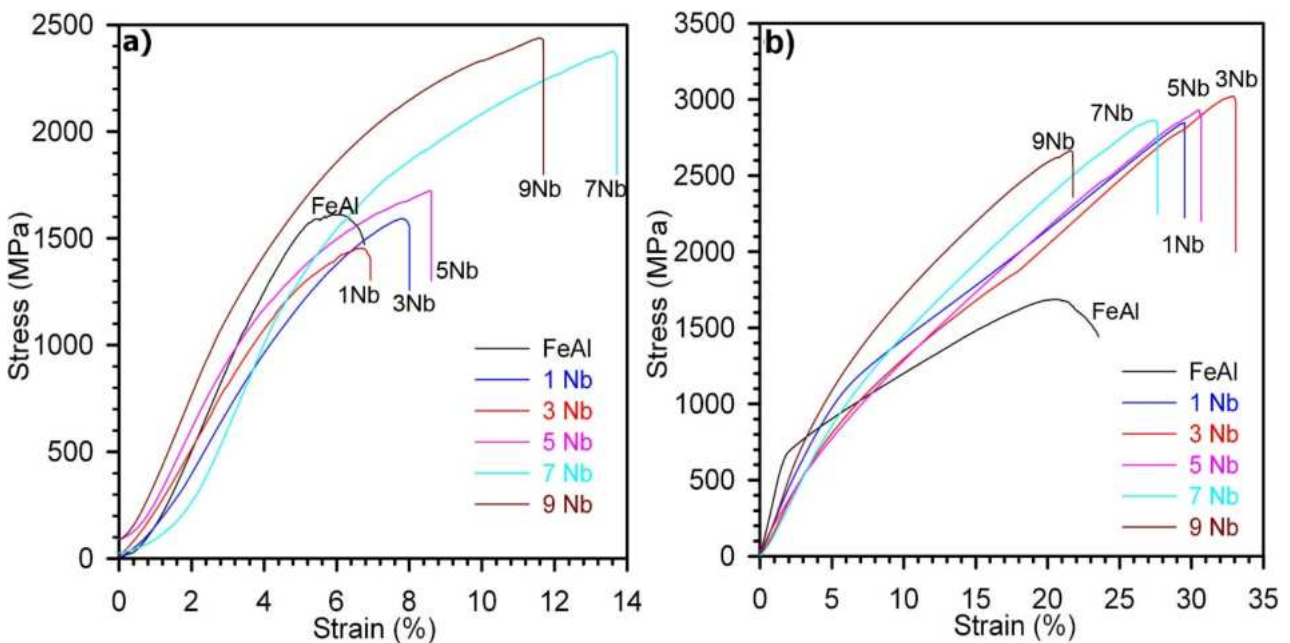
Fig. 2: Room temperature stress-strain compression curves of $Fe_{50}Al_{50-n}Nb_n$ alloys (a) as-cast (b) heat-treated..

References

[1] M.A. Mota, A.A. Coelho, J.M.Z. Bejarano, S. Gama, R. Caram, Journal of Alloys and Compounds. **2005**, *399*, 196-201.

[2] M.A. Mota, A.A. Coelho, J.M.Z. Bejarano, S. Gama, R. Caram, Journal of Crystal Growth, **1999**, *198-199*, 850–855.

[3] M. Palm, Journal of Alloys and Compounds, **2009**, *475*, 173-177.

[4] O. Prymak, F. Stein, Intermetallics, **2010**, *18*, 1322-1326.

[5] F. Stein, C. He, O. Prymak, S. Voß, I. Wossack, Intermetallics, **2015**, *59*, 43-58.

[6] M.Yıldırım, M.V. Akdeniz, A.O. Mekhrabov, Materials Science and Engineering A, 2016, *664*, 17-25.

O–IA 04

Low-temperature phase of η-Fe$_2$Al$_5$ with an ordered arrangement of aluminium atoms in the *C*-Axis chain sites

Norihiko L. Okamoto[1], Masaya Higashi[2], Jumpei Okumura[3], and Haruyuki Inui[4]

[1]Department of Materials Science & Engineering, Kyoto University, Kyoto 606-8501, Japan
Email: okamoto.norihiko.7z@kyoto-u.ac.jp

[2]Department of Materials Science & Engineering, Kyoto University, Kyoto 606-8501, Japan
Email: higashi.masaya.45m@st.kyoto-u.ac.jp

[3]Department of Materials Science & Engineering, Kyoto University, Kyoto 606-8501, Japan
Email: okumura.jumpei.24c@st.kyoto-u.ac.jp

[4]Department of Materials Science & Engineering, Kyoto University, Kyoto 606-8501, Japan
Email: inui.haruyuki.3z@kyoto-u.ac.jp

Introduction

The crystal structure of the η phase (Fe$_2$Al$_5$) is important because it comprises the majority of the coating layer of hot dip aluminized steels [1] as well as because it acts as an inhibition layer during the galvanizing/galvannealing process to suppress the excessively rapid reaction of the Zn coating with the substrate Fe [2]. Burkhardt et al. [3] have reported that the crystal structure of Fe$_2$Al$_5$ belongs to the orthorhombic space group *Cmcm* and includes two Al sites with partial occupancies (0.32 and 0.24 for Al2 and Al3 sites, respectively), which are arranged along the *c*-axis to form a chain. However, the chemical composition derived with the reported crystal structure (Fe$_2$Al$_{5.6}$) [3] is out of the solid-solubility range of the η phase in any of the currently available phase diagrams of the Fe-Al binary system [4-6]. Recently, Mihalkovič and Widom [7] have searched for a ground state of the η phase by exhaustive first-principles energy calculations and shown that an orthorhombic structure (Pearson symbol: *oP44*) with an ordered arrangement of Al atoms in the *c*-axis chains can be the ground state at 0 K. However, this superstructure has not been experimentally confirmed yet. In the present study, we have experimentally analyzed the crystal structure of a low-temperature phase of Fe$_2$Al$_5$ by electron diffraction combined with atomic-resolution scanning transmission electron microscopy (STEM) and found that the low-temperature phase of Fe$_2$Al$_5$ with an Al-rich composition possesses a tripled monoclinic superstructure with an ordered arrangement of Al atoms in the c-axis chain (Pearson symbol: *mC*44) [8], which is different from that reported by Mihalkovič and Widom [7].

Materials and Methods

Ingots with Al-rich compositions compared to the Fe$_2$Al$_5$ composition (Al-28.6 at.%Fe) were prepared by arc-melting Fe and Al (4N purity) under an Ar gas flow. The solidified ingots annealed at 900ºC for 3 days, then at either of 400, 350 or 300ºC for 28 days, followed by water quenching. The analysis details by electron diffraction and STEM are indicated elsewhere [8].

Results and Discussion

Electron diffraction analysis have indicated that the alloys with the Al-rich compositions exhibit many superlattice reflections in additions to the fundamental reflections corresponding to the orthorhombic structure (*Cmcm*) when annealed below 400ºC whereas no superlattice reflections are observed when annealed at 400 ºC. The superlattice reflections appeared at positions that divide the distances between the transmitted (000) and 131 or 202 fundamental spots by three, inferring that the superstructure unitcell of the low-temperature phase should be tripled compared to the orthorhombic unitcell. Symmetry analysis of the unitcell has revealed that the low-temperature phase crystallized into a base-centered monoclinic lattice (space group *C2/c*) with lattice constants of *a*=11.3926Å, *b*=6.4154 Å, *c*=8.7412 Å and β=103.37°, which are estimated based on those for the orthorhombic

unitcell [3]. The Al2 and Al3 sites in the orthorhombic unitcell split into two (4c and 8f) and three (8f, 8f and 8f) Wyckoff sites in the monoclinic unitcell. The STEM annular bright-field (ABF) image taken along the [101]$_{Cmcm}$ direction shows that the Al atoms in the c-axis chain site are indeed ordered as marked by dotted circle. The atomic sites corresponding to the Al2 sites are vacant whereas one of the three split Al3 sites (Al3'') are occupied by Al. The assumption that the Al3'' sites are fully occupied by Al gives the stoichiometric composition of Fe$_3$Al$_8$, instead of neither Fe$_2$Al$_5$ nor Fe$_2$Al$_{5.6}$ as previously reported for the high-temperature η phase. Fig. 2 shows a partial phase diagram of the Fe-Al system schematically illustrated on the basis of that reported by Han et al. [5]. The low-temperature phase with the tripled superstructure (η'-Fe$_3$Al$_8$) exists at the Al-rich side of the high-temperature η phase.

Since first principles calculations for structures with partial occupancies such as the high-temperature η phase are immensely challenging, certain ordered structures have been hypothesized previously for the η phase [7, 9]. Our first-principles total-energy calculations have indicated that our monoclinic (mC44) structure is slightly more stable than those hypothesized structures [7, 9]. Now that the ground state of the η phase has been determined, its various properties such as heat capacity, elasticity, electronic structures and so on can be theoretically assessed.
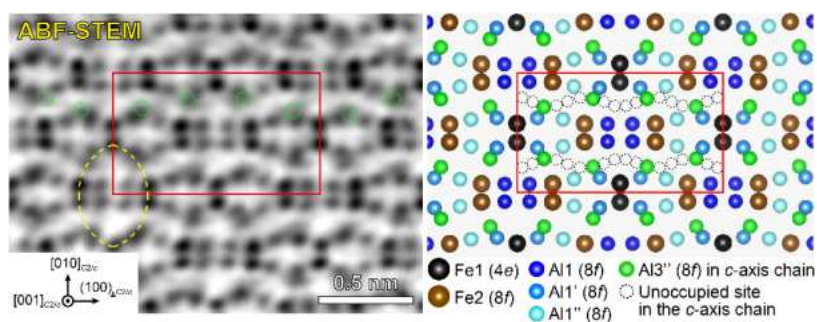
Fig. 1: STEM-ABF image and structural model of η'-Fe$_3$Al$_8$ projected along the [101]$_{Cmcm}$ (=[001]$_{C2/c}$) direction. The Al3'' sites in the c-axis chain are arranged in an ordered manner. The unitcell is indicated by a rectangular.
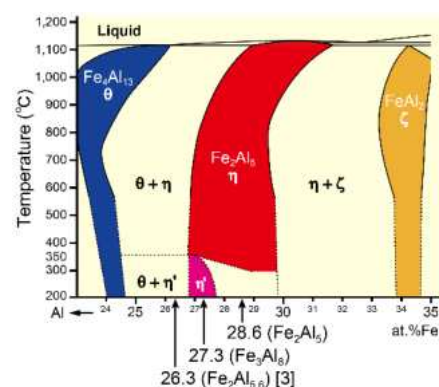
Fig. 2: Partial phase diagram of the Fe-Al system [5]. The low-temperature phase with the tripled superstructure (η'-Fe$_3$Al$_8$) exists at the Al-rich side of the high-temperature η-Fe$_2$Al$_5$ phase.

References

[1] R. W. Richards, R. D. Jones, P. D. Clements, H. Clarke, International Materials Reviews. **1994**, *39*, 191-212.

[2] T. Kato, K. Nunome, K. Kaneko, H. Saka, Acta Materialia. **2000**, *48*, 2257-2262.

[3] U. Burkhardt, Y. Grin, M. Ellner, K. Peters, Acta Crystallographica Section B-Structural Science. **1994**, *50*, 313-316.

[4] O. Kubaschewski: Iron - Binary Phase Diagrams. Springer-Verlage, Berlin, **1982**.

[5] K. Han, I. Ohnuma, R. Kainuma, Journal of Alloys and Compounds. **2016**, *668*, 97-106.

[6] X. L. Li, A. Scherf, M. Heilmaier, F. Stein, Journal of Phase Equilibria and Diffusion. **2016**, *37*, 162-173.

[7] M. Mihalkovic, M. Widom, Physical Review B. **2012**, *85*, 014113.

[8] N. L. Okamoto, J. Okumura, M. Higashi, H. Inui, Acta Materialia. **2017**, *129*, 290-299.

[9] T. Zienert, L. Amirkhanyan, J. Seidel, R. Wirnata, T. Weissbach, T. Gruber, O. Fabrichnaya, J. Kortus, Intermetallics. **2016**, *77*, 14-22.

O–IA 05

Microstructure formation due to phase transformation between η-Al$_5$Fe$_2$ and η'-Al$_8$Fe$_3$

Hanka Becker[1], Andreas Leineweber[2]

[1]Institute of Materials Science, TU Bergakademie Freiberg, Gustav-Zeuner-Straße 5, 09599 Freiberg, Germany, hanka.becker@iww.tu-freiberg.de

[2]Institute of Materials Science, TU Bergakademie Freiberg, Gustav-Zeuner-Straße 5, 09599 Freiberg, Germany, andreas.leineweber@iww.tu-freiberg.de

Introduction

The recently identified [1] and refined [2] η'-phase of the composition Al$_8$Fe$_3$ (72.7 at.% Al) with monoclinic *C*2/*c* symmetry was found to form at low temperatures (<350°C). It develops from the disordered, high-temperature η phase with orthorhombic *Cmcm* symmetry [3], usually referred to as η-Al$_5$Fe$_2$ existing between 70.6 at.% Al and 73.0 at.% Al at 750°C [2]. These two phases are characterized by a framework structure of a composition Al$_2$Fe forming channels along the $\mathbf{c}_\eta$ axis occupied by additional Al atoms. The monoclinic long-range ordering of some Al atoms in the channels of the η' phase is accompanied by a decrease of volume about 1.36% and a change of β angle pertaining to the original orthorhombic cell of the η phase to 89.49° [2]. A detailed understanding of these characteristic strains is important to understand microstructure formation in the course of processes during which the η- to η'-phase transformation potentially occurs: galvannealing processes [4] and bonding of steel and Al-alloy components [5] which are related to diffusion phenomena or in development of bulk lightweight, η and possibly η' containing iron aluminides which provide excellent high temperature strength and corrosion resistance [6].

Materials and Methods

Arc- and induction-melted Al-Fe alloys with 70.6 at.% Al - 73.0 at.% Al [2] including an 72.8 at.% Al alloy related to another study [7] were used in the present study. The compact material was heat treated at 1000°C for 120 h and at 750°C for 48 h for homogenization. After milling by hand, the powders were annealed at 750°C for 24 h. Subsequently, the powder was subjected to heat treatment at 250°C for 624 h or alternatively 350°C for 332 h, respectively. During all heat treatments, the material was encapsulated in fused silica tubes under Ar atmosphere. All heat treatment steps were followed by quenching of the fused silica tubes in water.

Cross sections of the powder particles were prepared by metallographic methods. Thorough electron backscatter diffraction (EBSD) analysis was carried out for local microstructure investigation, determination of phase distribution and crystallographic orientations. Therefore, a FEG SEM LEO 1530 GEMINI was used operating at 20 kV acceleration voltage in high-current mode equipped with a Nordlys II EBSD-Detector (Oxford Instruments). The HKL Channel5 software (Oxford Instruments) was utilized for acquisition and indexing of the EBSD patterns. Special care was taken for reliable differentiation between η and η' phases and the emerging orientation variants of the η'-Al$_8$Fe$_3$ phase.

Results and Discussion

In 2D cross sections of the powder particles, the η' phase emerges as bands with tapered ends (Fig. 1). These are embedded in a matrix of a disordered orthorhombic phase or another type of superstructure as powder X-ray diffraction has revealed [2]. Symmetry analysis reveals that the reduction from *Cmcm* (η) to *C*2/c (η') symmetry leads to loss of point symmetry elements which imply occurrence of two different twin variants of the η' phase inside the orthorhombic matrix. The resulting orientation relationships of the two η' domain variants to the surrounding phase referring it to the orthorhombic η phase are $[010]_\eta||[010]_{\eta'}$, $(001)_\eta||(201)_{\eta'}$ and $[010]_\eta||[0\bar{1}0]_{\eta'}$, $(001)_\eta||(201)_{\eta'}$. Each of these domain variants occurs with two distinct habit planes (Fig. 2). The ordering of Al atoms during η' phase formation from the high temperature η phase is accompanied by diffusion. That disqualifies the transformation from being called martensitic transformation, in spite of the appearance of the

microstructure. The habit planes of the η'- plates will be analysed in view of the crystal structure and in view of the ordering strains measured by X-ray diffraction.
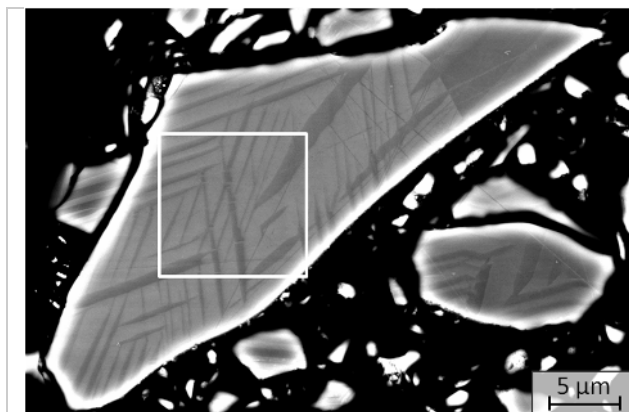

Fig. 1: Backscattered electron contrast image of cross section of the powder particles of a 72.8 at.% Al alloy quenched from 250°C. The white box marks the area of the EBSD maps in Fig. 2.
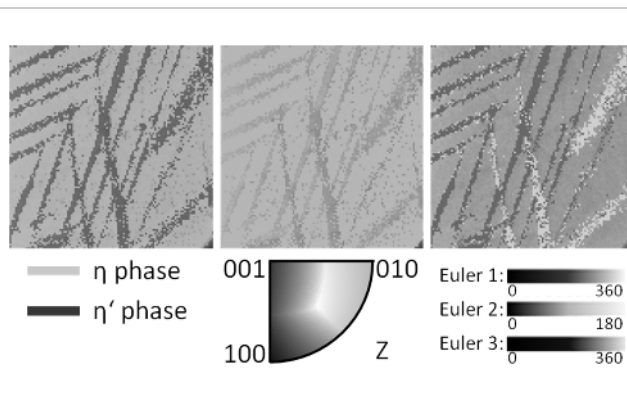
Fig. 2: From left to right: EBSD-phase map, and crystallographic orientation maps for the orthorhombic η phase and the monoclinic η' phase. The corresponding legends are shown below.

References

[1] N. L. Okamoto, J. Okumura, M. Higashi, H. Inui, Acta Materialia. **2017**, 129, 290-299.

[2] H. Becker, L. Amirkhanyan, L. Kortus, A. Leineweber: submitted to Journal of Alloys and Compounds. **2017**.

[3] U. Burkhardt, Y. Grin, M. Ellner, K. Peters, Acta Crystallographica **1994**, B50 313-316.

[4] N. Takata, M. Nishimoto, S. Kobayashi, M. Takeyama, Intermetallics. **2015**, 67, 1-11.

[5] M. Watanabe, K. Feng, Y. Nakamura, S. Kumai, Materials Transactions. **2011**, 52, 953-959.

[6] S. Hirose, T. Itoh, M. Makita, S. Fujii, S. Arai, K. Sasaki, H. Saka, Intermetallics. **2003**, 11, 633-642.

[7] X. Li, A. Scherf, M. Heilmaier, F. Stein, Journal of Phase Equilibia and Diffusion. **2016**, 37, 162-174.

O–IA 06

Thermodynamic modeling and heat capacity measurements in the binary Al-Fe system

Maximilian Rank[1], Peter Franke[1], Petronela Gotcu-Freis[1]
and Hans Jürgen Seifert[1]

[1]Karlsruhe Institute of Technology, Hermann-von-Helmholtz-Platz 1,
76344 Eggenstein-Leopoldshafen, Germany; maximilian.rank@kit.edu,
peter.franke@kit.edu, petronela.gotcu-freis@kit.edu, hans.seifert@kit.edu

Introduction

The Al-Fe system is a fundamental materials system important for many engineering applications. However, the materials constitution requires further investigation. A literature survey yields new experimental results [1, 2] regarding the homogeneity range of three intermetallic phases (stoichiometric compositions: Al_2Fe, Al_5Fe_2 and $Al_{13}Fe_4$). These values are yet not considered in any published thermodynamic assessment. In order to perform a new reliable modeling of the Al-Fe system using the Calculation of Phase Diagrams (CALPHAD) approach, experimental phase diagram and thermochemical data are mandatory input. Therefore, heat capacities of the mentioned three intermetallic phases with two slightly different compositions for each phase were measured with heat flux differential scanning calorimeters (DSC). The determined heat capacity values cover a temperature range from 273 to 973 K and were implemented into the model description of the phases, thus the physical background of the modeling was enhanced.

Materials and Methods

Different compositions of the three intermetallic phases were weight-in to their respective ratios with a precision balance. High purity iron and aluminum pieces (both: 99.99 %, Alfa Aesar) were used to synthesize the alloys for the heat capacity measurements. The pure components were arc-melted and subsequently heat-treated to obtain thermodynamically stable phases. Therefore, each material was placed in an Al_2O_3-crucible (FRIATEC AG) and encapsulated in SiO_2-quartz glass tube under vacuum (level: 10^{-3}-10^{-4} mbar) to avoid oxidation reactions during heat treatment. The samples were equilibrated in a chamber furnace at 1273 K for 168 h and subsequently furnace cooled. The obtained buttons were metallographically prepared for optical microscopy and SEM/EDX (XL30S-FEG, FEI/Philips) examinations as well as powder XRD (PAD II, GE Inspection Technologies / Seifert) characterization in order to confirm single phase status. In addition, chemical analysis by ICP-OES (OPTIMA 4300DV, Perkin-Elmer) was used to verify the chemical composition and CGHE (TC 600, LECO) for any oxygen or nitrogen impurities.

The heat capacity measurements cover a temperature range from 273 to 973 K and were performed in continuous mode with quasi-isothermal three step method [3], using three different heat flux DSC devices from NETZSCH. For high temperature measurements a Pegasus 404 C (type S-thermocouple Pt10Rh-Pt) and a 404 F1 Pegasus (type E-thermocouple NiCr-CuNi) were used at temperature ranges T = 450 - 973 K and T = 450 - 773 K, respectively. The low temperature range T = 273 - 473 K was covered with a Phoenix 204 (type-τ (CuNi-disk sensor)). As crucible material, a Pt/Rh pan and lid were used, with an Al_2O_3-inlay to prevent possible reactions between Pt/Rh and the sample. The heat capacities have been calculated for each phase following the procedure as described by Della Gatta et al. [3] via the determined heat flux signals for the three different steps. Two different alloys for each intermetallic phase and three heat flux DSC devices were employed.

Results and Discussion

All obtained values were considered to perform a Maier-Kelley fit [4] that is shown exemplary for the Al_2Fe-phase in Fig. 1. The experimental values are in agreement within the calculated experimental uncertainties. The deviation between the experimental results and the Neumann-Kopp estimation [5] probably originate from the bonding state of intermetallic phases. That is not considered by Neumann-Kopp [5], which furthermore gives unacceptable values at temperatures higher than the melting point of Al.
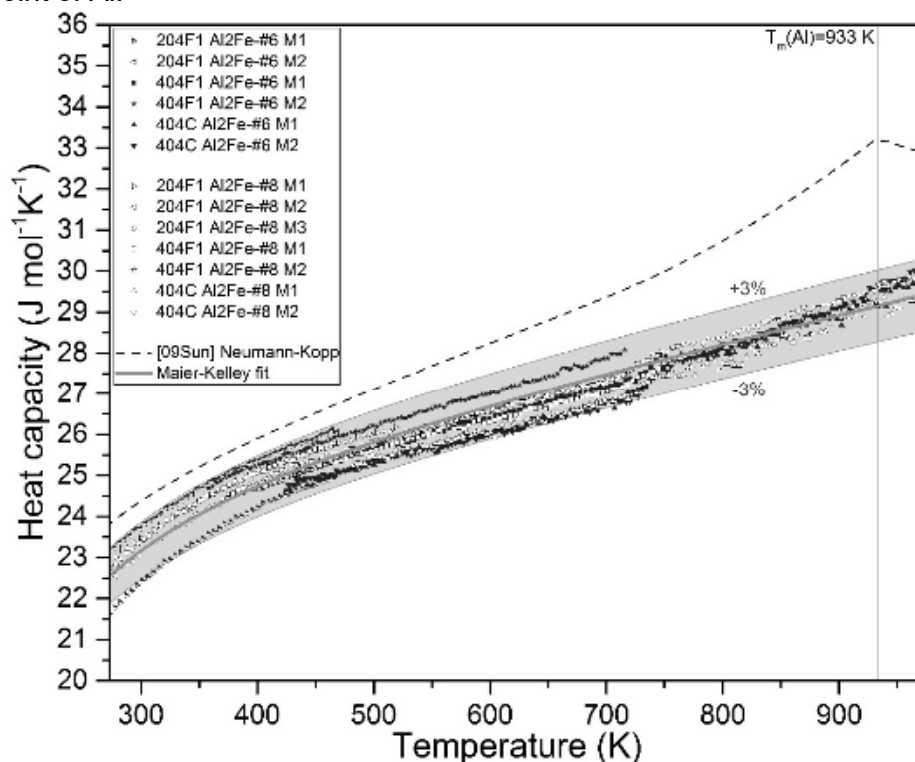
Fig. 1: Molar heat capacity of the Al2Fe-phase obtained by the method of Della Gatta et al. [3] in the temperature range between 273 K - 973 K. In comparison, the heat capacity calculated by the Neumann-Kopp rule [5] using the database from Sundman et al. [6].

CALPHAD was used to adjust the coefficients of the analytic descriptions of the Gibbs free energies of all system phases taking into account relevant publications on phase diagram data and thermochemical values. Additionally our own experimentally determined heat capacities of the Al_2Fe, Al_5Fe_2 and $Al_{13}Fe_4$ phases were considered in the Gibbs energy functions. An extended sublattice model had to be chosen to adapt the experimentally obtained [1, 2] non-stoichiometry of respective phases. The binary phase diagram, based on functions optimized with the PARROT module of Thermo-Calc, was calculated over the whole composition range and compared with all available phase diagram data. In addition fundamental thermochemical functions were calculated and compared to experimentally obtained heat capacities, activities at various temperatures, integral and partial mixing enthalpies of the liquid phase as well as enthalpies of formation at room temperature.

References

[1] K. Han, I. Ohnuma, R. Kainuma, J. Alloys Compd., **2016**, *668*, 97-106.

[2] X. Li, A. Scherf, M. Heilmaier, F. Stein, J. Phase Equilib. Diffus., **2016**, *37*, 162-173.

[3] G. Della Gatta, M. J. Richardson, S. M. Sarge, S. Stølen, Pure Appl. Chem., **2006**, *78*, 1455-1476.

[4] C. G. Maier and K. K. Kelley, J. Am. Chem. Soc., **1932**, *54*, 3243-3246.

[5] H. Kopp, Justus Liebigs Annalen der Chem., **1863**, *126*, 362-372.

[6] B. Sundman, I. Ohnuma, N. Dupin, U. R. Kattner, S. G. Fries, Acta Mat., **2009**, *57*, 2896-2908.

O–ML 01

Partitioning of elements in multi-phase alloys: modeling vs experiment

David Holec[1], Thomas Klein[1], Christoph Turk[1,2], Svea Mayer[1], Sophie Primig[3], and Helmut Clemens[1]

[1]Department of Physical Metallurgy and Materials Testing, Montanuniversiät Leoben, Leoben, Austria, david.holec@unileoben.ac.at, thomas.klein@unileoben.ac.at; svea.mayer@unileoben.ac.at, helmut.clemens@unileoben.ac.at

[2]Böhler Edelstahl GmbH & Co KG, Kapfenberg, Austria, christoph.turk@bohler-edelstahl.at

[3]School of Materials Science and Engineering, UNSW Sydney, Sydney, Australia, s.primig@unsw.edu.au

Introduction

Quantum mechanical modeling has become an integral part of the modern materials science. Due to the recent developments in its implementation as well as available computational resources it is nowadays possible to tackle problems of relevance even for complex multi-component and multi-phase systems of a practical relevance. In this contribution we will present several examples of modelled partitioning of elements in multi-phase systems which are corroborated by experimental observations using advance analytical techniques.

Materials and Methods

Quantum mechanical calculations were carried out within the framework of density functional theory (DFT) as implemented in the Vienna Ab initio Simulation Package [1] together with the generalized gradient approximation for electron-electron interactions [2]. Special quasi-random structures were constructed to account for the chemical and/or magnetic disorder [3].
Energy of formation per atom, E_f, is defined as

$$E_f(X) = E_{tot}(X) - \frac{\sum N_i \mu_i}{\sum N_i} \tag{1}$$

where X is the considered phase represented by a supercell consisting of N_i atoms of species i with the chemical potential μ_i. The chemical potential is typically set to the energy of the stable bulk phases of the species i, e.g., face centered cubic structure for Al etc. A prediction of partitioning of an element Y is subsequently given by Y contained in the considered (co-existing) phases, so that it minimizes the resulting overall energy of formation.
The supercell approach implies a practical obstacle since different unit cell sizes of the considered phases often result in (slightly) different numbers of atoms in the supercell, and hence in different concentrations of the alloyed element Y. The simplest approach to resolve this problem is to use linear interpolation of E_f between two close concentrations of Y, and hence to put the evaluation of the multi-phase configurations on an equal footing.

Results and Discussion

The above described method has been applied to two different alloying systems, namely intermetallic Ti-Al and Fe-Co alloys. In both cases, the DFT-based predictions were confirmed by atom probe tomography (APT) analyses.
Regarding the Ti-Al alloys (namely, so-called TNM alloys), the first principles calculations predicted Mo partitioning into the cubic β_o phase and an accompanied destabilization of the hexagonal ω_o phase. This prediction was confirmed by APT measurements and transmission electron microscopy [4]. Moreover, the calculated charge redistribution maps suggested that if Mo replaces Nb in the hexagonal ω_o phase, which is the energetically preferred site for Mo, it eventually leads to a charge redistribution on the neighboring Ti atoms to strengthen Mo-Ti bonds and a consequent weakening of the remaining bonds [4].
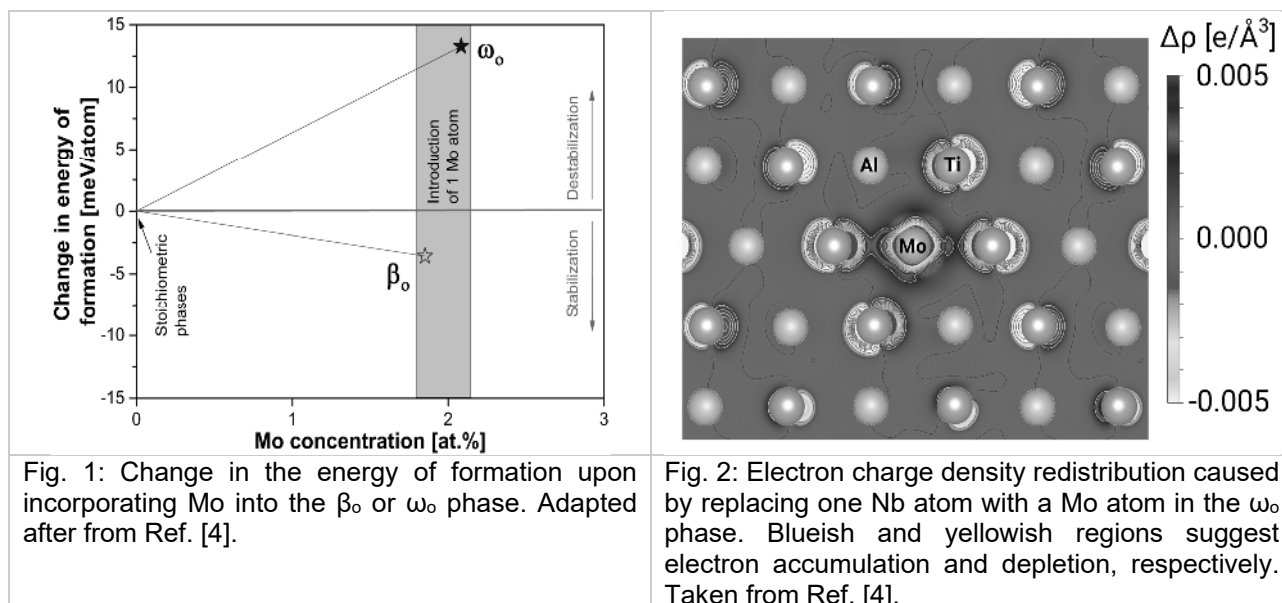
| Fig. 1: Change in the energy of formation upon incorporating Mo into the β_o or ω_o phase. Adapted after from Ref. [4]. | Fig. 2: Electron charge density redistribution caused by replacing one Nb atom with a Mo atom in the ω_o phase. Blueish and yellowish regions suggest electron accumulation and depletion, respectively. Taken from Ref. [4]. |

A second example concerns Si in the so-called TNM+ alloy [5]. The DFT calculations indeed confirmed the observation-based hypothesis that Si preferentially segregates in the ω_o phase, followed by the α_2 and γ phases, and being least favorable when solved in the β_o phase. By establishing this partitioning we were able to suggest that ζ-silicides, responsible for the Si-induced strengthening of the alloy, were most likely to precipitate from the β_o phase.

A final example includes the Fe-Co-Mo system and partitioning of a series of industrially relevant alloying elements into the μ-phase ($Mo_6[Fe_{1-x}Co_x]_7$) or the parent matrix ($Fe_{1-x}Co_x$). Our calculations suggest that Cu, Nb, Ti and V prefer the matrix while B, C, Cr, Mn, Ni, and Si preferably segregate into the μ-phase. These predictions have been confirmed by preliminary APT experiments. Moreover, our calculations predict that Ti and V stabilize the $Fe_{0.7}Co_{0.3}$ alloy while Si and Cr stabilize the μ-phase ($Mo_6[Fe_{0.7}Co_{0.3}]$).

References

[1]   G. Kresse, J. Furthmüller, Comput. Mater. Sci. **1996**, *6,* 15–50.

[2]   J.P. Perdew, K. Burke, M. Ernzerhof, Phys. Rev. Lett. **1996**, *77*, 3865–3868.

[3]   S.-H. Wei, L.G. Ferreira, J. Bernard, A. Zunger, Phys. Rev. B: Condens. Matter. **1990**, *42*, 9622–9649.

[4]   T. Klein, M. Schachermayer, D. Holec, B. Rashkova, H. Clemens, S. Mayer, Intermetallics **2017**, *85*, 26–33.

[5]   T. Klein, B. Rashkova, D. Holec, H. Clemens, S. Mayer, Acta Mater. **2016**, *110*, 236–245.

O–ML 02

Ab-initio study of C and N point defects in Fe₂Nb C14 Laves phase

Alvin Noe Ladines, Ralf Drautz and Thomas Hammerschmidt

ICAMS, Ruhr-Universität Bochum, Universitätstr. 150, Bochum, Germany,

alvin.collado@rub.de, ralf.drautz@rub.de, thomas.hammerschmidt@rub.de

Introduction

Nb is an important alloying element in steels due to its positive impact on high temperature mechanical properties. It has a high affinity to C which also makes it beneficial for corrosion resistance in chrome steels. However, the Nb content in steels is limited by the formation of Fe₂Nb Laves phase precipitates. These coarsen with time especially at high temperatures leading to reduced mechanical properties and subsequent failure of the material. The formation of Laves phase in Nb-alloyed steels can be controlled by the addition of C and N. They are generally known to inhibit the formation of Laves phases but the solution behavior of C and N in Fe₂Nb Laves phase is unclear from experiments [1,2]. In this study, the solution and interaction energies of C and N in the Fe₂Nb Laves phase C14 were calculated from DFT.

Materials and Methods

The DFT calculations were carried out using the VASP [3] code employing the PAW formalism. The p-semicore states of Fe and Nb and the valence states of C and N were calculated self-consistently. The exchange-correlation energy was evaluated from the PBE parameterization of the generalized gradient approximation [4]. A plane wave cut-off energy of 450 eV and Monkhorst-Pack k-points grid of 8x8x4 corresponding to the 12-atom primitive cell of the C14 Laves phase were used to converge the total energies to less than 2 meV/atom. A smearing width of 0.1 eV was applied to the occupation of the electronic states using the method of Methfessel and Paxton [5] during relaxations. The linear tetrahedron method with Blöchl corrections [6] was used for k-space integration to evaluate the total energies. To calculate the solution energies, a 2x2x2 supercell was constructed to minimize the interaction of the point defects with their images. The size of the supercell was increased to 3x3x2 containing 216+2 atoms for the calculation of the interaction energy of two point defects in C14-Fe₂Nb Laves phase. A full relaxation of the ionic positions and lattice vectors of the supercells was performed starting from the optimized values of primitive cell. The solution energy of a point defect X = C, N

$$E_{\text{sol}} = E(\text{Fe}_2\text{Nb} + \text{X}) - [E(\text{Fe}_2\text{Nb}) + E_{\text{ref}}(\text{X})] \qquad (1)$$

was calculated for all inequivalent interstitial sites in C14-Fe₂Nb. The interaction energy between two interstitial atoms is given by

$$E_{\text{int}}(\text{X}_1, \text{X}_2) = E(\text{X}_1 + \text{X}_2) - [E(\text{X}_1) + E(\text{X}_2) - E(\text{Fe}_2\text{Nb})]. \qquad (2)$$

The first term is the energy of the cell containing both defects while the second term contains the energy of the isolated defects and the bulk.

Results and Discussion

The solution energies of C and N as substitutional and interstitial defects are shown in Fig. 1. C and N are not stable in 9 of 18 inequivalent interstitial sites in C14-Fe₂Nb and relax to one of the stable sites. In general, the interstitial sites are more energetically more favourable compared to the substitutional sites for a C/N point defect. As expected, the solution energy decreases with the number of Nb neighbors due to the increase of the volume of the interstitial void. The scatter in the solution energies can be attributed to the dependence of the solution energy also to the local environment of the interstitial site. Our results suggest a low solubility for C in Fe₂Nb since the

minimum interstitial solution energy is around 1 eV. In contrast, the minimum solution energy of interstitial N is close to zero which suggests that N dissolves readily in C14-Fe_2Nb. Previous DFT calculations show similar solution behaviour of C and N in bcc-Fe with solution energies of 0.6 eV and 0.05 eV, respectively [7]. Our finding is consistent with an experiment suggesting the existence of Fe_2Nb Laves phase precipitates in nitrided steels but not after carburization [8]. Moreover, it is unlikely that the observed transformation of the Fe_2Nb Laves phase precipitates into NbC involves the diffusion of C into the Laves phase.

The interaction energy of a pair of C/N atoms at the interstitial sites with the lowest solution energy is plotted in Fig. 2 as function of the separation distance. The N-N interaction is consistently attractive which suggests a strong clustering tendency of N interstitials in Fe_2Nb Laves phase. The oscillating behavior of C-C interaction energy with distance reflects the strong direction dependence of the C bond with the neighboring Nb atoms.
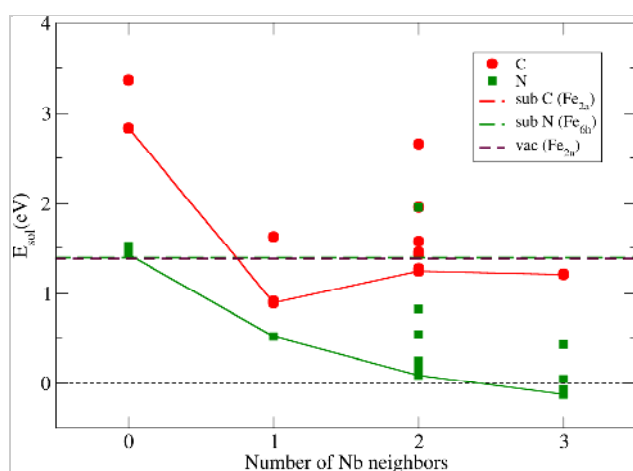
Fig. 1: Solution energies of interstitial and substitutional C and N as function of the number of nearest-neighbor Nb atoms [9].
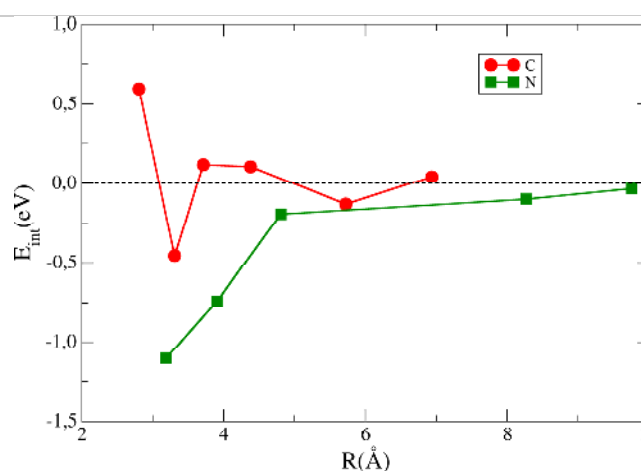
Fig. 2: Interaction energy of C and N pairs as function of distance [9].

References

[1] L.M. Lundin, Scripta Materialia. **1996**, *34*, 741–747.

[2] O. Dmitrieva, D. Ponge, G. Inden, J. Milln, P. Choi, J. Sietsma, D. Raabe, Acta Materialia. **2011**, *59*, 364–374.

[3] G. Kresse, J. Hafner. Physical Review B. **1993**, *47*, 558–561.

[4] J.P. Perdew, K. Burke, M. Ernzerhof, Physical Review Letters. **1996**, *77*, 3865–3868.

[5] M. Methfessel, A. T. Paxton., Physical Review B. **1989**, *40*, 3616-3621.

[6] P.E. Blöchl, O. Jepsen, O.K. Andersen. Physical Review B. **1994**, *49*, 16223–16233.

[7] A.F. Bialon, T. Hammerschmidt, R. Drautz., Physical Review B. **2013**, *87*, 104109-104121.

[8] S. Huth, W. Theisen, Powder Metallurgy. **2009**, *52*, 90–93.

[9] A.N. Ladines, R. Drautz., T. Hammerschmidt, J. Alloys Comp. **2017**, *693*, 1315-1322.

O–ML 03

Prediction of formation enthalpies using machine learning techniques for C14-Laves phase

Satoshi Minamoto[1], Toshiaki Horiuchi[2,3] and Seiji Miura[4]

[1] National Institute for Materials Science, Tsukuba, Ibaraki, Japan,
MINAMOTO.satoshi@nims.go.jp

[2]Division of Mechanical Engineering, Graduate School of Engineering,
Hokkaido University of Science

[3]Laboratory of Advanced Materials for Cold Region (LAM), Hokkaido University of Science,
7-15-4-1, Maeda, Teine-ku, Sapporo, Hokkaido 006-8585, Japan, horiuchi@hus.ac.jp

[4]Division of Materials Science and Engineering, Faculty of Engineering, Hokkaido University, Kita
13 Nishi 8, Kita-ku, Sapporo 060-8628, Japan, miura@eng.hokudai.ac.jp

Introduction

In the CALPHAD calculation, evaluation of interaction parameters between elements in a phase are crucial. Although the enthalpies of formation of end-members (the stoichiometric compounds formed when only one constituent is present in each sublattice) for the phase is important for the evaluation of the interaction parameters in multi-component system, it is very difficult to obtain experimental data, particularly for unstable phases. When evaluating the stability of the compound phase in a multi-component, composition continuity of solid solution among two or three intermetallic compounds is often difficult to evaluate. So far, prediction for the ternary system has been done by using for example the extended Miedema's model [1], while it seems that the accuracy of the prediction is insufficient. Therefore more precise estimation by using theoretical calculation is indispensable to improve the accuracy.

Methods

In this study, we assumed a hypothetical ternary compound constructing C14 Laves phase, and aimed to build a prediction model with better accuracy than existing models. We divided the C14 Laves structure into three sub-lattices based on the Wyckoff coordinates information. By assuming that 7 kinds of elements (Al, Nb, Cr, Ni, Co, Mo, Zr) could be contained in each sublattice, total of 343 first-principles energy calculations were performed for the end-members.
After examining the relationship between some physical property values and enthalpy of formation, some descriptors such as electron concentration and atomic radius based on the concept of Hume-Rothery rule are selected, and we built a model with the descriptors. Regarding the atomic radii, the Goldschmidt radii were used. For the number of average electron concentration per atom (e/a), the values obtained from the results of the first-principles calculation using the FLAPW-Fourier method [2] were used. Then we applied several machine learning methods, linear model, neural net, random forest, Cubist model and gradient boost technique. Furthermore, a prediction model was also examined for comparison with the one using VEC (valence electron concentration) as a descriptor, which is another way to express the electron concentration.

Results and Discussion

As a result of examining several machine learning models, by using the Cubist model and the gradient boost method, we have constructed a model that could predict with sufficient accuracy of several kJ per mol, regardless of positive or negative enthalpy of formation. The verification results evaluated by several models are shown in Fig. 1. Although there is no clear correlation between each descriptor and the formation enthalpy, we can associate them by incorporating machine learning method. In multi-component systems, electron concentration and atomic radius are found to be very important parameter.
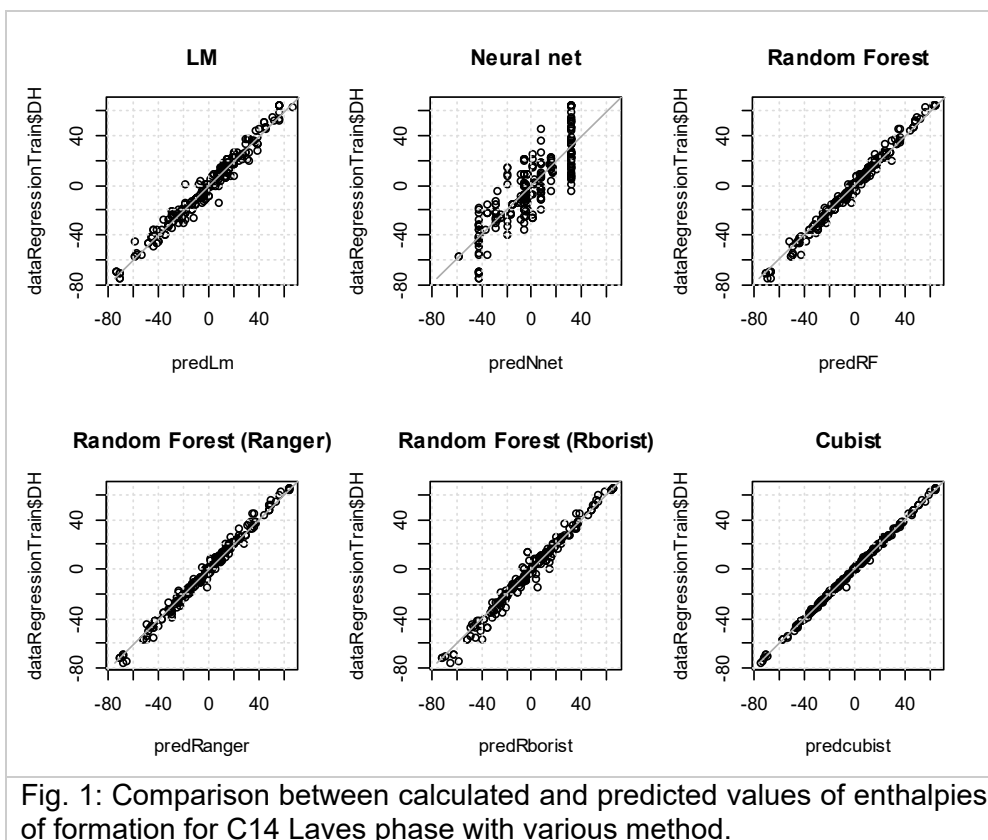
Fig. 1: Comparison between calculated and predicted values of enthalpies of formation for C14 Laves phase with various method.

References

[1] Ray, P. K., M. Akinc, and M. J. Kramer., *J. ALLOY COMPD.,* 489.2, **2010**, 357-361.

[2] R. Asahi, H. Sato, T. Takeuchi, and U. Mizutani, Phys. Rev. B 72, **2005**, 25102

O–ML 04

Investigation of precipitation and stability of complex intermetallic phases in a Co-3.9Nb alloy

Toshiaki Horiuchi[1,2], Frank Stein[3], Kohei Abe[4] and Konatsu Yamada[5]

[1]Division of Mechanical Engineering, Graduate School of Engineering,
Hokkaido University of Science

[2]Laboratory of Advanced Materials for Cold Region (LAM), Hokkaido University of Science,
7-15-4-1, Maeda, Teine-ku, Sapporo, Hokkaido 006-8585, Japan, horiuchi@hus.ac.jp

[3]Max-Planck-Institut für Eisenforschung GmbH
Max-Planck-Straße 1, D-40237 Düsseldorf, Germany, f.stein@mpie.de

[4]Division of Mechanical Engineering, Graduate School of Engineering, Hokkaido University of
Science, 7-15-4-1, Maeda, Teine-ku, Sapporo, Hokkaido 006-8585, Japan, q15101@hus.ac.jp

[5]Department of Mechanical Engineering, Faculty of Engineering, Hokkaido University of Science,
7-15-4-1, Maeda, Teine-ku, Sapporo, Hokkaido 006-8585, Japan, 1143030@stu.hus.ac.jp

Introduction

The Co-Nb binary system contains several complex intermetallic phases such as three types of Laves phases and the monoclinic phase Nb_2Co_7 that show interesting features [1-3]. The authors have previously reported that the precipitation behavior of intermetallic phases from the supersaturated Co solid solution of a Co-3.9 at.%Nb alloy is fairly complex [4]. The stability of the phases and the mechanisms behind that are still unclear. In the present study, a Co-3.9 at.%Nb alloy was prepared and heat-treated at various conditions in order to elucidate in detail these transformation and precipitation processes and phase stability.

Materials and Methods

The preparation of the Co-3.9 at.%Nb alloy was previously reported [4]. The differential thermal analysis (DTA) experiments were not only used to measure all occurring thermal effects but also to produce samples for further investigations under precisely controllable conditions in various stages of the transformation and precipitation process. The alloy was homogenization heat treated at 1240°C resulting in a single-phase fcc-Co solid solution and was subsequently cooled to 700°C/900°C/1000°C and kept for up to 100 h for isothermal heat treatments in order to elucidate various transformation and precipitation processes. In addition, long-term isothermal heat treatments of ϕ20 mm cylindrical specimens at 700°C or 900°C for 3000 h after homogenization heat treatment at 1240°C were also carried out to investigate the stability of the phases. Microstructure and crystal structure were observed and analyzed by scanning electron microscopy, transmission electron microscopy, X-ray diffraction and electron backscatter diffraction pattern analysis.

Results and Discussion

The DTA heat-flow curves during cooling after homogenization heat treatment at 1240°C are shown in Fig. 1. A distinct exothermic reaction peak was observed at around 790°C in some heat-treatment conditions even though in this temperature range there is no phase boundary in the equilibrium phase diagram. Although the peak intensity reduced with increasing isothermal holding time at 900°C, the onset temperature of the exothermic effect remained almost constant. After an isothermal heat treatment at 900°C for more than 10 h, no peak appeared during cooling. The Co matrix after direct cooling from 1240°C to room temperature has an fcc structure and the microstructure appears as single-phase Co solid solution without any visible precipitates. However, as shown in Fig. 2, detailed high-resolution TEM observation revealed that it contained finely dispersed $L1_2$ ordered regions with a significantly increased Nb content whereas Nb-depleted regions only showed basic fcc spots. This $L1_2$-type ordering was also confirmed by XRD. In addition, Shinagawa et al. reported that a metastable Co_3Ta $L1_2$ ordered phase exists in the Co-Ta binary system which has similar

characteristics in its phase diagram to the Co-Nb system [5]. These facts indicate the occurrence of a metastable disorder-order transformation from supersaturated fcc-Co to Co_3Nb $L1_2$ ordered phase during the solid state reaction observed below 791°C.

A distinct Widmannstätten-like discontinuous precipitation microstructure was observed after isothermal heat treatment at 900°C for more than 1 h, indicating rather fast precipitation reaction of an intermetallic phase from supersaturated Co solid solution. On the other hand, the underlying Co matrix was found to have an hcp structure in contrast to the expectations from the equilibrium phase diagram. The stability of these phases will be discussed in detail in the presentation by the results of long-term isothermal heat treatments of the specimens.
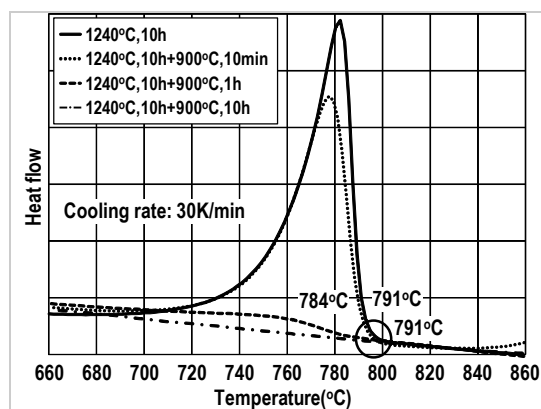
| Fig. 1: DTA heat-flow curves during cooling of Co-3.9 at%Nb alloy after homogenization heat treatment at 1240°C. | Fig. 2: (a) HAADF-STEM image of Co-3.9 at%Nb alloy after homogenization heat treatment at 1240°C, (b) magnified image from (a), (c) magnified image of double-lined square in (b), (d) diffraction pattern from double-lined square in (b) showing $L1_2$ superlattice spots, (e) diffraction pattern from broken-lined square in (b) showing only the spots of the disordered fcc solid solution. |
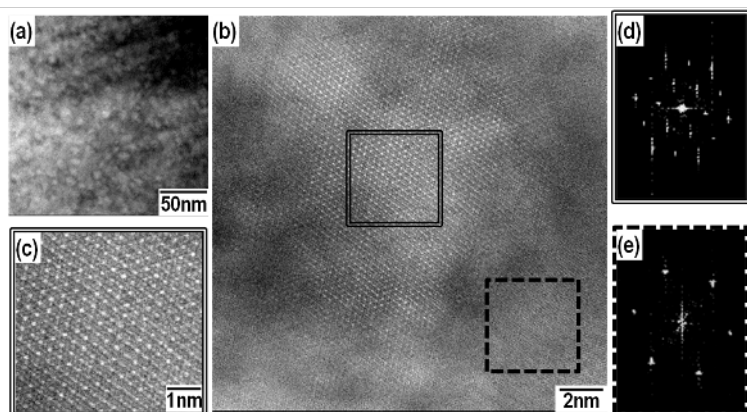
Acknowledgement

References

[1] F. Stein, D. Jiang, M. Palm, G. Sauthoff, D. Grüner, G. Kreiner: Intermetallics, **2008**, *16*, 785-792.

[2] A. Leineweber, G. Kreiner, D. Grüner, R. Dinnebier, F. Stein: Intermetallics, **2012**, *25*, 34-41.

[3] L. Siggelkow, U. Burkhardt, G. Kreiner, M. Palm, F.Stein: Materials Science and Engineering A, **2008**, *497*, 174-180.

[4] T. Horiuchi and F. Stein: Proc. Intermetallics 2015, Bad Staffelstein, Germany, **2015**.

[5] K. Shinagawa, H. Chinen, T. Omori, K. Oikawa, I. Ohnuma, K. Ishida, R. Kainuma: Intermetallics, **2014**, *49*, 87-97.

O–CO 01

MoSi$_2$ – a candidate material for biomass gasification atmospheres

Uwe Gaitzsch, Gunnar Walther, Thomas Weißgärber and Bernd Kieback

Fraunhofer Institut für Fertigungstechnik und Angewandte Materialforschung,
Winterbergstraße 28, 01277 Dresden, Germany
uwe.gaitzsch@ifam-dd.fraunhofer.de

Introduction

Biomass gasification coupled to gas engine driven electric generators are an important decentral energy source in the context of providing green energy [1,2]. Depending on the "purity" of the biomass a lot of corrosion facilitating media can be found, such as chlorine or sulfur containing species [3]. This results in special requirements for the materials in biomass gasification reactors. Gas inlet nozzles are the most stressed parts in gasification plant, both thermally and chemically. MoSi$_2$ was tested as an alternative material to commercially available and customized metallic alloys such as IN 625 or FeCrAl Alloys. Its capability of forming silicon oxide as a protective layer combined with the good self-healing properties make molybdenum disilicide a promising candidate for biomass gasification devices.

Materials and Methods

MoSi$_2$ was synthesized by alloyed powder provided by H.C. Starck. Thermogravimetry (TG) was used to characterize the oxidation behaviour in air. Synthetic biomass gasification atmosphere was used to test the material up to 1000 h at 1000°C. These tests were conducted by Fraunhofer Umsicht in Sulzbach-Rosenberg. The composition of the atmosphere is listed in table 1.

Table 1: composition of the synthetic gasification atmosphere

Gas	N$_2$	CO	CO$_2$	H$_2$	CH$_4$	O$_2$	H$_2$O	H$_2$S	Cl$_2$
Conc.	Bal. (~48)	18.5	12	10	5	0	6.5	0.030	0.002

The samples were half embedded in real biomass gasification ash provided by Qalovis. The composition of the main constituents is listed in table 2. The ash was not stable during the process due to formation of carbon oxides and was therefore refilled after 500 h. However the consumption of the ash took less than 500 h.

Table 2: main ash elements (XRF analysis)

Element	C	O	Si	Ca	K
conc	77.2	15.8	0.9	2.1	1.8

Results and Discussion

The TG results in a mass loss of 0,01 % after an initial period of 10 minutes at 1000°C. After that the mass is roughly constant. The mass loss is highly probable due to the evaporation of molybdenum oxide, which is partly compensated by the oxidation of Si to SiO$_2$. Once a dense layer of SiO$_2$ is formed the mass loss stops and the TG curve flattens out. A small increase of mass is to be expected due to the silicon oxide growth, but it was below the detection limit. SEM investigations revealed the oxide layer to be below 1 µm after 10 h of exposure.

After 233 h exposure at 850°C the oxide layer grew significantly in the gasification atmosphere test. Elements of the ash (Ca, K) were incorporated in the layer. No signs of internal oxidation were detected below the outer oxidation / reaction layer. Only traces of Fe and a second Mo-Si-Phase were detected in the bulk material. It should be noted, that they were already present in the hot pressed state. The thickness of the layer was determined by SEM to be about 2.4 µm (s. Fig. 1). In contrast, a reaction layer of 80 µm was detected on IN 625. The Fe-Cr-Al alloys were chemically stable at this temperature, only a 3 µm surfacial oxide was detected.
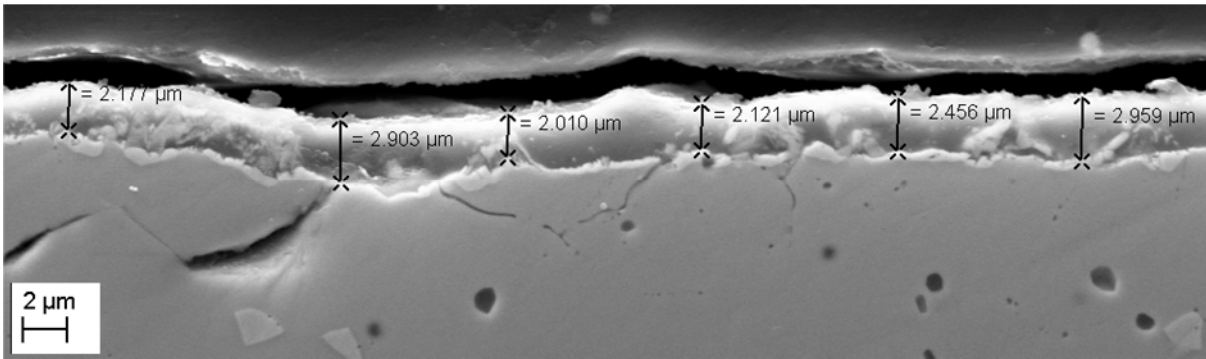
Fig. 1: $MoSi_2$ cross section after exposure to a biomass gasification-like atmosphere for 233 h at 850°C [4].

$MoSi_2$ resisted the corrosive atmosphere and ashes over a period of 1000 h, also at 1000 °C. After the test at 1000°C the oxide / reaction layer increased in size and some droplets were found on the surface. The thickness was less homogeneous and varied between 5.2 µm and 6.7 µm. An arithmetic mean of 6 µm was calculated from 10 thickness measurements. Some molybdenum rich inclusions were detected inside the reaction layer. And EDX mapping is shown in Fig. 2.
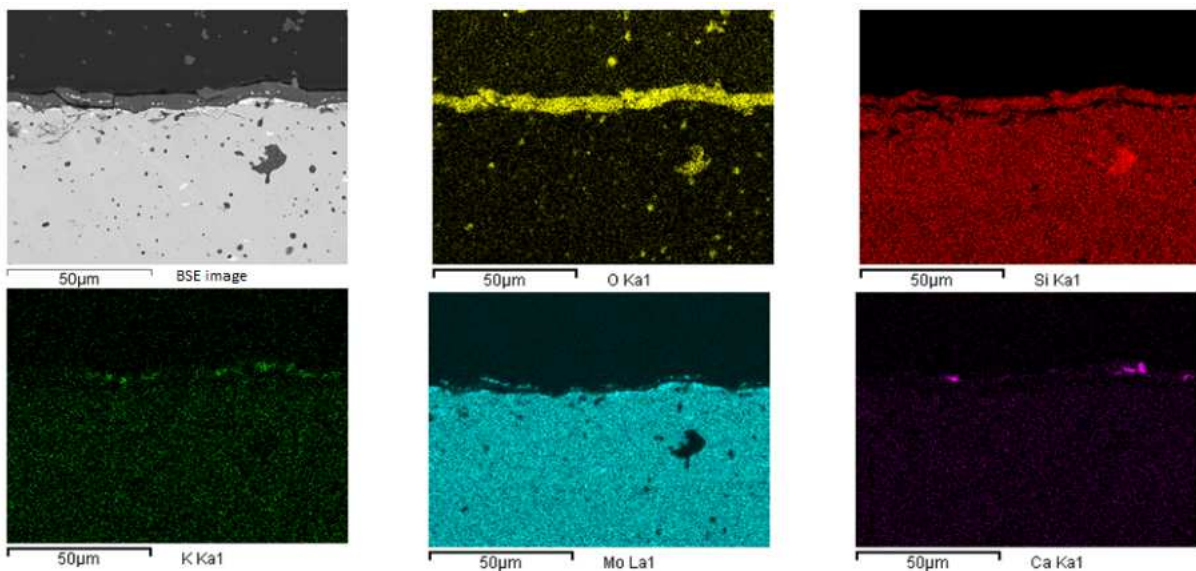
Fig. 2: EDX mapping of $MoSi_2$ cross section after exposure to synthetic biomass gasification atmosphere at 1000 °C

In addition to that joining of $MoSi_2$ to Nicrofer 3220H (alloy 800, 1.4876) was attempted. Several copper bases solders were investigated. A silicon diffusion barrier layer containing a refractory metal were implemented in the process, as well. Details will be revealed in the presentation.

References

[1] D. Pfeiffer, C. Krebs, J. Liebetrau, J. Zosel, M. Schelter, G. Haring, M. Somileitner, W. Zorner, Efficiency enhancement of biogas plants - results from the national funding program "biomass energy use," EU BCE 2012 20th Eur. Biomass Conf. Exhib. Setting Course Biobased Econ. Proc. **2012**. 1450–6.

[2] J. Werther, M. Saenger, E.U. Hartge, T. Ogada, Z. Siagi, Combustion of agricultural residues, Prog. Energy Combust. Sci., **2000**. 26, 1–27.

[3] B.M. Jenkins, L.L. Baxter, T.R. Miles, T.R. Miles, Combustion properties of biomass, Fuel Process. Technol., **1998**. 54. 17–46.

[4] T. Weißgärber, Refractory Metal Based Materials for Applications at High Temperatures, World PM 2016 Proc., **2016**. 1–4.

O–CO 02

Oxidation protection of gamma-TiAl by the F-effect – towards an industrial application

Hans-Eberhard Zschau[1], Bernd Möller[2], Dietmar Emig[2], Mathias C. Galetz[3], Michael Schütze[3]

[1]Werkstoffprüfung und –forschung, Roitzscher Weg 32 c, D-04808 Wurzen, Germany, Email: dr.zschau@hotmail.com

[2]Fluor Technik System GmbH, Altebergstraße 27-29, D-36341 Lauterbach, Germany, Email: b.moeller@fts-de.com   d.emig@fts-de.com

[3]DECHEMA-Forschungsinstitut, Theodor-Heuss-Allee 25, D-60486 Frankfurt, Germany, Email: galetz@dechema.de   schuetze@dechema.de

Introduction

The oxidation of γ-TiAl alloys at temperatures above 800°C shows the formation of a non-protective mixed oxide scale of TiO_2 / Al_2O_3 on the surface. A surface modification with fluorine changes the oxidation mechanism into the growth of a dense protective alumina scale. This Fluorine effect was explained in a thermodynamic model [1]. The beam line ion implantation was used to meet the conditions predicted by the thermodynamic model [2]. However, a cost-effective method of surface doping with fluorine in an industrial scale is still missing. In the present work the gas phase fluorination is applied to meet the conditions for the F-effect. The results obtained with ion implantation serve as a benchmark to identify the suitable gas phase fluorination parameters.

Materials and Methods

The commercial alloy TNB-V5 with elemental composition (Ti-45Al-5Nb-0.2B-0.2C, in at.%) was chosen for a preliminary study. The alloy was cut in coupons with size of 10 x 10 x 2 mm^3 followed by polishing of both sides down to 4000 grit. After ultrasonic cleaning the samples were exposed in the industrial fluorination equipment of Fluor Technik System GmbH (FTS). A gas atmosphere of (Ar-10%F_2) was used. As parameters suitable for the fluorination the temperature, time of exposition and the gas pressure were varied. The gas fluorination was performed using 5 parameter sets A, B, C, D, and F. The non-destructive PIGE (Proton Induced Gamma-ray Emission) was used to determine the F-depth profiles non-destructively. The PIGE-measurements were carried out at the 2.5 MV Van de Graaff-accelerator of the Goethe-University Frankfurt. The depth profiling was performed by using the nuclear reaction $^{19}F(p, \alpha\gamma)^{16}O$ at a resonance energy of 484 keV. A NaI(Tl) scintillation counter detected the high energetic γ-rays (5-7 MeV). After F-treatment the samples were oxidized isothermally in lab air at 900°C for 42-90 hours. Finally metallographic cross-sections were prepared for studying the oxide structure by using SEM/EDX.

Results and Discussion

The F-treatment by using beam line ion implantation showed the best results so far for the F-effect between the implantation parameters of 1 x 10^{17} and 2 x 10^{17} F cm^{-2} / 20 keV. The maximum F-content was found between 20 – 40 at.%.

The results show a strong dependence of the obtained F-depth profiles with respect to the parameter set of gas fluorination (temperature, exposition time, gas pressure). Especially the parameter set C showed the highest F-enrichment with a maximum F-concentration of 25 at.% and an integral F-dose of 1.1 x 10^{17} F cm^{-2} (fig. 1). These values meet the lower part of the corridor recommended by

F-implantation studies as mentioned above. After implantation (48 h/900°C) a protective alumina scale on the surface was formed (fig. 2).

In an ongoing project further investigations are planned to reach this corridor for other commercial gamma-TiAl alloys via a gas phase fluorine treatment which was developed for the treatment of polymers and is currently being adapted for metals.
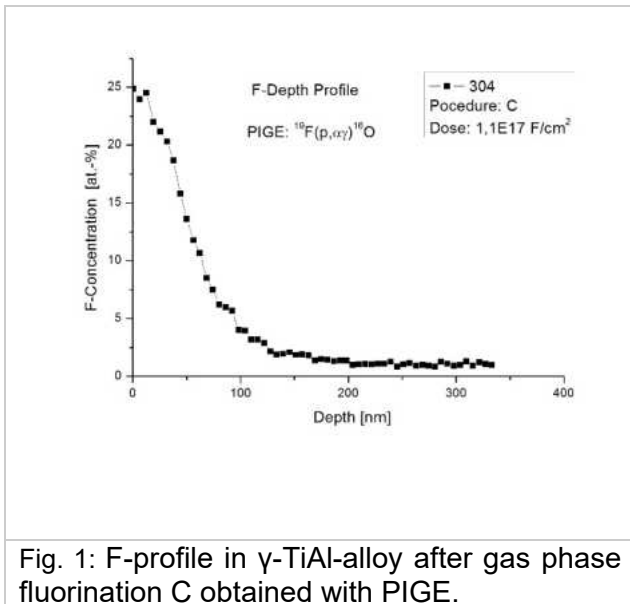

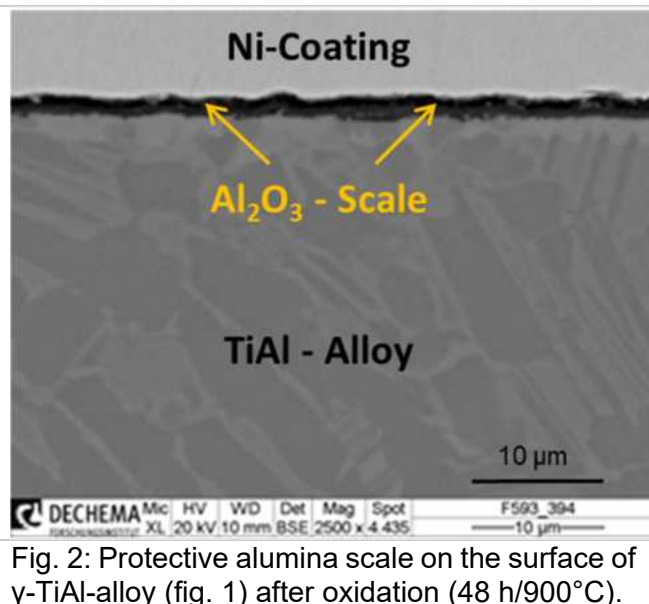| Fig. 1: F-profile in γ-TiAl-alloy after gas phase fluorination C obtained with PIGE. | Fig. 2: Protective alumina scale on the surface of γ-TiAl-alloy (fig. 1) after oxidation (48 h/900°C). |

References

[1] A. Donchev, B. Gleeson, M. Schütze, Intermetallics. 11, **2003,** 387-398.

[2] H.-E. Zschau and M. Schütze, in: Mark S. Goorsky (Ed.): Ion Implantation. InTech, Rijeka, **2012**, 409-436. Ebook: http://www.intechopen.com/books/ion-implantation

O–CO 03

High temperature oxidation behavior of TiAl based alloys

Alexander Donchev[1], Svea Mayer[2], Helmut Clemens[2] and Mathias Galetz[1]

[1]DECHEMA Forschungsinstitut, Theodor-Heuss-Allee 25, D-60486 Frankfurt, Germany, donchev@dechema.de

[2]Department of Physical Metallurgy and Materials Testing, Montanuniversität Leoben, Roseggerstr. 12, A-8700 Leoben, Austria, svea.mayer@unileoben.ac.at

Introduction

Intermetallic alloys based on the γ-TiAl phase are promising candidates for numerous high temperature applications [1]. Such alloys are already used as low pressure turbine blades in several jet engines [2]. One major drawback for a wider operating temperature range and consequently distribution of this class of materials is their limited high temperature oxidation resistance in oxidizing environments [3]. Therefore, the oxidation resistance has to be improved. The fluorine effect is the only reported surface treatment which lets TiAl withstand temperatures up to 1050°C, exposure times longer than 8000 hours and wet environments [4]. In this work results of isothermal and thermocyclic high temperature exposure tests with different commercially used TiAl alloys will be presented. The oxidation behavior of the untreated and fluorinated materials will be compared. The outcome will be discussed in view of a use of the alloys at temperatures higher than the ones reached so far.

Materials and Methods

Coupons of several technical TiAl alloys were cut from sheets and rods. The coupons of the size (15 x 10 x 2 mm^3) were ground to 1200 grit with SiC paper, cleaned ultrasonically in ethanol and dried in air. Such prepared specimens were exposed either isothermally or thermocyclically in the temperature range from 800 – 900°C up to 8760h in dry air. The cycling test was performed in this way that the samples were placed in the hot furnace for 24h, removed from the furnace, cooled down to room temperature within 10min and put back into the hot furnace after 1h, i.e. total cycle duration of 25h. Fluorine was applied by spraying a fluorine containing polymer homogenously over the whole surface of the samples and drying those samples in air. This set of samples was exposed in the same way as described above. Post experimental investigations included mass change documentation, macroscopic inspection, metallographic preparation [5], light optical microscopy (LM), scanning electron microscopy coupled with energy dispersive X-ray spectroscopy (SEM/EDX) and electron probe micro analysis (EPMA). Before the metallographic preparation, the specimens were galvanically coated with a Ni layer to protect the oxide scales.

Results and Discussion

The untreated specimens always form a mixed oxide scale (TiO_2/Al_2O_3) in which also nitrides (TiN/AlN) are found (Fig. 1). Therefore, the mass gain is higher than that of the F-treated ones. The thickness of these mixed layers can vary depending on the chemical composition and the microstructure of the investigated TiAl alloys but still rather thin scales consist of both oxides [6]. The F-treated specimens are covered by a thin protective alumina layer (Fig. 2). This outcome is achieved for all materials independent of the composition or their constitution.

The mixed layers tend to spall during cooling from service temperature. The spallation of the oxide scale is caused by the stresses due to the mismatch between the thermal expansion coefficients of the intermetallic substrates and the oxides/nitrides. Such spallation of the oxide scale can lead to an accelerated attack after reheating and further use at elevated temperatures due to an increased diffusion of oxygen through the damaged scale. Therefore, the load bearing cross section will be consumed rather quickly. This can finally lead to premature failure of the TiAl components which has to be avoided.

The fluorine treated specimens do not show any tendency of spallation during thermocyclic exposure even after very long exposure times of several thousand hours or in wet environments [4]. The

protective alumina layer is slowly growing and free of defects. Thus, the oxidation kinetics stays very low and steady over the whole period of exposure time.

The protective fluorine effect is based on the almost exclusive intermediate formation of gaseous aluminum fluorides which are finally oxidized to alumina [7]. The oxidation mechanism is changed because the partial pressures of the aluminum fluorides are several orders of magnitude higher than those of any other metal fluorides (e.g. Ti, Nb, Cr,…) at the metal/oxide interface. Hence, after a short incubation period only alumina is formed instead of a mixed scale.

There are several treatments available for the fluorination of real components with complex geometry [8]. Liquid phase treatments by spraying or dipping at room temperature can be applied as well as gas phase treatments at elevated temperatures. All of them are economically usable and show the desired result. The liquid phase treatments require an activation step at elevated temperature to start the fluorine effect, while the gas phase treatment could be applied directly during service.
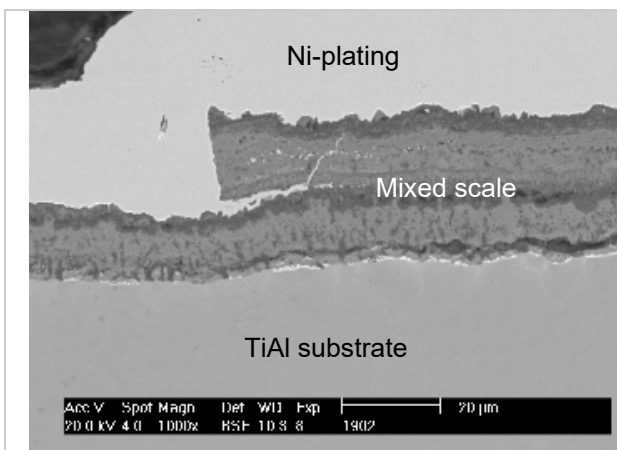
Fig. 1: SEM/BSE image of an untreated TiAl sample after thermocyclic exposure for 1200h at 900°C in laboratory air showing mixed oxide scale formation and partial spallation	Fig. 2: SEM/BSE image of a F-treated TiAl sample after thermocyclic exposure for 8760h at 900°C in laboratory air showing alumina formation and no spallation
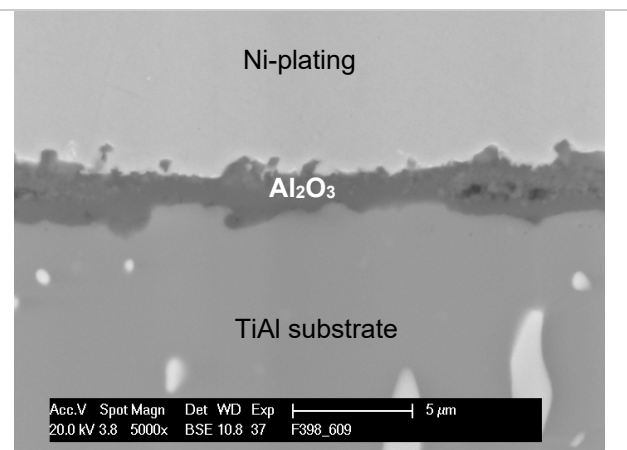
References

[1] S. Mayer, P. Erdely, F.D. Fischer, D. Holec, M. Kastenhuber, T. Klein, H. Clemens, Advanced Engineering Materials, 2017, DOI: 10.1002/adem.201600735.

[2] B.P. Bewlay, S. Nag, A. Suzuki, M.J. Weimer, Materials at High Temperatures, **2016**, 33, 549-559.

[3] G.H. Meier, F.S. Pettit, S. Hu, Journal de Physique IV, **1993**, 3, 395-402.

[4] A. Donchev, A. Kolitsch, W. Möller, M. Schütze, R. Yankov, in, Y.W. Kim, D. Morris, R. Yang, C. Leyens, (Eds.): Structural Aluminides for Elevated Temperatures, TMS Warrendale, **2008**, 323-332.

[5] E Berghof-Hasselbächer, S. Dilberto, P. Gawenda, P. Masset, G. Schmidt, M. Schütze, Sonderbänder der Praktischen Metallographie, **2008**, 40, 117-124.

[6] Y. Shida, H. Anada, Oxidation of Metals, **1996**, 45, 197-219.

[7] A. Donchev, B. Gleeson, M Schütze, Intermetallics, **2003**, 11, 387-398.

[8] A. Donchev, M. Schütze, A. Kolitsch, R. Yankov, MRS Symposium Proceedings, **2011**, 1295, 145-150.

O–CO 04

Investigation of the damage behavior of a β-stabilized TNM TiAl alloy by low cycle fatigue tests and hot corrosion experiments

Christian Löffl[1], Holger Saage[2] and Mathias Göken[3]

[1]Competence Center for Lightweight Design (LLK), Faculty for Mechanical Engineering, University of Applied Sciences Landshut, Germany, Christian.Loeffl@haw-landshut.de

[2]Competence Center for Lightweight Design (LLK), Faculty for Mechanical Engineering, University of Applied Sciences Landshut, Germany, Holger.Saage@haw-landshut.de

[3]Department of Material Science and Engineering Institute I, Friedrich-Alexander-University Erlangen-Nürnberg, Germany, mathias.goeken@fau.de

Introduction

High temperature structural components in aircraft turbines and internal combustion engines suffer from damage caused by a combination of fatigue, creep and corrosion. One of the innovative high-temperature light-weight materials specially developed for such applications are β-stabilized TNM TiAl alloys, whose maximum operating temperature is limited at about 850° C [1, 2]. The high temperature corrosion behavior was investigated by means of isothermal and cyclic TGA experiments under different composition of the atmosphere with oxygen, water vapor, nitrogen and sulfur dioxide (see for example in [3, 4]) in an uncoated and halogen coated state [5]. The thermomechanical damage behavior of TiAl alloys as well as the environmental influence (laboratory air and vacuum) was analyzed, for example, in [6-8]. However, the influence of an atmosphere close to realistic application conditions on the corrosion damage behavior has not yet been published.

Materials and Methods

The TiAl alloy TNM-B1 with a nominal chemical composition of Ti-43.5Al-4Nb-1Mo-0.1B (in atom percent) was obtained in the form of forging stocks in the cast/HIP state from the company GfE Metals and Materials GmbH, Nuremberg, Germany.

The damage behavior due to corrosion is analyzed with stationary thermal gravimetric analysis, TGA and with isothermal low cycle fatigue, LCF tests in synthetic air as well as reactive and inert atmospheres. The oxide layers and cracks formed during testing are examined without destruction ex- or in-situ by high resolution computer tomography (CT) as well as destructively by Scanning-Electron-Microscopy (SEM).

Results and Discussion

Figure 1 shows the cross-section of a sample which was exposed stationary to a reactive atmosphere at 850 °C for 100 hours by TGA. By comparison, Fig. 2 shows the cross-section of an LCF sample tested in the same atmosphere at a total strain amplitude of $\Delta\varepsilon/2 = 0.5\%$. The crack shown in Fig. 2 was formed after 875 cycles which corresponds to an experimental duration of about 5 hours. On the surface of both samples the same oxide structure has formed but with different thicknesses. Furthermore, along the crack path an oxide layer has developed with a comparable structure which led to crack closure during the LCF testing. Within the scope of the presentation, the results of experiments in reactive and inert atmospheres are presented and discussed in detail.
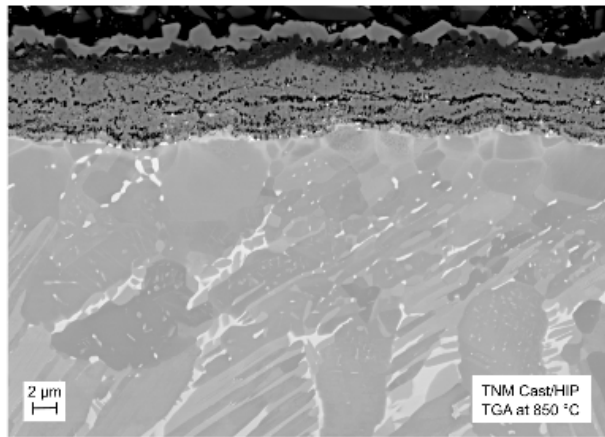
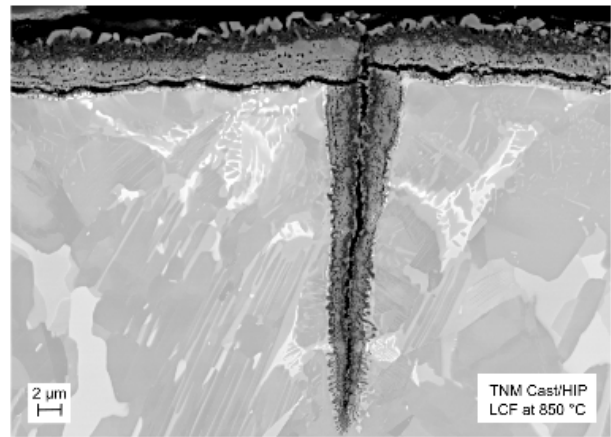| Fig. 1: Section of a TGA sample subjected to a reactive atmosphere for 100 h	Fig. 2: Section of a LCF sample after 875 cycles tested at a total strain amplitude of Δε/2 = 0.5% and the same reactive atmosphere of the sample in Fig.1

References

[1] H. Clemens, S. Mayer, Materials at High Temperatures. **2016**, 33, 560–570.

[2] H. Clemens, S. Mayer, Berg- und Hüttenmännische Monatshefte. **2011**, 156, 255–260, 2011.

[3] A. Rahmel, W.J. Quadakkers, M. Schütze, Materials and Corrosion. **1995**, 271– 285.

[4] R. Kremer, in: Untersuchung zur Hochtemperaturkorrosion heterogener (α2-γ) – und homogener γ-Titan-Aluminide, Ph.D. Thesis, Uni Erlangen-Nürnberg, **1996.**

[5] G. Hullin, in: Mikrostruktur und mechanische Eigenschaften gegossener TiAl-Legierungen, Dissertationsschrift FAU Erlangen-Nürnberg, **2015.**

[6] H.J. Christ, Materials Science & Engineering A. **2007**, 468 – 470, 98 – 108.

[7] M. Roth, H. Biermann, Scripta Materialia. **2006**, 54, 137–141.

[8] T. Heckel, H.J. Christ, Procedia Engineering. **2010**, 2, 845–854.

O–CO 05

Influence of the Al content on the aqueous corrosion resistance of binary Fe-Al alloys in H_2SO_4

Jian Peng[1], Frank Moszner[2], Dirk Vogel[1], Martin Palm[1]

[1] Max-Planck Institut für Eisenforschung GmbH, Max-Planck-Str. 1, 40237 Düsseldorf, Germany
j.peng@mpie.de

[2] Winterthur Gas & Diesel Ltd., Schützenstrasse 1-3, 8401 Winterthur, Switzerland

Introduction

Fe-Al-based alloys attract much attention for high temperature structural applications because of their outstanding physical and chemical properties. They exhibit a lower density of 5.7-6.7 g/cm^3 compared to other iron-base materials such as cast iron and stainless steels, superior high-temperature corrosion resistance, good wear resistance and low material costs [1, 2]. In addition, the equipment for their production and processing is readily available in industry [2]. Due to the practical and scientific importance, the aqueous corrosion behavior of Fe-Al-based alloys should be understood. A number of studies on the aqueous corrosion behavior of binary Fe-Al alloys have been reported so far, but they mainly focused on binary Fe-Al alloys with a limited variation in the Al content, e.g., (in at. %) Fe-28Al [3], Fe-40Al [4, 5], Fe-(8, 10, 22)Al [6] or Fe-Al alloys with additional alloying elements. A systematic investigation on the Influence of the Al content on the aqueous corrosion resistance of binary Fe-Al alloys is still needed. Therefore the aqueous corrosion behavior of binary Fe-Al alloys with Al contents up to 40 at. % was investigated in the present work.

Materials and Methods

A series of binary Fe-Al alloys with 5, 10, 15, 25, 30 and 40 at.% of Al were prepared by induction melting under argon atmosphere. H_2SO_4 with a pH of 1.6 was selected as the electrolyte. The three electrode-method [7] was employed for the electrochemical experiments. The Ag/AgCl reference electrode (3M KCl) was adopted. The open circuit potentials (OCPs) and potentiodynamic polarization curves were determined at 25 and 97 °C, respectively. Post mortem examination of the microstructures of the corroded samples were performed by scanning electron microscopy (SEM). A second series of the binary Fe-Al alloys was pre-oxidized before performing the electrochemical measurements.

Results and Discussion

All the potentials values obtained in the present work were converted into the value against a saturated calomel electrode (SCE).
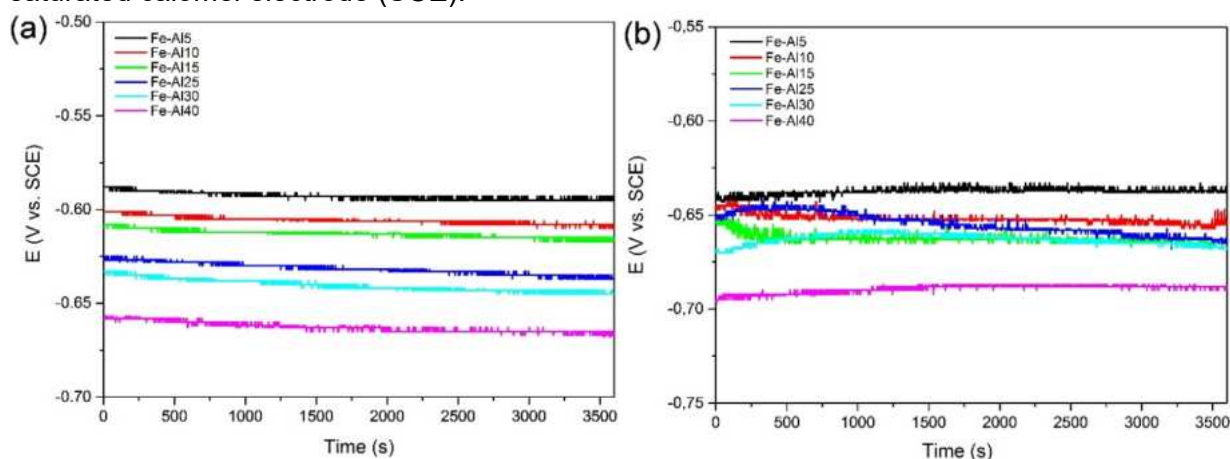
Fig. 1 The OCPs of binary Fe-Al alloys in H_2SO_4 of a pH 1.6 at (a) 25 °C and (b) 97 °C, respectively.

Fig. 1 shows the OCPs of the binary Fe-Al alloys in H_2SO_4 of a pH 1.6 measured for 3600 s at 25 °C and 97 °C, respectively. At both temperatures, the OCPs of the Fe-Al alloys decreased continuously

with increasing Al content, i.e. the Fe-Al alloy with higher Al content is potentially more active in H_2SO_4 of a pH 1.6. At 97 °C, the OCPs of all alloys were lower than corresponding one at 25 °C.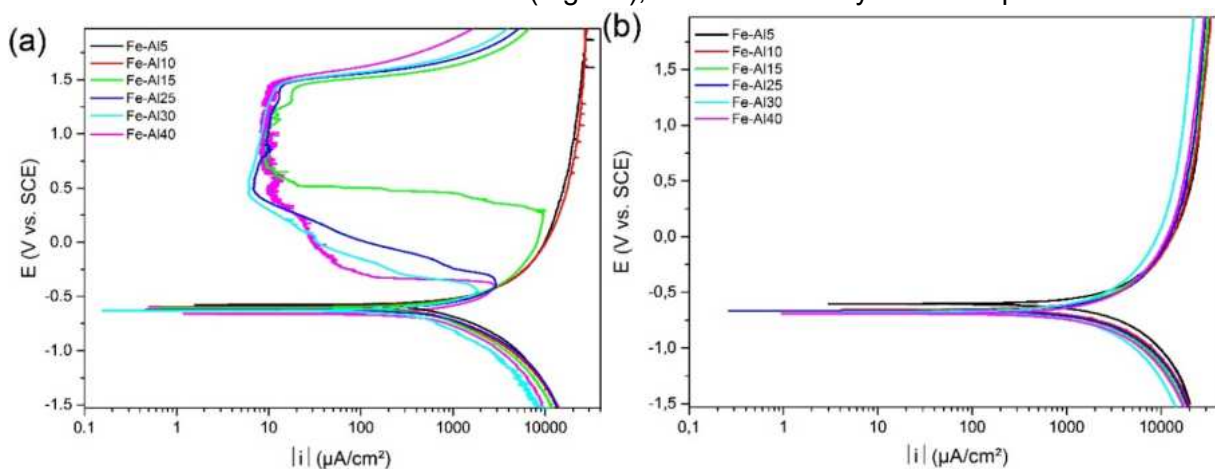 Fig. 2 shows the potentiodynamic polarization curves of Fe-Al alloys in H_2SO_4 of a pH 1.6 with the scan rate of 0.5 mV/s at 25 °C and 97 °C, respectively. At 25 °C (Fig. 2a), the alloys with 5 and 10 at. % Al only exhibited active behavior, while passivation behavior was observed for the alloys with Al contents of 15 at.% and higher. This is consistent with the general observation in oxidation experiments that the minimum Al content for the formation of protective Al_2O_3 scales on binary Fe-Al alloys is 16-18 at.% [1]. Such a correlation between wet corrosion behavior and oxidation resistance has already been found previously in case of Fe-Al-C alloys [8]. Whether the formed passive film on the surface of the alloys is a bilayer [4, 6] consisting of an Al-oxide enriched layer and a Fe/Al oxide layer or a single Fe/Al oxide mixed layer [9] is still under debate. When Al content increased from 15 to 25 at.%, the primary passive potential decreased considerably and the width of the passivation regions increased significantly. As the Al content further increased, both primary passive potentials and the width of the passivation regions almost kept constant, which indicated the increment of Al content only had slight influence on the passivation behaviors of Fe-Al alloys, when the Al content exceeded 25 at.%. At 97 °C (Fig. 2b), none of the alloys showed passive behavior.

Fig. 2 The potentiodynamic polarization curves of binary Fe-Al alloys in H2SO4 of a pH 1.6 with the scan rate of 0.5 mV/s at (a) 25 °C and (b) 97 °C, respectively.

References

[1]   P. Tomaszewicz, G. Wallwork, Reviews on High-Temperature Materials. **1978**, 4, 75-104.

[2]   M. Palm, International Journal of Materials Research. **2009**, 100, 277-287.

[3]   H.C. Choe, H.S. Kim, D.C. Choi, K.H. Kim, Journal of Materials Science. **1997**, 32, 1221-1227.

[4]   S. Frangini, N. De Cristofaro, A. Mignone, J. Lascovich, R. Giorgi, Corrosion Science. **1997**, 39, 1431-1442.

[5]   N. De Cristofaro, S. Frangini, A. Mignone, Corrosion Science. **1996**, 38, 307-315.

[6]   D. Schaepers, H.H. Strehblow, Corrosion Science. **1997**, 39, 2193-2213.

[7]   E. McCafferty, Introduction to Corrosion Science. Springer, New York, Dordrecht, Heidelberg, London, **2010**, p.168.

[8]   V. Shankar Rao, V.S. Raja: Corrosion. **2005**, 61, 751–756.

[9]   V. Shankar Rao, Electrochimica Acta. **2004**, 49, 4533–4542.

O–CO 06

The effect of alloying elements on the corrosion properties of DO3-FeAl intermetallics in naturally aerated acidic environments

Tatiana Nicole Kutz[1], Daniela Zander[2]

Lehrstuhl für Korrosion und Korrosionsschutz, RWTH Aachen University, Intzestr.5, 52072 Aachen, Germany

[1]t.kutz@gi.rwth-aachen.de   [2]d.zander@gi.rwth-aachen.de

Introduction

It is well recognized that iron aluminides pose high potential for application in high-temperature environments due to their strength-to-weight ratios and oxidation resistance; however, their substitution of current materials has been hindered due to limited ductility at room temperature.[1-3] The mitigation of this impediment has been the focus of a large collection of research and demonstrates promising advances. With an increase in ductility at ambient conditions, the application of iron aluminides can be expanded to include the replacement of stainless steels in aqueous sectors. [4]

As corrosion at ambient conditions in aqueous environments is an electrochemical process, the associated corrosion and passivation mechanisms of iron aluminides must be investigated and properly understood. The influence of alloying content on the electrochemical processes in 0.25M H_2SO_4 were determined via open circuit potential measurements, linear polarization resistance method, electrochemical impedance spectroscopy and potentiodynamic polarization. The iron aluminides demonstrated improved corrosion behavior in comparison to a common stainless steel.

Materials and Methods

The iron aluminides utilized for this study were provided by the Max-Planck-Institut für Eisenforschung in Düsseldorf, Germany, as vacuum induction melted cylindrical ingots with diameters of 32mm. The DO3 structures Fe-26Al served as the binary alloy system with which the influence of ternary elements (Cr, Mo, Nb, Ta, Ti and W) were compared. Furthermore, a common stainless steel, X8CrNiS18-9 (1.4305), was selected as a reference material.

The material characterization of the iron aluminides employed color-etching and microstructural analysis in addition to phase analysis via scanning electron microscopy (SEM), energy dispersive x-ray spectrometry (EDX) and x-ray diffraction (XRD).

Electrochemical analysis of the iron aluminides was performed with the implementation of a three-electrode cell regulated with a potentiostat. The polished samples served as the working electrodes while a platinum wire and a saturated calomel electrode inserted into a bridge-tube capillary served as the counter and reference electrodes, respectively. The 0.25M H_2SO_4 electrolyte was freely aerated and remained at room temperature (~20-25 °C) for the duration of all electrochemical experimentation. The open circuit potential (OCP) was recorded for 60 minutes, the polarization resistance was measured ±15mV from the OCP with a scan rate of 0.2 mV/s, the electrochemical impedance spectroscopy (EIS) was performed at the OCP with a ± 10mV perturbation and potentiodynamic polarization was conducted from -1.5 to 2.0 V vs SCE with a scanning rate of 0.2 mV/s.

Results and Discussion

In discerning the applicability of a material for certain operational aqueous environments, the corrosion mechanisms behind the observed corrosion processes at the free corrosion potential (also known as the corrosion potential or OCP) as well as those associated with passivation are of main interest.

This study shows that in comparison to the common stainless steel, the Fe-26Al-based iron aluminides exhibit more negative corrosion potentials, indicating that the steel is more noble and less prone to corrosion; however, when the polarization resistance values obtained via the linear polarization resistance method and EIS are evaluated, the stainless steel displays values 2-3 lower than those for the iron aluminides. As there is an inverse proportionality between polarization resistance and corrosion rate, the iron aluminides present lower corrosion rates in comparison to the steel. The Nyquist plots obtained from EIS analysis, in addition to the associated equivalent circuits, may reveal insight into the mechanisms behind this reduced corrosion rate. Due to the adsorption - desorption processes of the produced hydrogen gas in addition to the various dissolution steps of the various alloying elements, the formed electrical double layer structures due to the addition of Cr, Mo, Nb, Ta, Ti or W may provide more protective measures than those developed by the steel [5]

The potentiodynamic polarization curves confirm that all investigated iron aluminides produce a passive potential range twice that observed for the stainless steel, in addition to passive current densities reduced by a factor of approximately ten. This reduction in current density confirm that the passive layers developed on iron aluminides are more protective than those developed on the steel, under equal conditions. The stainless steel, the binary Fe-26Al as well as the ternary systems alloyed with Cr illustrate two passive plateaus, confirming the oxidation and transformation of the passive oxide layer with increasing potential; the other ternary systems do not illustrate an oxide transformation. Fig. 1 representatively illustrates these findings. Furthermore, the addition of the ternary elements reduce the activation peak required to reach the passive state, facilitating reduced material dissolution. These observations are most likely due to the development of a layered passivation mechanism. [6]

The processes behind the corrosion of iron aluminides during free corrosion as well as the passivation data obtained from the polarization curves confirm the potential application of iron aluminides in aqueous environments and advocated for further in-depth analysis.
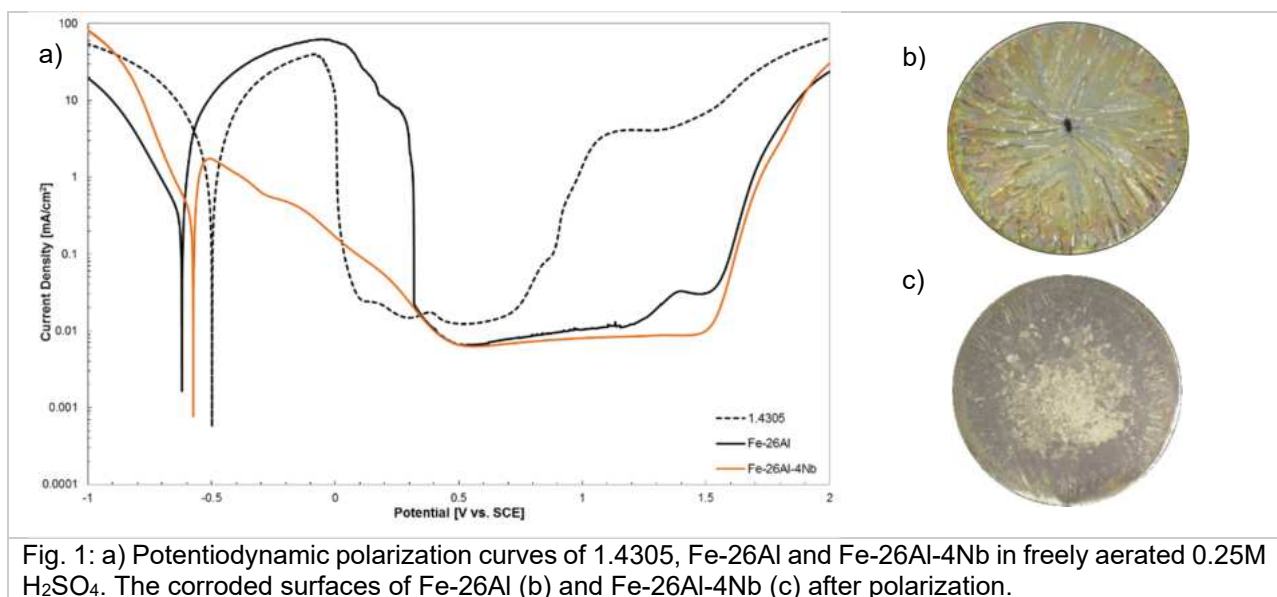
Fig. 1: a) Potentiodynamic polarization curves of 1.4305, Fe-26Al and Fe-26Al-4Nb in freely aerated 0.25M H_2SO_4. The corroded surfaces of Fe-26Al (b) and Fe-26Al-4Nb (c) after polarization.

References

[1]   V.S. Rao, Electrochimica Acta. **2004**, *49*, 4533-4542.

[2]   N.S. Stoloff, Materials Science and Engineering A. **1998**, *258*, 1-14.

[3]   N.S. Stoloff, C.T. Liu, S.C. Deevi, Intermetallics. **2000**, *8,* 1313-1320.

[4]   M. Zamanzade, A. Barnoush, C. Motz, Crystals. **2016**, *6*, 1-29.

[5]   M. Keddam, O.R. Mattos, H. Takenouti, Journal of the Electrochemical Society. **1998**, *128*, 257-274.

[6]   T. Kutz, D. Zander, CORROSION Journal. **2017**. (in press, http://dx.doi.org/10.5006/2208)

P-01

Hot deformation of dual phase titanium aluminide

Nitish Bibhanshu[1] and Satyam Suwas[2]

[1, 2]Department of Materials Engineering, Indian Institute of Science Bangalore, INDIA

[1]nitishbibhanshu@gmail.com, [2]satyamsuwas@materials.iisc.ernet.in

Introduction

Titanium aluminides have very high specific strength, low density and high operating temperature [1]. These properties make these materials amenable for the replacement of Ni-based superalloys used in gas turbines. Currently, TiAl is used in low pressure regime in as-cast condition. For the application in high pressure regime, it is desirable to develop wrought titanium aluminides. The objective of the present investigation is to develop a strategy for the processing of B modified TiAl.

Materials and Methods

Cast titanium aluminide with composition Ti-48Al-2V and Ti-48Al-2V-0.2B has been prepared from the vacuum arc melting. As cast structure shows the strong solidification texture. High temperature deformation behavior of dual phase Titanium Aluminide of composition Ti-48Al-2V and with the further addition of 0.2%B (which is a grain refiner and alpha phase stabilizer [2]) has been studied. Both the compositions have been deformed under compression at a temperature of 1200˚C with a strain rate of 10 s^{-1}. It has been found that "B" added TiAl show a higher softening behavior compared to that of Ti-48Al-2V. Fig. 1 shows the as-cast microstructure and Fig. 2 shows deformed microstructures of Ti-48Al-2V-0.2B.

Results and Discussion

It has been observed that "B" modified composition shows more softening behavior compare to the Ti-48Al-2V. During the deformation, softening has been observed because of the lath kinking, lath breaking, lath rotation, dynamic recrystallization and globalization. Dynamic recrystallization has been observed mainly in the shear band which is forming parallel to the kinked lamella. From the compression curves activation energy of deformation has been calculated, and has been found that its value increasing with the increasing the deformation temperature. This may be because of the increasing the phase fraction of alpha phase.
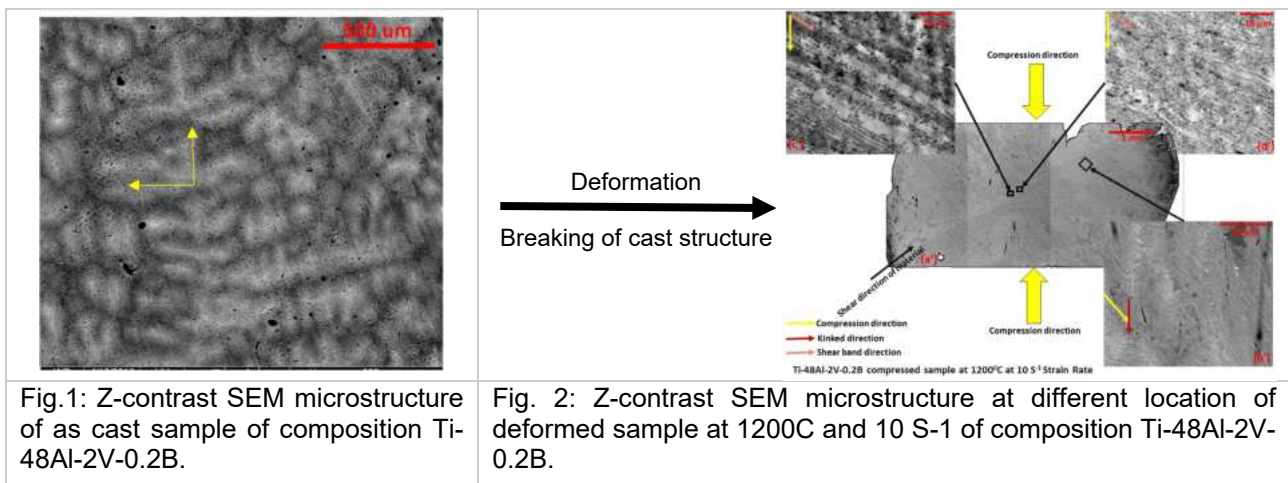
Fig.1: Z-contrast SEM microstructure of as cast sample of composition Ti-48Al-2V-0.2B.

Fig. 2: Z-contrast SEM microstructure at different location of deformed sample at 1200C and 10 S-1 of composition Ti-48Al-2V-0.2B.

References

[1] D.M. Dimiduk, Mater. Sci. & Eng., A263 (1999) 281-288.

[2] A.V. Kartavykh, M. V. Gorshenkov, D. A. Podgorny, Mater. Letters, 142 (2015) 294-298.

P–02

Crystal viscoplasticity modeling of Al-rich Ti-61.8at.%Al at 1050°C

Helal Chowdhury[1], Konstantin Naumenko[2], Holm Altenbach[2], Manja Krüger[3,4]

[1]Graduate school for 'Micro-macro interactions in structured media and particle systems', Otto-von-Guericke University (OVGU), 39106 Magdeburg, Germany, email: helal.chowhury@ovgu.de

[2]Institute of Mechanics, OVGU, Universitätsplatz 2, 39106 Magdeburg, Germany, email: konstantin.naumenko@ovgu.de, holm.altenbach@ovgu.de

[3]Faculty of Georesources and Materials Engineering, RWTH Aachen, 52056 Aachen, Germany

[4]Institute of Energy and Climate Research (IEK-2), FZ Jülich, 52425 Jülich, Germany, email: m.krueger@fz-juelich.de

Introduction

The generation of Ti-rich TiAl-based intermetallic materials has replaced many metals and alloys till 900°C providing a unique set of physical and mechanical properties. For temperatures up to 1050°C, phases from the Al-rich region of this alloy system are considered to be highly potential candidates for high temperature structural applications mainly due to higher oxidation resistance, 20% lower density and higher (about 150°C more) operating temperature possibility over Ti-rich side. Anisotropy in inelastic behavior is common for such high-temperature materials. Modeling rate dependent plastic anisotropy of such high temperature alloys is an integral part of modern engineering design. Even though anisotropy in Ti-rich side has been investigated reasonably for single-crystalline and polycrystalline alloys, however in Al-rich side of the Ti-Al system, it is not well documented either theoretically or experimentally. In this work, a two internal variable based phenomenological crystal viscoplasticity model has been applied with a modified hardening law for simulating isothermal, two phase, single crystal like Al-rich lamellar Ti-61.8at.%Al binary alloy at hot compression state (1050°C) by employing finite strain framework. A new relationship of critical stresses in different slip systems has also been proposed.

Materials and Methods

From the Al-rich Ti-Al family, an alloy with nearly 62 at.% Al is especially important due to the possibility of generating lamellar microstructures. Polycrystalline test samples with similar composition have been produced by centrifugal casting, subsequent annealing at 950°C/200h and water quenching. Directional solidification using a zone melting process has been applied to produce single crystal like specimen of Ti-61.8at.%Al with nearly lamellar morphology. Two stable phases of this alloy are γ-TiAl (matrix) + r-Al$_2$Ti (lamellae). The γ-phase has face centered tetragonal (with lattice parameters c/a=1.02) crystal structure, whereas the r-phase is an ordered six-fold superstructure of γ-phase together along [001]. Observations show that the microstructure can approximately be regarded as cubic-to-cubic relationship. Focused ion beam investigation shows that the average width of r-Al$_2$Ti lamellae in most regions is about 0.6±0.2 μm while the inter-lamellar spacing is about 1±0.3 μm. This alloy maintains the orientation relationship as: [001]$_\gamma$ || [001]$_r$ and <100>$_\gamma$ || <100>$_r$. At the lamellar boundary the interface planes are parallel, i.e. (001)$_\gamma$ || (001)$_r$. Beyond ordinary and super dislocation slips, investigations revealed that the significant amount of dislocations are present at the γ/r inter lamellar boundary interfaces, which result significant slips on (001) planes during deformation above the peak temperature of 800°C with two types of 1/2<110] dislocations. So we are considering both the octahedral and the cubic families e.g. {111} and {001}, are active at elevated temperature. This means twelve slip systems from the octahedral and six from the cubic family will be considered here. According to mean field homogenization approach, we have generated an idealized, sufficiently large (10*10*10 μm^3), lamellar representative volume element (RVE). Crystal viscoplasticity constitutive equations have been implemented in the user subroutine (UMAT) functionality of the software package ABAQUS.

Hardening and Recovery Driven Constitutive Equations

At high temperature regimes, deformation is not only driven by dislocation glide mechanism, there are climbs as well which assist to the recovery process of hardening. Crystal viscoplasticity modeling approach is well capable of reproducing rate depending plastic anisotropic data as long as critical resolved shear stress (CRSS) is chosen carefully. Since we are dealing with a very hot compression state, we need a set of constitutive equations with proper evolution equation of hardening and recovery. Two internal variables (slip system level back stress, $x^{(\alpha)}$ and threshold stress, $r^{(\alpha)}$) based on phenomenological crystal plasticity flow rule is a good candidate here. Detailed evolution equations of constitutive framework can be found in [1]. In order to maintain a generalized approach of glide and climb, we slightly modified the evolution of $r^{(\alpha)}$ as given below.

$$\dot{\gamma}^{(\alpha)} = \left\langle \frac{|\tau^{(\alpha)} - x^{(\alpha)}| - r^{(\alpha)}}{K} \right\rangle^n \mathbf{sgn}\left(\tau^{(\alpha)} - x^{(\alpha)}\right) \tag{1}$$

$$r^{(\alpha)} = r_0^{(\alpha)} + \sum_\beta H^{\alpha\beta} \left(1 + b^\beta\right) q^\beta \tag{2}$$

Here $\dot{\gamma}^{(\alpha)}$ is the slip rate, $\tau^{(\alpha)}$ is the resolved shear stress, $r_0^{(\alpha)}$ is the initial CRSS along the slip system α where $r^{(\alpha)}$ includes hardening and recovery effect. K is the temperature dependent drag, q is the governing variable for the evolution of $r_0^{(\alpha)}$, n is the rate sensitivity parameter, $H^{\alpha\beta}$ is the matrix for hardening interactions and b is responsible for the recovery.

Results and Discussion

Two sets of compression test data for three different strain rates have been shown in Figs. 1-2, where lamellar axis is perpendicular (Fig. 1) and parallel (Fig. 2) to the loading axis. Simulation results show that, for a specific set of material parameters, the mentioned set of equations can reproduce experimental data sets with very good agreement. We found n=4.5, K=122 MPa, and b=9, which are very reasonable for high temperature medium stress regimes. From a few reports, for example [2], we know that some slip systems are harder and some are softer. Specifically at high temperature, $r_0^{ordinary} < r_0^{super}$ for specific lamellar and loading orientation. In our case we additionally found that some ordinary slip systems lie in between i.e. superslips are harder, some ordinary slips are softer and some are in between. We found the ratio of the highest to the lowest CRSS is 1.8. The presence of long period superstructures might have suppressed the motion of dislocations along some ordinary systems as it is found at lower temperature [3]. Anisotropy is driven by both lamellar morphology and the presence of superstructures.
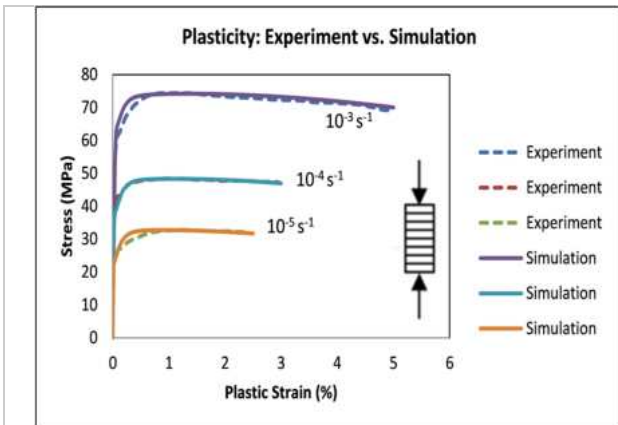

Fig. 1: Rate dependent plasticity data when lamellar and loading axes are perpendicular, experiment vs. simulation
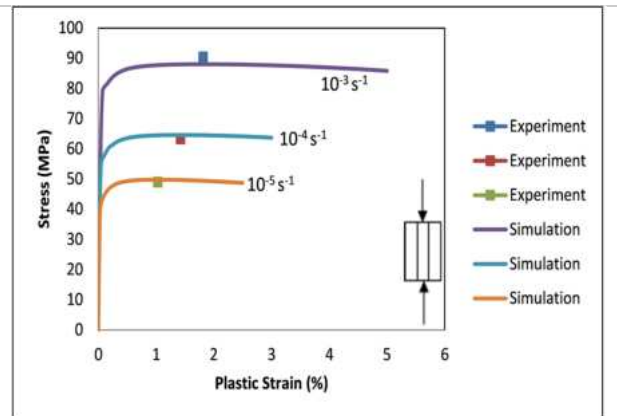
Fig. 2: Rate dependent plasticity data when lamellar and loading axes are parallel, experiment vs. simulation

References

[1] J.B. le Graverend, J. Cormier, F. Gallerneau, P. Villechaise, S. Kruch, J. Mendez, International Journal of Plasticity, 2014, 59, 55–83.

[2] H. Inui, M. Matsumuro, D. Wu, M. Yamaguchi, Phil. Magazine A, 1997, 75, 395-423.

[3] T. Nakano, K. Hayashi, Y. Umakoshi, Y. Chiu, P. Veyssiere, Phil. Magazine, 2005, 85, 2527-2548.

P–03

High temperature deformation behavior of B2-type Ti-Mo-Al alloys

Yuanyuan Lu[1], Kyosuke Yoshimi[2], Hidemi Kato[3]

[1] Department of Material Science, Graduate School of Engineering, Tohoku University, Sendai, Miyagi 980-8579, Japan, lu.yuanyuan.b4@tohoku.ac.jp

[2] Department of Material Science, Graduate School of Engineering, Tohoku University, Sendai, Miyagi 980-8579, Japan, yoshimi@material.tohoku.ac.jp

[3] Institute for Materials Research, Tohoku University, Sendai, Miyagi 980-8577, Japan, hikato@imr.tohoku.ac.jp

Introduction

Owing to the ordered crystal structure and directional bonding characteristics, B2 intermetallic compounds exhibit unique mechanical behaviors such as strong elastic anisotropy, distinctive slip system from that of disordered A2 structure, anomalous temperature dependence of yield stress [1,2]. For Ti-Al base alloys, ternary B2 phases have been commonly detected when refractory elements (e.g. Nb, Mo, W, Ta and V) are doped [3,4]. Although these B2 compounds were suggested to play a critical role in improving the mechanical performance of Ti-Al base alloys, a well knowledge of their deformation modes is still lacking. In our recent work, early yielding followed by strong strain hardening was observed in an as-cast $Ti_{50}Mo_{25}Al_{25}$ alloy compressed at 1073 K, which was not seen in other Ti-Mo-Al alloys with B2 structure [5]. Here we make further experimental efforts to elucidate the deformation mechanisms of stoichiometric and non-stoichiometric B2-type Ti-Mo-Al alloys by examing dislocation substructure of the samples deformed at high temperatures.

Materials and Methods

Ti-Mo-Al alloys with the nominal composition of $Ti_{50}Mo_{25}Al_{25}$, $Ti_{60}Mo_{25}Al_{15}$ and $Ti_{50}Mo_{35}Al_{15}$ (at.%) were prepared via conventional arc melting technique. The ingots were solution treated at 1423 K for 2 hours in Ar atmosphere and then quenched in ice water. The microstructures of quenched samples were characterized on a JEOL JSM-7800F scanning electron microscope (SEM) equipped with electron backscattered diffraction (EBSD). We further investigated their microstructure and lattice structure by transmission electron microscopy (TEM) on a JEOL JEM-ARM 200F microscope operated at 200 kV. Compression tests were conducted on an Instron 5982 machine at 973, 1073 and 1173 K, respectively. The dimension of compression specimens is ~2x2x4 mm³. All the compression tests were performed at a constant strain rate $\dot{\varepsilon}$ of 2.1×10^{-4} s^{-1}. Afterward, TEM specimens were sliced from the compressed samples and dislocation analysis was subsequently carried out using two-beam Bragg-contrast imaging.

Results and Discussion

All the quenched Ti-Mo-Al alloys have ordered B2 structure, as evidenced by the appearance of superlattice spots on TEM diffraction patterns. The EBSD analysis reveals the polycrystalline characteristics of these Ti-Mo-Al alloys while the grain size ranges from several tens of micrometers to a few hundred micrometers. A more detailed microstructure observation at higher magnifications was conducted on TEM, from which a large amount of subgrain boundaries made up of dislocation walls were seen in each grain. Similar to the as-cast samples [5], the quenched Ti-Mo-Al alloys exhibit impressive compression strength at high temperatures. Moreover, early yielding followed by strong strain hardening was also observed in the $Ti_{50}Mo_{25}Al_{25}$ sample quenched from 1423 K. Fig.1 illustrates representative TEM bright field micrographs of dislocations in a $Ti_{50}Mo_{25}Al_{25}$ alloy compressed at 1073 K to ~2% plastic strain under various two-beam conditions. According to the invisibility criterion ($\mathbf{g} \cdot \mathbf{b} = 0$), the burgers vector of dislocations shown in Fig. 1 was identified as $[\bar{1}11]$. Weak-beam dark-field imaging was also applied to characterize the dislocation substructure.
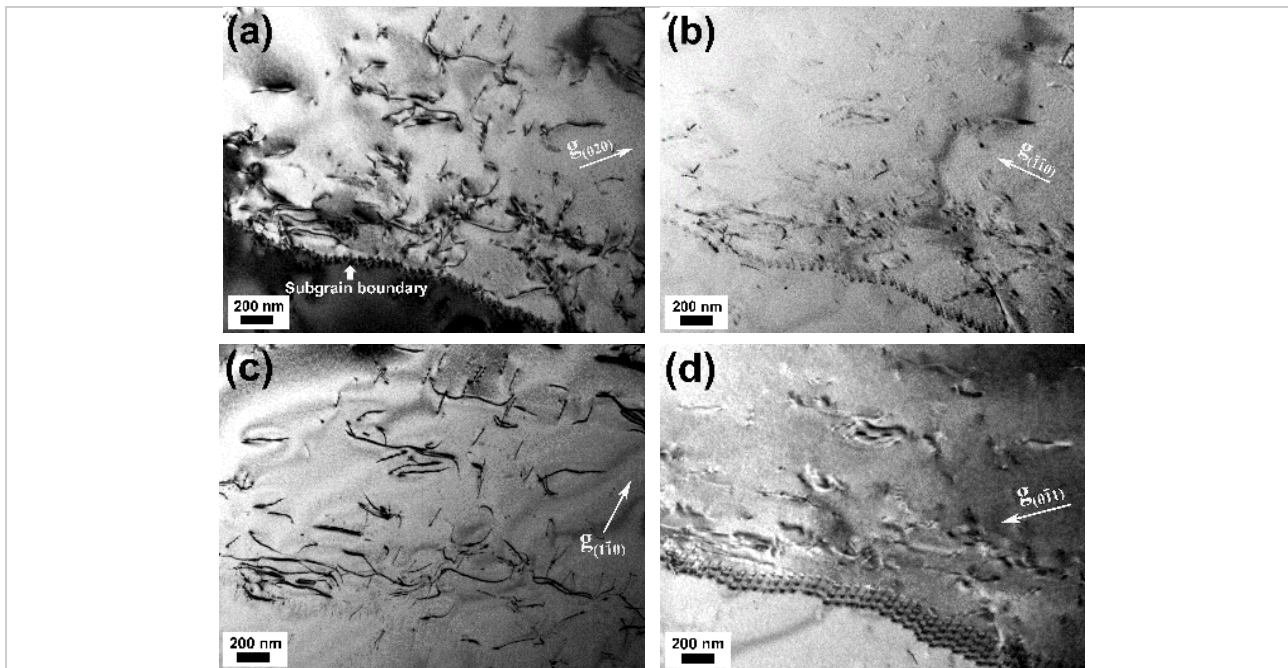
Fig. 1: TEM bright field micrographs of dislocations in a $Ti_{50}Mo_{25}Al_{25}$ alloy compressed at 1073 K to ~2% plastic strain under various two-beam conditions (a)-(c) **B**=[001] (d) **B**=[011].

References

[1] M. Yoo, T. Takasugi, S. Hanada, O. Izumi, Materials Transactions, JIM. **1990**, *31*, 435-442.

[2] I. Baker, Materials Science and Engineering: A. **1995**, *192*, 1-13.

[3] A. Gogia, D. Banerjee, T. Nandy, Metallurgical Transactions A. **1990**, *21*, 609-625.

[4] M. Thomas, S. Naka, T. Khan, Materials Transactions, JIM. **1994**, 35, 787-793.

[5] Y. Lu, J. Yamada, J. Nakamura, K. Yoshimi, H. Kato, Journal of Alloys and Compounds. **2017**, *696*, 130-135.

P–04

Carbide growth in TiAl alloys studied by SAS

Sören Gayer[1], Andreas Stark[2], Peter Staron[2], Florian Pyczak[2] and Andreas Schreyer[3]

[1]Helmholtz-Zentrum Geesthacht, Institute of Materials Research, Germany, soeren.gayer@hzg.de

[2]Helmholtz-Zentrum Geesthacht, Institute of Materials Research, Germany

[3]European Spallation Source, Sweden

Introduction

Intermetallic γ-TiAl based alloys are a class of advanced lightweight alloys for high temperature applications, and their first major use in industrial application has recently been as turbine blades in aero-engines. Alloying with carbon can improve their mechanical properties, such as strength and creep resistance, especially at high working temperatures. In general, this strengthening effect of carbon can be attributed to either solid solution hardening of the matrix phases or precipitation hardening. Effective precipitation hardening requires small and densely spaced precipitates and has been reported in the form of perovskite-type (P-phase) Ti_3AlC particles in binary TiAl alloys by Tian et al. and Christoph et al. [1, 2].

However, in studies on ternary Nb-rich TiAl alloys (Ti-45Al-5Nb-xC), improved mechanical properties have been attributed to solid solution hardening since no precipitates were detected [3]. Scheu et al. [4] explain this behaviour with an increased C solubility caused by Nb. But recent transmission electron microscopy (TEM) and high-energy X-ray diffraction (HEXRD) studies on the same alloys after annealing, as well as in situ HEXRD studies during annealing, indicate that—in spite of the high Nb content—P-phase particles form in the matrix [5, 6]. However, these methods suffer from two limitations: TEM observes a small 2D area which might not be representative of the bulk material and the contrast for very small carbides is weak and HEXRD does not give a signal from very small precipitates. SAXS data from carbide-strengthened TiAl alloys are scarce.

Materials and Methods

We conducted several high-energy small-angle X-ray scattering (HESAXS) experiments during aging of TiAl samples with a dilatometer. The High Energy Material Science (HEMS) Beamline P07 at PETRA 3 allows also simultaneous XRD measurements to observe the phase composition in the sample. Although the SAXS measurements provided us with a very high time resolution (<1 min) of the growth process, the size resolution is rather limited. For the missing information, ex-situ SANS measurements of the same samples were done, which provided us with limits for the size distribution fitted to the in-situ SAXS measurements.

The investigated samples were HIPed powders of TiAlNbC alloys with varying Al, Nb and C contents. With the dilatometer we solution treated the samples at 1150°C or 1250°C and subsequently quenched to 800°C or 900°C. The samples were annealed at these temperatures for several hours.

Results and Discussion

With the conducted experiments, we were able to measure the growth of carbides in different alloys with very high time resolution during the early stages of solution heating and annealing, where fast changes in size and number density of the carbides occur (Fig 1.). This data isn't accessible with ex-situ techniques and provides us with valuable information to understand the kinetics of carbide growth in TiAl.

The additional phase information of the simultaneous XRD measurements shows a similar increase in the carbide phase content, increasing the confidence in the SAXS data.

Fig. 1: Preliminary results for mean sphere size (black, upward triangle) and number density (grey, downward triangle) of carbides in Ti45Al5Nb0.5C treated with the shown temperature profile (dashed line).
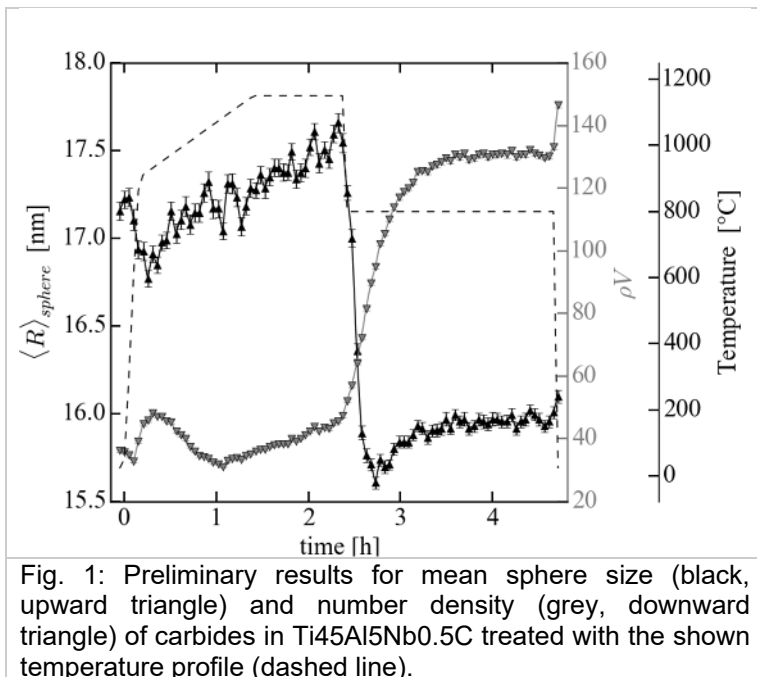
References

[1] U. Christoph, F. Appel, R. Wagner, "Dislocation dynamics in carbon-doped titanium aluminide alloys", Materials Science and Engineering A 239-240, (1997) 39-45.

[2] Tian, W.H., Nemoto, M. Effect of carbon addition on the microstructures and mechanical properties of γ-tial alloys (1997) Intermetallics, 5 (3), pp. 237-244.

[3] R. Gerling, F.-P. Schimansky, A. Stark, A. Bartels, H. Kestler, L. Cha, C. Scheu and H. Clemens, "Microstructure and mechanical properties of Ti 45Al 5Nb + (0-0.5C) sheets", Intermetallics 16, (2008) 689-697. doi: 10.1016/j.intermet.2008.02.004

[4] Scheu, C., Stergar, E., Schober, M., Cha, L., Clemens, H., Bartels, A., Schimansky, F.-P., Cerezo, A. High carbon solubility in a γ-TiAl-based Ti-45Al-5Nb-0.5C alloy and its effect on hardening (2009) Acta Materialia, 57 (5), pp. 1504-1511. doi: 10.1016/j.actamat.2008.11.037

[5] H. Gabrisch, A. Stark, F.-P. Schimansky, L. Wang, N. Schell, U. Lorenz, and F. Pyczak, "Investigation of carbides in Ti-45Al-5Nb-xC alloys (0≤x≤1) by transmission electron microscopy and high energy-XRD", Intermetallics 33, (2013) 44-53. doi: 10.1016/j.intermet.2012.09.023

[6] Li Wang, Heike Gabrisch, Uwe Lorenz, Frank-Peter Schimansky, Andreas Schreyer, Andreas Stark, Florian Pyczak, "Nucleation and thermal stability of carbide precipitates in high Nb containing TiAl alloys", Intermetallics 66, (2015) 111-119. Doi: 10.1016/j.intermet.2015.07.001.

P–05

Precipitation in Ti-Al-Nb alloys with Si and C additions

Maria Victoria Castro Riglos[1], Andreas Stark[1], Jonathan Paul[1], Florian Pyczak[1]

1Helmholtz Zentrum Geesthacht, Max Planck Strasse 1, 21502, Geesthacht, Germany. e-mail: Maria.Castro-Riglos@hzg.de, Florian.Pyczak@hzg.de

Introduction

Automotive and aerospace industries are always looking for innovative lightweight materials that offer good performance even under high temperature conditions. Within this group one of the most promising materials are intermetallic Ti-Al based alloys. Besides their low density, the advantages presented by this class of alloys are their good strength and creep properties up to 750 ºC, their high oxidation resistance and good thermal conductivities [1]. However, there exist some drawbacks of these alloys like low ductility and toughness at room temperature, poor workability, and limited high temperature strength above 750 °C [2]. In order to improve creep and oxidation resistance Niobium is usually added in an amount within 5 to 10 at.%. Another inclusion that was successfully tested into this type of alloys was Carbon, added as a microalloying element (0-1 at.%). Carbon showed to strengthen the material by precipitation of secondary phases or by solid solution strengthening [3]. Silicon is expected to have a similar effect as that provided by C additions but there are still limited studies on the effects of silicon in Ti-Al alloys. For this reason, in the present work it was analyzed how the mechanical properties and microstructure are affected by Si addition in some Ti-Al-Nb based alloys with different C contents.

Materials and Methods

Five Ti-Al-Nb based alloys having Ti-45Al-5Nb-1Si-xC composition (in at.%) were studied. The amount of C introduced as microalloyed element varied between 0.5; 0.25; 0.1; 0.05 and 0 (in at.%). These alloys were numbered from **Alloy 1** to **Alloy 5** by decreasing C content. This means **Alloy 1** was the one with highest C amount (Ti-45Al-5Nb-1Si-0.5C) while **Alloy 5** was the one having no C (Ti-45Al-5Nb-1Si). Each alloy was studied after heat treatment at 800ºC for 168 hours. Vickers Micro Hardness measurements were performed using a Mitutoyo Hardness Testing machine with a load of 1kg. The microstructure was first observed in a FEI Tecnai G2 transmission electron microscope (TEM). Afterwards, High Energy X-Ray measurements were performed at DESY synchrotron in transmission, using a wavelength of λ=0.142350 Å. The raw data were analyzed by means of *Fit2d* software. Experimental diffraction spectra were compared to diffraction spectra simulated with *Powder Cell* software.

Results and Discussion

Comparing to previous studies [3], results obtained from Hardness measurements (Figure 1) showed for all of the five studied alloys a remarkable increase in Hardness with respect to otherwise equivalent Si free systems (hardness increased by around 100-150 HV units). On the other hand, when comparing **Alloy 5** (no C content) with the other four alloys (alloys containing both additions, C and Si) only a slight increment in Hardness was observed.

By TEM observations (not shown here) it was established that all alloys exhibited a lamellar microstructure typical for the Ti-45Al-5Nb, base composition. The lamellar microstructure consists of alternating α_2 and γ lamellas. Unlike a typical Ti-45Al-5Nb alloy microstructure, many precipitates from a new phase could be seen that were usually located at α_2/γ interfaces.

In order to identify the type of these precipitates High Energy X-Ray Diffraction measurements were carried out. For **Alloy 1** a general view of the diffractogram is presented in Figure 2A. Figures 2B-D show the detailed regions where the determination of each phase was performed by fitting the peak positions with simulated diffraction profiles from each individual phase. The phases of the Ti-Al system (γ and α_2) were easily identified. The presence of γ phase was assured by the positions of 002γ and 200γ peaks (Fig. 2B). Similarly, α_2 was recognized mainly by the diffraction peaks from $100\alpha_2$, $101\alpha_2$. On the other hand, the main interest was to determine to which phase

POSTER PRESENTATION

the new inter-lamellar precipitates did belong. Figure 2D presents three individual peaks (light gray line) that were in accordance with diffraction from planes 200, 111 and 002 from the silicide phase Ti_5Si_3 (SG: $P6_3$/mcm, a=b=0.7461 nm, c=0.51508 nm), same as found by Noda et al. for a similar Ti-Al alloy containing Si additions [4]. Finally, this analysis also demonstrated that no carbides were formed. It is important to point out that as the specimens presented crystalline texture these X-Ray measurements were not suitable for quantification of volume fractions of the different phases.

Fig. 1: Vickers Hardness evolution with increasing C content in Ti-45Al-5Nb-1Si-xC, at.% (black squares). Data from similar no Si containing alloys (white circles) are displayed [3].

Fig. 2: (A) General XRD pattern for **Alloy 1** (x=0.5 at.%). Diffractograms are displayed as a function of the scattering vector, **q** (**q** = 4π.sin ϱ/λ). (B-D) For phase determination, XRD patterns from γ, α_2 and Ti_5Si_3 phases are shown simultaneously overlapped to the alloy pattern in the region of interest for each phase. No carbide peaks were observed.

References

[1] H. Clemens, S. Mayer, Advanced Engineering Materials. **2013**, 15 (4), 191-215.

[2] F. Appel, J.D.H. Paul, M. Oehring: Gamma Titanium Aluminide Alloys: Science and Technology. Wiley-VCH, 1st edition, **2011**.

[3] H. Gabrisch, A. Stark, F.P. Schimansky, L. Wang, N. Schell, U. Lorenz, F. Pyczak, Intermetallics, **2013**, 33, 44-53.

[4] T. Noda, M. Okabe, S. Isobea, M. Sayashi. Mat. Sci. Eng. A.**1995**, 192/193, 774-779.

P–06

P-type carbides in TiAl alloys – a study on stability and morphology development

Li Wang[1], Uwe Lorenz[2], Andreas Stark[3], Florian Pyczak[4]

[1] Helmholtz Zentrum Geesthacht, Max Planck Strasse 1, 21502, Geesthacht, Germany. e-mail: Li.Wang1@hzg.de

[2] Helmholtz Zentrum Geesthacht, Max Planck Strasse 1, 21502, Geesthacht, Germany. e-mail: Uwe.Lorenz@hzg.de

[3] Helmholtz Zentrum Geesthacht, Max Planck Strasse 1, 21502, Geesthacht, Germany. e-mail: Andreas.Stark@hzg.de

[4] Helmholtz Zentrum Geesthacht, Max Planck Strasse 1, 21502, Geesthacht, Germany. e-mail: Florian.Pyczak@hzg.de

Introduction

It is attractive to increase the temperature capability of TiAl alloys for applications in aero engine turbines and automotive engine components. One means to achieve this is the addition of carbon as alloying element to benefit from improved creep strength utilizing the precipitation hardening effect of carbides [1-3]. Of the two types of carbides which can form in γ-TiAl alloys, perovskite P-Type and hexagonal H-type carbides, P-type carbides are the more desirable. They can precipitate coherently in the $L1_0$-γ TiAl phase and thus form a population of homogeneously distributed fine particles in the material most suited to hinder the movement of dislocations and increase the creep strength of the material by this effect. Unfortunately, the stability of those P-type carbides as well as their morphology development when exposed to high temperatures for extended times are not well investigated [4]. To monitor the morphology development of those nano-scaled particles transmission electron microscopy (TEM) or other observation tools with high resolution are necessary while the measuring of the low carbon contents of interest is inherently difficult and the diffraction peaks of the low volume fractions of small particles are often overshadowed by the background when using lab X-ray sources. Here a combined TEM and synchrotron high energy X-ray diffraction (HEXRD) study of the carbide phase in aged TiAl-alloys with different contents of carbon, aluminium and niobium is presented.

Materials and Methods

Two alloy series were produced. The first with aluminium content of 45 at.% and carbon contents of 0.5, 0.75 and 1.0 at.%. These three alloys also contained 5 at.% niobium. For comparison a niobium free alloy with the composition Ti-45Al-0.5C was included in the investigation. The second series of alloys with a higher aluminium content of 51 at.% had the compositions of Ti-51Al-5Nb-xC and Ti-51Al-xC (x between 0.0 and 0.5), respectively. Selected samples of both alloy series were aged at 800 °C for different ageing times ranging from 24 to 5000 hours. The carbon concentration in the alloys was measured using a LECO CS-444 melt extraction system.
The specimens were subsequently characterized using a Philips CM200 and a FEI TITAN 80-300 transmission electron microscope. HEXRD investigations were performed at the Helmholtz-Zentrum Geesthacht run beamlines at the DESY synchrotron in Hamburg using X-ray beam energies of 80 and 100 keV.

Results and Discussion

The specimens of the Ti-51Al series either with or without Nb addition exhibited a nearly single γ phase microstructure. Thus, these specimens are suited to investigate the influence of niobium on the carbon solubility in the γ phase. First the carbon concentration in the γ phase is directly accessible by measuring the overall carbon concentration in the specimen and second no effects of additional phases like α_2 to consume carbon or niobium have to be considered. It was found that

niobium did not increase the carbon solubility significantly. The carbon concentration did influence the stability of the carbides. With increasing carbon content the H-type carbides formed together with P-type carbides. The onset of the formation of H-type carbides is 0.5 at.% carbon in the Ti-51Al series of alloys and 1.0 at.% carbon in the Ti-45Al-5Nb series of alloys after annealing. For extended ageing periods an unusual morphology change of P-type carbides was observed. Initially P-type carbides have a needle-like shape (Fig. 1) and change this to a plate-like shape when growing. These plates later split up in arrangements of small sub-particles. The latter process is probably caused by elastic interaction between the sub-particles. In the series of Ti-45Al alloys with and without niobium the development of carbide morphology could be observed up to extended ageing times. An effect of Nb addition was a slowdown of carbide precipitation and coarsening. The higher the carbon content the earlier the splitting into sub-particles takes place while higher niobium content delays the process. The P-type carbide needles, plates as well as the P-type carbide sub-particle compounds are coherent with the γ-TiAl phase and retain an orientation relationship with it. Only for very extended ageing times first signs of a loss of coherency between P-type carbides and γ-TiAl phase are found as the formation of dislocations at the carbide-matrix interface and the assumption of an irregular shape by the carbides.
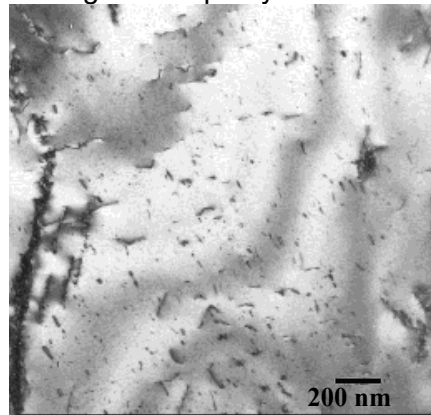
Fig. 1: P-type carbides in Ti-51Al-5Nb-0.05C aged for 168h at 800 °C

References

[1] P.I. Gouma, Subramanian, K., Kim, Y. W., Mills, M. J., Intermetallics. **1998**, *6*, 689-693.

[2] W.H. Tian, M. Nemoto, Intermetallics. **1997**, *5*, 237-244.

[3] H. Gabrisch, A. Stark, F.P. Schimansky, L. Wang, N. Schell, U. Lorenz, F. Pyczak, Intermetallics. **2013**, *33*, 44-53.

[4] L. Wang, H. Gabrisch, U. Lorenz, F.P. Schimansky, A. Schreyer, A. Stark, F. Pyczak, Intermetallics. **2015**, *66*, 111-119.

P–07

Oxidation behavior of two different titanium aluminides and its impact on mechanical properties

Lukas Mengis[1], Anke Silvia Ulrich[1] and Mathias Christian Galetz[1]

[1]DECHEMA Forschungsinstitut, Theodor-Heuss-Allee 25, 60486 Frankfurt am Main,
mengis@dechema.de

Introduction

Due to their specific high temperature strength, elastic modulus as well as their low density, γ-TiAl alloys have already substituted heavier nickel-based alloys in specific automotive and especially aerospace applications [1]. However, a major drawback of these representatives of the intermetallic phases is their oxidation behavior at temperatures above 750°C. Besides the formation of a thick mixed oxide scale, which leads to a consumption of load-bearing cross section, an undesirable degradation of mechanical properties occurs [2], caused by an environmental induced embrittlement of the subsurface zone underneath the oxide scale. Recently, a coating concept was developed to improve the impact of oxidation on (multiphase) γ-TiAl alloys including the deposition of a single-phase γ-TiAl coating using pack-cementation process as well as a subsequent fluorine treatment. Hereby, γ-TiAl is chosen due to its compatibility with the substrate and its low oxygen solubility [3]. For comparison, coatings were deposited on a two-phase (48-2-2) as well as a three-phase TiAl alloy (TNM-B1). As high temperature materials require both oxygen resistance and mechanical strength, four-point bending tests were performed to investigate the coating´s decisive influence on the mechanical properties.

Materials and Methods

The γ-TiAl alloys investigated in this present study are a 2nd generation two-phase (γ-TiAl and α_2-Ti_3Al) Ti-48Al-2Cr-2Nb [at%] alloy as well as a 3rd generation multiphase (γ-TiAl, α_2-Ti_3Al and β/β_0-Ti(Al)) TNM-B1 alloy with a nominal composition of Ti-43.5Al-4Nb-1Mo-0.1B [at%] Both were supplied by *GfE Metalle und Materialien GmbH* by means of vacuum arc remelting and hot isostatic pressing (HIP). For pivotal oxidation investigations, both alloys were primarily cut into small buttons (15 mm diameter). Additionally, four-point-bending samples were prepared (80 x 6 x 4 [mm]). All samples were manually ground using SiC paper and ultrasonically cleaned with acetone for 15 minutes. Out-of-pack cementation experiments were conducted with optimized parameters based on former investigations performed at the *DECHEMA-Forschungsinstitut* [4]. Afterwards, coated samples were fluoridated using a PTFE spray and pre-oxidized at 900°C for 24 h in laboratory air to take advantage of the halogen-effect providing a dense alumina layer on top of the aluminum-rich coating [5][6]. Finally, samples were oxidized under isothermal conditions in laboratory air up to 1000 h in a chamber furnace. For metallographic investigations X-ray diffraction measurements (Bruker D8 Advance, Cu-Kα radiation) were used as well as a scanning electron microscope (Zeiss ultra 55 scanning electron microscope) and back scattering electron imaging (JEOL JXA-8100 electron probe micro analyzer (EPMA)). Finally, four-point bending flexural tests were carried out at room temperature after exposure using a Hegewald & Peschke testing machine. During investigations, displacement data were continually recorded by LVDT extensometers that serve as a basis for the calculation of the stress-strain diagrams.

Results and Discussion

In figure 1 a 48-2-2 sample is shown after out-of-pack cementation process. A thin γ-TiAl layer (7.7 ± 0.8 μm) has formed on top of the substrate. After additional fluorine treatment and pre-oxidation at 900°C for 24 hours a dense alumina layer (after an initial Al_2O_3 and TiO_2 scale) with a thickness of approximately 2 μm was built. Uncoated samples as well as aluminized and subsequently fluorine treated samples were exposed at 900°C up to 100 h. At this, a fast growing non-protective mixed scale (Al_2O_3+TiO_2) with a thickness of 7.9 ± 1.0 μm was observed on top of the uncoated samples. On the other hand, coated samples show an improved behavior during thermal exposure

suppressing oxygen inward diffusion. Hereby, the γ-TiAl coating underneath the Al_2O_3 layer functions as an aluminum reservoir maintaining the self-healing character in cases of Al_2O_3 failure. Figure 2 illustrates the influence of the coating application on the mechanical properties in contrast to the uncoated sample (TNM-B1); in this particular case on the behavior during four-point bending tests after isothermal exposure at 900°C for 100 respectively 1000 h. The uncoated sample reveals a strong decrease of ultimate stress from roughly 900 MPa to 350 MPa after 1000 h. In comparison, stress (and fracture strain) parameters of pack aluminized and fluorine treated samples remain more or less constant during the long-term investigations. Moreover, they show an improved behavior at 1000 h compared to the uncoated samples. Obviously, coating deposition has a certain impact on the mechanical properties. To analyze this impact more precisely four-point-bending tests were carried out after each deposition step.
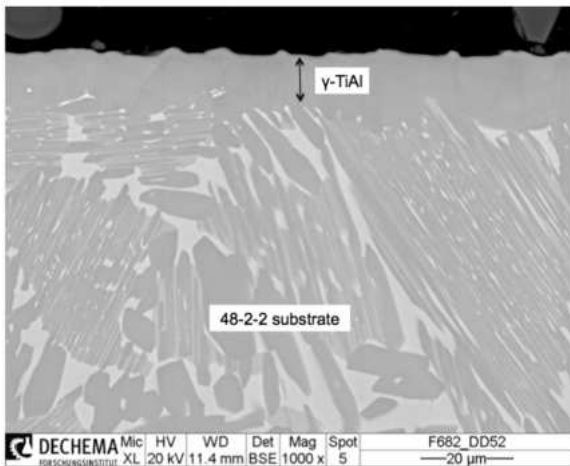
Fig. 1: BSE image of an out-of pack cemented 48-2-2 substrate
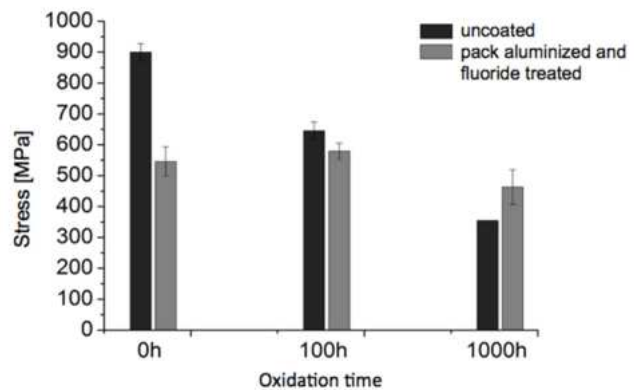
Fig. 2: Comparison of stress parameters of the uncoated versus pack aluminized and fluorine treated samples dependent on the oxidation time at 900°C (TNM-B1)

All in all, application of a single intermetallic γ-TiAl layer in combination with a subsequent fluorine treatment reduces the consumption of the load bearing cross section as well as the degradation of mechanical properties especially for the desired long-term high temperature exposure

References

[1] M. Weimer, B. Bewlay, T. Schubert, 4th International Workshop on Titanium Aluminides, Nürnberg, Germany, **2011**, 4-8

[2] S.L. Draper, D. Isheim, Intermetallics, 22 (**2012**), 77-83

[3] J.L. Smialek, J.A. Nesbitt, W.L. Brindley et al., Mat. Res. Soc. Symp. Proc., Vol. 364, **1994**, 1273-1284

[4] J. Grüters, M.C. Galetz, Intermetallics, 60 (**2015**), 19-27

[5] S. Friedle, N. Nießen, R. Braun, M, Schütze, Surface & Coating Technology, 212 (**2012**) 72-78

[6] A. Donchev, M. Schütze, Materials Science Forum Vols. 638-642 (**2010**), 1294-1299

P–09

Effect of microstructure containing β-Ti phase on crack propagation behavior of wrought γ-TiAl based alloys

Loris Signori[1], Taiki Nakamura[1], Yotaro Okada[2], Hirotoyo Nakashima[2] and Masao Takeyama[2]

[1]Dept. Metallurgy and Ceramics Science, [2]Dept of Materials Science and Engineering, Tokyo Institute of Technology, S8-8, 2-12-1 Ookayama, Meguro-ku, Tokyo, Japan.
e-mail: signori.l.aa@m.titech.ac.jp

Introduction

In an environmental and economical context, more and more strained due to the necessity to reduce CO_2 emission and the continuous rise of kerosene price, engine companies look ceaselessly for new solutions to improve the efficiency. One of the ways to solve the problems is to use light-weight materials for jet engines in order to decrease fuel consumption. Titanium aluminides are one of the promising materials which show half density of conventional heat resisting alloys (Fe and Ni base) and potential mechanical properties up to 800°C. These materials have been investigated in order to replace the last stage of low pressure turbine (LPT) blades and possibly high pressure compressor (HPC) blades. Recently, a wrought material was commercially applied to LPT blades which do not exceed 650°C. The wrought process using β-Ti phase was already proposed in our previous study [1] and a TiAl based turbine blade has successfully been made. However, due to brittle characteristics of γ-TiAl based alloys, the crack propagation behavior could lead to critical damages, so that understanding the crack initiation and propagation behavior of these materials is crucial for development of new class of TiAl alloys. In the present study, although β-Ti phase is in general considered as detrimental for both creep and toughness, the fatigue crack growth behavior of a wrought TiAl based alloy with different microstructures containing β phase has been examined using *in-situ* and *ex-situ* observations, and the role of β phase on crack propagation behaviors will be discussed.

Materials and Methods

TiAl alloys presented in this study are Ti-Al-M1-M2 where M1 and M2 are β-stabilizer (Nb, V…) and present a unique phase transformation pathway $\beta+\alpha\rightarrow\alpha\rightarrow\alpha+\gamma\rightarrow\beta+\gamma$ used to design microstructures. Alloy pancake was elaborate using cold crucible induction melting (CCIM) with a size of 70 mm in diameter and 900 mm in height. Then, the columnar ingot was cut in pieces with 100 mm in height, and hot free-forged in β+γ two-phase region around 1573K with height reduction to 45 mm by one stroke. Two distinct microstructures were designed: nearly lamellar microstructure (NL) and nearly duplex microstructure (NDP). The nearly lamellar microstructure (Fig.1a) presents equiaxed α_2/γ lamellar grains with an average size of 50 μm surrounded by duplex microstructure (DP) which consist of β and γ grains with a DP fraction (V_{DP}) around 10 %. This microstructure was realized by heating up the as-forged specimen at 1573 K in β+α two-phase region, followed by air cooling where the lamellar microstructure is formed by the $\alpha\rightarrow\gamma$ phase transformation, and then, subsequently heat treated at 1173 K for 1 h to stabilize the microstructure. In contrast, the second microstructure (Fig.1b) consists of γ and β grains ($V_{DP} > 95$ %) with 20 μm in size with a small amount of α_2 grains and remaining α_2/γ lamellar grains. This microstructure was done by holding the as-forged sample at 1373 K for 42h in $\beta+\alpha_2+\gamma$ three-phase region, followed by air cooling. Fatigue crack growth (FCG) test was carried out using a half size compact tension specimen (CT) in accordance with ASTM E-647. Precracks were introduced at the tip of the CT specimen notch with 1.2 mm in length by cyclic tension-tension load in elastic region. The fatigue crack growth tests were conducted at room temperature in air under cyclic stress intensity (ΔK) control with load ratio R=0.1 and a frequency of 20 Hz. K-decreasing test and K-increasing test were respectively conducted by load shedding and by constant load amplitude

independently, where *K* is stress intensity factor at the tip of the crack. Normalized K gradient of 0.08/mm was used during load shedding. Crack size was measured using direct current potential drop technique (DCPD). *In-situ* observation of crack growth behavior was performed by CCD camera and *ex-situ* microstructure analysis was done by SEM.

Results and Discussion

Fig.2 shows the fatigue crack propagation curves of NL and NDP specimens, together with GE alloy (4822) with fully lamellar microstructure [2]. Precracks have been successfully introduced at the specimen notch. The NL specimen exhibits the higher fatigue crack growth threshold ΔK_{th} of 10.9 MPa√m and the lower crack growth rate corresponding to the Paris slope. In contrast, the NDP specimen shows the lowest ΔK_{th} and the lowest crack growth rate. These results clearly demonstrate that the introduction of a small volume fraction of DP microstructure at lamellar colony boundaries is effective in increasing the fatigue properties. However, the fatigue properties become worse if the DP volume fraction becomes too high. Fig.3 shows the difference in the crack propagation pathway for both microstructures. In NL specimen, the morphology of the cracks is zigzagged with many secondary branches and ligament bridges (Fig.3a), whereas the crack goes straight through the NDP specimen, (Fig.3b). The zigzagged morphology depends on α_2/γ lamellar orientation of each grain with respect to the stress axis. However, it should be noted that, regardless of the orientation, the crack is arrested at DP area, indicating that DP microstructure is effective in crack propagation resistance when it decorates the colony boundaries. The detailed mechanism of the role of β phase in DP microstructure in cracking will be presented.
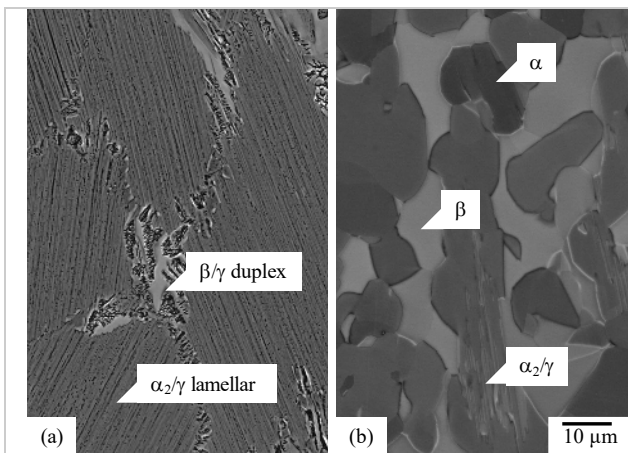
Fig. 1: BSE image of initial microstructure (a) nearly lamellar and (b) nearly duplex
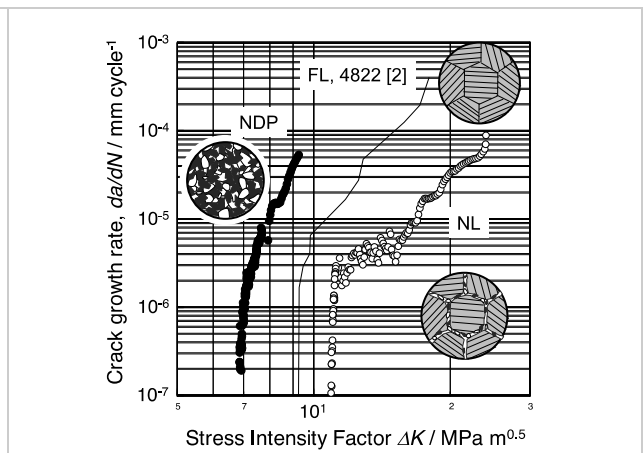
Fig. 2: Fatigue crack growth curve obtained for different microstructures
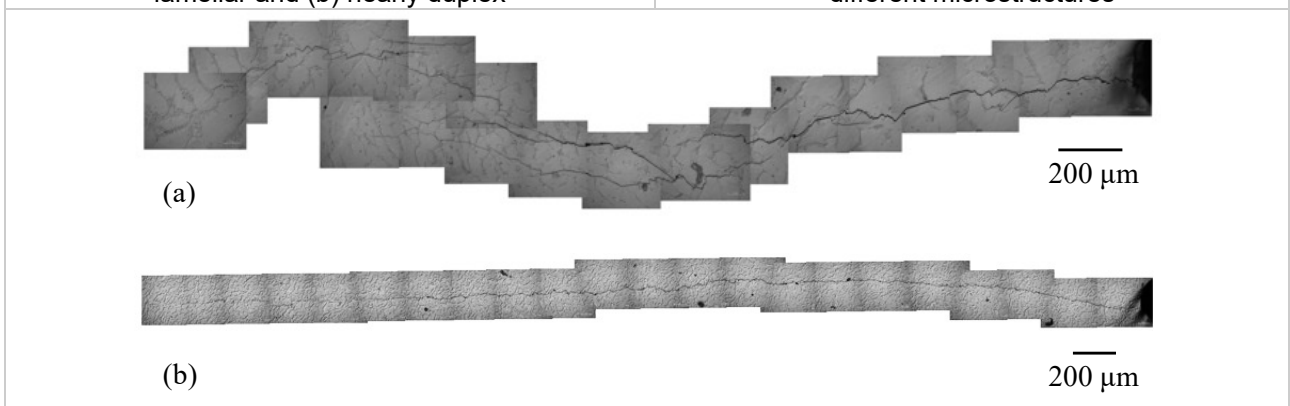
Fig. 3: Comparison of crack propagation pathway (a) nearly lamellar and (b) nearly duplex

References

[1]   M. Takeyama, Satoru Kobayashi, Intermetallics, 2005, 13, 993-999

[2]   M. S. Dahar, S. M. Seifi, B.P. Bewlay, J. J. Lewandowski, Intermetallics. 2015, 57, 73-82

P–10

Powder metallurgy of intermetallic alloys: peculiarities of technology

I.M. Razumovskiy, I.A. Logachev, A.I. Logacheva

OJSC «Kompozit», 141076, Russian Federation, Korolev, Pionerskaya St. 4

info@kompozit-mv.ru

We discuss the distinguishing features of production of intermetallic alloys by applying the Plasma Rotating Electrode Process (PREP) and subsequent Hot Isostatic Pressing (HIP). A complex treatment PREP+HIP allows one to produce different kinds of microstructures that are especially important in a case of intermetallic alloys having a large tendency to embrittlement at ambient temperatures. We use the following approach to fabricate a small-grained microstructure in the compacted state with an acceptable level of ductility. Firstly, we improved the existing PREP technology so that it can effectively suppress impurities' contamination during atomization and allows one to obtain predominantly spherical particles with a small diameter ≤ 100 µm. Secondly, we applied a special approach to determine the parameters of HIP (the temperature T_{HIP} and the pressure P_{HIP}). If one needs to conserve a small-grained microstructure in the compacted state after HIP, P_{HIP} pressure at a given temperature T_{HIP} has to be smaller than $\sigma_{0.02}$ (0.02 proof stress) and a condition of the large diffusion path of vacancies in the microstructure has to be fulfilled. Finally, data dealing with microstructure, mechanical and functional properties of the intermetallic alloys based on Ni_3Al and $NiAl$ are presented.

P–11

Tensile creep of directionally solidified eutectic NiAl-(Cr/Mo) micro-specimens

LiKang Luan[1], Heinz Riesch-Oppermann[2] and Martin Heilmaier[3]

[1] Karlsruhe Institute of Technology, Institute for Applied Materials (IAM), Hermann-von-Helmholtz-Platz 1, D-76344 Eggenstein-Leopoldshafen, Germany, likang.luan@kit.edu

[2] Karlsruhe Institute of Technology, Institute for Applied Materials (IAM), Hermann-von-Helmholtz-Platz 1, D-76344 Eggenstein-Leopoldshafen, Germany, heinz.riesch-oppermann@kit.edu

[3] Karlsruhe Institute of Technology, Institute for Applied Materials (IAM), Engelbert-Arnold-Straße 4, D-76131 Karlsruhe, Germany, martin.heilmaier@kit.edu

Introduction

The intermetallic phase NiAl is a promising high-temperature structural materials candidate owing to a number of attractive properties such as low density (5.95g/cm3), high melting temperature (1638°C), as well as good oxidation and corrosion resistance. However, its poor creep properties limit the application at elevated temperatures.

It has recently been proven by several studies [1-4] that eutectic composites of directionally solidified NiAl/X with refractory metal reinforcement (X= Cr, Mo) have significantly improved creep properties based on a highly aligned fiber or lamella micro structure. A systematic study of the creep behaviour of NiAl-refractory metal composites on the micro-scale is needed to understand its mechanism. For this purpose, tensile creep tests with micro specimens were carried out to study the creep properties influenced by the miniaturized specimens size compared to conventional specimens, as well as the microstructure, specially under the consideration of the fiber/lamella orientation and misalignment [2].

Materials and Methods

A customized-built setup is adapted for tensile creep tests of micro specimens at temperatures up to 1000°C [5]. The micro specimens of directionally solidified NiAl-refractory metal composites have a dog-bone shape with a gage length of 1 mm, a quadratic cross-section of 0.2x0.2 mm^2 and were manufactured by EDM (Electrical Discharge Machining). The specimens were tested under different tensile stress and temperatures until fracture. A contactless strain measurement with accuracy of better than 10^{-4} is obtained by Digital Image Correlation (DIC) which additionally provides the local strain distribution on the specimen surface. The tensile creep tests are performed under constant load conditions controlled by a load cell and an actuator. The maximum error in the applied stress is less than 0.5%. The microstructure of the specimens and the fracture mechanism were analyzed with SEM and TEM before and after tensile creep tests.

Results and Discussion

The tensile creep tests on micro specimens with our custom-built setup could be performed with a high accuracy and stability at temperatures up to 1000°C. This was established by calibration experiments with Nimonic 75, where conventional creep results are readily available [6]. Results on the tensile creep behavior of the directionally solidified NiAl-refractory metal composites, however, show pronounced differences even at the same experimental conditions, as shown in Fig.1. The differences are attributed to features of the directionally solidified microstructure, especially:

1. A localization of the strain distribution on the micro specimens. This leads to local stress concentrations and affects the strain measurement in the tertiary creep stage. A DIC analysis allows to determine the initiation time and position of the stress concentration process.

2. The miniaturization of the NiAl-(Cr/Mo) specimens increases the sensitivity of the creep behavior to the corresponding microstructure, for example, the boundaries caused by the misalignment of fiber/lamella.

Tensile creep tests with single crystalline NiAl specimens will be carried out to study the size influence of the micro specimens compared to conventional specimens. NiAl-(Cr/Mo) specimens with different fiber/lamella orientation and microstructure will be researched to understand the creep mechanism.
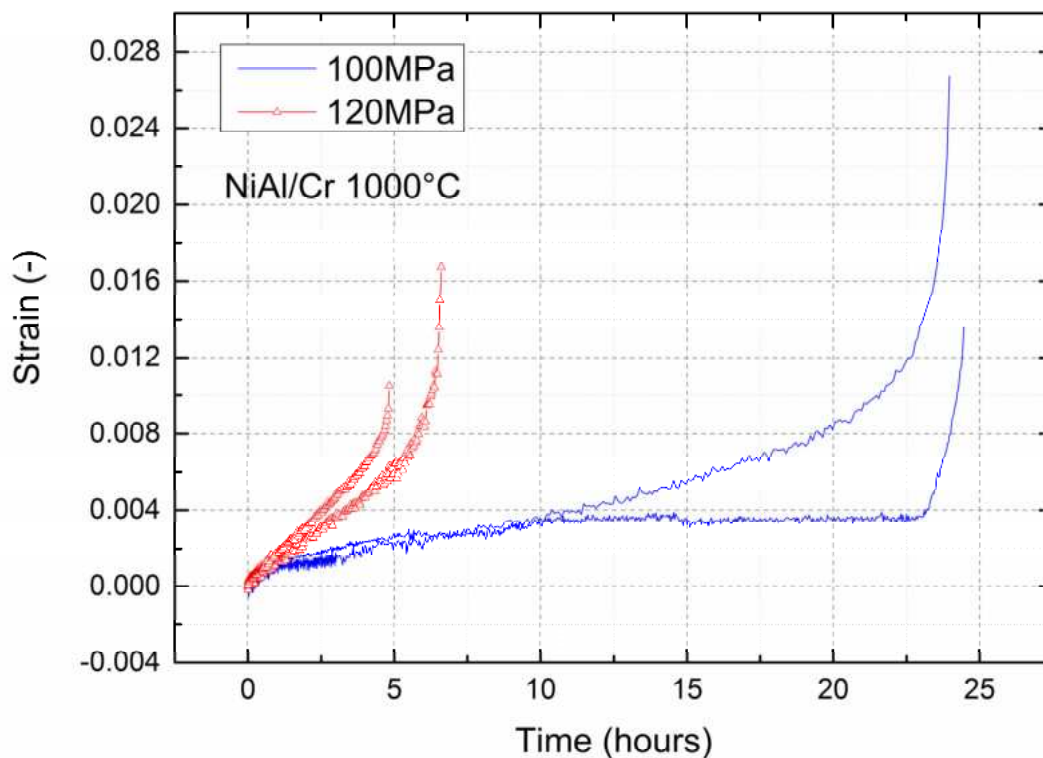
Fig. 1: Tensile creep curves of micro NiAl/Cr specimens at 1000°C with stress 100 MPa and 120 MPa.

References

[1] L. Hu et al., "Tensile Creep of Directionally Solidified NiAl–9Mo in Situ Composites," *Acta Materialia* 61, no. 19 (2013): 7155–65.

[2] C. Seemüller et al., "Influence of Fiber Alignment on Creep in Directionally Solidified NiAl–10Mo in-Situ Composites," *Intermetallics* 35 (2013): 110–15.

[3] M. Dudová et al., "Creep in Directionally Solidified NiAl–Mo Eutectics," *Scripta Materialia* 65, no. 8 (2011): 699–702.

[4] D. R. Johnson et al., "NiAl-Based Polyphase in Situ Composites in the NiAl-(Ta/X) (X= Cr, Mo, or V) Systems," *Intermetallics* 3, no. 6 (1995): 493–503.

[5] D. Leisen et al., "Mechanical Characterization between Room Temperature and 1000 °C of SiC Free-Standing Thin Films by a Novel High-Temperature Micro-Tensile Setup," *Review of Scientific Instruments* 86, no. 5 (2015):

[6] Heilmaier M. "Modellkompatible Beschreibung des Kriech- und Zeitstandverhaltens oxiddispersions-gehärteter Nickelbasissuperlegierungen" . Düsseldorf: VDI-Verl., 1993.

P–12

Characterising the interaction of a NiAl-based anchor phase with CMSX-4

M. R. McGregor[1,a], M. E. Hancock[2,b], L. Pallett[2,c] and W.J. Clegg[1,d]

[1]University of Cambridge, Department of Materials Science & Metallurgy, CB3 0FS, United Kingdom

[2]Rolls-Royce plc., Derby, United Kingdom

[a]mrm48@cam.ac.uk, [b]matthew.hancock@rolls-royce.com, [c]lloyd.pallett@rolls-royce.com, [d]wjc1000@cam.ac.uk

Introduction

In a gas turbine engine, leakage of gas from the flow path reduces the efficiency of the engine. Currently, this leakage is reduced in the high pressure turbine by using shrouded turbine blades. However, this can have several disadvantages, such as reduced disc life. One way to tackle this, and achieve better sealing, is to tip shroudless turbine blades with an abrasive system that cuts into a surrounding abradable material. Currently, such systems are composed of c-BN abrasive particles embedded in an MCrAlY anchor phase. Previous work has shown that at operating temperatures, the MCrAlY is too weak to retain the embedded c-BN particles under abrasion [1]. A new two-phase anchor phase system based on NiAl, strengthened with a reinforcing Laves phase, NiTaAl, has been identified as a possible replacement material with sufficient strength.

Compatibility between the anchor phase and the underlying CMSX-4 turbine blade at operating temperatures is essential. The interaction of MCrAlYs with CMSX-4 is well known, as they are frequently used as bond coats in thermal barrier coatings [2]. However, the interactions between NiAl-NiTaAl and CMSX-4 are unknown. In this work, diffusion couples have been used to investigate the interaction of $Ni_{45.3}Al_{44.7}Ta_{10}$ with CMSX-4 above 900 °C, and to examine the effect of a platinum layer between the two materials.

Materials and Methods

Diffusion couples were prepared using CMSX-4 rods, 9mm in diameter, provided by Roll-Royce plc., and arc melted NiAl-NiTaAl. The compositions of the two materials used are, in at.%, 63.75Ni-12.59Al-9.26Co-7.58Cr-2.18Ta-1.98W-1.27Ti-0.98Re-0.38Mo-0.03Hf for CMSX-4 and 45.3Ni-44.7Al-10Ta for the anchor phase system under investigation. The materials were bonded using an induction heating vacuum diffusion bonder, under a load of 10kg at 1000 °C for 1 minute. The faces to be bonded were polished to a 1 μm finish using diamond paste. Sections of the couple were then heat treated under vacuum for 16 hours at 900 °C, 1000 °C or 1100 °C. The interdiffusion zone between the two materials was characterized using scanning electron microscopy and energy-dispersive X-ray spectroscopy.

Results and Discussion

Fig.1 shows the microstructure of the diffusion couple immediately after bonding, with CMSX-4 on the left and NiAl-NiTaAl on the right. The Laves phase structure is significantly larger in scale than the CMSX-4 precipitate size, and the bonding process has caused little disruption in both microstructures. Fig. 2 show the microstructure of the diffusion couple after 16 hours at 1100 °C. The heat treatment has led to the development of an interdiffusion zone, similar to that seen in aluminised CMSX-4 [3]. EDX showed that nickel has diffused from the CMSX-4 into the NiAl-NiTaAl, and aluminium and tantalum have diffused in the opposite direction, from the NiAl-NiTaAl into the CMSX-4. The combination of these fluxes destabilises the continuous Laves phase, NiTaAl, and stabilises the discontinuous Heusler phase Ni_2TaAl. This reduces the effectiveness of the anchor phase, as the continuous Laves phase is required to provide greater strengthening.

Investigation of the effectiveness of a platinum layer on the CMSX-4 at preventing diffusion is ongoing.
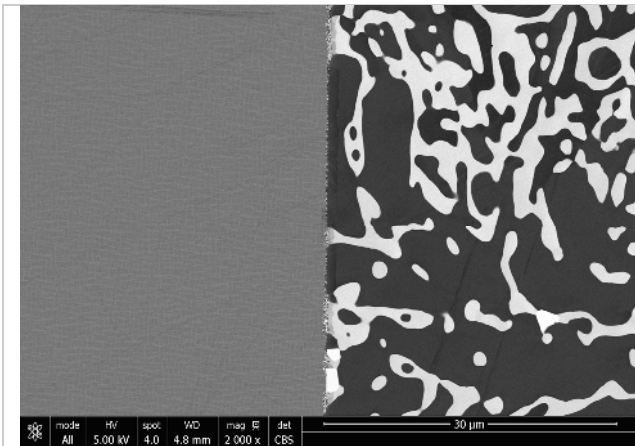

Fig. 1: BSE SEM image of the microstructure of a CMSX-4/NiAl-NiTaAl diffusion couple before heat treatment. CMSX-4 is on the left and NiAl-NiTaAl is on the right. NiAl is the darker phase, and NiTaAl is the brighter phase.
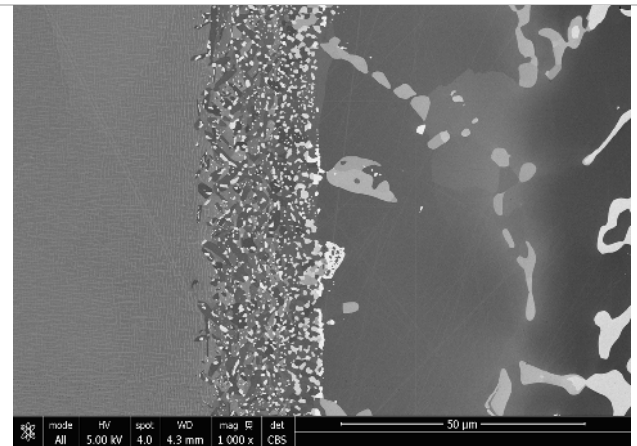
Fig. 2: BSE SEM image of the microstructure of a CMSX-4/NiAl-NiTaAl diffusion couple after heat treatment. An interdiffusion zone has formed underneath the coating, where the CMSX-4 microstructure is disrupted by the formation of TCPs. The Laves phase near the interface has started to break up.

References

[1] J. R. Davenport, L. Mendez-Garcia, S. Purkayastha, M. E. Hancock, R. J. Stearn, W. J. Clegg, Materials Science and Technology. **2014**, *30*, 1877-1883.

[2] N. P. Padture, M. Gell, E. H. Jordan, Science. **2002**, 296, 280-284

[3] C. M. F. Rae, M. S. Hook, R. C. Reed, Materials Science and Engineering A. **2005**, *396*, 231-239

P–13

Phase-field simulation of the microstructure evolution during directional solidification in the eutectic NiAl-9Mo system

Kaveh Dargahi Noubary[1,*], Michael Kellner[1,2], Philipp Steinmetz[1], Johannes Hötzer[1,2], Britta Nestler[1,2]

[1]Institute of Applied Materials, Karlsruhe Institute of Technology (KIT), Straße am Forum 7,

76131 Karlsruhe, Germany

[2]Institute of Materials and Processes, Karlsruhe University of Applied Sciences,

Moltkestrasse 30, 76133 Karlsruhe, Germany

*corresponding author

kaveh.noubary@kit.edu, michael.kellner@kit.edu, philipp.steinmetz@kit.edu, johannes.hoetzer@kit.edu, britta.nestler@kit.edu

Introduction

With its high melting point and low density, the intermetallic compound NiAl is interesting for industrial applications at high temperatures [1-3]. In order to improve material properties of this alloy like the fracture toughness and its ductility at room temperature, additional refractory elements (e.g. Cr, Mo, W) are added [4], resulting in a second reinforcing phase. This modification leads to systems with a quasi-binary eutectic composition. During directional solidification at these eutectic compositions, rods of the refractory elements evolve embedded in a NiAl matrix. Depending on the process parameters like the temperature gradient and a controlled solidification velocity, various arrangements of the rods evolve on different length scales. These rod arrangements influence the resulting material properties. Simulation studies allow to investigate affecting parameters in detail. Therefore, the directional solidification process of the eutectic NiAl-9Mo system is simulated with the phase-field model in large domains similar to the investigations for the eutectic system NiAl-34Cr in [5]. In addition to [5] the crystallographic anisotropy of NiAl-9Mo is included in the simulations and its influence on the microstructure evolution is systematically studied.

Materials and Methods

The simulation studies are based on, a phase-field model formulated in terms of the grand potential approach is used [6, 7]. The utilized thermodynamic CALPHAD database is presented in [8]. The coupling between databases and the phase-field model to increase the thermodynamic consistence is published in [5, 9]. The input data for a comparison with experimental results like temperature gradient and solidification velocity are derived from [10].

In order to simulate directional eutectic solidification of NiAl-9Mo and to study the influences of the anisotropy on the evolving microstructure, two distinct approaches are investigated. First, simulations of a real ternary system are performed in which Al, Mo and Ni are defined as three distinct components. Afterwards, to reduce computational efforts, the intermetallic phase NiAl is modeled with a combined definition of the two components Ni and Al, resulting in a pseudo-binary system.

For both simulation studies the Gibbs energies, derived from the thermodynamic database are fitted to model the equilibrium of the liquid phase with the two solids in the eutectic reaction. From the fitted Gibbs energies, the grand potentials are calculated. Their differences act as driving forces for the phase transition. In the first case of a ternary system, the information of the Gibbs energies are derived from the three-dimensional phase diagram while in quasi-binary system, its two-dimensional cut is used (Fig.1).

Results and Discussion

In Fig. 2 the result of a two-dimensional simulation of the pseudo-binary system NiAl-9Mo is depicted. The NiAl-rich matrix phase is indicated in black and the Mo-rich rod in dark grey. Both phases grow simultaneously in the light grey liquid phase. The simulations are validated analytically by two- and three-dimensional Jackson-Hunt analyses for several solidification velocities and different strength and orientations of the surface energy anisotropy. The curves of the undercooling over the spacing show the typical Jackson-Hunt-like behavior with a minimum undercooling at λ_{JH}.

With three-dimensional large-scale simulations, the influences of the process (temperature gradient, solidification velocity) and material parameters (anisotropy) on the phase fractions, rod spacings and rod shapes are investigated. In 3D similar trends and correlations as discussed by the 2D Jackson-Hunt analysis are found.
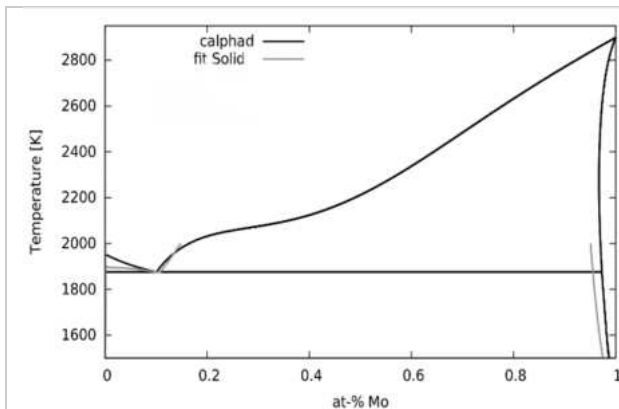
Fig. 1: Pseudo-binary phase diagram of NiAl-9Mo.	Fig. 2: Concentration distribution of Mo during eutectic solidification in pseudo-binary NiAl-9Mo system.
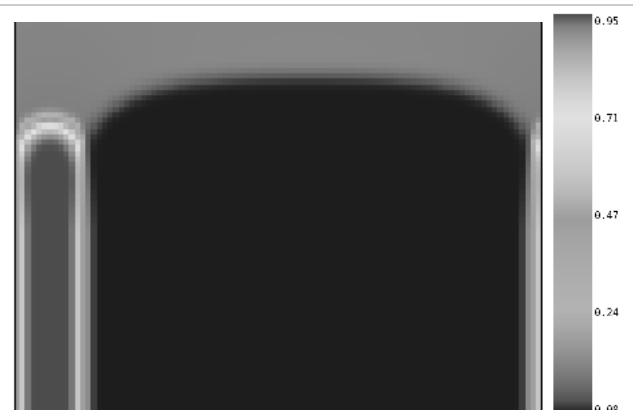
References

[1] D.B. Miracle, Acta Metallurgica et Materialia. **1993**, 41.3, 649-684.

[2] D. Ram. JOM Journal of the Minerals, Metals and Materials Society. **1991**, 43.3, 44-49.

[3] K. Vedula, V. Pathare, I. Aslanidis, R. H. Titran, MRS Proceedings. Vol. 39. Cambridge University Press, **1984**.

[4] G. Frommeyer, R. Rablbauer, and H. J. Schäfer, Intermetallics. **2010**, 18.3, 299-305.

[5] M. Kellner, I. Sprenger, P. Steinmetz, J. Hötzer, B. Nestler Computational Materials Science. **2017**, 128, 379-387.

[6] A. Choudhury, B. Nestler Physical Review E. **2012**, 85.2, 021603.

[7] J. Hötzer, M. Jainta, P. Steinmetz, B. Nestler, A. Dennstedt, A. Genau, U. Rüde, Acta Materialia. **2015**, 93, 194-204

[8] P. Jian, P. Franke, and H.J. Seifert. Journal of Phase Equilibria and Diffusion. **2016**, 37.5, 592-600.

[9] A. Choudhury, M. Kellner, B. Nestler, Current Opinion in Solid State and Materials Science. **2015**, 19.5, 287-300.

[10] J.F. Zhang, S.H.E.N. Jun, Z. Shang, W.A.N.G. Lei, H.Z. Fu, Transactions of Nonferrous Metals Society of China. **2013**, 23(12), 3499-3507.

P–14

Characterization of Al/Ni intermetallic formed by
high energy ball milling (HEBM) at low temperature

Mingu Han,* Keundeuk Lee, Sang-Hyun Jung, and Sojung Lee

Agency for Defense Development (ADD), Yuseong POB 35-42, Daejeon 305-600, South Korea
E-mail: mingu@add.re.kr

Introduction

Owing to higher heat of reaction (ΔH_R) for the intermetallic (Al/B, B/Ti, Al/Ni) compare to other conventional energetic materials including TNT, RDX, and HMX [1], the metals comprised of a fuel and an oxidizer have been attractively studied and utilized in the explosive, propellants, and pyrotechnic area for military applications. An intermetallic reaction being a solid state diffusion controlled reaction, the maximized interfacial contact area between metals is preferred for achieving high energy release. The ultrasonic mixing and the high energy ball milling (HEBM) have been utilized as effective means to enhance intermetallic performance. This mechanical approaches, however, are negatively affects both refinement rate and final product performance because of frequently happened alloying by mechanically triggered exothermic reaction between metals during the process. Even though the HEBM at cryogenic temperature (77K) was considered as an alternative for suppressing undesired reaction [2,3], the fundamental understanding of their behaviors for the milling at low temperature is still deficient.

In this work, we investigated morphological and thermal characteristics of Al/Ni intermetallic materials, which are synthesized with different milling dose at -50°C using a high energy ball milling. Moreover, the compressive properties for compacts formed by hydraulic press of intermetallic powders under different pressure and their combustion behaviors were studied.

Materials and Methods

The 31.5 wt. % of aluminum (45 μm, Changsung) and the 68.5 wt. % of Nickel (45 μm, Vale) based intermetallic with different milling dose were synthesized at -50°C. The HEBM (PBM-150, Nanointech) equipped with the nozzle for controlling temperature by spraying liquid N_2 at exterior of milling jar was operated for preparation of samples. The Hexane (Aldrich) was used as a process control agent (PCA). All milling experiments were conducted with 10 mm (or 3mm) diameter of stainless steel, or zirconium oxide balls with ball to powder ratio (BPR) at 5 under Ar atmosphere.

Results and Discussion

The development of micro-structure phase for Al/Ni intermetallic powders prepared by HEBM at -50°C is relatively slower than those of materials prepared at room temperature. After 15 min of milling, the exothermic peak caused by reaction of solid Al and Ni appears with the existing eutectic peak for reaction between melted Al and solid Ni. And only solid-solid exothermic peak appears at 450°C after 60 min of milling. In the case compacts manufactured by high pressure press, the overall trends for thermal properties was similar with powders. Unlike the DSC curves for powder, the applied pressure for forming compacts can additionally decrease the inter-particle distance with no or low milling dose so that new exothermic peak was occurred at 530°C.

The compressive stress measured with 10 mm/min of compression rate and at 25°C were proportional to the applied pressure (2.3 - 7.0 kbar) for forming compacts and the highest value among samples was about 1414 bar, which was obtained in the sample (Milling time: 40 min, temperature: -50°C) pressed at 7.0 kbar. The compressive stress values for all compacts formed at 7.0 kbar were similar with the highest one except a bare one (1200 bar). Since the practically applied pressure for forming compacts might be reduced by increasing effect of work hardening on intermetallic materials occurred by the repetitive milling process consisting of sequence of flattening, welding, fracturing, and re-welding, the relatively low compressive stress was obtained

in the highly milled sample (60min, -50°C) at 2.3 - 3.7 kbar pressure range than that of bare sample.

The combustion behavior of samples ignited by a NiCr wire were recorded using the high speed camera and their heat of combustion was calculated by the bomb calorimeter. As shown in the figure 1 and 2, the value of heat of combustion for of Al/Ni samples were measured in proportion to violent reaction pattern of combustion. The heat of combustion for bare, 40 min, and 60 min samples were 6.0 kJ/g, 7.8 kJ/g, and 11.1 kJ/g, respectively. Despite highly violent combustion behavior for sample prepared in room temperature, its heat of combustion was only 7.7 kJ/g.
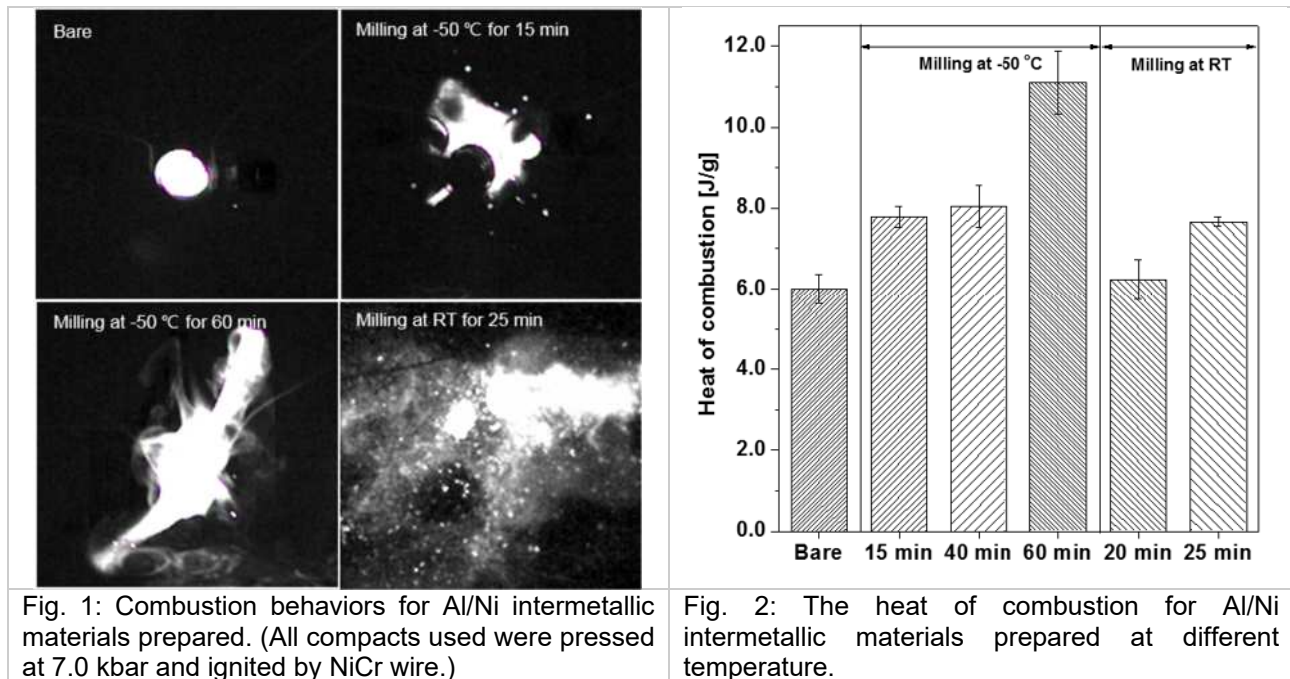
| Fig. 1: Combustion behaviors for Al/Ni intermetallic materials prepared. (All compacts used were pressed at 7.0 kbar and ignited by NiCr wire.) | Fig. 2: The heat of combustion for Al/Ni intermetallic materials prepared at different temperature. |

References

[1] S.H. Fischer, M. Grubelich, 32th AIAA/ASME/SAE/ASEE joint propulsion conference and exhibit, Orlando, FL USA, 1-3 July 1996,

[2] E.J. Lavernia, B.Q. Han, J.M. Schoenung, Materials Science and Engineering A. **2008**, *493*, 207-214.

[3] C. Badiola, M. Schoenitz, X. Zhu, E.L. Dreizin, Journal of Alloys and Compounds. **2009**, 488, 386-391.

P–15

As-cast and directionally solidified microstructures along the eutectic trough of the NiAl-Cr-Mo system

Camelia Gombola[1], Ioannis Sprenger[1], Michael Kellner[1], Kaveh D. Noubary[1] and Martin Heilmaier[1]

[1]*Karlsruhe Institute of Technology, Institute for Applied Materials*, Germany,
Camelia.Gombola@kit.edu; Ioannis.Sprenger@kit.edu; Michael.Kellner@kit.edu;
Kaveh.Noubary@kit.edu; Martin.Heilmaier@kit.edu

Introduction

The challenges in power generation and air transportation require new high-temperature materials to increase the efficiency. Therefore investigations have been carried out in order to develop NiAl-based in-situ composites during the last years. Due to the higher melting temperatures, lower densities, higher thermal conductivities and excellent high-temperature oxidation resistance of NiAl-based alloys compared to Ni-based superalloys, these are alloys of interest for high-temperature applications. However, such alloys suffer from low creep resistance and insufficient strength at elevated temperatures as well as poor ductility and fracture toughness at room temperature. These disadvantages can in principle be compensated by alloying NiAl with refractory metals such as Mo, Cr, V, Hf and Re. By doing so, pseudo-binary eutectic alloys are formed and further processing by directional solidification results in aligned microstructures consisting of the NiAl matrix and the refractory metal as strengthening phase exhibiting superior mechanical properties at both ambient and elevated temperatures. In the pseudo-binary systems the amount of the reinforcing phase at the eutectic compositions are invariant. In case of multinary systems, a possible adjustment of the volume fraction of the reinforcing phase can be established. In the present work, experimental investigations of the NiAl-Cr-Mo system were performed. In particular, we focus on the microstructure along the eutectic trough of the NiAl-Cr-Mo system which was calculated by Peng et al. [1] shown in Fig. 1. As-cast as well as directionally solidified microstructures are investigated for several different alloys.

Materials and Methods

The alloys with the nominal composition of NiAl-**x**Cr-**y**Mo (**x**=31…0.5 at.%; **y**=3…10.3 at.%) were produced using an arc-melting device with protective argon atmosphere. The alloy compositions are highlighted with dots on the liquidus projection in Fig. 1. In the first step, buttons were synthesized from high purity Ni, Al, Cr and Mo (>99.99 % pure) and re-melted five times to achieve a sufficient homogeneity. The loss of mass due to the sample preparation is lower than 0.3 wt.%. Thus, changes in alloy composition by evaporation are negligible and the nominal compositions are used throughout this contribution. In the second step, samples were sliced by electro-discharge machining and prepared for microstructural analysis. For the directional solidification, the alloys were drop cast into a copper mold with cylindrical shape with a diameter of 12.5 mm and a length of 170 mm. The cast rods were then directionally solidified using horizontal float zone technique with an induction coil as heating source. Constant growth rates of 18 mm/h and 60mm/h were chosen, respectively. The feed and seed rods were rotated in opposite direction at a rotational speed of 15 rpm to achieve a homogeneous concentration profile in the melt. Microstructure investigations by scanning electron microscopy (SEM) were carried out on transverse sections.

Results and Discussion

By adjusting the Mo content in Cr-rich pseudo binary eutectic alloys, the morphology of the reinforcing phase can be modified. Fibrous microstructure exists up to NiAl-33.5Cr-0.5Mo whereas already 0.1 at.% additional Mo leads to a faceted structure. Finally, at 1 at.% Mo the microstructure was described as lamellar [2,3]. Such an as-cast lamellar microstructure is shown in Fig. 2a for a NiAl-31Cr-3Mo alloy. For decreasing Cr and increasing Mo content, microstructure remains similar, but reinforcing phase fraction changes significantly. First indication for fiber formation was

observed at 9.6 at.% Cr. The as-cast state of NiAl-1Cr-9.9Mo (Fig. 2b) exhibits similar microstructure when compared to the Cr-free alloy. In summary, the morphology of the reinforcing phase of NiAl-Cr-Mo composites changes along the eutectic trough from fibers to lamella and back to fibers.

For the further processing two alloys, namely NiAl-9.6Cr-10.3Mo and NiAl-0.5Cr-9.9Mo, were chosen. The NiAl-9.6Cr-10.3Mo possesses an alternating, irregular microstructure, while a promising microstructure has been observed for the NiAl-0.5Cr-9.9Mo alloy. Equilibrium calculations were carried out in order to determine liquidus and solidus temperatures along the eutectic trough for the respective alloy compositions. The interval between those temperatures is significantly increased in the case of multinary compositions when compared to the pseudo binary border systems. In detail, 64 K for NiAl-9.6Cr-10.3Mo surpasses the undercooling in the liquid zone for the present zone melting device resulting in the observed irregular microstructure. In contrast, NiAl-0.5Cr-9.9Mo solidifies within 10 K under equilibrium conditions and exhibits well-aligned microstructure subsequent to directional solidification and can be considered for future investigations.
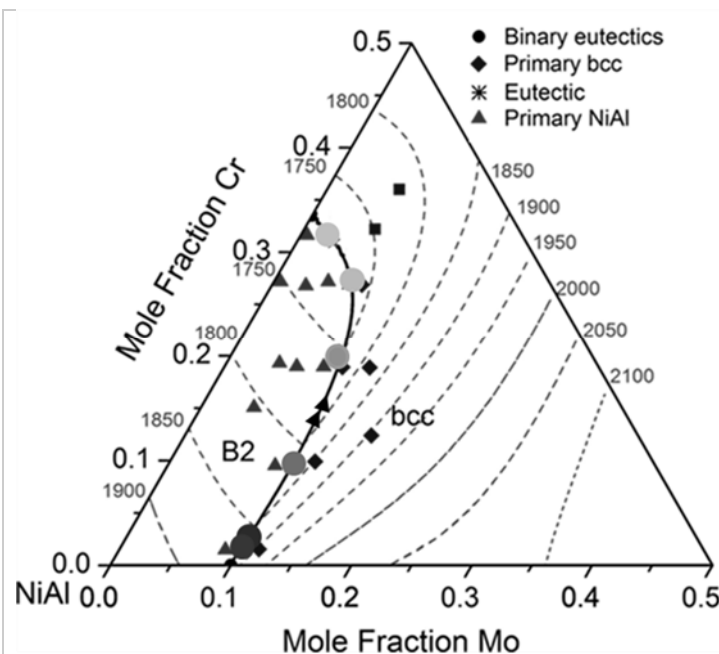
| Fig. 1: Calculated liquidus projection of the NiAl-Cr-Mo system [1] | Fig. 2: As-cast microstructure in BSE contrast: a) NiAl-31Cr-3Mo; b) NiAl-0.5Cr-9.9Mo |
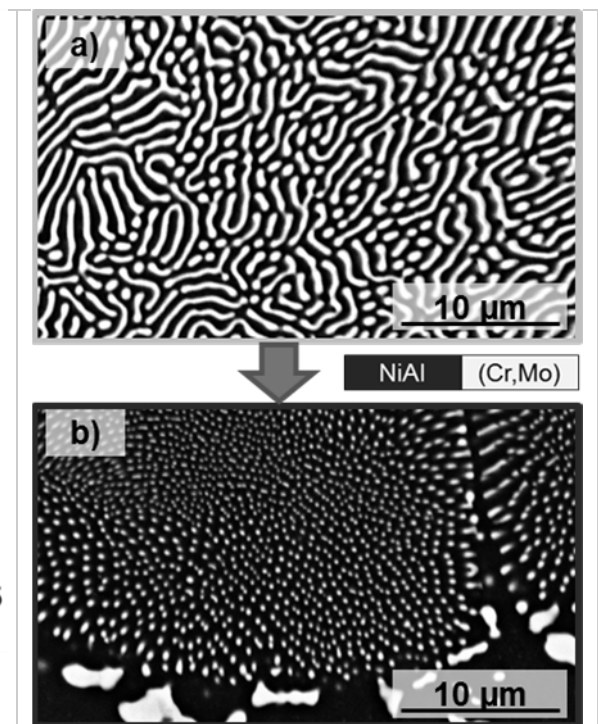
References

[1] J. Peng, P. Franke, H. J. Seifert: Journal of Phase Equilibria and Diffusion, Vol. 37 No. 5, **2016**, 592-600.

[2] H. E. Cline, J. I. Walter: The Effect of Alloy Additions on the Rod-Plate Transition in the Eutectic NiAl-Cr, Metallurgical Transactions Vol. 1, **1970**, 2907- 2917.

[3] J. D. Whittenberger, S. V. Raj, I. E. Locci, J. A. Salem: Elevated Temperature Strength and Room-Temperature Toughness of Directionally Solidified NiAl-33Al-33Cr-1Mo, Metallurgical and Materials Transactions A Vol. 33, **2002**, 1385-1397.

P–16

Microstructure and oxidation behavior of Si- and Ti-enriched MoSiBTiC alloys

Tomotaka Hatakeyama[1], Kyosuke Yoshimi[2]

[1]Department of Materials Science, Tohoku University, Japan, tomotaka@dc.tohoku.ac.jp

[2]Department of Materials Science, Tohoku University, Japan, yoshimi@material.tohoku.ac.jp

Introduction

Recently, TiC added Mo-Si-B alloys so-called 1st generation MoSiBTiC alloy has been developed as a novel ultra-high temperature mateiral. TiC addition to Mo-Si-B ternary alloys improves their fracture toughness as well as high temperature strength [1, 2]. 1st generation MoSiBTiC alloy mainly consists of Mo_{ss}, Mo_5SiB_2 (T_2) and TiC phases and their excellent mechanical properties are considered to result from the synergy effect of the constituent phases. On the other hand, the oxidation resistance of the alloy is poor at elevated temperature due to the small amount of Si content (about 5 at.%), and thus it needs to be improved for ultra-high temperature applications.

To improve the oxidation resistance of the alloy, Si concentration need to be increased. According to the reported isothermal phase diagram of the Mo-Si-B system [3], Mo_{ss}-Mo_3Si-T_2 three phase region may be preferred because Mo_{ss} phase is necessary for fracture toughness of the alloy. However, since Mo_3Si phase doesn't have oxidation resistance by itself [4], further improvement in alloy design should be required. Substitution of Ti for Mo in the MoSiBTiC alloy is expected to improve oxidation resistance since it destabilizes Mo_3Si and stabilizes Ti_5Si_3 which has a higher Si content than the former [5, 6].

In this study, Si- and Ti-riched MoSiBTiC alloys are designed with the concept as described above. The microstructure and high temperature oxidation behavior is investigated as a possible candidate for next generation MoSiBTiC alloys in this study.

Materials and Methods

Sample compositions employed in this study were Mo-14Si-6B-xTi-6C (x=6, 19, 24 and 28 at. %). These alloys were prepared by conventional arc-melting. Homogenization heat treatment was carried out at 1800°C for 24 hours in Ar atmosphere. Microstructure analysis and phase identification were conducted by SEM, SEM-EDX and XRD. Density were determined by the Archimedes method. Oxidation tests were performed using 4 x 3 x 0.5 mm^3 specimen at 800°C by TGA in a 40 ml/min Ar plus 10 ml/min O_2 flow atmosphere.

Results and Discussion

The density of 6Ti, 19Ti, 24Ti and 28Ti alloys are 8.8, 8.0, 7.7 and 7.4 g/cm^3, respectively. The 15% weight saving was successful by the Ti substitution for Mo in 28Ti alloy compared with 6TiC alloy or 1st generation MoSiBTiC alloy.

Heat-treated 6Ti, 19Ti and 24Ti alloys were composed of continuous Mo_3Si with Mo_{ss}, Mo_5SiB_2(T_2) and TiC phase, while in 28Ti alloy, as shown in Fig.1, Mo_3Si phase were totally replaced by Ti_5Si_3 phase with an increased volume fraction of Mo_{ss}, which would increase the fracture toughness of the alloy. In each phase, there had little change in Si concentration with Ti substitution, while the balance between Mo and Ti concentrations changed to Ti-rich as the amount of Ti substitution increased. It indicates that Ti behaves as a substitutional element in Mo, leading to solid solution hardning.

As shown in Fig.2, Mo_3Si-containing alloys showed catastrophic oxidation behavior at 800°C. Linear and steep mass loss due to the sublimation of MoO_3 was observed. The sublimation rate of MoO_3 is so fast that all molybdenum in the specimens had thoroughly sublimated as MoO_3 just within a first few hours and whole specimens became oxide. Moreover, mass loss rate didn't change with Ti substitution in the Mo-Mo_3Si-T_2-TiC system. On the other hand, Ti_5Si_3-containing

alloy showed moderate oxidation resistance at the same temperature. It suggests that the oxidation resistance of the alloy system can be improved by introduced Ti_5Si_3 phase.
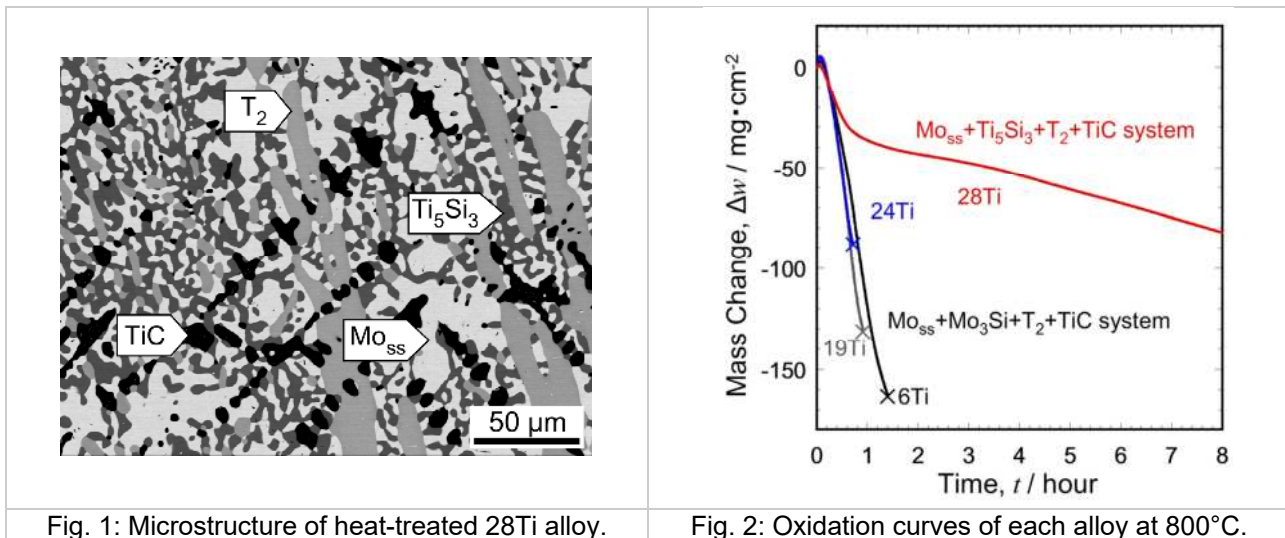

Fig. 1: Microstructure of heat-treated 28Ti alloy.	Fig. 2: Oxidation curves of each alloy at 800°C.

References

[1] S. Miyamoto, K. Yoshimi, S. H. Ha, T. Kaneko, J. Nakamura, T. Sato, K. Maruyama, R. Tu and T. Goto, Metall. Mater. Trans. A, **2014**. 45. 1112-1123.

[2] T. Moriyama, K. Yoshimi, M. Zhao, T. Masnou, T. Yokoyama, K. Maruyama, H. Katsui and T. Goto, Intermetallics, **2017**. 84. 92-102.

[3] S. H. Ha, K. Yoshimi, K. Maruyama, R. Tu, and T. Goto, Mater. Sci. Eng. A, **2012**. 552. 179-188.

[4] F. A. Rioult, S. D. Imhoff, R. Sakidja and J. H. Perpezko, Acta Mater., **2009**. 57. 4600-4613.

[5] Y. Yang, Y. A. Chang, L. Tan and Y. Du, Mater. Sci. Eng. A, **2003**. 362. 281-293.

[6] R. Sakidja, J. H. Perpezko, S. Kim and N. Sekido, Acta. Mater., **2008**. 56. 5223-5244.

P–17

Tensile creep resistance of 65Mo-5Si-10B-10TiC (at. %) alloy in the range of 1400−1700 °C

Shiho Kamata[1], Tetsuya Saito[2], Kouichi Maruyama[3] and Kyosuke Yoshimi[4]

[1] Department of Materials Science, Graduate School of Engineering, Tohoku University, 6-6-02 Aramaki Aza Aoba, Aobaku, Sendai, Miyagi 980-8579, Japan, shiho.yamamoto.p8@dc.tohoku.ac.jp

[2] Department of Materials Science, Graduate School of Engineering, Tohoku University, 6-6-02 Aramaki Aza Aoba, Aobaku, Sendai, Miyagi 980-8579, Japan, teysuya.saitou.p8@dc.tohoku.ac.jp

[3] Department of Materials Science, Graduate School of Engineering, Tohoku University, 6-6-02 Aramaki, Aza Aoba, Aobaku, Sendai, Miyagi 980-8579, Japan, maruyama@material.tohoku.ac.jp

[4] Department of Materials Science, Graduate School of Engineering, Tohoku University, 6-6-02 Aramaki Aza Aoba, Aobaku, Sendai, Miyagi 980-8579, Japan, yoshimi@material.tohoku.ac.jp

Introduction

Mo-Si-B based alloys are one of promising candidates as ultrahigh-temperature materials (UHTMs) beyond nickel-based superalloys. However, their wide applications have been restricted by several drawbacks such as relatively high density and poor room-temperature fracture toughness [1, 2]. To solve these problems, the alloying effects of 4th and 5th element on the overall performance of Mo-Si-B based alloys have been extensively investigated. Recently, TiC added Mo-Si-B alloys, named as 1st generation MoSiBTiC alloy, has been developed by conventional casting techniques, which exhibited outstanding mechanical properties. The 1st generation MoSiBTiC alloy generally possess fine microstructure consisting of three- and four-component eutectic phases, lower density comparable to that of nickel-based superalloys (≤ 9.0 g/cm^3), excellent high-temperature compressive strength as well as good fracture toughness at room-temperature [3–6]. As a potential alloy system applied in extremely high temperature environment like gas turbines and jet engines, the systematic evaluation of its tensile creep properties is essentially critical [7]. The purpose of the work here is to investigate the tensile creep strength of the 1st generation MoSiBTiC alloy in the temperature range of 1400−1700 °C and to elucidate its estimated life time.

Experimental Procedure

Button ingots with nominal composition of 65Mo-5Si-10B-10TiC (at. %) were prepared by conventional arc-melting in Ar atmosphere. Each ingot was melt and flipped over five times to ensure homogeneity. Annealing treatment was performed on the as-cast alloy at 1800 °C for 24 h in Ar atmosphere. Tensile creep tests were carried out on the annealed sample using Instron8862 machine under the applied stress of 50–300 MPa at 1400 °C, 1500 °C, 1600 °C, and 1700 °C respectively.

Results and Discussion

The annealed 65Mo-5Si-10B-10TiC alloy is composed of Mo solid solution (Mo_{ss}), Mo_5SiB_2 (T_2), (Ti, Mo)C and a small amount of (Mo, Ti)$_2$C while the primary phase is (Ti, Mo)C with dendrite morphology, in consistence with our previous study [3]. Fig. 1 illustrates the creep strain (ε) vs time (t) curves of annealed 65Mo-5Si-10B-10TiC (at. %) alloy under constant stess of 137 MPa at 1400 °C, 1500 °C and 1600 °C, respectively. The creep strain, ε, was calculated according to the equation $\varepsilon = \ln(1 + e)$, where e is the nominal strain. As shown in Fig.1, all the tensile creep curves exhibit primary and prolonged tertiary regions. Moreover, the investigated alloy shows excellent tensile creep resistance. In specific, its rupture time is 400 h with a minimum creep rate $\dot{\varepsilon}_{min}$ of 3.27×10^{-7} s^{-1} at 1400 °C, 44 h/3.08×10^{-6} s^{-1} at 1500 °C and 5 h/2.33×10^{-5} s^{-1} at 1600 °C. The stress exponent, n, in stress range of 50–300 MPa was calculated to be ~3, suggesting that the creep deformation of 65Mo-5Si-10B-10TiC alloy is dominated by dislocation creep in Mo_{ss}.
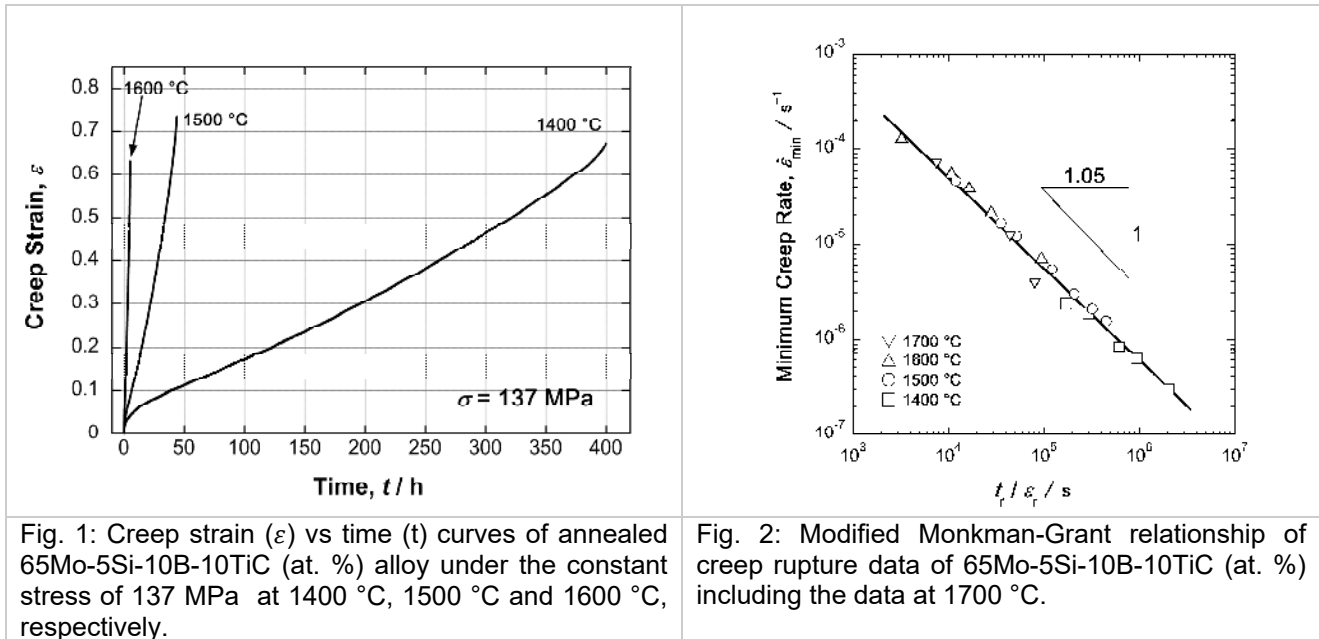
Fig. 1: Creep strain (ε) vs time (t) curves of annealed 65Mo-5Si-10B-10TiC (at. %) alloy under the constant stress of 137 MPa at 1400 °C, 1500 °C and 1600 °C, respectively.

Fig. 2: Modified Monkman-Grant relationship of creep rupture data of 65Mo-5Si-10B-10TiC (at. %) including the data at 1700 °C.

With the optimized Larson-Miller constant (C) of this alloy (~14.9), its durability temperature was estimated around 1362 °C, which is 260 °C higher than that of TMS-162 alloy [8].

The relation between creep life (t_r) and $\dot{\varepsilon}_{min}$ is expresses by an equation, $\dot{\varepsilon}_{min}^{m\prime} \cdot \left(\frac{t_r}{\varepsilon_r}\right) = C_{MMG}$, where $m\prime$ and C_{MMG} are constants independent of stress and temperature. As shown in Fig. 2, creep data obtained by this research including the creep data at 1700 °C are well fitted in the modified Monkman-Grant relationship, when $m\prime$=1.05 and C_{MMG}=0.33 respectively. The modified Monkman-grant relationships would be useful for creep prediction of the 1st generation MoSiBTiC alloy.

References

[1] M. Helmaier, M. Krüger, H. Saage, J. Rösler, D. Mukherji, U. Glatzel, R. Völkl, R. Hüttner, G. Eggeler, Ch. Somsen, T. Depka, H.-J. Christ, B. Gorr and S. Burk, JOM. **2009** 61 61–67.

[2] R. Mitra, International Materials Reviews. **2006,** 51, 13–64.

[3] S. Miyamoto, K. Yoshimi, S.-H. Ha, T. Kaneko, J. Nakamura, T. Sato, K. Maruyama, R. Tu and T. Goto, Metallurgical and Materials Transactions A. **2014**, 45,1112–1123.

[4] K. Yoshimi, J. Nakamura, D. Kanekon, S. Yamamoto, K. Maruyama, H. Katsui and T. Goto, JOM. **2014**, 66, 1930–1938.

[5] S. Yamamoto, K. Yoshimi, J.-W. Kim and K. Yokoyama, Japan Institute Metals, **2016**, 80, 51–59.

[6] T. Moriyama, K. Yoshimi, Mi Zhao, T. Masnou, T. Yokoyama, J. Nakamura, H. Katsui and T. Goto, Intermetallics. **2017**, 84, 92–102.

[7] K. Yoshimi, D. Kanekon, S. Yamamoto, J.-W. Kim, J. Nakamura and K. Maruyama, JSPS Report of the 123rd Committee on Heat Resisting Materials and Alloys. **2015**, 350–353.

[8] H. Harada and T. Yokokawa, Materia Japan. **2003**, 42, 621–625.

P–18

Development of high temperature Mo-Si-B based alloy through laser additive manufacturing

S. K. Makineni, D. Raabe and B. Gault

Department of Microstructure Physics and Alloy Design,
Max-Planck-Institut für Eisenforschung GmbH, 40237 Düsseldorf, Germany

Introduction

Mo-Si-B alloys are ultrahigh temperature materials that have potential to replace existing Ni-based superalloys [1]. This would enable gas-turbine engines to run at higher temperatures and thus allowing for significant improvements in fuel efficiency. Mo-Si-B-alloys sustain environment above 1300°C and are protected against high temperature oxidation thanks to the formation of borosilicate layer on the surface. In this system, the two main phase regimes have been explored that are α-Mo + Mo_3Si + Mo_5SiB_2 (T2 phase) and Mo_3Si + Mo_5Si_3 (T1 phase) + Mo_5SiB_2 (T2 phase) with the former composition showing more promise [2]. It exhibits relatively more ductility and damage tolerance due to the presence of α-Mo solid solution compared to the intermetallic phases, which are brittle [3]. These alloys possess low fracture toughness values at ambient temperatures (~ 5 MPa√m) and doping with rare earth oxides (such as La_2O_3) was shown to improve the fracture toughness up to 12.5 MPa√m [4]. However, due to the high melting point of the constituents, the fabrication of Mo-Si-B based alloys involves complex and energy expensive metallurgical process such as high-temperature furnaces and sintering methods. Additionally, dispersing rare earth oxide particles in these alloys will be difficult without these methods.

Here, we have prepared Mo-Si-B based alloys and demonstrated the feasibility of dispersing rare earth oxide particles through laser additive manufacturing. An alloy with composition Mo-4.2Si-1.1B with 1wt% La_2O_3 was successfully synthesized having the microstructural phases α-Mo, Mo_3Si and Mo_3SiB_2 (T1 phase) with uniform dispersion of oxide particles.
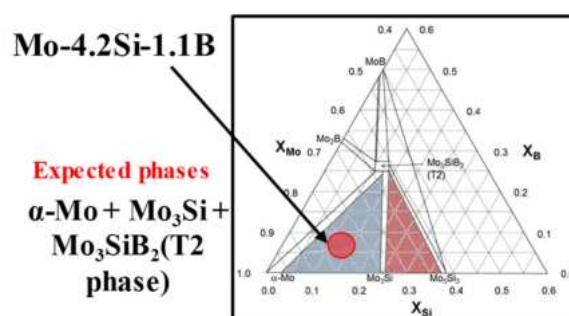
Fig 1: Mo rich Mo-Si-B ternary phase diagram

Materials and Methods

Alloy Synthesis

Pure elemental powders of Molybdenum, Silicon and Boron were homogenously mixed with and without 1wt.% La_2O_3 particles in a conventional ball mill (Fritsch make). A thin layer of powder bed was placed manually on a steel substrate and subsequently exposed to conventional welding laser available at MPIE. The process was repeated until a sample of thickness of 5 mm is reached. The cross section samples were cut using diamond cutter and were polished for microstructural analysis.

Microstructural analysis and Mechanical properties

Detailed microstructural characterization were carried out using electron microscopy (both SEM and TEM), phase identification through X-ray diffraction technique (XRD) and Atom Probe Tomography (APT). Mechanical properties measured using micro-indentation and micro-mechanical tests were evaluated.

Results and Discussion

Figure 2a and b shows comparison of laser melted microstructure for Mo-Si-B and Mo-Si-B-La_2O_3. Both cases show formation of a typical metallic alloy solidified dendritic microstructure exhibiting different phase contrast. Additionally, the alloy containing La_2O_3 possess relatively finer microstructure. Figure 1c shows magnified image taken in back scattered mode with clear three phase contrast and presence of dark round particles embedded mostly in inter dendritic regions. These particles have an average diameter of 154 ± 74 nm.

From X-ray diffraction patterns (figure 3a) for ball milled homogenized alloy and laser melted alloy, it can be deduced that only after laser melting, diffraction peaks corresponding to three different phases evolves. These peaks were indexed as α-Mo, Mo_3Si and Mo_3SiB_2(T2 phase) that were expected from the ternary phase diagram. Figure 3b shows an APT reconstruction tip having all the three phases. The measured compositions were exactly matches with the same three stochiometric phases.

Additional detailed results on TEM analysis and mechanical properties will be discussed during the conference session.

Figures
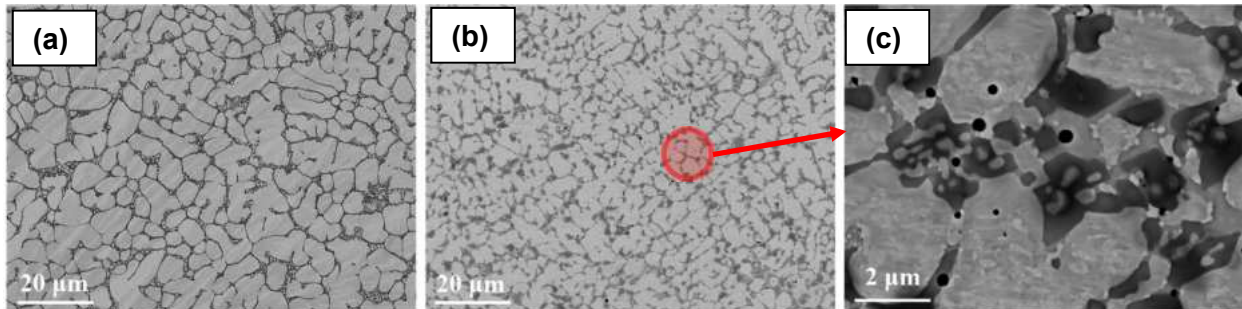
Fig. 2: SEM backscattered micrographs for laser melted (a) Mo-4.2Si-1.1B (b) Mo-4.2Si-1.1B- 1wt% La_2O_3 alloys and its (c) Magnified Image
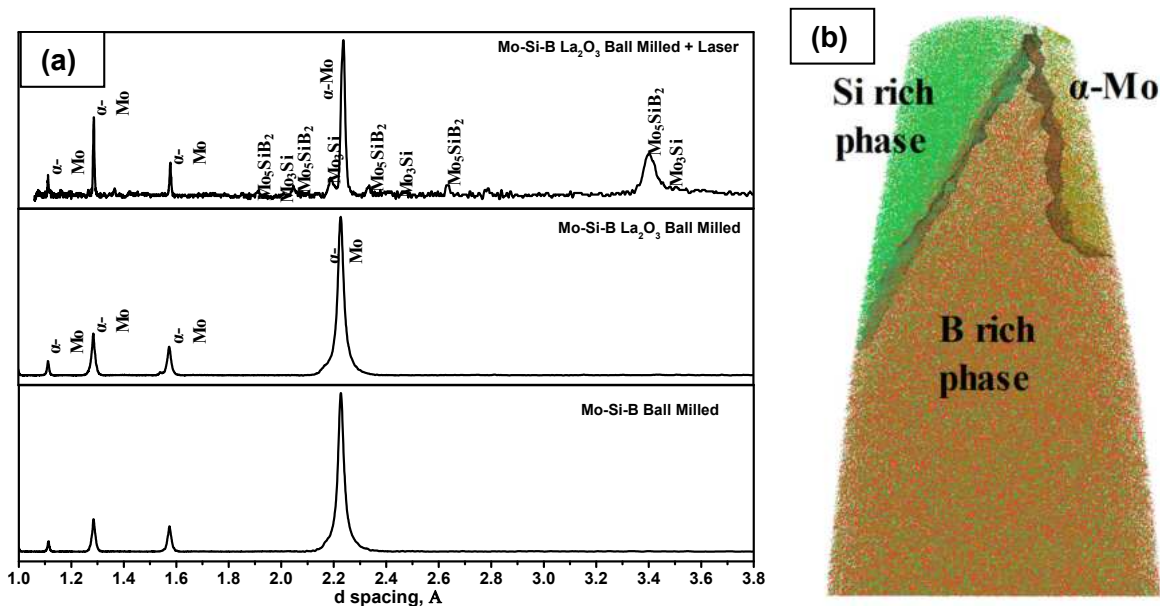
Fig. 3: (a) Comparison of XRD patterns for ball milled Mo-4.2Si-1.1B and Mo-4.2Si-1.1B- 1wt% La_2O_3 alloys with Laser melted Mo-4.2Si-1.1B- 1wt% La_2O_3 alloy (b) APT reconstructrion of a tip showing all the three phases (α-Mo + Mo_3Si + Mo_3SiB_2(T2 phase)).

References

[1] J. H. Perpezko, Science. **2009**, 326, 1068-1069.

[2] J. A. Lemberg, R. O. Ritchie, Advanced Materials, 2012, 24, 3445-3480.

[3] P. Jain, K.S. Kumar, Scripta Materialia, **2010**, 62, 1-4.

[4] W. Li, G. Zhang, S. Wang, B. Li, J. Sun, Journal of Alloys and Compounds, 2015, 642, 34-39.

P–20

Formation, structures and electronic bandstructure of Ga-rich (Mo/Ga/In, Mo/Ga/Sn and Mo/Ga/In/Sn) and Zn-rich alloys (Mo/Zn/Ga)

J. Platzek, H. Hillebrecht

Formation, structures and electronic bandstructure of Ga-rich (Mo/Ga/In, Mo/Ga/Sn and Mo/Ga/In/Sn) and Zn-rich alloys (Mo/Zn/Ga)

The structure of gallium-rich molybdenum intermetallics $(MoGa_5)_nGa$ ($n = 6,8$) and $(MoGa_5)_nX$ ($X =$ In, Sn) ($n = 4,6,8$) are structurally closely related. The common feature are $MoGa_{10}$ polyhedra ("centaur"-polyhedra) which are connected to octameric units with a cube-like arrangement. With $n = 8$ there is a rhombohedral unit cell (V_8Ga_{41} type [1]) with isolated units, with $n = 6$ there are dimers in Mo_6Ga_{31} and a monoclinic structure [2] and with $n = 4$ there is a tetragonal structure with linear chains ($Mo_4Ga_{20}S$ type [3]).

We have investigated the reactivity of Mo with Ga-rich alloys Ga/Sn, Ga/In, and Ga/Sn/In according to the following temperature program:

$$RT \xrightarrow{60°C/h} 900°C \ (24h) \xrightarrow{3°C/h} 400°C \xrightarrow{100°C/h} RT$$
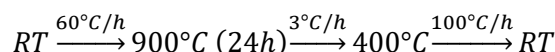
X-ray diffractic experiments show, that with the binary systems rhombohedral structures are formed. In agreement with the results of the crystal structure refinement and elemental analysis by EDX the approximate compositions are $Mo_8Ga_{40}Sn$ and $Mo_8Ga_{40}In$, respectively. With the ternary alloy Ga/Sn/In we observed the formation of the tetragonal structure with increased In/Sn content: $Mo_4Ga_{16}(In,Sn)_{~4}$. EDX measurements showed a In/Sn ratio of 2:1. At lower temperatures (500°C) tetragonal structures are formed in all cases.

The structure of the zink-rich alloys $MoZn_{6-x}Ga_x$ can be described as a defect close packed structure. The close packed layers conform to the $AuCu_3$-type, in every second layer the Mo-Atoms are missing, resulting in alternating layers with the composition $MoZn_3$ and $\square Zn_3$ ($\square$ = vacancy). Mo and Zn are coordinated by cuboctahedra/anticuboctahedra. In the Zn-Polyhedra two positions are empty. Depending on the Zn-Ga ratio we found cubic, hexagonal and rhombrohedral structures.

The compounds were synthesized following the temperature program below:

$$RT \xrightarrow{60°C/h} 850°C \ (96h) \xrightarrow{6°C/h} 500°C \ (96h) \xrightarrow{18°C/h} RT$$
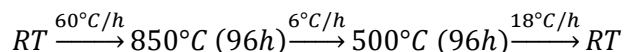
Electron bandstructure calculations were performed for Ga-rich and Zn-rich alloys using DFT (PBE-GGA (Perdew-Burke-Enzerhof 96)) and the Muffin-Tin approximation implemented in WIEN2k to investigate the DOS giving insight into the bonding situation of the particular compounds.

[1]   K. Yvon, *Acta Crystallogr*. B, **1975**, *31*, 117-120

[2]   K. Yvon, *Acta Crystallogr. B*, **1974**, *30*, 853-861.

[3]   M. Wolcyrz, R. Andruszkiewicz, K. Lukaszewicz, *Acta Crystallogr. C*, **1989**, *45*, 991-993.

[4]   R. Lux, Dissertation, Freiburg, **2004**

[5]   Peter Blaha, Karlheinz Schwarz, Georg K. H. Madsen, Dieter Kvasnicka, Joachim Luitz, WIEN2k_13.1 (Release 06/19/2013),

P–21

Concentration dependences of structural characteristics, magnetic and superconducting properties in V-Ta-Zr, V-Zr-Hf and V-Zr-Fe systems

B.N. Kodess[1,2], E.N. Nechaeva[2]

[1]VNIIMS, 46 Ozernaya, Moscow, Russian Federation, 119361, *kodess@mail.ru*,

[2]ICS&E, 20725 E. Bellewood Pl. Aurora, CO, 80015, USA, *kodess@mail.ru*

The results of the investigation of intermetallics of structural type C15 (Laves phase) with very high critical fields in binary and quasibinary systems are compared with the same data of the features of the electronic structure and lattice dynamics of the initial elements from which these intermetallic compounds are prepared. A multifactors concept (description) of the phase space of condensed matter is also used. This allows us to establish the relationship between structural, magnetic and superconducting phase transitions and also to estimate the effect of deformation on the characteristics (control parameters) of these transitions.

For this investigation the samples of intermetallics were prepared from high-purity components (iodide zirconium and hafnium, vanadium and tantalum after zonal purification, and isotope of Iron[57]) by crucibleless levitation techniques. The remelting of the charge materials was carried out in a high-frequency field at an inert gas pressure of one atmosphere, which ensured the constancy of the specified charge composition after melting (the metal loss was no more than 0.05 wt.%).

The annealing was carried out at temperature of 1150 °C in sealed quartz ampoules filled with an inert gas-argon, while the annealing at a temperature of 1300 °C was carried out in a special chamber on a tantalum substrate. The diffraction patterns were obtained using the radiation from Cu-anode (diffractometer DRON-4). The analysis of the profiles of the diffraction pattern was carried out using the CSD software. The lattice parameters were calculated using the Nelson-Riley extrapolation function. The Mössbauer spectra were measured on an installation with constant acceleration at temperatures of 150 and 300 K [1]. Both measurement methods – the induction method for the temperatures of transition from normal to superconducting state, Tc, and the method of paramagnetic susceptibility values – are described in [2,3].

Results and Discussion

In the measured dependences of Tc on the composition in V-Zr binary system and V2Zr-V2Hf quasibinary system the position of the maximum Tc is consistent with the data found in the published papers. The Tc maximum for the composition V2(Zr0.5Hf0.5) corresponds to the minimum of the temperature of the structural transition and the maximum on the temperature dependence of the paramagnetic susceptibility. In the system V2(Zr-Ta), the value of Tc also has a maximum value in the range of 4-6 at.% Ta (after annealing at 1150 °C) and at 8 at.% Ta (after annealing at 1300 °C).

It was possible to fix by fast quenching the metastable state of both the binary alloy V2Ta and solid solutions with of 1-1.5 at.% Zr. The measured value of Tc showed the increase from 2.9 K to 8-10 K. For the binary system V-Zr, V-Hf and V-Zr-Hf, the values of Tc for cast samples were also found to be higher than for samples of the same compositions after annealing. In contrast with the annealed and cast samples the deformation by grinding the samples into powders led to a decrease in the values of Tc, a monotonous increase was observed in the paramagnetic susceptibility in the total investigated temperature range of 20-300 K.

The annealing of the deformed samples at 850 °C led to the returning of the initial Tc value. The X-ray measurements of the temperature dependence of the integrated intensity showed the anomalies inherent in the pre-martensitic state, that were observed for other compounds of the structural type with high Tc, for example A 15 and B1 with [3]. In addition the effect of uniform

pressure on the same samples also resulted in a noticeable increase in Tc for V2Hf at 30 Kbar and in a slight change in Tc for the same samples of V2Zr [4]. The lines of gamma-resonance spectra are components of the double structure caused by the quadruple interaction of the nucleus with an electric field gradient and this state exist to reach concentrations of 2 at.% Fe^{57}.

The measurements results are considered as genetic memory of the features of an electronic structure and lattice dynamics of the initial elements. The description is based on the model of the phase space of the condensed matter using multifactor description of the control parameters [5]. Actually, it is known that anomalies of properties are found in vanadium with the impurities (even of hydrogen atoms) at low temperatures which are connected with structural and quite possible magnetic transitions. Also the anomalies of thermal expansion were found us for the hexagonal phase of Ti at low temperatures, that are associated with electronic topological phase transitions in the range of 30 K [6]. This transition adds more to the data about the various instabilitis of the crystal lattice of titanium, for example which occurs at high temperatures (the transition from a hexagonal to a space-centered unit cell) and in the films of titanium (the transition to a face-centered cubic unit cell) and under the pressure (the transition to another hexagonal epsilon-phase with structural type AlB2).

The arisen space-time subsystem (reflecting phase transitions and the evolution of the state of the substance) are related to another subsystems, which orthogonal in phase space. The second subsystem descibes the way of localization of structural elements in real space. Simultaneously, the results in both are related to a third orthogonal subsystem describing the energy characteristics (from interatom and electron-electron interactions to the level of stored energy in the defects and/or within boundaries of the polycrystals of the analyzed substances). The increase in the value of Tc, mentioned above, for the cast samples and the results of influence on Tc at the initial stages of high uniform pressure can be connected with a lowering of the temperature of the structural phase transition at temperature Tm, which happen due to residual stresses. To conclude, the interrelation of structural and superconducting phase transitions can be associated with the manifestation of magnetic phase transitions of electron type. The possibility of magnetic transition is indicated in the works of N. Keifer (1984), H.R. Khan and Loebich (1988), and also in the analyses of NMR spectra conducted by A.V. Skripov et al. (1981, 1991).

References

[1] B.N. Kodess, A.A. Solodov, K.P Mitrofanov, M.V. Plotnikova, Bulletin of College and Universities. **1978**, No 10, pp.128-130.

[2] B.N. Kodess, Sov. Phys. Solid State, **1973**, v.15, N4, p.844-846; B.N. Kodess, I. Korkin, S.V. Stolbov, Yu.Ya. Nikiforov, **1982**, Zhurnal Eksperimental'noj i Teoreticheskoj Fiziki, (JETP)., 82, 1924-1935.

[3] B.N. Kodess Sov. Phys. Solid State, 1973, v.15, N4, p.844-846; B.N. Kodess, Solid State Communications. **1973**, *13*(5), 527-530.

[4] I.V. Berman, N. B. Brandt,, B.N. Kodess, I. E. Kostyleva, V.I & Sidorov, **1984**, Sov. Phys. Solid State; 26(6), pp. 1095-1098; Berman, I. V., Kostyleva, I. E., Kodess, B. N., & Sidorov, V. I. **1987**, Sov. Phys. Solid State, 29 (7), 1119-1121.

[5] B.N. Kodess. E.N. Nechaeva, **2016**, The model of evolution of the crystalline substance. Proc. of Crystallographic Congress, Moscow 21-26 November 2016, p. 300.

[6] B. N. Kodess, H. Hope, Acta Crystallographica. **2015**, v.A71S, Part 3, s. 316.

P–22

Casting of Cr,Ti-containing iron aluminides

Bruna Niccoli Ramirez[1], Carlos Alberto Marchioli[2], Igor Colado Porto Martins[3], Cláudio Geraldo Schön[1]

[1]Escola Politécnica da Universidade de São Paulo- Av. Professor Mello Moraes, 2463 - Butantã, São Paulo, Brasil - SP, 05508-030

[2]Serviço Nacional de Aprendizagem Industrial - Rua Ari Barroso, 305 -Presidente Altino, Osasco, Brasil – SP, 06216-240

[3]Instituto de Pesquisas Energéticas e Nucleares – Av. Lineu Prestes, 2242 – Cidade Universitária, São Paulo, Brasil – SP, 05508-000

Introduction

Iron aluminides form an interesting class of materials which combine excellent corrosion and oxidation resistance with good mechanical properties at moderate to high temperatures (up to 500°C). These materials, however, suffer from a low room temperature ductility (under 5% elongation in tension), which is mostly due to environmental effects. Casting is a processing route which is traditionally applied to brittle alloys (e.g. gray cast irons), but in order to cast a part without defects, several thermochemical properties are needed, as well as information on the tendency the alloy present to form foundry defects (e.g. shrinkage voids, pores). The present work aims at providing this information in parts produced in laboratory scale. In particular, the solidification contraction and the efficiency of TiB_2 as inoculant, for grain size control in the "as cast" part, are investigated.

Materials and Methods

Three alloys with nominal compositions (in at.%) Fe28Al, Fe28Al6Cr and Fe28Al6Cr1Ti have been molten in an Argon flux protected induction furnace (about 1.5 kg for each melt) using conventional raw materials (carbon steel, commercial aluminum, metallic chromium and commercial ferrotitanium). The produced melts were treated by adding Al – TiB_2 alloy used in the aluminum industry and poured into "staircase" molds, designed to investigate feeding distance effects in complex parts. The produced parts were investigated by X ray tomography, to characterize the internal shrinkage voids and pores, and by Scanning Electron Microscopy and Optical microscopy to investigate the produced "as cast" microstructures. Following the preliminary results, large scale casting were carried out in order to investigate the industrial use of the alloys. We also investigated the influence of the inoculant content on the alloy with a better control to reduce fade effects. Test specimens were prepared for mechanical tensile tests, in addition to the microstructural characterization of the alloy.

Results and Discussion

The choice of TiB_2 as an inoculant is due to the classical heterogenous nucleation theory, in which a comparison is made between the lattice parameters of substrate and nucleus. According to classic heterogeneous nucleation theory, inoculation effectiveness depends only on the disregistry, which is typically limited by a maximum value of 15% [1]. Iron aluminides at the solidification temperature, are expected to be found either in the B2 or in the A2 structures, typical lattice parameters range from 0.283 to 0.303 nm (the lowest value refers to room temperature) [2, 3], while TiB_2 present lattice reported parameters between 0.306 and 0.327 nm [4], disregistry between TiB_2 and iron aluminides, therefore is expected to be in the range $1 < \delta < 15.5\%$. Some authors report a strong inoculation effect when $\delta < 15\%$ or even $\delta < 20\%$ (in these cases a simple dislocation model can compensate lattice mismatch [1, 5]), therefore TiB_2 is expected to be effective.

Figure 1 shows the microstructure of the transverse section of the ingots of Fe28Al melts without and with the addition of inoculant, where it is possible to verify the formation of equiaxed grains in the alloy without inoculant and columnar in the other. However, the effect expected from the addition of inoculant tends to be more intense [6, 7], in order to consider that TiB_2 as inoculant is not efficient in the present case, possible due to fade effects.
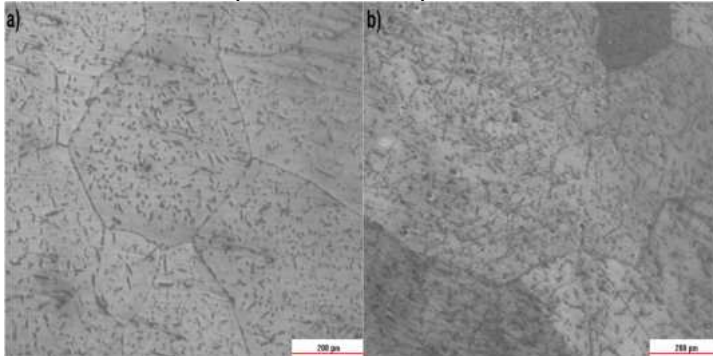

Figure 1 - Alloy Fe28Al, optical micrograph of the center of the rectangular ingot obtained without (a) and with the addition of TiB_2

The three alloys obtained have chemical composition Fe28Al, Fe28Al6Cr and Fe28Al6Cr1Ti. Figure 2-a and figure 2-b shows the microstructures observed in the longitudinal section of the Fe28Al6Cr and Fe28Al6Cr1Ti, respectively, in the same value of cooling rate during solidification. In the case of this image from we observe large (about 100 µm long) acicular precipitates. EDS analysis suggests that these are κ carbide precipitates. There is also a significant number of micropores in this microstructure. Hardness of this alloy is 302 ± 6 HV_{3N}. Similar results were found for the other alloys. The addition of Cr and Ti in the alloy promoted a considerable reduction of grain size, as can be seen in figure 2.
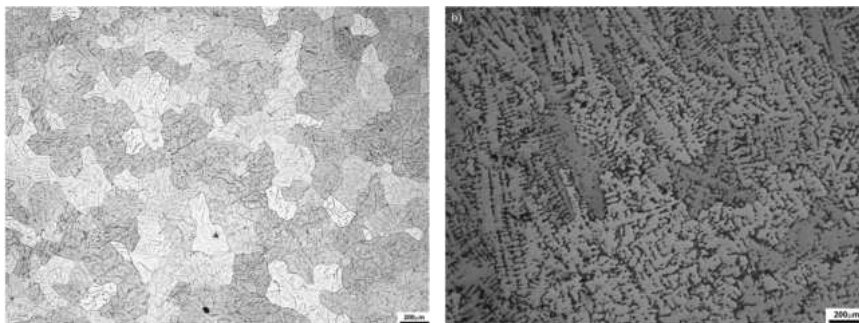
Figure 2: a (to the left) Alloy Fe28Al6Cr, "staircase" part. Optical micrograph; b (to the right) Alloy Fe28Al6Cr1Ti.

References

[1] B. L. Bramfitt, "The effect of carbide and nitride additions on the heterogeneous nucleation behavior of liquid iron" Metal. Trans. 1 (1970) 1987 – 1995.

[2] C. L. Fu, M. H. Yoo, "Deformation behavior of B2 type aluminides: FeAl and NiAl" Acta Metal. Mater. 40 (1992) 703 – 711

[3] M. Friák, J. Neugebauer, "Ab initio study of the anomalous volume-composition dependence in Fe – Al alloys" Intermetallics 18 (2010) 1316 – 1321.

[4] R. G. Munro, "Material properties of titanium diboride" J. Res. NIST 105 (2000) 709 – 720.

[5] G. J. Davies, Solidification and casting. New York: Willey, 1973, 93 – 115.

[6] L. Elmquist, P A. Sonawane, "On the relation between primary and eutectic solidification structures in gray iron" IOP Conf. Ser.: Mater. Sci. Eng. 27 (2011) 012060.

[7] Z. Chen, T. Wang, L. Gao, H. Fu, T. Li, "Grain refinement and tensile properties improvement of Al foundry alloys by inoculation with Al – B master alloy" Mater. Sci. Eng. A 553 (2012) 32 – 36.

P–23

Hydrogen embrittlement in FeAl revealed via in-situ microcantilever tests

Yun Deng[1], Afrooz Barnoush[1]

[1]Department of Mechanical and Industrial Engineering, NTNU, Trondheim, Norway,
yun.deng@ntnu.no; afrooz.barnoush@ntnu.no

Introduction

FeAl (B2) phase is of particular research interest for its promising properties including good corrosion resistance, low material cost, conservation of strategic elements, and relatively low density when compared with stainless steels [1]. The FeAl intermetallic alloys are considered for many potential applications, for example, as structural materials to serve in high temperature and/or hostile environments [2]. However, limited ductility at ambient temperatures has largely retarded those applications. Studies have shown that the ductility decrease in many intermetallic alloy systems that contain a large amount of reactive elements, such as Al, Si and Ti, was due to their chemical reaction with water molecules:

$$2Al + 3H_2O = Al_2O_3 + 6H^+ + 6e^-$$

The produced chemisorbed H diffuses to the crack tip and results in the so-called hydrogen embrittlement (HE).

Several hypothesis has been proposed to reason the phenomena while without reaching common agreement. One of the major reasons for the endless arguments of HE mechanisms is the lack of a proper experimental design. The previous experimental methods are either macroscopic tests overlooking the active length scale of H with crystal defects, or nano-scale tests inside ETEM with tiny sample size that cannot ensure a certain constant strain/stress states and cannot avoid the proximity effect from the sample surface. The recently works [3, 4] of micro-cantilever bending tests with in-situ hydrogen charging provide a good compromise by using the micro-sized sample that meet both the small scale required to capture the H effect and the enough bulk size to avoid the shortages from ETEM.

Materials and Methods

The single crystalline FeAl alloy received from the Max-Planck-Institut Für Eisenforschung GmbH (MPIE) was grown by a modified Bridgman technique in BN-crucibles under argon atmosphere. From this specimen, cantilevers were cut by a focused ion beam (Helios Nanolab Dual Beam FIB, FEI Inc., USA) to ~3X3X12 µm. The pre-notch was aligned to analyse the (001) <100> crack system, and the depth of the pre-notch were measured around 300 nm prior to fracture from the side view.
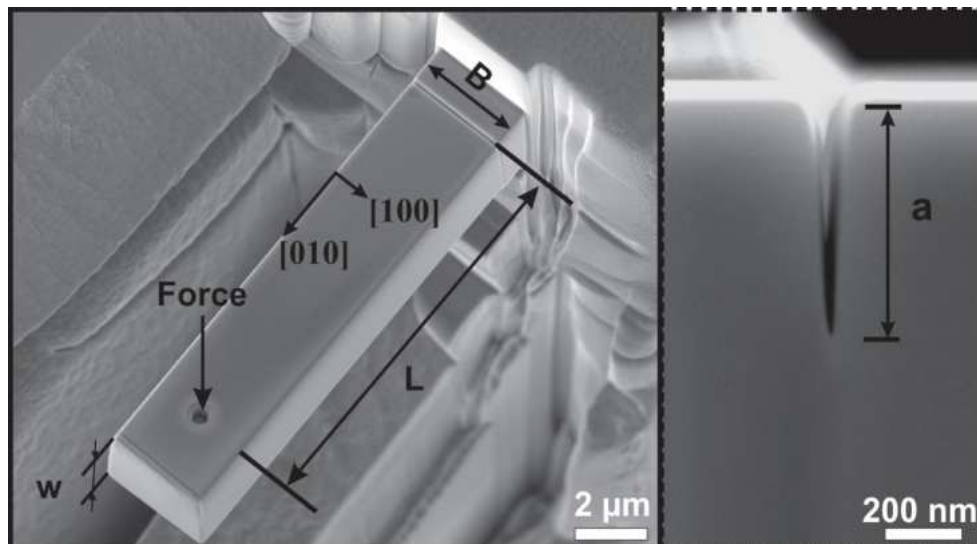
Fig. 1 Secondary electron image of a FeAl cantilever with characteristic dimensions

The beams were loaded in-situ using the PI-85 Pico-indent system (Hysitron Inc., USA) inside the ESEM (Quanta FEG 650 ESEM, FEI Inc., USA) with a 1 nm/s loading rate in displacement-controlled mode. Bending tests were performed in vacuum (~5X10^{-4} Pa) and water vapor (450 Pa, 900 Pa) conditions. The microstructure after bending was characterized using EBSD as well as TEM (JEM-2100, Jeol Inc., Japan).

Results and Discussion

The primary mechanical results show a reduction of fracture toughness together with an enhanced crack initiation and propagation for beams under H exposure. The further postmortem microstructure analysis suggests the H enhanced dislocation nucleation and H pinning dislocation at the crack tip are responsible for the embrittlement in FeAl.
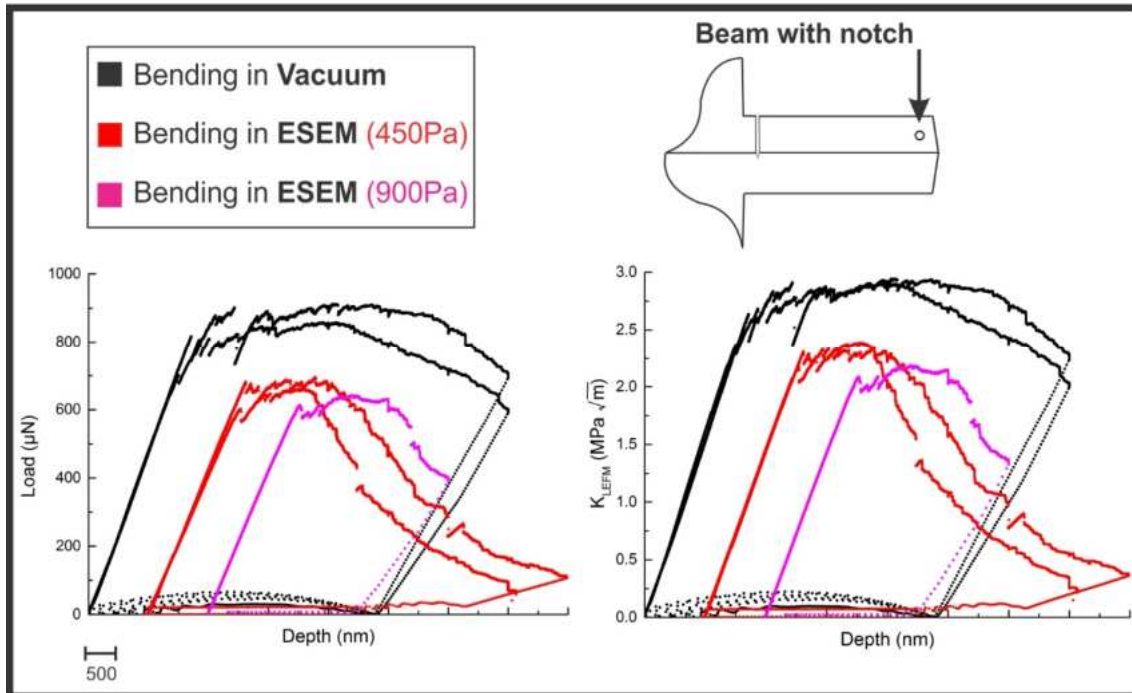
Fig. 2 The experimental Load-Displacement curves for beams bent in vacuum and ESEM (450Pa, 900Pa) respectively a), the converted fracture toughness based on linear elastic fracture mechanics with respect to displacement b).

References

[1] N. Ziegler, Trans. Am. Inst. Min. Met. Eng, 100 (1932) 267-271.

[2] N.S. Stoloff, R.G. Davies, Acta Metallurgica, 12 (1964) 473-485.

[3] Y. Deng, T. Hajilou, D. Wan, N. Kheradmand, A. Barnoush, Scripta Materialia, 127 (2017) 19-23.

[4] T. Hajilou, Y. Deng, B.R. Rogne, N. Kheradmand, A. Barnoush, Scripta Materialia, 132 (2017) 17-21.

P–24

Creep properties of Co-based superalloys with improved oxidation resistance

Zhenghao M.T. Chen[1], Norihiko L. Okamoto[2] and Haruyuki Inui[3]

[1]Department of materials science and engineering, Kyoto University, Kyoto, Japan
chen.zhenghao.45e@st.kyoto-u.ac.jp

[2] Department of materials science and engineering, Kyoto University, Kyoto, Japan
okamoto.norihiko.7z@kyoto-u.ac.jp

[3] Department of materials science and engineering, Kyoto University, Kyoto, Japan
haruyuki.ihui.3z@kyoto-u.ac.jp

Introduction

Recently, a new ternary L1$_2$ (γ′) phase Co$_3$(Al,W), which can coexist with a fcc solid-solution phase (γ) based on Co, has been discovered. With precipitation strengthening by the γ′ phase, Co-base alloys have demonstrated increased high-temperature strength compared with that of conventional Co-base alloy. However, the ternary alloy does not exhibit excellent creep properties due to the low high-temperature strength of the γ′ strengthening phase and the lack of the volume fraction of γ′. The oxidation resistance of the ternary alloy is also insufficient. In previous studies, the effect of alloying elements on Co-base superalloys has been investigated. Ni and Ta are effective in improvement of γ′ high-temperature strength by widening the temperature region of Yield Stress Anomaly. Ni, Ta and Ti increase the γ′ volume fraction by increasing γ′ solvus temperature [1]. Cr and Si are benefit to the oxidation resistance but decrease the γ′ solvus temperature [2]. However, the interaction of co-addition of the alloying elements mentioned above is still unclear. In the present study, we investigated the effect of co-addition of alloying elements Ni, Ta, Ti, Cr, Si on Co-base superalloys in order to find out a composition exhibiting excellent creep property and sufficient oxidation resistance, simultaneously.

Materials and Methods

Ingots of (Co$_{0.8}$, Ni$_{0.2}$)-aAl-bW-xTa-yTi-8Cr-Si (at.%; a, b, x, y≥0) were prepared by arc melting. These ingots were homogenized at 1200 ℃ for 24 h in vacuum, followed by heat treatment at a sub-solvus temperature for 96 h. The γ′ solvus temperatures were determined by differential scanning calorimetry (DSC), and the microstructures were examined by scanning electron microscope (SEM). Single crystals with selected compositions exhibiting exclusive γ/γ′ two-phase cuboidal structure and reasonable γ′ solvus temperature were prepared by modified Bridgman technique, followed by heat treatment at 900 ℃ for 96 h. Creep tests were performed in tension under a constant stress of 137 MPa at 1000 ℃ and 428 MPa at 900 ℃, respectively. Oxidation resistance behavior at 900 ℃ were investigated with cyclic oxidation test for 200 h (20 cycles).

Results and Discussion

Cr and Si alloying decrease γ′ solvus temperature drastically, the γ′ solvus temperature of (Co$_{0.8}$, Ni$_{0.2}$)-8Al-7W-8Cr-Si is no higher than 1200 ℃. However, substituting W with Ta is effective in increase of γ′ solvus temperature without precipitating any secondary phases (such as D0$_{19}$). Similarly, substituting W and Al with Ti is also an effective way to increase γ′ solvus temperature. The γ′ fraction at 1000 ℃ and γ′ solvus temperature of the selected composition compared to a Cr, Si-free composition Co-7Al-8W-Ta-4Ti [3] are plotted in Fig.1. It is demonstrated that alloying with Ta is more effective in increase of γ′ solvus temperature than that with Ti. On the other hand, the γ′ fraction at 1000 ℃ for Ti-addition is higher than that of Ta-addition, due to the higher solubility limit (8 at.% for Ti and 4 at.% for Ta. respectively) and the better γ′ stability at high temperature [4]. Creep properties and oxidation resistance behavior of (Co$_{0.8}$, Ni$_{0.2}$)-8Al-2W-4Ta-8Cr-Si, (Co$_{0.8}$, Ni$_{0.2}$)-5Al-4W-8Ti-8Cr-Si and (Co$_{0.8}$, Ni$_{0.2}$)-6Al-2W-2Ta-6Ti-8Cr-Si alloys are investigated.

Results of cyclic oxidation test are shown in Fig. 2. It is demonstrated that the oxidation resistance behavior of Co-7Al-8W-Ta-4Ti is catastrophic, although this compound is reported to exhibit reasonable γ′ fraction and γ′ solvus temperature [3]. Compared to Co-7Al-8W-Ta-4Ti, Cr, Si-alloyed Co-base superalloys exhibit superior oxidation resistance behavior at 1000 °C, due to the continuance of oxidation film.

Rupture time of tensile creep at the condition of 900 °C /428 MPa of $(Co_{0.8}, Ni_{0.2})$-8Al-2W-4Ta-8Cr-Si is much shorter than that of Co-7Al-8W-Ta-4Ti (approximately one-thirteenth) due to the lack of γ′ volume fraction. However, the proportion is very close to that of Co-7Al-8W-Ta to Co-7Al-8W-Ta-4Ti, which is approximately one-eleventh [3], indicating that the creep property of Cr, Si-alloyed $(Co_{0.8}, Ni_{0.2})$-8Al-2W-4Ta-8Cr-Si is comparable to that of corresponding Cr, Si-free alloy Co-7Al-8W-Ta. Thus, it is feasible to coexist the creep property and the oxidation resistance behavior in Co-base superalloys, with alloying elements co-addition.

Figures (or Table)
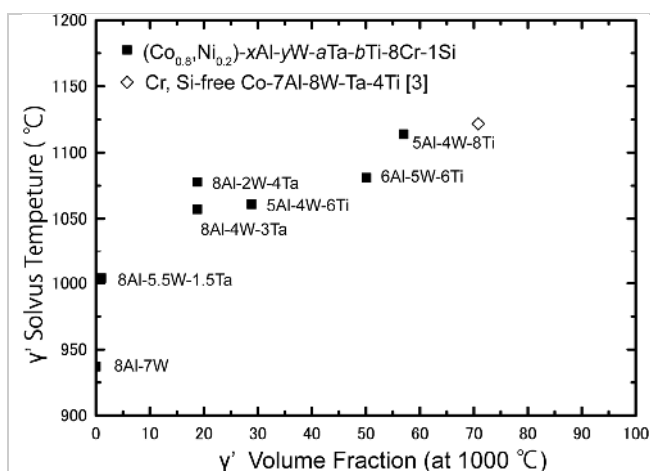
Fig. 1: γ′ solvus temperatures and γ′ fraction at 1000 °C. Black cube: selected $(Co_{0.8}, Ni_{0.2})$-aAl-bW-xTa-yTi-8Cr-Si (a, b, x, y≥0) investigated in the present study. Hollow rhomboid: Cr, Si-free Co-7Al-8W-Ta-4Ti [3].
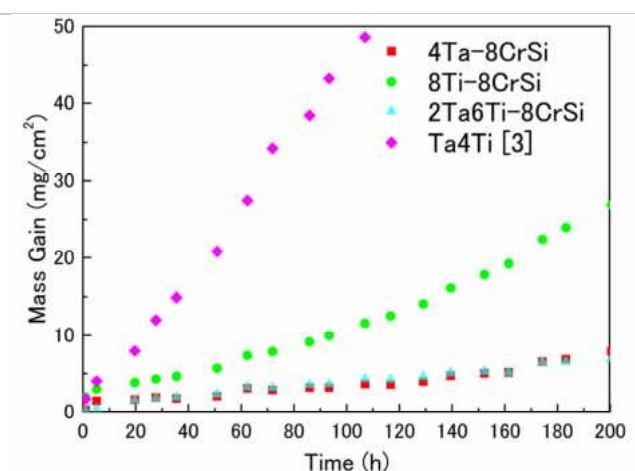
Fig. 2: Mass gain in cyclic oxidation test at 1000 °C.

References

[1] M. Ooshima, K. Tanaka, NL. Okamoto, K. Kishida, H. Inui*, Journal of Alloys and Compounds*. **2010**, *508*, 71-78.

[2] H.-Y. Yan, V.A. Vorontsov, D. Dye, Corrosion Science. **2014**, *83*, 382–495.

[3] F. Xue, H.J. Zhou, Q. Feng, JOM. **2014**, *66*, 2486-2494.

[4] S. Kobayashi, Y. Tsukamoto, T. Takasugi*, Intermetallics*. **2011**, *19*, 1908-1912.

P–25

Plastic deformation in the equiatomic CrMnFeCoNi high entropy alloy with the FCC structure

Makoto Asakura[1], Marino Kawamura[1], Norihiko L. Okamoto[1],
Haruyuki Inui[1], Takashi Fukuda[2], and Tomoyuki Kakeshita[2]

[1]Department of Materials Science & Engineering, Kyoto University, Kyoto 606-8501, Japan,
asakura.makoto.66n@st.kyoto-u.ac.jp, kawamura.marino.52c@st.kyoto-u.ac.jp,
okamoto.norihiko.7z@kyoto-u.ac.jp, inui.haruyuki.3z@kyoto-u.ac.jp

[2]Department of Materials Science & Engineering, Osaka University, Osaka 565-0871, Japan,
fukuda@mat.eng.osaka-u.ac.jp, kakeshita@mat.eng.osaka-u.ac.jp

Introduction

The high entropy alloys (HEAs) are equiatomic or nearly equiatomic solid solution alloys consisting of at least five elements [1]. These alloys may exist as a stable single-phase because the contribution of configurational entropy to the Gibbs free energy may be high enough to suppress compound formation and phase separation. HEAs are known to exhibit various interesting properties: very low diffusion coefficients [2], excellent high-temperature strength [3], and so on. Especially, the equiatomic CrMnFeCoNi HEA with the FCC structure [4] has been reported to exhibit excellent ductility [5,6] and exceptional fracture toughness at cryogenic temperatures [7]. Although the strength of HEAs will be explained in terms of solid solution strengthening, the classical theories of solid solution strengthening, such as Fleischer's and Labusch's models, is not applicable to HEAs because they were established mainly for *dilute binary* solid solution alloys [8] and also because the definition of solvent and solute atoms in HEAs is difficult. In order to evaluate how much the HEAs are strengthened by the solid solution effect, the critical resolved shear stress (CRSS) value of single crystals is necessary instead of yield stress values of polycrystals. We have recently obtained the CRSS value of the equiatomic CrMnFeCoNi HEA (38 ± 5 MPa) by compression tests of single-crystal micropillars at room temperature [9] because bulk single crystals were inaccessible. Very recently, however, we have succeeded in growing bulk single crystals of the HEA by the Bridgeman method. In the present paper, we investigate the temperature dependence of CRSS for bulk single crystals of the HEA in compression and tension to elucidate whether the HEA can be categorized into normal FCC solid solution alloys or not.

Materials and Methods

Ingots of the equiatomic CrMnFeCoNi HEA were prepared by arc melting of the constituent elements under an Ar gas flow. Single crystals were grown by the Bridgeman method (details will be described elsewhere [10]). Rectangular parallelepiped specimens with a size of $2\times2\times5$ mm^3 for compression and dog-bone-shaped specimens with a gauge size of $2\times2\times4.5$ mm^3 for tension were machined by electric discharge machining. The compression axes were [$\bar{1}23$] and [$\bar{1}26$] while the tensile axis was [$\bar{1}23$]. Compression and tensile tests were performed at 77 K and room temperature at an engineering strain rate of 1.0×10^{-4} s^{-1}. Deformed specimens were observed by scaning electron microscopy (SEM).

Results and Discussion

Fig. 1 shows representative engineering stress-strain curves at 77 K and room temperature for compression and tension. SEM observations on the deformed specimens indicate that the primary slip system (111)[$\bar{1}01$] operates for all the deformation conditions. The CRSS values for the [$\bar{1}23$] and [$\bar{1}26$] compression at room temperature calculated with the yield stress values as well as the corresponding Schmid factors are virtually identical with each other (44.3 and 44.0 MPa, respectively) and comparable to that obtained by micropillar compression. In addition, the CRSS value for the [$\bar{1}23$] tension at room temperature is 48.8 MPa, indicating no tension-compression

asymmetry of CRSS. In both compression and tension, on the other hand, the CRSS value at 77K is more than twice that at room temperature (110 and 116 MPa, respectively). This significant temperature dependence is, however, not peculiar. Basinski et al. proposed a concept called "stress equivalence", in which a proportionality is found between the strength at liquid nitrogen temperature and the differential strength between room and liquid nitrogen temperatures for many FCC solid solution alloys [11] as shown in Fig. 2. The equiatomic CrMnFeCoNi HEA is plotted right on the proportionality line although they are significantly larger than the Cu- and Ag-based FCC alloys. Thus, the CrMnFeCoNi HEA is categorized into normal FCC solid solution alloys in terms of the temperature dependence of CRSS.
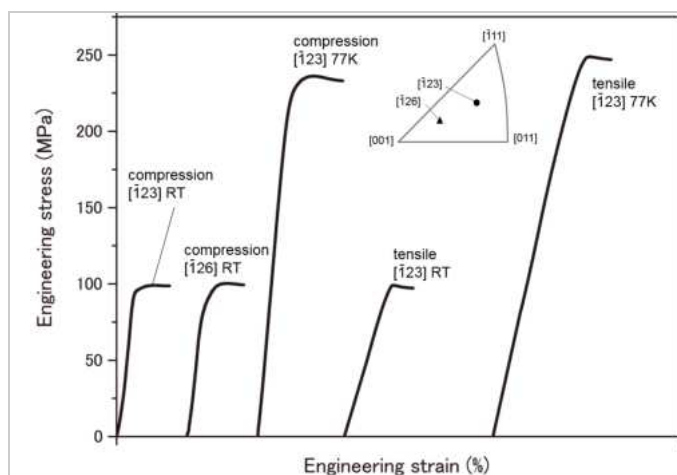
Fig. 1. Engineering stress-strain curves obtained for bulk single crystals of CrMnFeCoNi HEA in compression and tension at room temperature and 77 K.	Fig. 2. Differential CRSS values between room and liquid nitrogen temperatures plotted against the CRSS value at liquid nitrogen temperature for Cu- and Ag-based alloys as well as the equiatomic CrMnFeCoNi HEA.
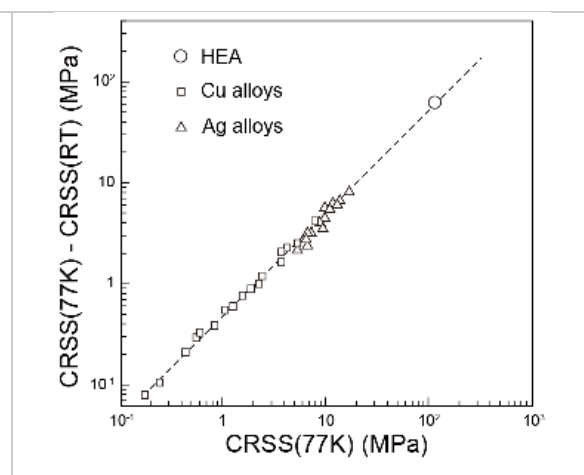
References

[1] J.-W. Yeh, S.-K. Chen, S.-J. Lin, J.-Y. Gan, T.-S. Chin, T.-T. Shun, C.-H. Tsau, S.-Y. Chang, Adv. Eng. Mater. **2004**, *6*, 299–303.

[2] K.Y. Tsai, M.H. Tsai, J.W. Yeh, Acta Mater. **2013**, *61*, 4887–4897.

[3] O.N. Senkov, G.B. Wilks, J.M. Scott, D.B. Miracle, Intermetallics. **2011**, *19*, 698-706.

[4] B. Cantor, I. T. H Chang, P. Knight & A. J. B. Vincent, Mater. Sci. Eng. **2004**, *A 375*, 213–218.

[5] F. Otto, A. Dlouhý, K.G. Pradeep, M. Kuběnová, D. Raabe, G. Eggeler, E.P. George, Acta Mater. **2013**, *61*, 5743–5755.

[6] A. Gali, E.P. George, Intermetallics. **2013**, *39*, 74-78.

[7] B. Gludovatz, A. Hohenwarter, D. Catoor, E. H. Chang, E. P. George, and R. O. Ritchie, Science. **2014**, *345*, 1153-1158.

[8] N. L. Okamoto, K. Yuge, K. Tanaka, H. Inui, and E. P. George, AIP Adv. **2016**, *6*, 125008.

[9] N. L. Okamoto, S. Fujimoto, Y. Kambara, M. Kawamura, Z. M. T. Chen, H. Matsunoshita, K. Tanaka, H. Inui and E. P. George, Sci. Rep. **2016**, *6*, 35863.

[10] N. L. Okamoto, M. Asakura, M. Kawamura, H. Inui, T. Fukuda and T. Kakeshita, to be submitted.

[11] Z.S. Basinski, R.A. Foxall, R. Pascual, Scr. Metal. **1972**, *6*, 807-814

P–26

Deformation of micropillars of cubic and hexagonal NbCo$_2$ Laves phases under uniaxial compression at room temperature

Wei Luo, Christoph Kirchlechner, Gerhard Dehm, and Frank Stein

Max-Planck-Institut für Eisenforschung, Max-Planck-Straße 1, D-40237 Düsseldorf, Germany,
w.luo@mpie.de

Introduction

Transition metal-based Laves phases have high strength and good creep resistance which make them potential candidates for high-temperature applications. On the other hand, they exhibit pronounced brittleness at low temperature. Due to their brittleness, the difficulty of producing sufficiently large and flaw-less bulk samples for conventional mechanical testing limits the study of their mechanical properties [1]. The existing literature indicates that the mechanical properties of transition metal-based Laves phases significantly depend on their composition. Most of the reported information of mechanical properties is from hardness measurement. However, the reported results are quite contradictory. While Zhu et al. [2] reported that the hardness of NbFe$_2$, NbCo$_2$ and NbCr$_2$ increases as the composition deviates from the stoichiometric composition, which indicates defect-hardening, Voß's results [3] show that the hardness of NbFe$_2$ and NbCo$_2$ decreases as the composition deviates from the stoichiometric composition, which indicates defect softening. Recently, it has been shown that by reducing the sample size, cracking could be suppressed and even brittle materials can deform plastically at room temperature. In the present work, micropillar compression tests were performed to study the deformation and the composition dependence of the critical resolved shear stress of cubic and hexagonal NbCo$_2$ Laves phases at room temperature.

Laves phases with AB$_2$ stoichiometry may have three structure types, cubic C15 (MgCu$_2$-type), hexagonal C14 (MgZn$_2$-type) and hexagonal C36 (MgNi$_2$-type). All three types of Laves phases exist as stable phases in the Co-Nb system and the C15-NbCo$_2$ Laves phase has a large composition range of 26.0±0.5 − 35.3±0.3 at.% Nb. It makes the NbCo$_2$ Laves phases a perfect candidate to study not only the deformation behavior of transition metal based Laves phases but also the influence of composition and crystal structure on the strength.

Materials and Methods

To get micropillars of cubic and hexagonal NbCo$_2$ Laves phases with different compositions, the diffusion couple technique was used. Co/NbCo$_2$ and NbCo$_2$/Nb diffusion couples were prepared from 5×5×10 mm^3 slices of pure Co, pure Nb and a C15-NbCo$_2$ Laves phase alloy with composition of Co-30 at.% Nb. After heat treatments at 1200 °C for 96 h and 1350 °C for 24 h, the microstructures of the diffusion couples were analyzed SEM, the crystallographic grain orientations were measured using EBSD, and the concentration profiles of the diffusion couples were measured by EPMA. The grain size of the cubic and hexagonal NbCo$_2$ Laves phases is larger than 100 μm. The thickness of the diffusion layer of the C14- and C36-NbCo$_2$ is 40 and 60 μm, respectively, and the diffusion zone of C15-NbCo$_2$ is 400 μm in Co/NbCo$_2$ and 200 μm in NbCo$_2$/Nb, respectively. As there are concentration gradients in the diffusion layers, micropillars with different compositions can be obtained by FIB milling at selected positions in the diffusion layers.

Results and Discussion

In order to study the size effect on the yield strength, a series of micropillars with the same composition of Co-30 at.% Nb (single-phase C15 NbCo$_2$ Laves phase) but different top diameter ranging from 0.5 to 8 μm were studied by compression tests inside an SEM chamber. Representative engineering stress-strain curves are shown in Fig. 1. An SEM image of a micropillar after deformation is shown in Fig. 2. For the small pillars with top diameter of 0.5 and 0.8 μm, the stress increases linearly with the strain to a very high stress around 10 GPa followed

by a rapid strain burst. For the pillars with top diameter from 3 to 8 μm, in some cases they show linear increases of stress with strain followed by rapid strain bursts or even fracture, which is similar to the small pillars but the yield strength decreases. However, in other cases they show plastic flow at lower stress. ECCI observations show that the dislocation density in cubic and hexagonal $NbCo_2$ Laves phases in the as-cast state is very low. It is very likely that the small pillars are nearly dislocation free. Therefore, high stress around G/30 is required for dislocation nucleation on the pillar surface. Due to the lack of dislocation sources, large pillars behave like small pillars but as the volume becomes larger the number of possible sites for dislocation nucleation increases and thus the stress required for dislocation nucleation decreases. In some cases, when dislocation sources are already available in the large pillars, they yield and show plastic flow at lower stress. Overall, as the pillar size increases the critical resolved shear stress decreases approaching 2 GPa which is consistent with the value estimated from hardness measurements.

A set of micropillars with 3 μm in top diameter and different compositions were prepared. Micropillars with compositions of 24 and 36 at. % Nb are C36- and $C14-NbCo_2$ Laves phase, respectively. The others are $C15-NbCo_2$ Laves phase. Micropillar compression tests were performed to study the effect of composition and crystal structure on the strength of $NbCo_2$ Laves phase.

TEM studies with specimens prepared from deformed micropillars by lift-out technique show that slip bands are formed by gliding of dislocations emitted from pillar surfaces. Only a few dislocations sources were activated and very few dislocations were found in the other areas, which indicates that the deformation of micropillars of the cubic and hexagonal $NbCo_2$ Laves phases at room temperature might be a dislocation nucleation controlled process.
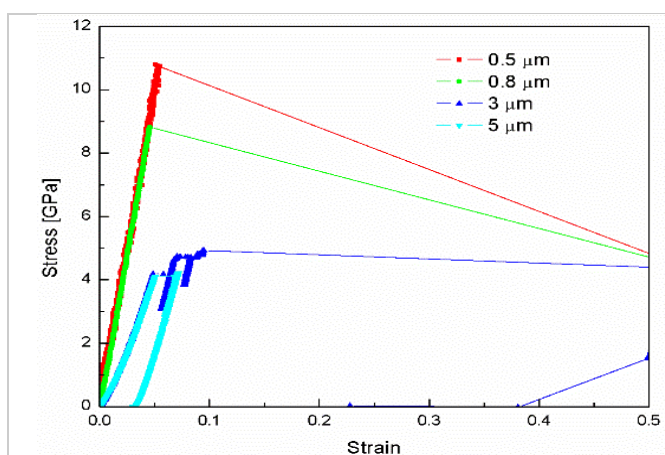
Fig. 1 Representative engineering stress-strain curves of C15 NbCo2 Laves phase micropillars with 30 at.% Nb	Fig. 2 SEM image of a representative single-phase C15 NbCo2 Laves phase micropillar with 5 μm in top diameter after deformation
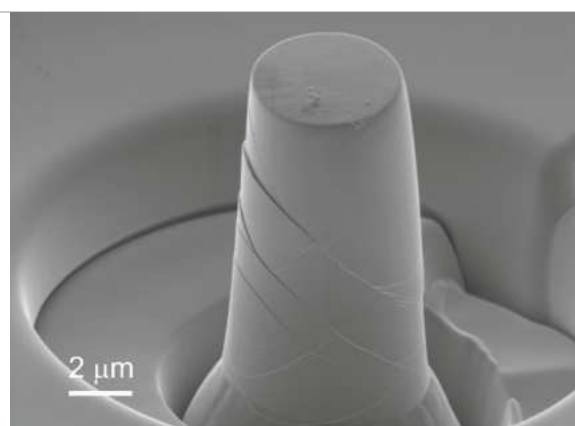
References

[1] S. Voß, F. Stein, M. Palm, D. Raabe, Materials Science and Engineering A. **2010**, 527, 7848-7853.

[2] J.H. Zhu, L.M. Pike, C.T. Liu, P.K. Liaw, Acta Materialia. **1999**, 47, 2005-2018.

[3] S. Voß, F. Stein, M. Palm, D. Grüner, G. Kreiner, G. Frommeyer, D. Raabe, MRS Online Proceedings Library. **2008**, 1128, 469-474.

P–27

In-situ observation of phase and microstructure evolution during directional solidification of novel intermetallic structural materials

Florian Gang[1], Georg Hasemann[2], Michael Oehring[3], Malte Blankenburg[3], Norbert Schell[3], Peter Staron[3], Florian Pyczak[3], <u>Manja Krüger</u>[2], Martin Heilmaier[1]

[1]Karlsruhe Institute of Technology (KIT), Institute for Applied Materials (IAM-WK), Engelbert-Arnold-Str. 4, 76131 Karlsruhe, Germany, florian.gang@kit.edu

[2]Otto von Guericke University, Institute for Materials & Joining Technology, Universitätsplatz 2, 39106 Magdeburg, Germany, georg.hasemann@ovgu.de

[3]Helmholtz-Zentrum Geesthacht, Centre for Materials and Coastal Research, Institute of Materials Research, Max-Planck-Str. 1, 21502 Geesthacht, Germany, florian.pyczak@hzg.de

Introduction

For several decades, directional solidification has been applied on an industrial scale, mostly to nickel-based superalloys since the 1970s [1]. Especially for these high temperature materials, loaded under creep conditions, directional solidification is a promising moulding process. Due to the formation of single-crystalline components or components at least exhibiting an elongated microstructure parallel to the loading direction, grain boundaries as source of creep pores and, therefore, creep rupture can be reduced or even eliminated. Aiming at new high temperature materials beyond nickel-based superalloys, additional microstructural features apply. For example, incorporating an aligned second phase (e.g. Cr or Mo) into NiAl [2] increases the creep properties along the growth direction or may act as a crack arrester, increasing the damage tolerance of the component.

Even though directional solidification has been applied on an industrial scale for a considerable amount of time, advancing this method beyond the current applications is still challenging. Novel materials or changes in the component geometry require significant changes in the process parameters, which is mostly done on a trial-and-error basis. A knowledge-based advancement of the process is difficult, as to some extent the possibility to characterize the production process as well as the materials behaviour "*in-situ*" is limited. Investigations are almost exclusively limited to a post-process characterization of developed microstructure.

X-ray diffraction methods are more suitable for *in-situ* studies of the process. With these technique, the investigation of the melting zone and solidification front is possible in transmission mode. Due to the high temperatures and the difficulties in handling sufficient amounts of hot melt, studies of the melting and solidification behaviour so far have almost exclusively been performed for metals with considerable low melting points, e.g. magnesium or gallium-indium alloys [3, 4]. Extending the possibilities for *in-situ* characterization to materials systems for structural applications, considerably exceeding melting points of 1000 °C, is the overall goal of the BMBF-funded joint project "FlexiDS" between the Otto-von-Guericke University Magdeburg (OVGU) and the Karlsruhe Institute of Technology (KIT), in cooperation with the Helmholtz-Zentrum Geesthacht (HZG).

Materials and Methods

The aims of this joint project are to gain unprecedented *in-situ* insights into the solidification of the aligned microstructure and clarification of the influence of varying solidification parameters (e.g. solidification velocity, temperature gradient) on the microstructure evolution in intermetallic compounds of the systems Fe-Al, Ti-Al, Nb-Si-Cr, Mo-Si-B or Mo-ZrB$_2$. Moreover, solid-state reactions occurring only slightly below the solidus temperature (e.g. eutectoid decomposition of the ε-phase in Fe-Al) should be observed *in-situ*.

For this purpose, a state-of-the-art industrial relevant floating zone furnace (see Fig. 1) will be set up at the High Energy Materials Science Beamline (HEMS, P07) at DESY. Within this furnace, directional solidification can be performed under *in-situ* observation employing synchrotron

measurements. The system is using inductive heating employing a HF coil to induce a locally confined melting zone (see Fig. 2) in rod-shaped samples up to 12 mm diameter and 150 mm length. The possible melting temperatures are up to 2200 °C. The melting zone is moved through the rod by moving the rod longitudinally through the HF coil. Therefore, a solidification direction and velocity is impressed. Rotation of the sample allows e.g. for texture measurement. The directional solidification process is performed under protective atmosphere (e.g. Ar) to avoid oxidation of the sample material. Melting temperature and temperature gradient are checked by pyrometric measurements. Moreover, the whole process is monitored employing high-resolution ZSB cameras.

Fig. 1: Design of floating zone furnace
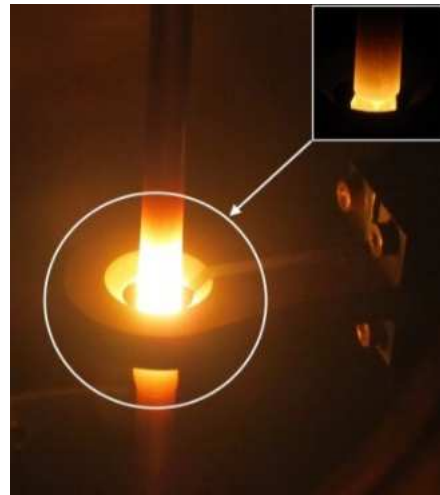
Fig. 2: Confined melting zone

Results and Discussion

Depending on the materials system, different questions will be addressed. For example, for Al-rich Fe-Al alloys, consisting of 55 – 65 at% Al, the phase relations between the high temperature ε phase (Fe_5Al_8) and the by eutectoid decomposition evolving phases FeAl and $FeAl_2$, which are stable at ambient temperature, will be reviewed. As the ε phase solidifies directly from the melt, has a narrow compositional range and cannot be stabilized to ambient temperatures, results can only be obtained employing *in-situ* experiments at elevated temperatures. For the ternary eutectic composition in the system Nb-Si-Cr, the growth characteristics (coupled or non-coupled) as well as the texture evolution during directional solidification will be clarified. Moreover, the unknown phase relations between $Nb_9(Si,Cr)_5$, decomposing into Nb_5Si_3 and Nb solid solution will be examined. In the eutectic system Mo-Si-B, the phase evolution of complex microstructures during solidification is in the focus of the current research. For TiAl alloys the growth mode and growth direction of the solidifying phases will be studied in dependence of the solidification conditions.

References

[1] R. C. Reed: The Superalloys: fundamentals and applications, Cambridge University Press, Cambridge, UK, **2006**.

[2] T. Haenschke, A. Gali, M. Heilmaier et al.; J. Physics: Conference Series. **2010**, *240*, 012063, doi:10.1088/1742-6596/240/1/012063.

[3] N. Shevchenko, S. Boden, G. Gerbeth et al., Metal. Mater. Trans. A. **2013**, *44A*, 3797.

[4] A. Saad, Ch.-A. Gandin, M. Bellet et al., Metal. Mater. Trans. A. **2015**, *46A*, 4886,

P–28

Microstructure evolution and mechanical properties of a multi-phase alloy in the Cr-Mo-Nb system

Li Peng[1], Ken-ichi Ikeda[1], Seiji Miura[1] and Toshiaki Horiuchi[2]

[1]Division of Materials Science and Engineering, Faculty of Engineering, Hokkaido University, Kita 13 Nishi 8, Kita-ku, Sapporo 060-8628, Japan, peng@eng.hokudai.ac.jp, ikeda.ken-ichi@eng.hokudai.ac.jp, miura@eng.hokudai.ac.jp

[2]Department of Mechanical Engineering, Faculty of Engineering, Hokkaido University of Science, Sapporo 006-8585, Japan, horiuchi@hus.ac.jp

Introduction

The AB_2-type intermetallic Laves phases with topologically close-packed (TCP) structures have been considered for high-temperature structural materials, because of their high melting points and attractive mechanical properties at elevated temperature. Although the concept of ductile phase toughening has been applied to improve their room temperature toughness of some alloys including $Nb/NbCr_2$ [1] and $Cr/TaCr_2$ [2], the large volume fraction of ductile phases resulted in lower strength of the alloys.

In this study, a BCC_1-BCC_2-$NbCr_2$ three-phase alloy was put forward in Cr-Mo-Nb system. The BCC_1-BCC_2 interphase boundary was brought into the conventional single BCC ductile phase by introducing second BCC phase with a fine structure. Similarly with Ni-based γ/γ' alloys [3,4], high-temperature strength and creep resistance might be obtained by the microstructure control. In the meantime, Laves phase $NbCr_2$ dispersed along with the two BCC phases. Therefore, good high temperature strength, as well as microstructure stability, can be expected.

Materials and Methods

Raw materials Nb, Cr and Mo with a purity above 99.9% were employed. Alloys with a nominal composition of Cr-30Mo-20Nb (at%) were prepared in the form of small button ingots by arc melting on a water-cooled copper hearth in a high purity Ar atmosphere. The as-cast alloys were first homogenized at 1,700 °C for 1 h under vacuum condition, then aged at 1200 °C for various periods up to 100 h, followed by water quenching.

The microstructure was observed using scanning electron microscope (SEM) attached with Electron Probe Micro-Analyzer (EPMA), with which chemical analysis of constituent phases was also conducted. The X-ray diffraction was performed to identify the crystal structures of each phase with the 2θ scan from 30° to 120°. The strength of the alloys heat-treated at different conditions was evaluated by Vickers hardness test with a load of 0.5 kgf and compression test with an initial strain rate of 1×10^{-4} s^{-1}, both at room temperature.

Results and Discussion

Fig. 1 shows the microstructure evolution of alloy Cr-30Mo-20Nb aged at 1200°C for various time periods after heat treatment at 1700 °C for 1 h. Single BCC phase alloy was obtained after heat-treating at 1700 °C for 1h, as shown in Fig.1(a). "Growth-ring-shaped" structures were formed during heat-treatment at 1200 °C. The black phases alternating with white phases were proved to be Cr-rich BCC_1 (black) and Mo-rich BCC_2 (white) by EPMA analysis and XRD. With the extension of aging time, the original BCC phase disappeared and replaced by the two BCC phases. In the meantime, Laves phase $NbCr_2$ formed at some time and the growth of Laves phase $NbCr_2$ at the latter stage of aging dominated the microstructure evolution while the two BCC phases remained a fine microstructure, as shown in Fig. 1(d).

Fig. 2 shows the Vickers hardness test and compression test results of alloy Cr-30Mo-20Nb. The microhardness changed slightly at an early stage, then it reached a minimum of 773 HV at 24 h where the two BCC phases occupied the structure. After that, it increased and reached a plateau of 840 HV due to the growth of Laves phase. The highest value of fracture strength was also

obtained at 24 h, which coordinated to the result of Vickers hardness. Although the crack initiation strength of 48 h was higher than that of 24 h, its fracture strength was no more than that of 24 h.
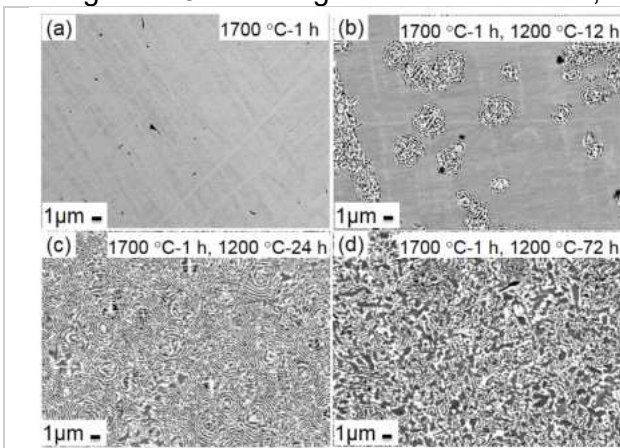

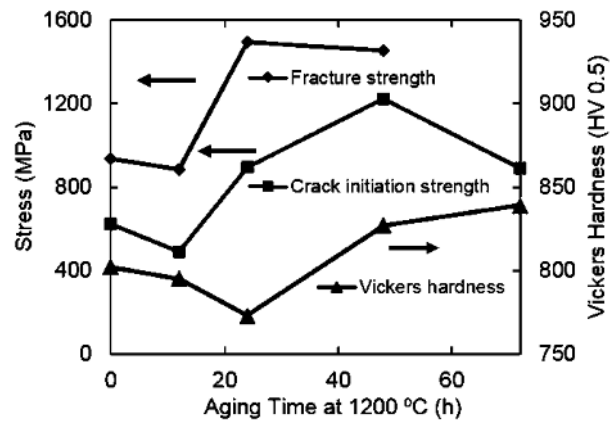| Fig. 1: Microstructure evolution of alloy Cr-30Mo-20Nb aged at 1200 °C (following the annealing at 1700 °C for 1 h).	Fig. 2: The effect of annealing time at 1200 °C on the strength of alloy Cr-30Mo-20Nb following the annealing at 1700 °C for 1 h.

Acknowledgement

References

[1] M. Yoshida, T. Takasugi, Materials Science and Engineering A, **1997**, *234*, 873-876.

[2] R.H. Tien, J.H. Zhu, Intermetallics, **2005**, *13*, 361-366..

[3] T. Murakumo, Y. Koizumi, T. Kobayashi, H. Harada, Superalloys 2004, Proc. 10th Int. Symp. on Superalloys, **2004**,155-162.

[4] T.M. Pollock, S. Tin, Journal of Propulsion and Power, **2006**, *22*, 361-374.

P–29

Novel rotatable load frames for neutron diffraction studies on stress/strain, texture, phase transformations or elastic constants

M. Hoelzel[1], A. Heldmann[1], M. Hofmann[1], W.M. Gan[2], W.W. Schmahl[3]

[1]Heinz Maier-Leibnitz Zentrum (MLZ), Technische Universität München, Garching, Germany

[2]German Engineering Materials Science Centre, Helmholtz-Zentrum Geesthacht, Geesthacht, Germany

[3]Department für Geo- und Umweltwissenschaften, Ludwig-Maximilians Universität München, Germany

Introduction

In-situ neutron or synchrotron diffraction under mechanical load allows to correlate the mechanical behavior of materials with their structural features. Typical applications of in-situ diffraction with load frames include stress/strain analyses, texture evolution or stress-induced phase transformations. In this contribution we present unique load frames which allow an orientation of the load axis with respect to the incident beam by an Eulerian cradle type design (ω, χ and ϕ axis) [1]. One version ("uniaxial version") of the rig is optimized for texture analysis allowing a free sample rotation around the ϕ axis under uniaxial tension or compressive stress. By this design a movement of the load frame columns through incident or scattered beam during the measurements can be avoided. Thus complete pole figures under mechanical load can be derived. A second version ("multiaxial version") enables torsion in addition to tension or compression. The load frames were designed at Heinz Maier-Leibnitz Zentrum (MLZ / FRM II, Garching near Munich) for routine usage at the diffractometers SPODI (high resolution diffractometer) and STRESS-SPEC (strain scanner and texture diffractometer). There compact design allows a usage also on other neutron diffractometers.
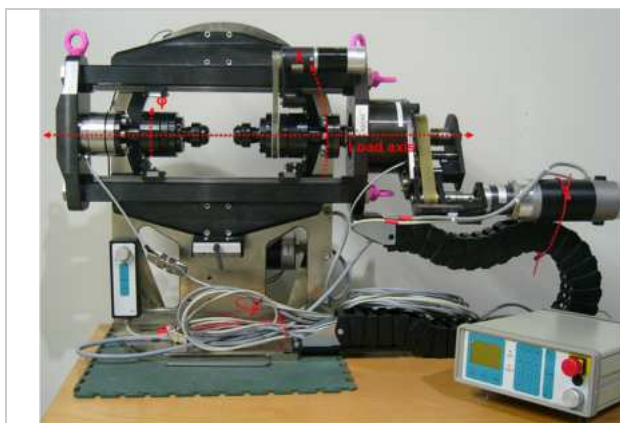
Fig. 1: Uniaxial version of the load frames	Fig. 2: Multiaxial version at the diffractometer SPODI (FRM II)
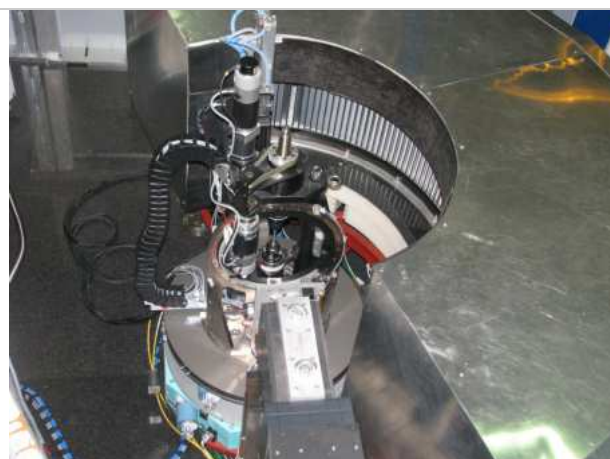
Layout and Specifications

The tensile rigs are essentially double column load frames which are attached to rotation frames – allowing a rotation of the load axis by 90° with respect to the scattering plane of the neutron diffractometers (corresponding to a χ tilting in classical Eulerian cradles). The ω-rotation of the load axis with respect to the incident neutron beam is done by the main sample tables of the diffractometers.

The load frames are integrated in the instrument control of our diffractometers SPODI and STRESS-SPEC and can be remotely operated by means of a software interface including the

target values for force, sample extension, position of the crossbar, torque or torsion angle. Experiments can be carried out in load control, strain control or position control, respectively.

The macroscopic strain can be measured by clip-on extensometers. Alternatively, a digital image correlation (DIC) system can be used to determine the sample deformation. The load frames can be equipped with either a resistance heating device or a mirror furnace to investigate the mechanical behavior of samples at high temperatures up to 1000 °C.

Applications and Results

Strain mechanisms in shape memory alloys

Martensitic nickel titanium shape memory alloys (50.14% Ni, monoclinic symmetry) have been investigated to elucidate and quantify the contributions of ferroelastic twin accommodation and elastic lattice strain for different strain levels. Twinning/detwinning processes result in changes of intensities of Bragg reflections while lattice strain is accompanied by peak shifts. Thus, both contributions could be clearly separated in diffraction experiments, which were carried out at diffractometer SPODI at different strain levels up to 8% and different tilting angles χ from 0° to 90° between the load axis and the incident beam.

At diffractometer STRESS-SPEC in-situ texture measurements have been carried out for further analysis of the twinning/detwinning processes. The possibility to obtain complete pole figures under load with the novel tensile rigs is particular beneficial in low symmetry alloys such as monoclinic nickel-titanium alloys [1].

In-situ intensity and strain pole figures in engineering allyos

In addition to intensity pole figure measurements for texture analysis, also strain pole figures can be derived under mechanical load, reflecting the orientation distribution of strains in the material. By this means, the orientation distribution of crystallites and lattice strains as a function of applied stress can be obtained in one experiment. A corresponding study on austenitic steels has been carried out at STRESS-SPEC [2].

Diffraction elastic constants and single crystalline elastic constants

The analysis of residual stresses by diffraction is related to the determination or knowledge of diffraction elastic constants (DEC) which in turn are linked to the single crystal elastic constants of the constituent crystallites. Diffraction elastic constants for ductile cast iron samples were determined by measuring the lattice strain as a function of the applied load for various tilt angles χ of the load frame [1]. Here the angle χ corresponds to the angle ψ in the classical $\sin^2\psi$ scans.

To derive the elastic constants from diffraction data several authors proposed methods which can be regarded as reverse way of classical stress analysis [3]. Here the strain is measured for the defined stress. In particular textured samples require measurements in all possible grain orientations. Thus, these methods require diffraction data over a wide range of reflections under mechanical load for a series of orientations of the load axis with respect to the incident beam. Our load frames are exactly designed for these measurements. In proof-of-principle experiments, elastic constants in steels and aluminum alloys could be determined which match well with literature data. The method and recent results will be presented in more detail in the contribution of A. Heldmann et al.

References

[1] M. Hoelzel, W.M. Gan, M. Hofmann, C. Randau, G. Seidl, Ph. Jüttner, W.W. Schmahl, Nucl. Instr. **2013**, *A711*, 101–105.

[2] W.M. Gan, C. Randau, M. Hofmann, H.G. Brokmeier, M. Mueller, A. Schreyer, J. Phys. : Conf. Ser. **2012**, *340*, 012100.

[3] T. Gnäupel-Herold, P. C. Brand, H. J. Park, J. Appl. Cryst. **1998**, *31*, 929-935.

P–30

Effect of Pd-site substitutional elements on
phase stability and mechanical property of B2 compound PdAl

Tomonori Soma, Seiji Miura

Division of Materials Science and Engineering, Faculty of Engineering, Hokkaido University, Kita 13 Nishi 8, Kita-ku, Sapporo 060-8628, Japan, t-soma@lms4-ms.eng.hokudai.ac.jp, miura@eng.hokudai.ac.jp

Introduction

To improve gas turbine efficiency by increasing combustion temperature, Nb-based alloys has attracted attentions as candidates of materials for heat-resisting components because they have not only higher melting temperature than Ni-based superalloys but also low density. However, they have disadvantages such as inadequate oxidation resistance and strength at high temperature atmosphere. B2-PdAl has a potential to improve oxidation resistance by applying as oxidation resistant coatings on Nb-based alloys without the formation of brittle phase between Nb-bcc and PdAl-B2 [1]; however, cracks are formed in PdAl during phase transition between the high temperature B2 phase and low temperature rhombohedral phase. Some elements such as Ni, Rh and Ru forms B2 aluminides without phase transition. In this study the effect of Ni, Rh and Ru on the phase transition temperature is investigated. The deformation mechanisms of B2-PdAl examined by in-situ high temperature compression test will also be discussed.

Materials and Methods

An equiatomic PdAl alloy ingot and ternary 40Pd-10x-50Al (at.%, x=Ni, Rh and Ru) alloy ingots were prepared by arc melting, followed by the heat-treatment at 1000°C for 168h and then quenched into water. The crystal structure was examined by XRD using Cu-Kα radiation. Composition analysis of the phases was conducted by the use of EPMA. DTA analysis was conducted on alloys under flowing Ar atmosphere with heating rate of 20°C/min up to about 1000°C. In-situ surface observation during heating was performed in a gold image furnace under flowing Ar atmosphere by the use of a laser confocal microscopy.

Results and Discussion

Fig.1 shows the result of the surface observation of binary PdAl. The flat surface was undulated during heating, and many cracks were found in the specimen. It is caused by low toughness and difference of volume per atom between B2 phase and rhombohedral phase. The DTA results show that the phase transition temperature decreases with ternary additive elements, and almost no transition is found in 40Pd-10Ni-50Al alloy. It suggests that the B2 PdAl is stabilized by adding relatively small amount of the elements which form stable B2 aluminides.
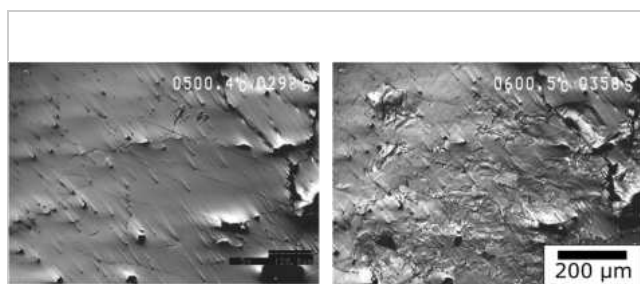
Fig. 1: The surface of binary PdAl during heating (a) before transition (b) after transition

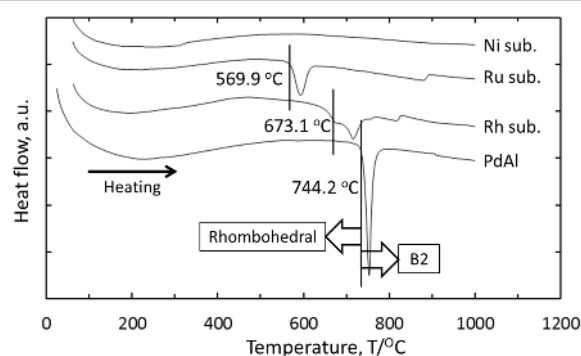Fig. 2: The results of DTA analysis of PdAl-B2 compounds with and without ternary additive elements during heating

Acknowledgement

Reference

[1] P. Cebra, M. Vilasi, B. Malaman, J.Steinmetz, Journal of Alloys and Compounds. **1993**, *201*, 57-60.

P–31

Grain boundary precipitation behavior of Fe$_2$Ti-Laves phase in Fe-Cr-Ti ternary ferritic alloy

Yutaro Oki, Satoru Kobayashi and Masao Takeyama

Tokyo Institute of Technology, 2-12-1 Ookayama, Meguro-ku, Tokyo Japan 152-8552
kobayashi.s.be@m.titech.ac.jp

Introduction

Ferritic heat resistant steels are used for high temperature components in thermal power plants, etc. and are required to keep their creep resistance at 873 K for time periods longer than 100,000 h. It is very important to cover grain boundaries by stable precipitates in heat resistant steels and alloys used in such long term creep conditions. In conventional ferritic steels, grain interior and grain boundaries are strengthened with carbonitride and carbide particles, which are however transformed to less effective nitride (Z phase) particles. Laves phase is not intentionally precipitated as strengthening phase in conventional ferritic steels, but is thermodynamically stables. Thus, the objectives of this research is to investigate the precipitation behaviors of Laves phase especially on grain boundaries in a ferrite matrix in a model alloy aiming to find a way to increase the area fraction of precipitates on grain boundaries and keep it for long time in ferritic heat resistant steels.

Materials and Methods

The alloy studied is an Fe-5.2Cr-4.2Ti ternary alloy. This alloy was prepared by argon-arc melting, solution treated for 10~30 min at 1423 K in the ferrite (α) single phase field and aged for 15 s ~ 5000 h at 973~1373 K in the two-phase field of α+Fe$_2$Ti, followed by rapid cooling. The heat treatments were performed in an Ar atmosphere using an infrared furnace with vacuum and gas cooling systems. The microstructures were observed with optical microscope and scanning electron microscope.

Results and Discussion

The precipitation of Laves phase on grain boundaries causes an increase in the area fraction of Laves phase on grain boundary (ρ) up to 100 % at short time aging (Fig. 1(a,b)). The ρ decreases while the size of Laves phase particles on grain boundaries increase with further aging (Fig. 1(b-d)). In order to understand the change in the ρ with aging time, the length (L), the width (W) of grain boundary Laves phase and the number of Laves phase particles per unit grain boundary length (N) were quantitatively measured (Fig. 2). The L and W increase with aging, but show a plateau region from 1.5 h to 24 h. The N increases rapidly in the beginning of precipitation and then decreases with increasing aging time. The volume fraction of Laves phase per unit grain boundary length (V), calculated by the product of L, W and N, increases with aging with a plateau region from 1.5 h to 24 h. The onset of the plateau region almost corresponds to the time when the ρ reaches to the maximum. This correspondence on the time dependence allows us to speculate that the increase in ρ is caused by the nucleation/growth of the Laves phase on grain boundaries using the supersaturation of Ti in the vicinity of grain boundaries as driving force, while the decrease in ρ is caused by coarsening of the precipitates due to interfacial energy as driving force. The increase in the V in the coarsening process is probably due to the diffusion of the solute element from inside of the grains. It is therefore important to choose alloying elements of which diffusion is slow and that forms Laves phase with small interfacial energy with the ferrite matrix to retard and minimize the decrease in the ρ in the long time exposure. Detailed results on analysis of chemical composition, aging temperature dependence and microstructures of alloys with different alloying elements and the interfacial energy consideration will be shown in the presentation.
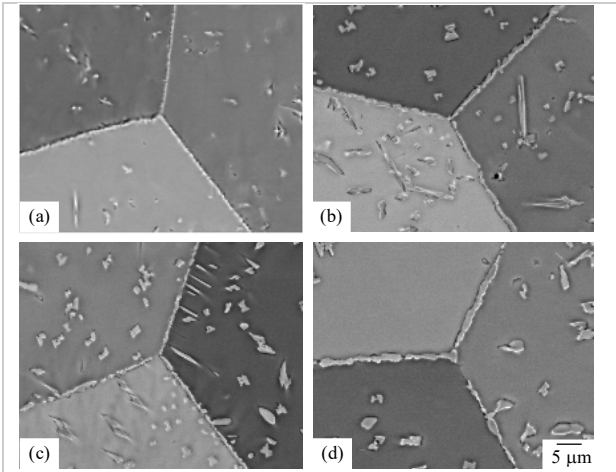
Fig. 1: Backscattered electron images of the Fe-5.2Cr-4.2Ti ternary alloy aged at 1073 K for (a) 5 min, (b) 1.5 h, (c) 24 h, (d) 400 h, followed by rapid cooling.
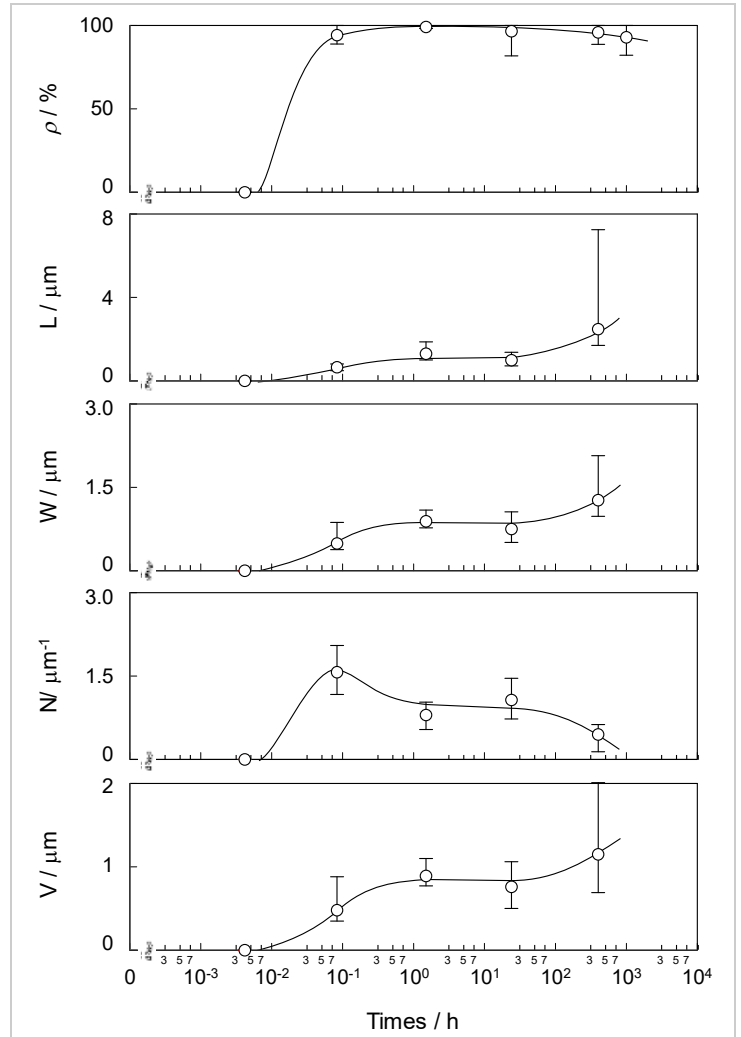

Fig. 2: Change in the area fraction (ρ), the length (L) and width (W) of grain boundary Laves phase, the number (N) and the volume fraction (V) of the Laves phases per unit grain boundary length, with aging at 1073 K in the alloy studied.

P–32

Ab initio full-potential study of structural properties and magnetic phase stability of SmX$_2$ (X = Co and Fe) intermetallic compounds

Ali Bentouaf[1,2], Hicham Ramdoum[2], Rezki Mabsout[3], Mohammed Ameri[2], Zahira Bouyakoub[2]

[1] University of Dr. Tahar Moulay, Faculty of Technology 02000 Saida, Algeria, lilo.btf@gmail.com

[2] Laboratory of Physical Chemistry of Advanced Materials, University of Djillali Liabes, BP 89, Sidi-Bel-Abbes 22000, Algeria.

[3] University of Djillali Liabes, BP 89, Sidi-Bel-Abbes 22000, Algeria.

Introduction

The cubic Laves phase compounds RX$_2$ (R = rare earth, X = transition metal) have been one of highly interesting subjects in solid state physics since the nineteen sixty years due to the metamagnetic RX$_2$ transition owing to the instability of the metal transition moment [1–5]. Among the various intermetallic compounds of rare-earths with transition-metals, the RX$_2$ binary Laves phase alloys with ferromagnetic X (Fe and Co) have been particularly attractive both for fundamental investigation of their physical properties -including their electronic structure, the high Curie temperature, then for their technological applications potential. To the best of our knowledge, no detailed theoretical study have been yet performed on the SmCo$_2$ and SmFe$_2$ compounds which constitutes the main focus of our paper, which reports on the theoretical investigation of the structural, electronic, magnetic and elastic properties of the cubic MgCu$_2$-type binary Laves phases SmCo$_2$ and SmFe$_2$ compounds. After briefly describing the computational techniques employed in this study, the result and discussions are presented together with the summary of the main findings and conclusions.

Method of calculations

We have used the all electrons full-potential linearized augmented plane waves (FP-LAPW) within the density functional theory (DFT) [6, 7] basis set and method [8] as implemented in the WIEN2k code [9-11]. For the exchange-correlation functional, we have used the generalized gradient approximation GGA [12] and GGA+U (U-Hubbard Hamiltonian) [13,14] beyond the local density approximation as proposed by Perdew et al. [14]. The satisfactory degree of convergence was achieved by considering a number of FP-LAPW basis function up to RMTK$_{max}$= 8, (where RMT is the smallest radius of the muffin-tin spheres and the K$_{max}$ is the plane wave cut-off, i.e. the maximum value of the wave vector K=k+G, and the maximum length of G for expanding the interstitial density and potential. RMT for Sm, Fe, and Co are 2.2, 1.8, and 1.8 (a.u), respectively. Within the spheres, the charge density and potential are expanded -in terms of crystal harmonics- up to angular momenta L$_{max}$=10, and a plane wave is used in the interstitial region. The value of the magnitude of the largest vector in charge density Fourier expansion G$_{max}$=12. The cut-off energy, which defines the separation of valence and core states, was chosen as -6 Ry. We also selected the charge convergence as 0.0001e during self-consistency cycles.

Results and Discussion

The SmCo$_2$ and SmFe$_2$ Laves phase has an ordered C15-type structure with space group 227 (Fd-3m). The Sm atoms occupy the tetrahedral 8a Wyckoff site $(\frac{1}{8},\frac{1}{8},\frac{1}{8})$ and the Co atoms occupy the octahedral 16d site $(\frac{1}{2},\frac{1}{2},\frac{1}{2})$, as displayed in Fig. 1. The structural properties are obtained by the minimization of the total energy depending on the volumes of SmCo$_2$ and SmFe$_2$ within GGA and GGA+U methods. We have computed the lattice constants, the bulk moduli and the first pressure derivatives of the bulk moduli by fitting the total energy with respect to the volume according to the Murnaghan's equation of state [15]:

$$E_T(V) = \frac{B_0 V}{B'_0}[\frac{(V_0/V)^{B'_0}}{B'_0 - 1} + 1] + E_0 - \frac{V_0 B_0}{B'_0 - 1}$$

(1)

The comparison of the optimized lattice parameters with previous studies has shown that the calculated values corroborated efficiently the experimental values. The obtained results are listed in Table 1.

X	Lattice parameter a (Å)		Bulk modulus B (GPa)
	Our work	Other work	Our work
SmCo$_2$			
GGA	7.0402	-	110.402
SmFe$_2$			
GGA	7.1176		95.464

Table 1: Equilibrium parameters of the SmCo$_2$ and SmFe$_2$: lattice constant a, bulk modulus B.

We have then studied the correlation effects on the electronic properties where we pointed out that when the on-site Coulomb interaction is induced by the GGA + U, the magnetic moments increased. This increase was explained in terms of the energy shift of the partial densities of Co, Fe and Tb by the electron-electron correlation in the GGA+ U calculation. Finally, this model (GGA + U) was found to require a strong interaction (high U) to obtain a qualitative agreement with experimental values, such as behaviour states d, f and the magnetic moments. Furthermore, in order to obtain further insight into the type of states associated with each orbital, the projected DOS of Co-3d and Fe-3d orbitals were calculated using GGA and GGA+U.
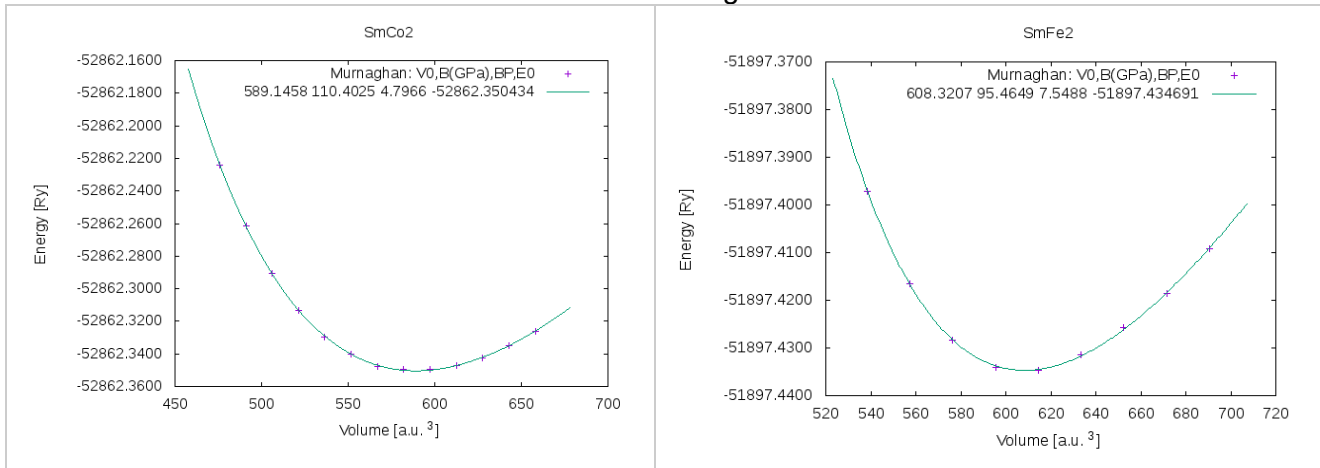
Fig. 1: The total energy E_{tot} of the SmCo$_2$ and SmFe$_2$ compounds studied as a function of the volume with GGA calculation adjusting by Murnaghan equation.

References

[1] M.I. Batashevich, H.A. Katori, T. Goto, H. Wada, T. Maeda, T. Mori, M. Shiga, Physica B, **1997**, *229*, 315.

[2] T. Goto, H.A. Katori, T. Sakakibara, H. Mitamura, K. Fukamichi, K. Murata, J. Appl. Phys., **1994**, *76*, 6682.

[3] T. Goto, K. Fukamichi, H. Yamada, Physica B, **2001**, *300*, 67.

[4] S. Khmelevskyi, P. Mohn, J. Phys.: Condens. Matter, **2000**, *12*, 9453.

[5] E. Gratz, A.S. Markosyan, J. Phys.: Condens. Matter, **2001**, *13*, 385.

[6] P. Hohenberg, W. Kohn, Phys. Rev. B, **1964**, *136*, 864.

[7] W. Kohn, L. J. Sham, Phys. Rev., **1965**, *140*, A1133.

[8]   J.C. Slater, Adv. Quant. Chem., **1964**, *1*, 5564.

[9]   P. Blaha, K. Schwarz, G.K.H. Madsen, D. J. Kvasnicka, WIEN2K, an Augmented Plane Wave +Local orbitals program for calculating crystal properties, Karlheinz Schwarz, Technische Universität, Wien, Austria, **2001**, ISBN 3-9501031 1-2.

[10] P. Blaha, K. Schwarz, P. Sorantin, S.B. Tricky, Comput. Phys. Commun., **1990**, *59*, 399.

[11] K. Schwarz, P. Blaha, G.K.H. Madsen, Comput. Phys. Commun., **2002**, *147*, 71.

[12] D. C. Langreth, J. P. Perdew, Phys. Rev. B, **1980**, *21*, 5469.

[13] J.P. Perdew, S. Burke, M. Ernzerhof, Phys. Rev. Lett., **1990**, *77*, 3865.

[14] J.P. Perdew, S. Burke, Y. Wang, Phys. Rev. B, **1996**, *54*, 16533.

[15] F.D. Murnaghan, Proc. Natl. Acad. Sci. USA, **1944**, *30*, 244.

[16] H. Samata et al., Jpn. J. Appl. Phys. **1998**, *37*, 5544-5548.

P–33

Thermodynamic assessment of Co-Cr-Mn system for improved calphad prediction of σ-phase in high entropy alloys

K. Guruvidyathri[1,2], Soumya Sridar[1], B. S. Murty[1], J. W. Yeh[2] and K. C. Hari Kumar[1]

[1]Department of Metallurgical and Materials Engineering,
Indian Institute of Technology Madras, Chennai – 600 036, INDIA
guruvidyathri@gmail.com, soumya_sridar@yahoo.co.in, murty@iitm.ac.in, kchkumar@iitm.ac.in

[2]Department of Materials Science and Engineering,
National Tsing Hua University, 101, Section 2, Kuang-Fu Road, Hsinchu, Taiwan 30013
jwyeh@mx.nthu.edu.tw

Introduction

Presence of intermetallic phases in high entropy alloys (HEAs) is not uncommon [1]. The ability to predict these phases in HEAs using Calphad method has been shown to accelerate the identification of promising compositions [2]. However, most of the existing commercial thermodynamic databases based on which these calculations are done, have severe shortcomings. This is mainly because most of these databases are developed for commercial alloys that do not have concentrated multicomponent compositions like HEAs. Nevertheless, there are even attempts to quantify the credibility of CALPHAD calculations with existing commercial databases [3]

In the present study, Calphad calculation of equilibrium phases in CoCrCuMnNi equiatomic alloy is attempted using TCHEA [4] database. Calculations showed disagreement with experiments on temperature range of the existence of the σ-phase. This discrepancy is probably due to poorly determined Gibbs energy functions of the σ-phase in the Co-Cr-Mn ternary subsystem. In order to address this issue, a thermodynamic assessment of Co-Cr-Mn system is performed, specifically concentrating on the thermodynamic description of the σ-phase. Required data are generated using *ab initio* calculations and experiments on selected compositions of Co-Cr-Mn alloys. The Gibbs energy functions thus obtained are used to replace corresponding functions in the TCHEA database in order to improve the calculation results.

Materials and Methods

Evolution of equilibrium phases in CoCrCuMnNi equiatomic alloy as a function of temperature is computed using Thermo-Calc software in combination with the TCHEA database.

The required alloys for the constitutional studies were made by vacuum arc melting of elements of purity 99.5%. The arc melting chamber is evacuated to less than 10^{-5} mbar of pressure and is then filled with 99.99% purity argon till it reached atmospheric pressure. Alloys were flipped and remelted 4 times for better homogeneity. Cast samples were vacuum sealed in quartz tubes and subjected to heat treatment. For CoCrCuMnNi alloy the heat treatment was done at 800°C for 3 days as well as 10 days. Co-Cr-Mn alloys were heat treated for 3 days at 1100°C and 800°C for achieving equilibrium microstructures. Characterization using XRD and SEM were carried out. Equilibrium phases, their compositions and corresponding phase fractions were thus obtained.
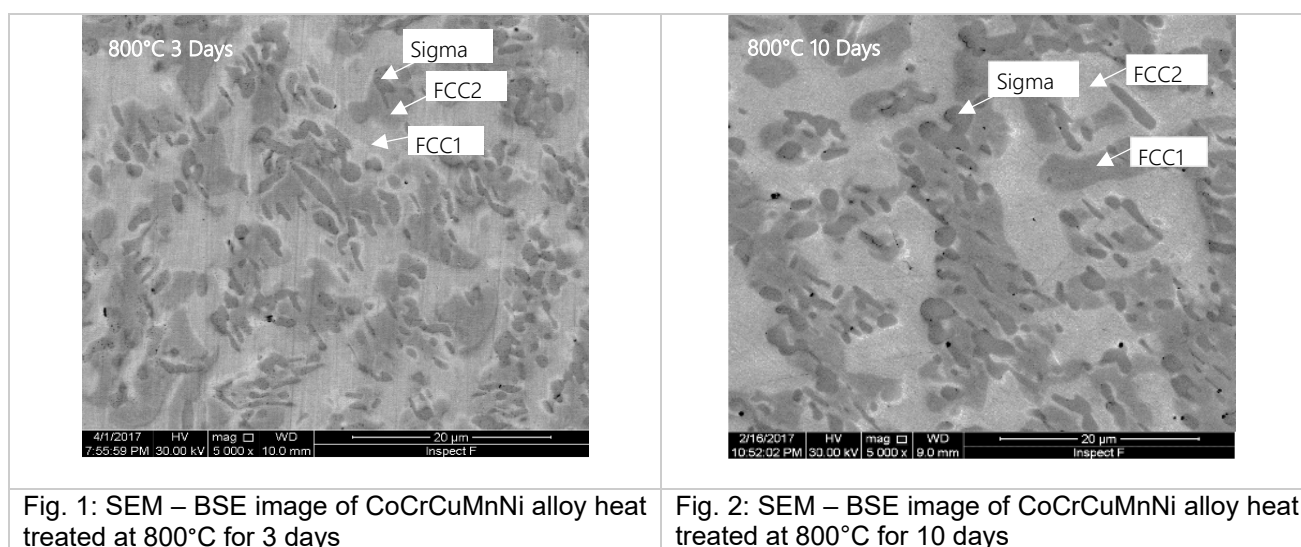
Enthalpies of formation of the end-members for the ternary σ-phase are estimated using *ab initio* calculations. Vienna Ab initio Simulation Package (VASP) is used for calculations.

The experimental constitutional and *ab initio* thermochemical data obtained from current work are used for optimizing the Gibbs energy model parameters. After assessment, the ternary Co-Cr-Mn Gibbs energy data is appended with TCHEA database to improve the prediction of σ-phase in the present quinary alloy.

Results and Discussion

In the Calphad calculation of CoCrCuMnNi alloy performed using the original TCHEA database, σ-phase is not seen as an equilibrium phase at 800°C. However, heat treatment of the arc melted alloy showed the presence of σ-phase rich in Cr, Co and Mn both in samples heat treated at 800 °C for 3 days as well as 10 days (Fig. 1 and Fig. 2, respectively). There was no significant variation in amount and composition of the σ-phase between the two durations. The calculations using ternary Co-Cr-Mn Gibbs energy functions appended with TCHEA database, however, resulted in the prediction of the σ-phase.

Figures

| Fig. 1: SEM – BSE image of CoCrCuMnNi alloy heat treated at 800°C for 3 days | Fig. 2: SEM – BSE image of CoCrCuMnNi alloy heat treated at 800°C for 10 days |

References

[1]   B.S. Murty, J.W. Yeh, S. Ranganathan, High-Entropy Alloys, Cambridge University Press, Cambridge, **2014**, 201-202.

[2]   O.N. Senkov, J.D. Miller, D.B. Miracle, C. Woodward, Nature Communications, **2015**, 6,6529.

[3]   O.N. Senkov, J.D. Miller, D.B. Miracle, C. Woodward, Calphad. **2015**, *50*, 32–48.

[4]   https://www.thermocalc.com/

[1]   B.S. Murty, J.W. Yeh, S. Ranganathan, High-Entropy Alloys, Cambridge University Press, Cambridge, **2014**, 201-202.

[2]   O.N. Senkov, J.D. Miller, D.B. Miracle, C. Woodward, Nature Communications, **2015**, 6,6529.

[3]   O.N. Senkov, J.D. Miller, D.B. Miracle, C. Woodward, Calphad. **2015**, *50*, 32–48.

[4]   https://www.thermocalc.com/

P–34

Microstructure evolution of diffusion welded SS-304L/Zircaloy4 with copper interlayer/ Influence of the holding temperature

D. Aboudi[1.2], S. Lebaili[1], J. Zollinger[2]

[1]Laboratoire de Science et Génie des Matériaux (LSGM), F.G.M.G.P., Université des Sciences et de la Technologie Houari Boumediene, 16000 Algiers, Algeria, daboudi@usthb.dz

[2]Université de Lorraine, Institut Jean Lamour, Department of Metallurgy & Materials Science and Engineering, Parc de Saurupt, Nancy F-54011, France, julien.zollonger@univ-lorraine.fr

Introduction

The studies on direct diffusion bonding between Zircaloy and steel AISI 304L can lead to variable reaction layer thicknesses [1,2] and to reaction layers containing several microstructurally different areas [3], depending on the processing parameters. The complex microstructure observed in diffusion bonded Zircaloy4 (Zy4) - stainless steel AISI 304L (SS-304L) joints is inherited from the coexistence of numerous phases, from solid solutions to intermetallics and Laves phases. The Laves phases in particular are expected to be the main source of crack initiation during mechanical testings due to their very high hardness.

A common solution is to use a metallic layer to avoid the formation of embrittling phase that is commonly copper, nickel or niobium [4–6]. This paper focuses on the use of a 50 lm copper layer to diffusion weld SS 304L to Zy. Different samples were held from 1173 to 1323 K for 45 min. The emphasis is held on the phase identification, the mechanisms of microstructure and phases formation and the consequences on the hardness of the reaction zone of the welded specimens depending on the welding temperature.

Materials and Methods

The nominal composition of study materials, the shape and the dimensions of welded samples as well as the experimental approach for welding realization are described in details in our previous works [7].

Results and Discussion

The diffusion welded microstructure overviews at the SS 304L/Cu/Zy interfaces are shown in the Fig. 1 (a,b) on SEM BSE images and correspond to the investigated temperatures of 1173, and 1223K during a holding time of 45 min.

Fig. 1 (a) shows the microstructure observed in the reaction layer at 1173 K. On the steel side, a 10 µm thick layer remains untransformed. Adjoined to the copper is a phase which could not be identified with EBSD due to a grain size lower than 100 nm, but whose composition has exactly the stoichiometry of the $Cu_{51}Zr_{14}$ phase. This phase interpenetrates another phase that is liquid at the treatment temperature. More precisely, the liquid phase seems to dissolve the $Cu_{51}Zr_{14}$ phase into liquid and the $Zr_5(Sn,Cu)_3$ compound. Upon cooling from 1173 K, the liquid phase solidies into a phase that could not be identified either, but its composition is compatible with the liquid composition taken from the binary Cu-Zr phase diagram at this temperature, e.g. 43 at.% Zr [8]. According to the existing thermodynamic descriptions of the the Cu-Zr system, a liquid having this composition should transform into the $Cu_{10}Zr_7$ compound. Tagushi et al. reported that this compound requires long incubation time to nucleate from solid state diffusion couples [9]. The data available about the formation of this phase from the liquid state is rather limited, since research has been more oriented on amorphous alloys which can be obtained in this composition range. Large cracks can also be seen on the figure across the RL. Crack propagation stops at the copper interlayer and at the RL/zircaloy interface.

At 1223 K the copper layer is completely dissolved; the obtained microstructure is presented in the Fig. 1 (b). Once a zirconium rich solution is in contact with the steel, a chromium rich α-(Fe,Cr) ferrite layer of about 5 µm forms at the steel interface, as previously reported in [14]. This α-(Fe,Cr). In the direct vicinity of the ferrite layer is a C36-(Fe,Cr) Laves phase (dark grey on the

image) is observed which contains a high amount of chromium. Concerning the composition of the compound, the measured values are in good agreement with the thermodynamic description of Yang et al. [10] for the amount of chromium though a higher amount of Zr was measured in this work. It has to be noted that this phase dissolves a very low amount of Ni and Cu. In the reaction layer, the C36 Laves phase is in equilibrium and interconnected with a phase identified as the tetragonal t-FeZr phase which was liquid at the treatment temperature. Its low melting point of 1220 K in the binary Fe-Zr system [11] can be decreased with the presence of significant amounts of Ni and Cu. The t-FeZr$_2$ phase was found to contain an amount of Cr below 1 at.%, again in agreement with the litterature [10], while significant amounts of copper and nickel were measured in this phase.
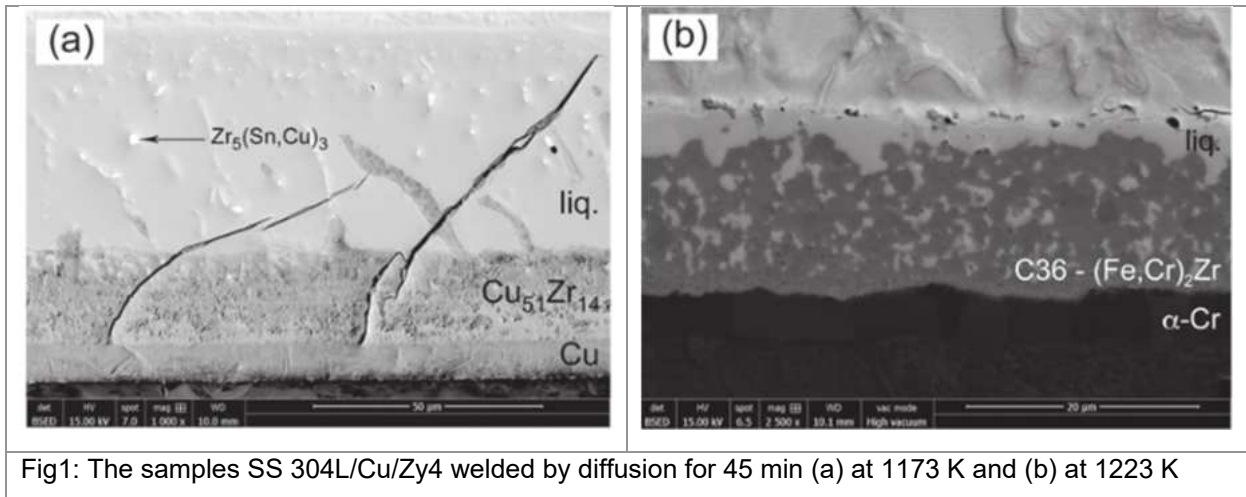
Fig1: The samples SS 304L/Cu/Zy4 welded by diffusion for 45 min (a) at 1173 K and (b) at 1223 K

References

[1] P.S. Hill, R.I. Todd, N. Ridley, J. Mater. Proce. Tech. 135 (2003) 131–136.

[2] M. Mazar Atabaki, A. Talebi Hanzaei, Mater. Char. 61 (2010) 982–991.

[3] M. Taouinet, S. Lebaili, N. Souami, Phy. Proc. 2 (2009) 1231–1239.

[4] H.I. Shaaban, F.H. Hammad, J.L. Baron, J. Nucl. Mater. 78 (1978) 431–433.

[5] J.I. Akhter, M. Ahmad, M. Iqbal, M. Akhtar, M.A. Shaikh, J. Alloys Comp. 399 (2005) 96–100.

[6] H. Chen, C. Long, T. Wei, W. Gao, H. Xiao, L. Chen, Mater. Desi. 60 (2014) 358–362.

[7] D. Aboudi, S. Lebaili, M.Taouinet, and J. Zollinger, Mater. Des. 116 (2017) 386–394.

[8] W. Gierlotka, K.C. Zhang, Y.P. Chang, J. Alloys Comp. 509 (2011) 8313–8318.

[9] O. Taguchi, Y. Iijima, K. Hirano, J. Alloys Comp. 215 (1995) 329–337.

[10] Y. Yang, L. Tan, H. Bei, J.T. Busby, J. Nucl. Mater. 441 (2013) 190–202.

[11] F. Stein, G. Sauthoff, M. Palm, J. Phase Equil. 23 (2002) 480–494.

www.conventus.de

Thinking
outside
the box

As a full-service PCO, we provide you with intelligent and innovative solutions in an advisory and implementing manner.

conventus
CONGRESSMANAGEMENT

© victor zastol'skiy / Fotolia